

# **Squeezing in the Audio Gravitational Wave Detection Band**

**Kirk McKenzie**

B. Sc. (Hons), Australian National University, 2002.

A thesis submitted for the degree of  
Doctor of Philosophy  
at the Australian National University



Submitted  
6 February 2008



For

my parents and grandparents.



---

# Declaration

---

This thesis is an account of research undertaken between March 2002 and February 2008 at The Department of Physics, Faculty of Science, The Australian National University, Canberra, Australia.

Except where acknowledged in the customary manner, the material presented in this thesis is, to the best of my knowledge, original and has not been submitted in whole or part for a degree in any university.

---

Kirk McKenzie  
February, 2008



---

# Acknowledgements

---

I would like express my sincere gratitude to the many people who supported me and contributed the research throughout my PhD.

Firstly, I would like to acknowledge my supervisors: Professor David McClelland, Professor Ping Koy Lam, and Associate Professor Malcolm Gray, for their contributions to the research presented here and its success.

I have studied with David at the Centre for Gravitational Physics (or its former identities) since the year 2000. I greatly appreciate David's contribution to my research and to my development as a scientist. David's ability to understand experimental intricacies whilst maintaining a view to the big picture has been invaluable. I also appreciate the many possibilities that David has given me to travel, collaborate, and research internationally.

Ping Koy has offered constant assistance and insight and understanding into many areas of quantum optics pursued in this thesis and also my prior research. Ping Koy's ability to break down complex phenomena into simple models and enthusiasm for the research were greatly appreciated.

Much of the success of the laboratory work is attributable to Mal's insight into optics problems and his laboratory skill. I admire and try to emulate Mal's rigour in experimenting. Mal was also largely responsible for the design of many of the electronics used in the experiments.

I would like to acknowledge Nicolai Grosse for the help on audio frequency squeezing work presented in chapter 6. The original setup for that experiment was built and designed by Warwick Bowen. Stan Whitcomb also offered valuable and timely assistance for that project. The squeezing experiments presented in chapter 7 were undertaken with Stefan Gossler and, later, Ben Buchler. Stefan also (re)designed and built the high resonant frequency PZT. Sheon Chua made valuable contributions homodyne noise measurements in chapter 7. Thanks to our MIT colleagues: Keisuke Goda, Nergis Mavalvala, and Eugeny Mikhailov for the fruitful collaborations and their contribution to the theory of noise coupling in down-conversion and to the theory of quantum noise locking. Thanks to James Dickson for designing, building, and debugging many of the electronic devices used in the experiments.

I would like to thank the many talented people that form my peer group at uni: Jong Chow, Conor Mow-Lowry, Glenn de Vine, David Rabeling, Simon Haine, Stefan Gossler, Ben Sheard, Ben Buchler, Nicolai, Magnus Hsu, Bram Slagmolen, James Dickson, Jeff Cumpston, and Daniel Shaddock. I have genuinely enjoyed my time as a PhD student largely due to interacting with these folk on a day to day basis and have learned a great deal though many detailed discussions. Particular mention goes to Conor, Jong, Glenn, Daaf, Simon, and Ben S who undertook this PhD journey at, more or less, the same time as me and who always had time for a chat or a 'meetings' at the coffee shop.

Many of the components used in the experiments were original designs built in-house by the workshop staff: Paul MacNemara, Paul Tant and Neil Delvin. Thanks go to these guys for their assistance. Thanks to go the physics department administration staff, particularly to Damien Hughes, who fought many battles to ensure I was getting paid.

Was fortunate enough to visit the Caltech 40m interferometer between October 2006 and March 2007 on the LIGO Visitor Program. Although the research I was involved in there isn't presented in this thesis, I learned a great deal in experimental gravitation there. Would like express

my gratitude to Alan Weinstein and the 40m team. Specifically, I would like to thank Rana Adhikari, Robert Ward, Steve Vaas, Sam Waldman, Valera Frolov, Tobin Fricke, Osamu Miyakawa, Keisuke Goda and Bram Slagmolen. Thanks also go to Robert and Marie-Helene, and Stan and Laurie, for their hospitality during my stay in Pasadena.

Thank you to David, Ben, Mal, Dad, Angie for proof read this thesis. In particular, thanks to Conor who read it in its entirety and significantly improved the clarity and style.

Sometimes it has seemed like a marathon to submission (if only it was so easy!). I thank my family and friends for being there for me every step of the way and offering valuable distractions. Thanks Angie, Zoe B, Hugh, Dave, Lee, Maya, Elijah, Riley Asha, Zoe C, Tom, Debbie and Ken. Kyoto for being an excellent distraction and an impeccable running partner. Mum and Dad for unwavering encouragement and support.

Lastly, I owe my deepest thanks to Ella for her love and companionship.

---

# Abstract

---

Quantum mechanical fluctuations of the electromagnetic field impose the ultimate limit to the precision of interferometric measurements. The first generation of long baseline interferometric gravitational wave detectors see this *quantum noise limit* over much of their sensitive frequency band. Second generation detectors, which are planned to be ten times more sensitive, are expected to be quantum noise limited over the majority of the audio gravitational wave detection band (Fourier frequencies of 10Hz to 10kHz).

This thesis presents research toward breaching the quantum noise limit in interferometric gravitational wave detectors. Specifically, we report the first measurement of squeezed states audio gravitational wave detection band.

A below threshold optical parametric oscillator is used to generate a squeezed vacuum states. Quantum noise suppression down to sideband frequencies of 70Hz is measured with up to 5.5dB (72%) of locked suppression measured at higher frequencies. We compare the squeezing produced in optical parametric amplifiers and optical parametric oscillators theoretically and experimentally. We find that classical noise sources, such as laser amplitude and phase noise, couple into the squeezed states produced by optical parametric amplifiers but have negligible effect on squeezing produced by a below threshold optical parametric oscillators. This makes below threshold optical parametric oscillators ideal for producing audio frequency squeezing. We trial Mg:LiNbO<sub>3</sub> and PPKTP as nonlinear medium and find that PPKTP has advantages of a higher nonlinearity, broader phase matching curve, and smaller photothermal effect.

Also presented are two control techniques that were developed in parallel to the audio frequency squeezing research. These techniques are; quantum noise locking, and phase matching locking.

Quantum noise locking is used to control the quadrature phase of squeezed vacuum states for the long term measurements in this thesis. Quantum noise locking is relied upon since standard readout techniques cannot be used for squeezed vacuum states. A detailed theoretical and experimental investigation of quantum noise locking in two experimental systems is undertaken. The first system is quantum noise locking of squeezed states. The second system is the quantum noise locking of the phase of two coherent fields. This second system allows quantum noise locking is compared directly to a standard dither locking technique and found to have inferior noise performance. The quantum noise locking experiments operate with a noise floor of about  $1\text{nm}/\sqrt{\text{Hz}}$ .

Phase matching locking technique is a new technique developed to readout the phase mismatch of second order nonlinear interactions interferometrically. We describe the technique theoretically and demonstrated it experimentally in a doubly resonant optical parametric amplifier. Phase matching locking is found to be useful to negate offsets in phase matching condition and to reduce the phase matching jitter compared to a system without it. We achieve relatively fast temperature feedback to the phase matching condition using the photothermal effect, by modulating the amplitude of pump beam of the optical parametric amplifier.



---

# Contents

---

<b>Declaration</b>	<b>v</b>
<b>Acknowledgements</b>	<b>vii</b>
<b>Abstract</b>	<b>ix</b>
<b>1 Introduction</b>	<b>1</b>
<b>I Background</b>	<b>5</b>
<b>2 The detection of gravitational waves</b>	<b>7</b>
2.1 Gravitational waves . . . . .	7
2.1.1 Gravitational wave sources . . . . .	8
2.2 Gravitational wave detectors . . . . .	9
2.2.1 Resonant mass detectors . . . . .	9
2.2.2 Inteferometric Detectors . . . . .	9
2.2.3 Interferometer configurations . . . . .	10
2.3 Current Interferometric Gravitational Wave Detectors . . . . .	10
2.3.1 Second generation detectors . . . . .	11
2.4 Noise sources in terrestrial interferometric detectors . . . . .	12
2.4.1 Noise sources . . . . .	12
2.5 Space based interferometric gravitational wave detectors . . . . .	14
2.6 Chapter summary . . . . .	15
<b>3 Quantum optics and nonlinear devices</b>	<b>17</b>
3.1 The quantised electromagnetic field . . . . .	17
3.1.1 The Heisenberg uncertainty principle . . . . .	18
3.1.2 Important states of light . . . . .	19
3.2 Mirrors, photodetection, and losses . . . . .	22
3.2.1 A partially transmissive mirror . . . . .	22
3.2.2 Direct photodetection . . . . .	23
3.2.3 The two-ported homodyne detector . . . . .	24
3.2.4 The effect of optical losses . . . . .	26
3.3 Fabry-Perot interferometers . . . . .	27
3.3.1 Equation of motion for an optical resonator . . . . .	27
3.3.2 Compact matrix formalism for the equations of motion . . . . .	28
3.3.3 Reflected and transmitted fields . . . . .	29
3.3.4 Noise variances of the reflected and transmitted fields . . . . .	31
3.3.5 Useful cavity parameters . . . . .	32
3.4 Nonlinear interactions . . . . .	33
3.4.1 $\chi^{(2)}$ nonlinear interactions . . . . .	34

3.4.2	Coupled wave equations and phase matching . . . . .	34
3.5	$\chi^{(2)}$ nonlinearity in an optical cavity . . . . .	38
3.5.1	Equations of motion . . . . .	38
3.5.2	Optical parametric amplification: a semiclassical approach . . . . .	39
3.5.3	Classical parametric gain . . . . .	40
3.5.4	Noise variances in parametric down-conversion . . . . .	41
3.5.5	Optical parametric amplification verses optical parametric oscillation . . . . .	43
3.6	Chapter summary . . . . .	44
<b>4</b>	<b>Quantum noise and squeezing in interferometric gravitational wave detectors</b>	<b>45</b>
4.1	Overview . . . . .	45
4.2	Quantum noise limits . . . . .	45
4.2.1	Input-output relations of a Michelson interferometer . . . . .	46
4.2.2	Quantum noise limited sensitivity . . . . .	48
4.3	Gravitational wave detectors with quantum correlations . . . . .	49
4.3.1	Quantum noise of conventional interferometers . . . . .	50
4.3.2	Signal recycled gravitational wave detectors . . . . .	52
4.3.3	Squeezing in a signal recycled interferometer . . . . .	53
4.4	Chapter summary . . . . .	54
<b>II</b>	<b>Development of Audio Frequency Squeezing</b>	<b>55</b>
	<b>Overview: Low Frequency Squeezing for Gravitational Wave Detectors</b>	<b>57</b>
<b>5</b>	<b>Noise couplings in parametric down-conversion</b>	<b>63</b>
5.1	Introduction . . . . .	63
5.2	Equations of motion and cavity fields . . . . .	64
5.3	Quadratures of the transmitted fields . . . . .	67
5.4	Variances of the transmitted fields . . . . .	68
5.4.1	A simplified case . . . . .	69
5.5	Noise budget of a OPA . . . . .	71
5.5.1	Model parameters . . . . .	71
5.5.2	A simplified case . . . . .	73
5.5.3	Including cavity detuning . . . . .	74
5.6	Discussion of the squeezing from a parametric down-converter . . . . .	75
5.7	Summary . . . . .	77
<b>6</b>	<b>Squeezing in the audio gravitational wave detection band</b>	<b>79</b>
6.1	Introduction . . . . .	79
6.2	Experiment Details . . . . .	79
6.3	Squeezing from an OPA . . . . .	82
6.4	Squeezing from an OPO . . . . .	84
6.5	Chapter summary . . . . .	86
<b>7</b>	<b>Stable audio frequency squeezing from a doubly resonant OPO</b>	<b>87</b>
7.1	Introduction . . . . .	87
7.2	OPO design considerations . . . . .	88
7.2.1	Doubly resonant OPO vs. singly resonant OPO . . . . .	88

7.2.2	Traveling-wave vs. standing-wave cavity . . . . .	89
7.3	The experiment . . . . .	89
7.4	Squeezed state measurements . . . . .	91
7.5	Limits to balanced homodyne detection at low frequencies . . . . .	94
7.5.1	Balanced homodyne detector noise budget . . . . .	95
7.5.2	Discussion of candidates for the low frequency excess noise . . . . .	100
7.6	Chapter summary . . . . .	100
<b>8</b>	<b>Squeezing in second generation gravitational wave detectors</b>	<b>101</b>
8.1	Introduction . . . . .	101
8.2	Models for noise . . . . .	102
8.2.1	Hardware and facility noise . . . . .	102
8.2.2	Quantum noise . . . . .	102
8.3	Results . . . . .	106
8.4	Discussion of assumptions and values . . . . .	108
8.4.1	Squeezing magnitude and frequency dependence . . . . .	108
8.4.2	Levels of optical losses in the interferometer and detection . . . . .	109
8.4.3	Laser power . . . . .	109
8.4.4	Hardware and facility noise . . . . .	109
8.5	Chapter summary . . . . .	110
<b>III</b>	<b>Locking Techniques</b>	<b>111</b>
<b>9</b>	<b>Quantum noise locking</b>	<b>113</b>
9.1	Introduction . . . . .	113
9.2	Derivation of the noise locking error signal . . . . .	115
9.2.1	Case I: Locking the phase of coherent fields . . . . .	116
9.2.2	Case II: Locking a squeezed vacuum state . . . . .	118
9.3	Experimental demonstration of quantum noise locking . . . . .	120
9.3.1	Experimental analysis of case I: Locking of coherent fields . . . . .	120
9.3.2	Experimental analysis of case II: Locking of a squeezed vacuum state . . . . .	124
9.4	Analysis of the noise performance of quantum noise locking . . . . .	126
9.4.1	Case II: A squeezed vacuum state . . . . .	126
9.4.2	Case I: Locking coherent fields . . . . .	128
9.5	Discussion . . . . .	129
9.6	Chapter summary . . . . .	130
<b>10</b>	<b>Phase matching locking via optical readout</b>	<b>131</b>
10.1	Introduction . . . . .	131
10.2	Nonlinear gain in a doubly-resonant OPA . . . . .	133
10.3	Derivation of a phase matching locking error signal . . . . .	136
10.4	An experimental demonstration of phase matching locking . . . . .	139
10.4.1	Experimental setup . . . . .	139
10.4.2	Results . . . . .	140
10.4.3	Discussion . . . . .	141
10.5	Chapter summary . . . . .	143

<b>11</b>	<b>Conclusions and further work</b>	<b>145</b>
11.1	Summary of audio frequency squeezing research . . . . .	145
11.2	Summary of locking techniques . . . . .	146
11.3	Further work . . . . .	146
11.3.1	Shot noise limited measurement of squeezing across the audio band . . .	146
11.3.2	Considerations for a squeezer to use in an interferometric gravitational wave detector . . . . .	147
<b>A</b>	<b>Quantum Noise in a Michelson Interferometer</b>	<b>151</b>
<b>B</b>	<b>Comparison of MgO:LiNbO<sub>3</sub> and PPKTP for OPO</b>	<b>157</b>
B.1	Phase-matching curves . . . . .	157
B.2	Measurement of the parametric gain . . . . .	158
B.3	Squeezing from a doubly resonant OPO . . . . .	158
<b>C</b>	<b>Experimental components and techniques</b>	<b>163</b>
C.1	The laser, SHG, and modecleaner . . . . .	163
C.1.1	The laser . . . . .	163
C.1.2	The second harmonic generator . . . . .	164
C.1.3	The Modecleaner Cavity . . . . .	164
C.2	Dispersion compensation in a doubly resonant cavity . . . . .	166
C.3	High resonance frequency PZT Design . . . . .	167
<b>D</b>	<b>Homodyne detector noise budget</b>	<b>171</b>
D.1	Homodyne detector experiment . . . . .	171
D.1.1	Local oscillator intensity noise coupling . . . . .	171
D.1.2	Beam jitter noise . . . . .	172
D.1.3	The use of a ‘low’ local oscillator power . . . . .	173
<b>E</b>	<b>Photodetector Circuit</b>	<b>175</b>
<b>F</b>	<b>The shot noise limit of phase-matching locking</b>	<b>177</b>
F.0.4	The shot noise in of the dither locking error signal in transmission . . . .	179
F.0.5	Shot noise limited displacement sensitivity of PDH . . . . .	180
F.0.6	Shot noise in phase matching locking . . . . .	180
	<b>Bibliography</b>	<b>183</b>

---

# List of Figures

---

1.1	Structure of this thesis. . . . .	2
2.1	The distortion that a gravitation wave causes as it passes (into the page) through a ring freely falling particles. The two polarizations, $h_+$ and $h_\times$ , are shown at different intervals of the gravitational wave period, $T$ . The strain amplitude in the figure is $h = 0.25$ . . . . .	8
2.2	(a) Layout of the Michelson interferometer. (b) Layout of a power- and signal-recycled Michelson interferometer with Fabry-Perot arm cavities. . . . .	9
2.3	Design strain sensitivity of LIGO, VIRGO, GEO, and Advanced LIGO. . . . .	11
2.4	Design strain sensitivity of LIGO with the three limiting noise sources seismic noise, suspension thermal noise and quantum noise. . . . .	12
2.5	Expected displacement contributions of various noise for the Advanced LIGO detector in wideband operation. Plot made using Bench, Version 6.2 [1]. . . . .	13
2.6	The LISA constellation. LISA will have 5,000,000 km long arms. The constellation is inclined to the ecliptic by $60^\circ$ and orbits the Sun $20^\circ$ behind the Earth. Adapted from [2] . . . . .	15
2.7	The designed LISA strain sensitivity. From [3] . . . . .	15
3.1	Ball and stick picture for four states of light: (a) The coherent state, (b) The vacuum state, (c) The amplitude squeezed states, and (d) The classically noisy state. . . . .	20
3.2	The frequency domain phasor diagram, or sideband picture of (a) the coherent state, and (b) the amplitude squeezed state. The coherent state has white noise distributed equally in all quadratures whereas the amplitude squeezed state has increased noise in the phase quadrature and reduced noise in the amplitude quadrature. . . . .	21
3.3	A partially transmissive mirror at normal incidence has two inputs and two outputs. The fields $a, b, c, d$ are labeled for a partially transmissive mirror with fields at (a) normal incidence incident and (b) at $45^\circ$ . The + and - signs indicates the side where the amplitude reflectivity receives a minus sign. Note that we have only considered half of the inputs and outputs of figure (b). . . . .	23
3.4	a) The two-ported homodyne detector. The small signal $a$ is interfered on a beam-splitter with the local oscillator, $b$ . The detected photocurrents can be either added or subtracted. (b) A model for inefficient detection where a mirror represents the loss introduced by a non-ideal photodetector. . . . .	25
3.5	Layout of a ring cavity. The cavity is made from three mirrors: the input coupler, with decay rate, $\kappa_{in}$ ; the output coupler, with decay rate, $\kappa_{out}$ ; and a mirror to represent intra-cavity loss, with decay rate, $\kappa_l$ . The cavity mode is labeled $a$ . The extra-cavity fields are: $A_{in}, A_{ref}, A_{trans}, \delta A_{out}, A_{loss}$ , and $\delta A_l$ . . . . .	27
3.6	(a) The reflectivity and transmissivity and (b) the phase shift in reflection and transmission of an overcoupled cavity as a function of detuning. Parameters: $L = 2\text{m}$ , $\lambda = 1\mu\text{m}$ , $T_{in} = 0.11$ , $T_{out} = 0.10$ , and $T_{loss} = 0$ . . . . .	30

LIST OF FIGURES

---

3.7	The amplitude quadrature noise variances of the reflected and transmitted fields relative to the shot noise limit (SNL) with 10dB of excess amplitude noise on the input field. Cavity parameters are the same as described in the caption of figure 3.6.	32
3.8	A representation of different $\chi^{(2)}$ nonlinear interactions. Left: Up-conversion; Two low energy photons (at $\omega_1$ and $\omega_2$ ) are converted into one higher photon (at $\omega_3$ ). Right: Down-conversion; One high energy photon (at $\omega_3$ ) is converted into two lower energy photons (at $\omega_1$ and $\omega_2$ ).	34
3.9	Real and imaginary components of the phase matching parameter, $g(\Delta kL)$ .	35
3.10	Phasor representation of the resultant second harmonic field ( $E^{2\omega}(z)$ ) for: (a) a phase mismatched material, (b) a quasi phase matched material, and (c) a phase matched material. (reproduced from [4] and [5])	36
3.11	The power in the second harmonic vs the interaction length. Curve (i) shows a phase mismatched material with $\Delta kz = \pi/2$ . Curve (ii) is the quasi phase matched material with $\Delta kz = \pi/2$ and domain period $\Lambda = l_c$ . Curve (iii) represents the phase matched case ( $\Delta kz = 0$ ).	37
3.12	A schematic of an OPA. The fundamental and harmonic cavity modes are $a$ and $b$ . Extra-cavity fields are denoted with capital letters. DC is a dichroic mirror.	39
3.13	Parametric gain of the seed field given by equation 3.116. Amplification ( $\phi = 0$ ) and deamplification ( $\phi = \pi$ ) are shown in curves (i) and (ii).	41
3.14	Variances of the transmitted field from an OPA plotted relative to the shot noise limit (SNL). Figure (a) is plotted as a function of pump power, and figure (b) as a function of sideband frequency. Curves (i) and (ii) show the variances neglecting intra-cavity losses and curves (iii) and (iv) show the variances calculated with intra-cavity losses. In both figures the variances of the input fields have been set in the vacuum state: $V_{1,2}^{(in)} = V_{1,2}^{(out)} = V_{1,2}^{(l)} = 1$ . Cavity parameters: $L = 2\text{m}$ , $\lambda = 1\mu\text{m}$ , $T_{out}^a = 0.10$ , $q = \kappa^a/2$ . In the lossless case: $T_{in}^a = T_l^a = 0$ , with losses $T_{in}^a = 0.001$ , $T_l^a = 0.01$ .	42
3.15	(a) Schematic of the OPA process. In OPA the seed field has a coherent amplitude and the squeezed state produced is a bright squeezed state. (b) Schematic of the OPO process operated below threshold. The seed field in OPO is the vacuum state and the squeezed state produced is a squeezed vacuum state.	44
4.1	(a) A Michelson interferometer. The asymmetric port input and output fields are denoted $a_i$ and $b_i$ . The laser power at the symmetric port is $I_0$ . (b) A Michelson interferometer with a squeezed state injected into the asymmetric port.	46
4.2	Phasor representation of the input-output relations of a Michelson interferometer. The input field is shown in the leftmost column, and the outputs in the middle column and the rightmost column. The output contains a classical gravitational wave signal and the fluctuations of the outgoing field. In the radiation pressure noise limited (RPNL) regime, the output phase noise is dominated by the amplitude induced phase fluctuations, whereas in the shot noise limited (SNL) regime, it is simply the phase fluctuations of the vacuum input field.	47
4.3	(a) Quantum noise limited strain sensitivity of a Michelson interferometer. (b) Michelson interferometer strain sensitivity with 10dB of squeezing injected into the dark port, with different squeezing angles.	48

LIST OF FIGURES

---

4.4	Phasor representation of the input-output relations of a Michelson interferometer with (a) phase squeezing and (b) amplitude squeezing. For comparison, the input-output relations are also plotted for the vacuum state, indicated by the circle and ellipses with dashed lines. . . . .	50
4.5	(a) Strain sensitivity of a conventional interferometer. (b) Strain sensitivity of a conventional interferometer with 10dB of squeezing injected into the dark port, with different squeezing angles. $m = 40\text{kg}$ $L = 3995\text{m}$ , $T = 0.033$ , $\omega_0 = 1.77 \times 10^{15}\text{rads}$ and $I_0 = I_{SQL}$ . . . . .	51
4.6	(a) Quantum noise of a signal recycled Michelson interferometer with arm cavities. (b) Quantum noise with 10dB ( $R = 1.15$ ) and $\zeta = \pi/2$ for different $\lambda$ . Interferometer parameters can be found in Table 8.1 . . . . .	53
4.7	Reported squeezing level over the last two decades in continuous-wave experiments (except for Bergman <i>et al.</i> which was pulsed). All results except for Slusher <i>et al.</i> and Bergman <i>et al.</i> were produced by parametric down-conversion processes. The ‘*’ denotes experiments where the noise contribution of electronic noise was not subtracted from the data. References are: Slusher <i>et al.</i> [6]; Wu <i>et al.</i> [7]; Grangier <i>et al.</i> [8]; Xiao <i>et al.</i> [9]; Polzik <i>et al.</i> [10]; Breitenbach <i>et al.</i> [11]; Schneider <i>et al.</i> (1) [12] and (2) [13]; Lam <i>et al.</i> [14]; Buchler <i>et al.</i> [15]; Suzuki <i>et al.</i> [16]; McKenzie <i>et al.</i> (1) [this thesis]; Vahlbruch <i>et al.</i> (1) [17] and (2) [18]; Goda <i>et al.</i> [19]; and Takeno <i>et al.</i> [20]. . . . .	57
4.8	Reported sideband frequency vs time. (Left) is a depiction of classical laser noise as a function of frequency. References (some are given in the caption of figure 4.7.), Bowen <i>et al.</i> [21], Schnabel <i>et al.</i> [22] Laurat <i>et al.</i> [23] McKenzie <i>et al.</i> (2) [24],(3) [25], Vahlbruch <i>et al.</i> (3) [26]. . . . .	59
5.1	A schematic of the parametric down-converter. The fundamental and harmonic cavity modes are $a$ and $b$ , respectively. Cavity inputs and output are denoted with capital letters. . . . .	66
5.2	The noise budget of an amplitude squeezed state, plotted as a function seed power. (a) shows the amplitude quadrature, and (b) the phase quadrature. . . . .	73
5.3	Noise budget of an phase squeezed state, plotted as a function seed power. (a) shows the amplitude quadrature, and (b), the phase quadrature. . . . .	74
5.4	The noise budget of an amplitude squeezed state plotted as a function seed power with different cavity detunings. In (a) $\bar{\Delta}^a/(2\pi) = \bar{\Delta}^b/(2\pi) = 0.05\%\text{FWHM}$ , in (b) $\bar{\Delta}^a/(2\pi) = \bar{\Delta}^b/(2\pi) = 0.5\%\text{FWHM}$ . . . . .	75
6.1	Schematic of the experiment. The parametric down-converter (labeled OPA/OPO) was pumped with light from the SHG and was seeded with a bright field/vacuum field. The squeezed state (SQZ) was detected on a homodyne detection by interfering it with the local oscillator (LO). The control electronics are indicated with dashed lines. VA-variable attenuator, MC-Modecleaner cavity, PZT-Peizo-electric transducer, BPF-band pass filter, ED-envelope detector, G-gain stage, PM-phase modulator, M-mixer, DC-dichroric mirror, PD-Photodetector, SPD-Spit photodetector, FI-Faraday isolator. . . . .	80
6.2	(Best viewed in colour) The OPA spectrum 2kHz-100kHz with different seed powers. The variance of the seed beam with power $6\mu\text{W}$ was less than 4dB above the SNL across the spectrum. RBW=128Hz. Electronic noise (at -12dB) was subtracted from all traces. . . . .	82

LIST OF FIGURES

---

6.3	The average noise power from 5-6kHz as a function of seed power, experimental data indicated by 'x', model fit given by curve (i). Electronic noise (at -12dB) was subtracted from all data. . . . .	83
6.4	The OPO spectrum from 100Hz to 3.2kHz without (i) and with (ii) the Faraday isolator between the OPO cavity and homodyne detector. RBW=8Hz. Electronic noise (not shown) was not subtracted . . . . .	84
6.5	Measured noise spectra for the homodyne, curve (i), the squeezed light, curve (ii), and the electronic noise of the homodyne detection system, curve (iii).The traces are pieced together from three FFT frequency windows: 100Hz-3.2kHz, 1.6kHz-12.8kHz, and 3.8kHz-100kHz. Each point is the averaged RMS value of 500, 1000 and 2000 measurements made in the respective ranges. The RBW of the three windows was 8Hz, 32Hz and 128Hz, respectively. The electronic noise was -12dB below the quantum noise from 10kHz-100kHz. The 20kHz peak arises from the homodyne modulation locking signal and is labeled (m). Peaks at 50Hz harmonics are due to electrical mains supply, labeled (e). . . . .	85
6.6	The squeezed state at 11.2kHz as the phase of the homodyne is varied. RBW=1kHz, VBW=30Hz. Electronic noise (9dB below SNL) was subtracted from the data. . . . .	86
7.1	Schematic of the experiment. The OPO was pumped with the SHG and was seeded with vacuum. The bow-tie OPO cavity was resonant for both fundamental and harmonic frequencies, containing a PPKTP crystal and a dispersion compensation window (DCW). Control electronics are indicated with dashed lines. SQZ-squeezed state, LO-local oscillator, MC-Modecleaner, PZT-piezo-electric transducer, BPF-band pass filter, ED-envelope detector, G-gain stage, SHG-second harmonic generator, PM-phase modulator, PZT-piezo electric transducer, DC-dichroic mirror, PD-Photodetector, M-mixer. Modematching optics are not shown. . . . .	90
7.2	OPO cavity design. Length dimension are millimeters, angles in degrees. . . . .	91
7.3	Measured noise spectra for the homodyne noise limit; the squeezed light; the electronic noise of the homodyne detection system; and the calculated shot noise limit (SNL).The curves are pieced together from three FFT frequency windows 100kHz-1.024kHz, 3.2kHz-160Hz, and 200Hz-10Hz. The RBW of the three windows was 128Hz, 4Hz, and 1/2Hz, respectively. Peaks at 50Hz harmonics are due to electrical mains supply. . . . .	92
7.4	Measured noise spectra for: (i) the squeezed state; (ii) the homodyne detection noise limit; (iii) the calculated shot noise limit; and (iv) the electronic noise of the detection system. The curves are pieced together from three FFT frequency windows 100kHz-1.024kHz, 3.2kHz-160Hz, and 200Hz-10Hz. The RBW of the three windows was 128Hz, 4Hz, and 1/2Hz, respectively. . . . .	93
7.5	(a) The frequency dependence of the squeezed and anti-squeezed quadratures from the OPO. This show the reduction of squeezing and anti-squeezing amplitude outside the cavity linewidth. Also shown are theory curves with parametric gain of 12dB, and total detection efficiency of $\eta_{tot} = 0.74$ . Experimental parameters: $\eta_{hom} = 0.89$ , RBW = 100kHz, VBW = 1kHz. (b) The time domain measurement taken at 100kHz of: (i) the shot noise limit, (ii) the squeezed state with detection phase locked, (iii) the electronic noise of the detection system, and (iv) the squeezed state with the detection phase varied. RBW=1kHz, VBW=30Hz. . . . .	94

LIST OF FIGURES

---

7.6	Measurement of squeezing at 100kHz, curve (ii), as a function of time. Also shown: (i) the average value of the shot noise and (iii) the average value of the electronic noise. RBW = 10kHz, VBW = 30Hz. . . . .	95
7.7	An incomplete noise budget for the homodyne detector. Shown are contributions due to: (i) local oscillator intensity noise, (ii) beam jitter noise, (iii) photodetector electronic noise, and (iv) the measured homodyne spectrum. The ‘total’ noise, curve (v), is the quadrature sum of curves (i), (ii), (iii) and the calculated shot noise. . . . .	96
7.8	Schematic of the non-stationary noise characterisation experiment. PD - photodetector, BD - beam dump, L - lens . . . . .	98
7.9	Spectra from the balanced homodyne with the experiment; (i) open to the laboratory environment; and (ii) sealed in a black perspex box. The large peaks at 50Hz and harmonics were due to pick-up of the mains power. . . . .	99
7.10	Histograms of the homodyne photocurrent with the experiment (a)closed to the laboratory environment and (b) open to the laboratory environment. The insets are a zoomed look at the histogram at high bin power. . . . .	100
8.1	Layout of a the Advandc LIGO detector with squeezing injection. Also shown is the sources of quantum noise considered in the model. They are labeled: (I) from the dark port, which is either a vacuum state or a squeezed state; (II) vacuum noise due to loss on the signal recycling mirror; (III) vacuum noise due loss in the arm cavities; and (IV) vacuum noise due to photodetector loss. . . . .	103
8.2	The hardware and facility noise, $h_{hf}$ , the quantum noise, $h_{qn}$ , and the total noise, $h_{tot}$ , for the unsqueezed case (No Sqz.) and with squeezed input of $e^{-2R} = 0.1, \lambda = \lambda_{opt}$ (10dB Sqz.). The parameters used are those expected for Advanced LIGO. (a) Shows Advanced LIGO ‘wideband’ operation and (b) narrowband operation. .	106
8.3	The proportion of quantum noise in the total noise for the Advanced LIGO configuration with unsqueezed input (No Sqz.) and squeezed input (10dB, $\lambda = \lambda_{opt}$ ). (a) Shows is the Advanced LIGO wideband operation and (b) the narrowband operation.	107
8.4	The squeezing enhancement of Advanced LIGO operated in wideband mode for: (a) different squeezed state amplitudes; and (b) different interferometer and detection losses. . . . .	108
8.5	Quantum and total noise curves for wideband Advanced LIGO with baseline input laser power ( $I_0=125W$ ) and lower input power ( $I_0=25W$ ). Also shown is lower input laser power Advanced LIGO with squeezed input of 10dB, optimally frequency dependent squeezing ( $I_0=25W, 10dB$ ). . . . .	109
9.1	Setup of a balanced homodyne detector with input fields, $\hat{a}(t)$ and $\hat{b}(t)$ , interfering with relative phase, $\theta$ , on a balanced beamsplitter. Here the local oscillator beam $\hat{b}(t)$ passes through a phase modulator (PM) with applied sinusoidal modulation at frequency $\Omega_m$ . The output fields, $\hat{d}(t)$ and $\hat{c}(t)$ , are incident on the photodetectors, $PD_d$ and $PD_c$ . To derive the quantum noise locking error signal, the output of the homodyne is bandpass filtered (BPF) then envelope detected (ED). The output of the envelope detector is demodulated and low pass filtered (LPF). . . . .	114

LIST OF FIGURES

---

9.2 Phasor diagram of the fields incident on the detectors showing the carrier at  $\Omega_C$  modulation sidebands at  $\Omega_m$ , the quantum noise (small red vectors) and the frequency relation of the bandpass filter frequencies (which has bandwidth  $\Delta\Omega$ ). Top figure shows the fields for case I, here the quantum noise is shot noise, and the two carrier fields at  $\Omega_C$  represent the field amplitudes of  $a$  and  $b$  with relative (dc) phase of  $\theta_0$ . The bottom figure shows fields for case II. Here the quantum noise is squeezed vacuum and the phase  $\theta_0$  determines the measured quadrature. . . . . 116

9.3 (i) The power at  $PD_d$  of a Mach-Zehnder interferometer with fringe visibility 0.8 and (ii) the error signal as the relative phase is varied. The error signal's zero crossing points indicate that the homodyne angle can be locked to either a dark or bright fringe by choosing the appropriate feedback sign. . . . . 118

9.4 The noise variance of a phase squeezed beam relative to the shot noise limit and the quantum noise locking error signal as the relative phase is varied. The error signal's zero crossing points indicate that the homodyne angle can be locked to observe both squeezing and anti-squeezing. The scale of the error signal is arbitrary. . . . . 119

9.5 An experimental schematic of the setup used to analyze noise locking. In the optics section: FI - Faraday isolator; PM - Phase modulator;  $\lambda/2$  - half-wave plate; PBS - Polarizing beam splitter; PZT - piezo electric transducer bonded onto a mirror;  $PD_d, PD_c$  - photodetectors. In the electronics section; Lock-in - Lock-in amplifier; BPF - Band pass filter; ED - envelope detector; LPF - Low pass filter; and HV amp - High voltage amplifier. . . . . 120

9.6 (a) The DC voltage on  $PD_c$  as the fringe is scanned (the photodetector is negatively coupled, thus lower voltage corresponds to higher incident power). (b) (i) The corresponding dither locking error signal and (ii) the quantum noise locking error signal. (c) Lock acquisition curve showing the quantum noise locking error signal and the voltage on  $PD_c$ . Initially, the control loop is open. At 0.4 seconds the control loop is closed and the interferometer is locked to a bright fringe on  $PD_c$  (dark fringe on  $PD_d$ ). Lock-in amplifier settings; LPF Time constant = 10ms, 6dB/octave for the both dither locking techniques. . . . . 121

9.7 (a) Spectral densities of the error signals whilst the interferometer was locked using the dither locking technique. Curves (i) and (ii) are the out-of-loop quantum noise locking error signal spectra of the bright and dark fringes (on  $PD_d$ ). Curves (iii) and (iv) are the in-loop dither locking error signal spectra of the bright and dark fringes (on  $PD_c$ ). (b) Spectral densities of the error signals whilst the interferometer was locked using the quantum noise locking technique. Curves (i) and (ii) are the out-of-loop dither locking error signal spectra of the bright and dark fringes (on  $PD_d$ ). Curves (iii) and (iv) are the in-loop quantum noise locking error signal spectra of the bright and dark fringes (on  $PD_c$ ). The excess noise of the quantum noise locking readout can be seen from the different amplitudes of the dither locking and quantum noise locking error signal spectra. DF = dark fringe, BF = bright fringe. . . . . 122

9.8 An schematic of the experiment to quantum noise lock a squeezed vacuum state. The box labeled 'SQZ' represents the squeezing apparatus. . . . . 123

LIST OF FIGURES

---

9.9	(a) The noise power of squeezed field (i) and noise power of shot noise (ii). The noise power units here are arbitrary, however the squeezed quadrature is approximately 3dB below the shot noise limit and the anti-squeezed quadrature is approximately 9dB above the shot noise limit. (b) The corresponding quantum noise locking error signal and PZT ramp. (c) Noise power of the squeezed and anti-squeezed quadratures using quantum noise locking. The measured shot noise and electronic noise are also shown. Measurements taken with zero span at 1MHz, RBW = 100kHz, VBW = 3kHz. . . . .	124
9.10	(a) The quantum noise locking error signal spectra whilst locked to the squeezed quadrature, curve (ii) and anti squeezed quadrature, curve (i). (b) Measurement of the squeezed quadrature over 34 minutes. The electronic noise at -11dB was not subtracted. Measurements taken with zero span at 100kHz, RBW = 10kHz, VBW = 30Hz. ASQZ = anti-squeezed quadrature, SQZ = squeezed. . . . .	125
9.11	Squeezing angle stability vs squeezing factor, $R$ , for the cases of quantum noise locking to the squeezed and anti-squeezed quadrature, for various levels of detection loss, $\mathcal{L}$ . . . . .	127
10.1	Schematic of an experiment to derive phase matching locking error signal from a doubly-resonant optical parametric amplifier (DROPA). The red (unbroken) lines indicate the fundamental (seed) field and the green (dashed) lines indicate the harmonic (pump) field. PDH error signals are derived for both cavities and differenced to give the phase-matching locking error signal. SHG - second harmonic generator, PM - phase modulator, DC1 & DC2- dichroic mirrors used to separate the fundamental and harmonic frequencies. $\chi^{(2)}$ indicates the nonlinear medium. . . . .	132
10.2	Examples of nonlinear gain (equation 10.14) vs temperature offset from phase matching. Curve (i) is a doubly resonant (DR) OPA with the harmonic cavity held on resonance ( $\Delta^b = 0$ ) and the fundamental detuning given by equation 10.11. Curve (ii) is a singly-resonant (SR) OPA with the fundamental cavity held on resonance ( $\Delta^a = 0$ ). The dashed curve (iii) gives the nonlinear gain envelope of the DROPA found when both fundamental and harmonic cavities are held on resonance ( $\Delta^b = \Delta^a = 0$ ). Parameters used are $P_{in}^b = .1W$ , $\epsilon_0 = 60$ 1/s, and $\theta = 0$ . . . . .	135
10.3	(a) The reflected power of the harmonic field as a function of cavity detuning; (b) the corresponding PDH error signal (equation 10.15) derived from the reflected light; (c) the transmitted power of the fundamental field as a function of detunings; and (d) the corresponding PDH error signal derived on transmission. . . . .	137
10.4	(a) The transmitted power of the fundamental field as a function of detuning; and (b) the corresponding phase-matching error signal derived on transmission. Here $ \epsilon \bar{b}  = 0.28\kappa_a$ . . . . .	138
10.5	A schematic of the experimental layout. Most of the laser power is used to produce the harmonic beam for the OPA. The harmonic beam is passed though a broadband amplitude modulator (AM) and a resonant (70MHz) phase modulator (PM) before reaching the OPA. The cavity length error signal is derived from the reflected harmonic field, and is fed back to PZT1. The phase matching error signal is derived from the transmitted fundamental field, and is fed back to the amplitude modulator on the harmonic field. The temperature of the crystal oven is actively controlled to 63°C. . . . .	139

*LIST OF FIGURES*

---

10.6	(a) The transmitted power from the OPA as the temperature of the crystal was varied by sweeping the oven temperature. The nonlinear gain was dithered at approximately 1kHz, which showed the nonlinear gain envelope (amplification and de-amplification). (b) The corresponding error signal of the phase matching condition. The dither signal of the nonlinear gain was filtered out of the error signal. . . . .	140
10.7	(a) The transmitted power of the OPA as a function of time. (b) The phase matching error signal. At 12.5 seconds the control loop is closed and the nonlinear gain is optimized. . . . .	141
10.8	The calibrated spectra of the phase matching locking error signal (i) with the control loop open, and (ii) with the control loop closed. . . . .	142
10.9	Measured (solid line) and theoretical (dashed line) photothermal response of the nonlinear crystal. (a) the amplitude response, and (b) the phase response. . . . .	143
11.1	(a) A layout for a heterodyne detection system, and (b) a phasor diagram of the local oscillator field. . . . .	147
11.2	Schematic of a next generation squeezer. . . . .	149
A.1	The fields in the Michelson interferometer. Capitalised letters represent classical fields, the quadrature fields are represented by the lower case letters. . . . .	152
B.1	Experimental Setup used to measure single pass SHG efficiency vs temperature. . . . .	157
B.2	Single pass second harmonic nonlinear conversion efficiencies as a function of temperature for: (i) PPKTP and (ii) LiNbO <sub>3</sub> . Note the different temperature scales on the horizontal axis. . . . .	158
B.3	Measurements of parametric gain as function of pump power and fitted curves. . . . .	159
B.4	Measured noise relative to the shot noise limit (SNL) obtained from (a) LiNbO <sub>3</sub> with output coupler (A), (b) LiNbO <sub>3</sub> with output coupler (B) and (c) PPKTP with output coupler (A). Figure (a) was measured at 50kHz and had RBW=3kHz, VBW=30Hz. Figures (b) and (c) were measured at 100kHz with RBW=10kHz, VBW=300Hz. . . . .	160
B.5	Expected squeezing level as a function of total loss and measured data points (squares). . . . .	161
C.1	Top view of the modecleaner cavity design. Lengths are in millimeters, angles in degrees. modecleanerdesign. . . . .	165
C.2	The measured (solid lines) and fitted (dashed lines) frequency responses for the modecleaner in low finesse (LF) and high finesse (HF) modes. The notch at 10.5kHz in the HF trace is thought to be a result of interaction of the amplitude modulation sidebands and the cavity length servo. . . . .	166
C.3	Transmission of the doubly resonant bow-tie cavity as the cavity length was scanned. (a) was taken without the dispersion compensation plate in the cavity, and it can be seen that the resonances for the 1064nm and 532nm cavities do not coincide. In (b), the dispersion compensation plate was in the cavity and tuned such that the 1064nm and 532nm resonances overlap. The silicon photo-detector used for these measurements was sensitive to both the 1064nm and 532nm light. These measurements were taken without a nonlinear crystal in the cavity, so the dispersion seen was a result of the cavity mirror coatings. . . . .	167

LIST OF FIGURES

---

C.4	(a) The dispersion compensation plate. (b) differential phase shift as a function of angle of incidence. Parameters used match the experimental values, the thickness $d = 6.35\text{mm}$ , $n(\omega_a) = 1.50663$ , $n(\omega_b) = 1.51947$ . . . . .	168
C.5	Drawings of the high resonance frequency peizo mount. . . . .	169
C.6	Transfer function of the high resonance frequency PZT. The low pass filter shape was caused by the combination of the capacitance of the PZT and the resistance of the source. . . . .	170
D.1	Schematic of the experimental set up Homodyne detection system. The laser field is passed though a phase modulator (PM), a broadband amplitude modulator (AM) a modecleaner cavity and is incident on the fast steering mirror (FSM). The signal beam was a vacuum state. QPD - quad-photodetector . . . . .	172
D.2	(a) The common mode rejection of the homodyne detector as a function of frequency measured via a transfer function measurement (solid line) and fitted curve (dashed line). The variable electronic gain was set to optimize the common mode rejection at low frequencies. (b) Curve (i), the intensity noise spectrum of the laser relative to the shot noise limit (SNL) measured from 10Hz-100kHz. Curve (ii) the intensity noise contribution to the homodyne detector spectrum inferred using curve (a) and the measured common mode rejection. . . . .	173
D.3	(a) Beam jitter measurements for the (a) vertical axis and (b) horizontal axis using the quad photodetector. (b) The RIN of the low frequency homodyne spectrum taken with AC on, curve (a) and, the estimated $RIN_{BJ}$ noise contribution of beam jitter to the homodyne spectrum, curve (b). Curve (c) is the calculated $RIN_{SNL}$ for $P_{opt} = 380\mu\text{W}$ and $\rho=0.7$ Amps/Watt. . . . .	174
E.1	Circuit layout of the photodetectors used in the homodyne detection system. . . .	176

*LIST OF FIGURES*

---

---

# List of Tables

---

4.1	Signal recycled Michelson interferometer parameters . . . . .	52
5.1	Parametric down converter parameters . . . . .	76
6.1	Experimental parameters of the parametric down-converter . . . . .	81
7.1	Experimental parameters of the doubly resonant OPO . . . . .	91
8.1	Advanced LIGO interferometer parameters . . . . .	110
10.1	Doubly-resonant OPA Cavity/Mg:LiNbO <sub>3</sub> Parameters . . . . .	136
B.1	doubly resonant OPO cavity parameters for (i) PPKTP and (ii) Mg:LiNbO <sub>3</sub> . . .	159
B.2	Experimental Efficiencies . . . . .	161
C.1	Mephisto 1200 Properties. For additional details see [27] . . . . .	163
C.2	Diabolo Properties. For details see [27] . . . . .	164
C.3	Modecleaner Cavity Parameters . . . . .	165



---

# Introduction

---

A global array of kilometer-scale interferometers has been constructed to detect gravitational waves signals of astronomical origin. These interferometers operate with remarkable precision and are expected to make the first direct gravitational wave detection. The first detection will mark the dawn of a new era of gravitational wave astronomy.

Just as first generation interferometric detectors reach their design sensitivities [28], technology and techniques for the second and third generation interferometric detectors are nearing maturity. Ideally, second generation detectors will operate with an order-of-magnitude better sensitivity than first generation interferometers, which will increase the detection rate a thousandfold, and improve the detail of detected signals.

The sensitivity of second generation detectors, such as Advanced LIGO [29, 30], is expected to be limited by *quantum noise* across the majority of the audio gravitational wave detection band - at Fourier frequencies from 10Hz to 10kHz. Quantum noise is the fundamental limit of interferometry, imposed by the quantum mechanical fluctuations of the light [31, 32]. To improve sensitivity beyond the quantum noise limit a *quantum non-demolition* (QND) technique is required [33]. A promising QND techniques for interferometric gravitational wave detectors uses *squeezed states* of light to breach the quantum noise limit [34–40].

This thesis is concerned with the generation of squeezed states of light suitable for use in interferometric gravitational wave detectors. Though the motivation for this research is specific, it is relevant for other quantum noise limited applications, such as: atomic force microscopy [41]; spectroscopy [42]; and QND techniques of Bose-Einstein Condensation [43].

This thesis has two central themes:

- 1. The production of squeezing in the audio gravitational wave detection band** While quantum fluctuations can never be removed from a laser field, they can be manipulated. A squeezed state of light has reduced fluctuations in one of its observable parameters (for example, its phase), whilst the conjugate parameter (the amplitude) has increased fluctuations. The key difference between the squeezing reported here and that previously reported is the sideband frequency. Before this work squeezing was typically produced at sideband frequencies of 1MHz and above, whereas for gravitational wave detectors require squeezed states between 10Hz and 10kHz.
- 2. Control techniques in quantum and nonlinear optics** The second part of this thesis is concerned with control techniques developed in parallel with the squeezing research. Two concepts are presented. First, quantum noise locking, a technique to control the quadrature phase of a vacuum squeezed state, and second, a technique to readout and control the phase matching condition of nonlinear materials interferometrically.

## Overview of this thesis

The structure of the thesis is shown in figure 1.1 and comprises three major parts. The first part, chapters 1, 2, and 3, is intended to provide the necessary background information for, and give context to, the research presented. The second part, chapters 4, 5, 6, 7, and 8, detail the development of audio-frequency squeezing - the core component of the thesis. In the final part, chapters 9 and 10, control techniques in quantum and nonlinear optics are developed. These techniques are related to the development of audio-frequency squeezing and its implementation in gravitational wave detectors, but have wider implications for nonlinear optics and quantum measurement.

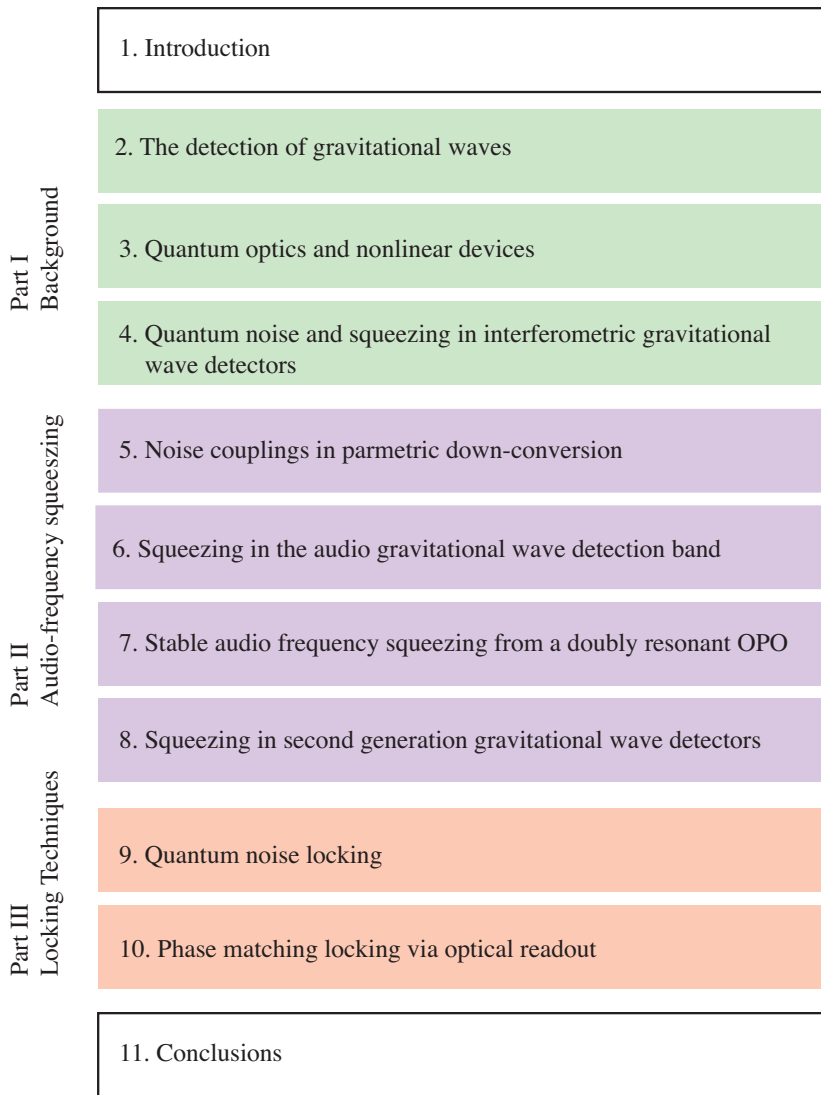


**Figure 1.1:** Structure of this thesis.

In detail, chapter 2 provides an introduction into gravitational waves and their detection. An overview of detectable sources, interferometric gravitational wave detector configurations, current and future detectors, and an overview into limiting noise sources in terrestrial interferometric detectors is presented.

Chapter 3 contains background into quantum optics and the formalism required to model the experiments in this thesis. It also contains an introduction to  $\chi^{(2)}$  nonlinearity, which is used to produce squeezed states of light.

---

Chapter 4 gives a detailed description of the quantum noise limit in interferometric detectors and possible squeezing enhancements. This chapter forms the basis of the theoretical investigations of chapter 8, where squeezing enhancements are considered in a more realistic interferometer.

Chapter 5 presents a theoretical model of the production of squeezed states from an optical parametric down-conversion process. This model shows key differences between optical parametric oscillators and optical parametric amplifiers. Sub-threshold optical parametric oscillation is shown to be an ideal means of producing low frequency squeezing.

In chapter 6 an experimental comparison of squeezed states produced in optical parametric oscillators and optical parametric amplifiers is made. A vital difference in classical noise coupling is found: the classical noise sources that degrades squeezing from an optical parametric amplifier do not couple to the squeezing from an optical parametric oscillator. This property allows squeezing to be produced from optical parametric oscillators at audio frequencies.

Chapter 7 details another audio-frequency squeezing experiment. This experiment addresses the main inadequacy of the experiment in chapter 6, namely, the long term stability. The squeezing produced was also of larger magnitude and measured at lower sideband frequencies. In the second part of the chapter, experimental limitations of homodyne measurements at low audio-frequencies are investigated.

Chapter 8 contains a calculation of the squeezing enhancements that can be made to a realistic detector. This calculation includes classical noise sources of the interferometer and optical losses. The Advanced LIGO detector is taken as a quantitative example, and the enhancements that can be made for different levels of laser power, squeezing, and loss are considered.

Chapter 9 presents an investigation into quantum noise locking, a technique based on determining the relative phase of an optical field from its quantum noise. Quantum noise locking of a squeezed vacuum state is demonstrated experimentally. Quantum noise locking is compared with a standard dither locking technique.

Chapter 10 describes a new interferometric technique developed to readout the phase matching condition of a  $\chi^{(2)}$  nonlinear process. The technique is described theoretically using quantum optics formalism, and is demonstrated experimentally.

Chapter 11 concludes the thesis. It includes a summary of the work contained in the thesis and discussion of possible extensions to this research.

## **Publications**

Some of the work presented in this thesis, and other work and completed during my time as a PhD student, has been published in, or submitted to, peer-reviewed journals. Papers published, accepted for publication, or submitted are listed below:

- *DC Readout experiment at the Caltech 40m prototype interferometer*  
R. L. Ward, R. Adhikari, B. Abbott, R. Abbott, D. Barron, R. Bork, T. Fricke, V. Frolov,

- J. Heefner, A. Ivanov, O. Miyakawa, K. McKenzie, B. Slagmolen, M. Smith, R. Taylor, S. Vass, S. Waldman, and A. Weinstein,  
Accepted for publication in *Classical and Quantum Gravity* (2008).
- *A Quantum-Enhanced Prototype gravitational wave Detector*  
K. Goda, O. Miyakawa, E. E. Mikhailov, S. Saraf, R. Adhikari, K. McKenzie, R. Ward, S. Vass, A. J. Weinstein, and N. Mavalvala,  
Submitted to *Nature Physics* (2008).
  - *Coating-free mirrors for high precision interferometric experiments*  
S. Goßler, J. Cumpston, K. McKenzie, C. M. Mow-Lowry, M. B. Gray,  
and D. E. McClelland,  
*Physical Review A* **76**, 053810 (2007).
  - *Using a Passive Fiber Ring Cavity to Generate Shot-Noise-Limited Laser Light for Low-Power Quantum Optics Applications*  
M. B. Gray, J. H. Chow, K. McKenzie, and D. E. McClelland,  
*IEEE, Photonics Technology Letters* **19**, 1063-1065 (2007).
  - *Technical limitations to homodyne detection at audio frequencies*  
K. McKenzie, M. B. Gray, P. K. Lam, and D. E. McClelland,  
*Applied Optics* **46**, 3389-3395 (2007).
  - *Nonlinear phase matching locking via optical readout*  
K. McKenzie, M. B. Gray, P. K. Lam, and D. E. McClelland,  
*Optics Express* **14**, 11256-11264 (2006).
  - *Harmonic entanglement with second-order non-linearity*  
N. Grosse, W. P. Bowen, K. McKenzie, and P. K. Lam,  
*Physical Review Letters* **96**, 063601(2006).
  - *Squeezed State Generation for Interferometric gravitational wave Detection*  
K. McKenzie, M. B. Gray, S. Goßler, P. K. Lam, and D. E. McClelland,  
*Classical and Quantum Gravity* **28**, S245-S250 (2006).
  - *Quantum Noise Locking*  
K. McKenzie, E. E. Mikhailov, K. Goda, P. K. Lam, N. Grosse, M. B. Gray, N. Mavalvala  
and D. E. McClelland,  
*Journal of Optics B* **7**, S421-S428 (2005).
  - *Photothermal Fluctuations as a Fundamental Limit to Low-Frequency Squeezing in a Degenerate Optical Parametric Amplifier*  
K. Goda, K. McKenzie, E. E. Mikhailov, P. K. Lam, D. E. McClelland and N. Mavalvala,  
*Physical Review A* **72**, 043819 (2005).
  - *Squeezing in the audio gravitational wave detection band*  
K. McKenzie, N. Grosse, W. P. Bowen, S. E. Whitcomb, M. B. Gray, D. E. McClelland and  
P. K. Lam,  
*Physical Review Letters* **93**, 161105 (2004).
  - *Analysis of a sub-shot noise power recycled Michelson interferometer*  
K. McKenzie, B. C. Buchler, D. A. Shaddock, P. K. Lam and D. E. McClelland,  
*Classical and Quantum Gravity* **21**, S1037-S1043 (2004)

**Part I**

**Background**



---

# The detection of gravitational waves

---

In Einstein's General Theory of Relativity [44], the force of gravity is described by the the curvature of space-time. A profound consequence of this theory is the prediction of gravitational waves [45], which are perturbations in space-time that propagate at the speed of light.

Indirect evidence for the existence of gravitational waves was provided by the discoveries of Hulse and Taylor, who were awarded in the Nobel Prize in 1993. They studied a binary neutron star system, PSR B1913+16 [46] in which one was a pulsar. Using pulsar timing measurements, it was found that orbital period of the binary system shifted over time, in a manner consistent with the system emitting quadrupole gravitational radiation [47, 48]. The direct detection of gravitational waves, however, is yet to be made.

This chapter provides an introduction to gravitational waves and their detection. Section 2.1 introduces gravitational waves and some of the most promising sources for detection. Section 2.2 provides an overview of gravitational wave detectors. Section 2.3 introduces current terrestrial interferometric detectors. In section 2.4 of terrestrial interferometric gravitational wave detectors are introduced. Limits come from classical displacements sources, such as seismic noise; from thermal noise; and from quantum noise of the electromagnetic field. The predicted values for the Advanced LIGO detector of these noise sources are presented as a quantitative example. A detailed study of the quantum noise limit in interferometric detectors is reserved for chapter 4. In section 2.5, we briefly introduce space-based detectors.

## 2.1 Gravitational waves

Gravitational waves are oscillations *in* space-time, fundamentally different to electromagnetic waves, which propagate *through* space-time. In this sense, gravitational waves are similar to pressure waves of sound propagating through air. Gravitational waves are emitted when a mass distribution changes in a non-spherically symmetric manner, and the lowest order mode of oscillation is quadrupole. They interact very weakly with matter, making them difficult to detect. It also means they propagate through space-time relatively unperturbed, offering a window on dynamics that are hidden to electromagnetic observations, such as stella core collapse in supernovae, or the workings of our galactic center.

The effect of a gravitational wave as it passes though a region of space can be visualised by considering its effect on a ring of particles in free fall, illustrated in figure 2.1. The effect of the two polarizations,  $h_+$  and  $h_\times$ , are shown over the wave period,  $T$ . As the gravitational wave passes perpendicular to the plane of the ring (i.e. into the page) the ring is stretched and squeezed in orthogonal directions. At the half period of the wave the axis of stretching and squeezing is reversed.

The amplitude of a gravitational wave can be characterized by the fractional length change it

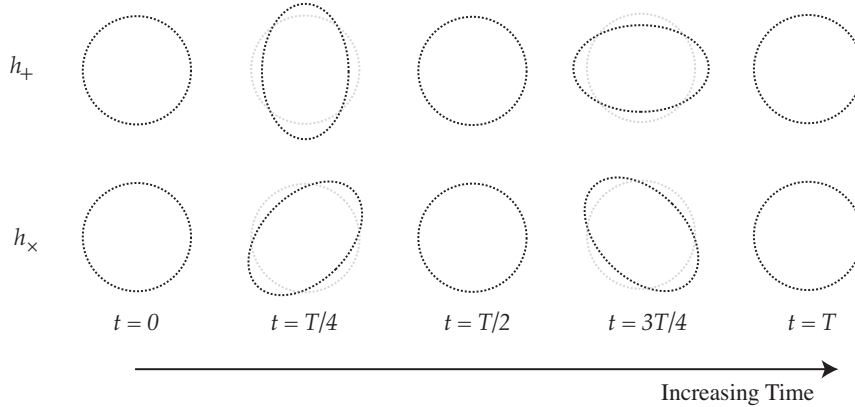


**Figure 2.1:** The distortion that a gravitation wave causes as it passes (into the page) through a ring freely falling particles. The two polarizations,  $h_+$  and  $h_\times$ , are shown at different intervals of the gravitational wave period,  $T$ . The strain amplitude in the figure is  $h = 0.25$ .

induces and is called *strain*,  $h$ , which is given by

$$h = \frac{\Delta L}{L}, \quad (2.1)$$

where  $\Delta L$  is a change in length over a given length,  $L$ . Even for astronomical scale events,  $h$  is expected to be very small. For example, the gravitational waves emitted by the coalescence of a binary neutron star system at a distance of a 100 Mpc are expected to have  $h \sim 10^{-21} - 10^{-22} 1/\sqrt{\text{Hz}}$  [49]. In figure 2.1 the strain amplitude has been vastly exaggerated for illustrative purposes, with  $h = 0.25$ .

### 2.1.1 Gravitational wave sources

The strongest emitters of gravitational waves are astronomical objects which have strong non-spherical dynamics. Examples of promising sources of detectable gravitational radiation are [50]:

**Binary inspirals** The coalescence of binary systems which contain high mass compact objects, such as neutron stars and black holes. Gravitational waves are emitted as the compact objects orbit, extracting energy and angular momentum from the binary system, causing the orbit to decay. As the orbital distance shrinks, the strength and frequency of the gravitational waves emitted increases, causing a chirp signal as the objects fall ever closer before they finally collide.

**Supernovae** If the stellar core collapse in a supernova is non-spherically symmetric, a burst of gravitational waves will be released. This is a potentially very interesting source to study, alongside electromagnetic and neutrino observations, as the internal dynamics of supernovae are poorly understood [49].

**Pulsars** Pulsars are born out of supernovae. If the pulsar is non-axisymmetric, then gravitational waves will be emitted as it spins. The amplitude of the gravitaitonal waves emmitted from a pulsar are proportional to the equatorial ellipticity and the square of the rotational frequency.

**Stochastic background** Analogous to the cosmic microwave background, the stochastic back-

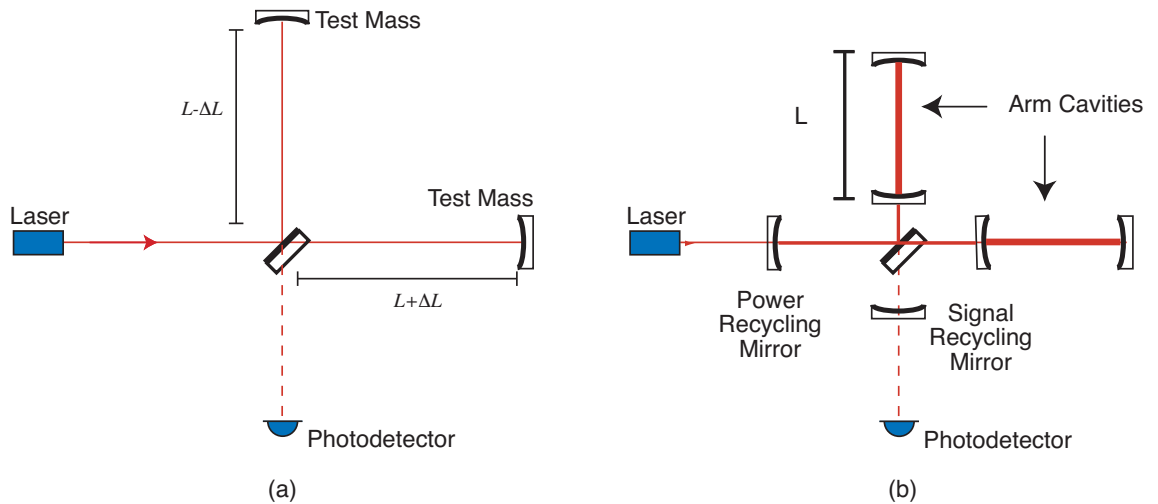


**Figure 2.2:** (a) Layout of the Michelson interferometer. (b) Layout of a power- and signal-recycled Michelson interferometer with Fabry-Perot arm cavities.

ground of gravitational waves is expected to originate from the dynamics in the early universe.

## 2.2 Gravitational wave detectors

There have been two technologies developed to detect gravitational waves directly. These are resonant masses and interferometers.

### 2.2.1 Resonant mass detectors

Half a century ago, Joseph Weber devised and built an instrument to detect gravitational waves directly [51]. Weber used metal cylinders, sometimes called ‘bars’, whose vibrational modes can be excited by gravitational radiation. Bar detectors offer high sensitivity to continuous wave sources at the resonance frequency of the bar (typically  $\sim 1\text{kHz}$ ), as the signal is resonantly enhanced. Bar detectors were the dominant gravitational wave antenna for the following four decades and offered strain sensitivity of up to  $10^{-21} 1/\sqrt{\text{Hz}}$  near  $1\text{kHz}$  [52].

### 2.2.2 Interferometric Detectors

Interferometric detectors were proposed by Gertsenshtein and Pustovoi [53] in the 1960’s. The first interferometric detector was built in the early 1970’s by a group led by Robert Forward [54]. At the same time, Rainer Weiss from Massachusetts Institute of Technology conceived long baseline interferometers and determined their noise limits. In the late 1990’s construction of these long baseline interferometers began. They have reached maturity in the last couple of years.

Interferometric detectors are based on sensing the motion of freely falling bodies, such as the suspended end mirrors of a Michelson interferometer. The Michelson interferometer, shown schematically in figure 2.2 (a), is the basic configuration of all ground based interferometric detectors. Typically, the Michelson interferometer is set to operate on ‘dark fringe’, which means the

arm length difference is controlled so that the laser field interferes destructively towards the photodetector port and constructively to laser port. A passing gravitational wave will modulate the arm lengths differentially, thereby changing the interference condition at the beamsplitter, resulting a signal that can be sensed on the photodetector.

There are two key advantages of interferometers that have seen them supersede bar detectors. Firstly, interferometers are inherently broadband devices, whereas the resonant nature of bar detectors means they are narrowband<sup>1</sup> (typically tens of Hertz [52]) devices. Secondly, the strain sensitivity of interferometers improves proportional to the interferometer length,  $L$ , up until  $L$  is greater than a quarter of the gravitational wave wavelength. Thus, increasing the arm length ‘dilutes’ the amplitude of displacement noise sources with respect to the gravitational wave signal. This scaling factor with arm length means that long baseline detectors are desired. Ground based interferometric detectors have arm lengths of  $L \sim 1$  km. Space based detectors will have lengths of  $L \sim 10^6$  km.

### 2.2.3 Interferometer configurations

Figure 2.2 (b) shows an advanced Michelson interferometer configuration. This is the configuration that the second generation detectors Advanced LIGO [29] and Advanced VIRGO [56] will use, and elements of it are used in the first generation detectors (introduced in section 2.3). This interferometer has Fabry-Perot cavities in the arms, consisting of the input test mass and the end test mass, and extra mirrors: one in the laser port, called the power recycling mirror and one in the photodetector port, called the signal recycling mirror. Arm cavities enhance the sensitivity by optimizing the gravitational wave signal storage time and increasing the power incident on the test masses. The power recycled mirror forms a cavity with the Michelson interferometer, called the power recycling cavity, which recycles the light that exits the laser port of the Michelson interferometer, resonantly enhancing the laser power at the beamsplitter. The signal recycled mirror forms a cavity with the Michelson interferometer called the signal recycling cavity. Analogous to power recycling, signal recycling resonantly enhances the gravitational wave signal at the signal recycling cavity resonance frequency. Signal recycling also enables the interferometer’s peak sensitivity to be tuned by adjusting the microscopic position of the signal recycling mirror.

## 2.3 Current Interferometric Gravitational Wave Detectors

There are currently six long baseline interferometric detectors:

- LIGO [57–59], the Laser Interferometer Gravitational-wave Observatory, consists of three interferometers located at two sites separated by 3002 km across the United States of America. The sites are located: in Washington state, which has two interferometers with arm lengths of 4km and 2km; and in Louisiana, which has a 4km interferometer. All three interferometers are power-recycled Michelson interferometers with arm cavities. In September 2007, LIGO finished its fifth science run (S5) which entailed a 365 days worth of triple coincidence from the interferometers.
- VIRGO [60, 61] is a French-Italian collaboration which has a 3km interferometer in Italy near Pisa. VIRGO is also a power-recycled Michelson interferometer with arm cavities. VIRGO has lower optimal strain sensitivity than LIGO, due to it’s shorter arms, but has a better projected low frequency sensitivity due to more advanced seismic isolation.

---

<sup>1</sup>Planned resonant mass such as DUAL [55] have a sensitive bandwidth approaching hundreds of Hertz.

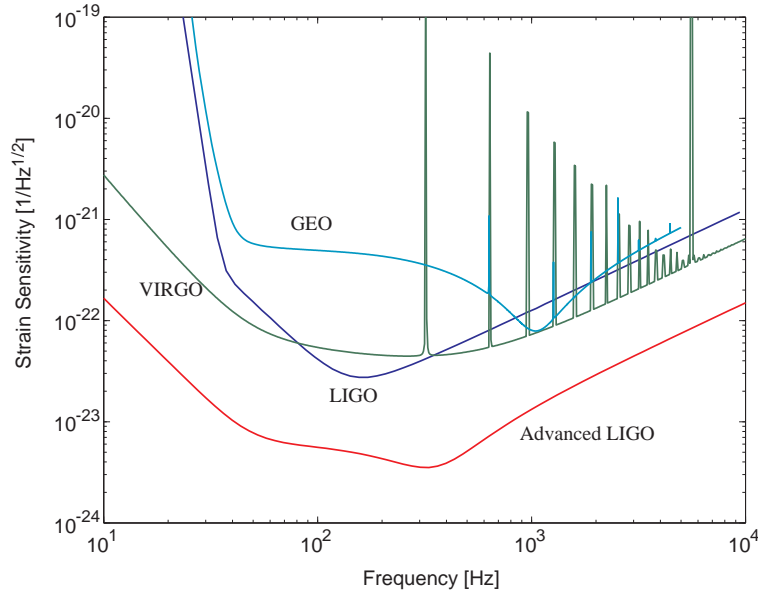


**Figure 2.3:** Design strain sensitivity of LIGO, VIRGO, GEO, and Advanced LIGO.

- GEO [62, 63] is a 600m interferometer located near Hannover in Germany, run by a German and British team. The GEO interferometer is a once-folded signal and power recycled Michelson interferometer which does not employ arm cavities. It is the only first generation detector to use signal recycling, allowing the signal response to be tuned.
- TAMA [64, 65] is a 300m interferometer located near Tokyo, Japan. TAMA is a power-recycled Michelson interferometer with arm cavities. TAMA was operational before the other detectors, and was responsible for setting early upper limits on the strength of gravitational radiation [64].

The design strain sensitivity of the LIGO, VIRGO, and GEO interferometers is shown in figure 2.3. Also shown is the design sensitivity of Advanced LIGO. The sensitivity of all first generation detectors is limited by the same noise sources: seismic noise at low frequencies; thermal noise of the mirrors and suspension wires and in the mid frequency band; and quantum noise at high frequencies. These noise sources are shown in figure 2.4 for the 4km LIGO detector as an example.

### 2.3.1 Second generation detectors

First generation detectors will be upgraded to improve sensitivity and increase the likelihood, rate and detail of detections. These second generation detectors are designed to improve sensitivity by an order of magnitude and broaden the measurement bandwidth. The upgrades include: updating the mirror suspensions and mirror substrates, adding signal recycling; increasing the laser power to reduce shot noise; and changing the detection scheme from a heterodyne based technique to a homodyne technique. The LIGO detectors will be upgraded to Advanced LIGO, and VIRGO will become Advanced VIRGO. The GEO detector will be upgraded to GEO HF [66], with HF standing for high frequency. There are also plans to build new advanced ground based detectors: In Japan, LCGT [67]; and in Australia, AIGO [68], but these projects are yet to be funded.

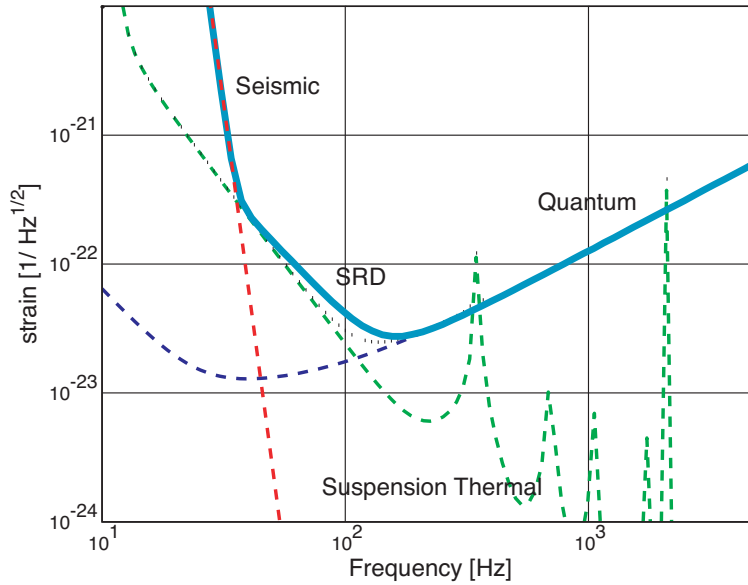


**Figure 2.4:** Design strain sensitivity of LIGO with the three limiting noise sources seismic noise, suspension thermal noise and quantum noise.

## 2.4 Noise sources in terrestrial interferometric detectors

To detect the incredibly small strain induced by gravitational waves, the differential or anti-symmetric motion of the test masses needs to be kept to a minimum and the arm length must be long. For the kilometer scale interferometers currently operating, the required displacement sensitivity is of order  $10^{-19} \text{m}/\sqrt{\text{Hz}}$  [50]. This is an incredible challenge in the audio gravitational wave detection band (10Hz to 10kHz) which is why it has taken decades to design, build, and optimise long baseline interferometers. There are many noise sources that can prevent the measurement of such a small displacement. The expected contributions from various noise sources of the Advanced LIGO detector are plotted in figure 2.5 as an example.

### 2.4.1 Noise sources

Interferometric detectors have sources of displacement noise which fall into three main categories: facility noise, hardware noise, and quantum noise<sup>2</sup>. Below is a short introduction to the different noise sources that are expected to limit Advanced LIGO.

**Gravity gradient** Fluctuations in the local gravitational field near the test masses cause uncorrelated displacement noise of the test masses [69, 70], resulting in gravity gradient noise. This is caused by fluctuating densities of medium, such as atmospheric pressure fluctuations and seismic waves; and by moving masses, such as cars, aeroplanes, and people. Gravity gradient noise represents the low frequency limit for terrestrial detectors. To detect gravitational waves at frequencies lower than a few Hertz, space based interferometers are needed, since this noise source cannot be mitigated in a terrestrial detector.

<sup>2</sup>There are other technical noise sources such as photodetector electronic noise and feedback control noise that are not included in this analysis.

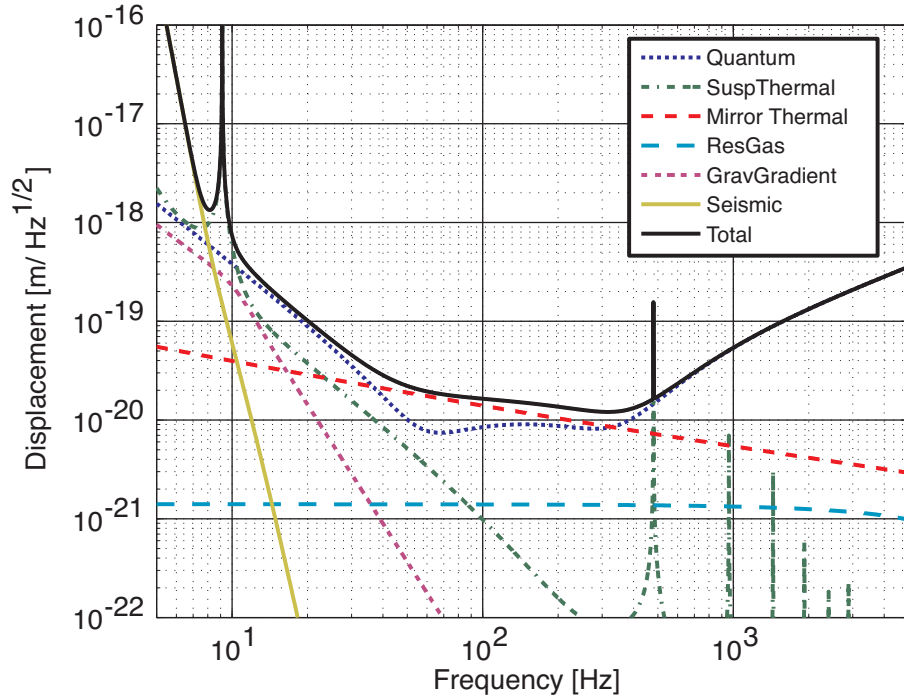


**Figure 2.5:** Expected displacement contributions of various noise for the Advanced LIGO detector in wideband operation. Plot made using Bench, Version 6.2 [1].

**Residual gas** The interferometers operate in an ultra high vacuum envelope. There is always some residual gas (the LIGO Facilities have a pressure of  $10^{-9}$  Torr [49]) which, as it passes through the beam path, gives a small refractive index change, resulting in displacement noise.

**Stray light** Light that scatters from the core mirrors or input and output optics can be scattered back into interferometer field. This process adds uncorrelated phase noise [71]. To minimize stray light the gravitational wave detection facilities are fitted with light baffles, and great effort is taken when absorbing (or dumping) beams from unused specular reflections.

Stray light, gravity gradient, and residual gas noises combine to form Facility noise [49].

**Seismic noise** The ground motion at the LIGO interferometer sites is approximately  $10^{-8}$  m/ $\sqrt{\text{Hz}}$  at 1Hz, and reduces at higher frequencies [72]. To obtain the required displacement, the test masses must be isolated from the seismic motion. Most detectors use some combination of active isolation at low frequencies and multi stage pendulums for passive isolation. Even so, seismic noise limits low frequency sensitivity.

**Thermal noise** The term ‘thermal noise’ refers to displacement noise induced by the statistical thermodynamic fluctuations of an object. Thermal noise can be understood through the fluctuation - dissipation theorem [73, 74], which describes how thermal fluctuations couple to a localised area of a material via the mechanical loss of the material. These thermal fluctuations cause expansion or contraction of the material, resulting in displacement noise. The amplitude of the off-resonance thermal noise is proportional to the intrinsic loss of the medium, thus low loss, high Q (quality factor) materials are desirable. Two manifestations of thermal noise are plotted in figure 2.5

1) Suspension Thermal Noise: The suspension wires that hold the test masses expand and contract due to thermodynamic fluctuations [74], generating displacement noise. Suspension thermal noise represents a low frequency limit to the Advanced LIGO displacement sensitivity.

2) Mirror Thermal Noise: Mirror thermal noise describes two sources of thermal noise - That from the coating (see, for example [75]), which is currently expected to be the primary contributor, and the thermal noise of the mirror substrate [50]. Coating thermal noise is of particular importance, since it represents the expected limit to sensitivity across the mid-frequency band - a few tens of Hertz to few hundred Hertz.

**Quantum noise** The origin of quantum noise in interferometric detectors is the quantum mechanical fluctuations of the electromagnetic field used to sense displacement. Quantum noise enters interferometric measurements in two ways:

1) shot noise. The measurement of the gravitational wave signal is a phase quadrature measurement. The quantum mechanical phase fluctuations of the light provide a fundamental limit to this measurement. The sensitivity of first and second generation detectors are shot noise limited above a few hundred Hertz. The shot noise limited signal-to-noise ratio scales inversely with square root of power at the beamsplitter input, thus shot noise can be reduced by increasing the laser power or power recycling factor. Shot noise is the limiting noise above a few hundred Hertz.

2) Radiation pressure noise. The quantum mechanical amplitude fluctuations do not directly couple to the measurement. Instead, they drive fluctuations in the test mass positions via radiation pressure. These fluctuations are anti-correlated in the two arms, causing anti-correlated displacement of the mirrors. This results in a phase noise. The radiation pressure limited signal-to-noise scales with the square root of the power at the beamsplitter, Thus radiation pressure noise becomes significant when high powers are used. Second generation detectors operating at high laser powers are expected to be limited by radiation pressure noise at frequencies between about 10Hz and 70Hz.

Quantum noise in interferometric detectors, and methods to circumvent it are detailed in chapter 4.

There are many other hardware and facility noise sources not mentioned here, such as photothermal [76] and photo-refractive noise [77] sources, that are expected to be smaller than the noise sources presented here and beyond the scope of this discussion.

## 2.5 Space based interferometric gravitational wave detectors

The laser interferometer space antenna (LISA) is a joint NASA/ESA mission planned to launch in 2018 [78]. The LISA constellation, shown in figure 2.6, consists of three spacecraft arranged in an equilateral triangle with 5 million km sides. The LISA constellation will orbit the sun at the same distance as the Earth, but will lag the Earth's orbit by 20 degrees.

LISA will detect gravitational waves by measuring the distance between the spacecraft using interferometry and looking for tiny length perturbations. There are two lasers located on each spacecraft which send a laser beam to each of the other two spacecraft. By making precise phase measurements of the incoming laser fields, LISA expects to reach a strain sensitivity of  $h = 10^{-20} 1/\sqrt{\text{Hz}}$  and be sensitive enough to detect gravitational waves across a frequency band from  $100\mu\text{Hz}$  to 1Hz. The design sensitivity of LISA is shown in figure 2.7. This frequency band

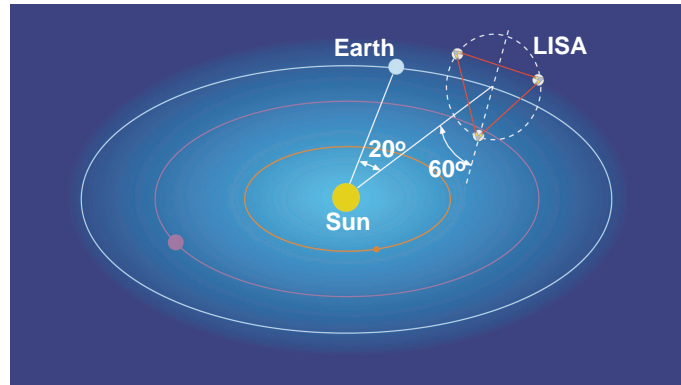


**Figure 2.6:** The LISA constellation. LISA will have 5,000,000 km long arms. The constellation is inclined to the ecliptic by  $60^\circ$  and orbits the Sun  $20^\circ$  behind the Earth. Adapted from [2]

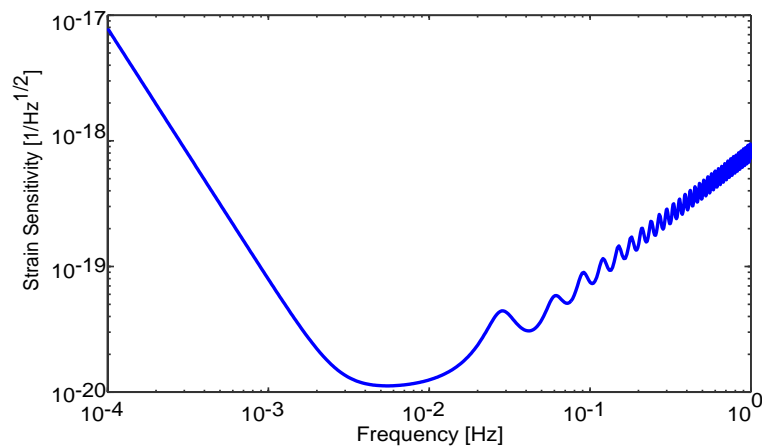


**Figure 2.7:** The designed LISA strain sensitivity. From [3]

is fundamentally inaccessible for terrestrial detectors due to gravity gradient noise, and is expected to contain an abundance of measurable sources.

LISA also has a planned upgrade, the big bang observatory (BBO) [79], with an expected launch date of 2030.

## 2.6 Chapter summary

This chapter has presented an overview into the concepts of gravitational waves and their detection. The basic configurations and noise sources of ground based interferometric detectors have been introduced and current operational detectors have been listed.



---

# Quantum optics and nonlinear devices

---

The beginning of the twentieth century saw the works of Max Plank and Albert Einstein transform the understanding of the mechanics of electromagnetism from an infinitely divisible, classical description of James Maxwell, to the understanding of discrete light quanta. The revolution of quantum mechanics that followed was one of the profound discoveries of the 20th century.

The quantised nature of light means that it must be treated statistically for high precision measurements. Repeated measurements of the electromagnetic field amplitude, for example, yield different results, and the measurement results obey the Poissonian distribution. This uncertainty limits the accuracy that interferometric measurements can be made, and results in what is termed quantum noise. This thesis is concerned with the quantum limits of laser interferometric displacement measurements and producing modified quantum states to surpass these quantum limits.

This chapter provides background into the quantum mechanical nature of the electromagnetic field and introduces the mathematical framework to represent it. The second part of the chapter introduces second order ( $\chi^{(2)}$ ) nonlinearity, which is the mechanism used to create squeezing.

The chapter is laid out as follows: In section 3.1 the quantised electromagnetic field is introduced using standard quantum optics formalism found in text books such as Walls and Milburn [80]. We then introduce the Heisenberg uncertainty principle [81] for the electromagnetic field and the properties of some *states of light* found in quantum optics experiments. In section 3.2 and section 3.3 devices and processes typical in quantum optics experiments are introduced. These are: the photodetection of optical fields; the effects of optical loss; and the Fabry-Perot interferometer. The second part of this background chapter introduces the basics of nonlinear interactions. Section 3.4 focusses on the  $\chi^{(2)}$  nonlinear interaction in dielectric media. Parametric up- and down-conversion are introduced, along with conservation laws and phasematching. In section 3.5 the equations of motion of an optical cavity with a  $\chi^{(2)}$  nonlinear medium are presented. These equations are used to examine the classical and quantum behaviour of an optical parametric amplifier (OPA) using a semi-classical approach.

## 3.1 The quantised electromagnetic field

Properties of the quantised electromagnetic field are introduced in the context of an optical cavity mode with angular frequency  $\omega_k$ . The positive and negative component of the electric field can be written in terms of the boson creation and annihilation operators,  $a_k^\dagger$  and  $a_k$ , and the spatial mode

function,  $\mathbf{u}(\mathbf{r})$

$$\mathbf{E}^{(+)}(\mathbf{r}, t) = i \sum_k \left( \frac{\hbar \omega_k}{2\epsilon_0} \right)^{\frac{1}{2}} a_k \mathbf{u}(\mathbf{r}) e^{-i\omega_k t}, \quad (3.1)$$

$$\mathbf{E}^{(-)}(\mathbf{r}, t) = -i \sum_k \left( \frac{\hbar \omega_k}{2\epsilon_0} \right)^{\frac{1}{2}} a_k^\dagger \mathbf{u}(\mathbf{r})^* e^{+i\omega_k t}, \quad (3.2)$$

where  $\hbar$  is the reduced Plank constant and  $\epsilon_0$  is the Permittivity of free space. The sum of the positive and negative components give the total electric field [80]

$$\mathbf{E}(t) = i \sum_k \left( \frac{\hbar \omega_k}{2\epsilon_0} \right)^{\frac{1}{2}} \left[ a_k \mathbf{u}(\mathbf{r}) e^{-i\omega_k t} - a_k^\dagger \mathbf{u}(\mathbf{r})^* e^{i\omega_k t} \right]. \quad (3.3)$$

The creation and annihilation operators are dimensionless and satisfy the boson commutation relations

$$[a_k, a_{k'}] = [a_k^\dagger, a_{k'}^\dagger] = 0, \quad [a_k, a_{k'}^\dagger] = \delta_{kk'}. \quad (3.4)$$

These commutation relations illustrate an important distinction between classical and quantum optics. The classical optics equivalent of equation 3.3 can be found by replacing the annihilation and creation operators with complex field amplitudes. The complex field amplitudes in classical optics commute, avoiding the Heisenberg uncertainty relation and its consequences.

In quantum mechanics, operators must be Hermitian to represent observable quantities. The annihilation and creation operators are not Hermitian and as such are not observables. They can be written in terms of the Hermitian operator pair for the *amplitude quadrature*,  $X_1$ , and the *phase quadrature*,  $X_2$ ,

$$a = \frac{1}{2}(X_1 + iX_2), \quad (3.5)$$

$$a^\dagger = \frac{1}{2}(X_1 - iX_2), \quad (3.6)$$

the quadrature operators for the amplitude and phase are

$$X_1 = a + a^\dagger, \quad (3.7)$$

$$X_2 = -i(a - a^\dagger). \quad (3.8)$$

The amplitude and phase quadratures represent non-commuting observable parameters. A operator for an arbitrary quadrature,  $\zeta$ , can be defined using a linear combination of  $X_1$  and  $X_2$

$$X_\zeta = X_1 \cos \zeta + X_2 \sin \zeta. \quad (3.9)$$

### 3.1.1 The Heisenberg uncertainty principle

The Heisenberg uncertainty principle (HUP) [81] quantifies the ultimate precision of simultaneous measurement of non-commuting observable parameters. A standard example of the HUP is the measurement of the position and momentum of a particle (for example, see Griffiths [82]). The HUP states that if any two observable parameters,  $O_1$  and  $O_2$ , satisfy the commutation relation

$$[O_1, O_2] = \xi, \quad (3.10)$$

then they are bounded by the HUP

$$\Delta O_1 \Delta O_2 \geq \frac{|\xi|}{2}, \quad (3.11)$$

where  $\Delta O$  is standard deviation of the operator  $O$ . The standard deviation is defined,

$$\Delta O = \sqrt{\langle O^2 \rangle - \langle O \rangle^2}. \quad (3.12)$$

The variance of the operator is the square of the standard deviation,

$$V = (\Delta O)^2. \quad (3.13)$$

The commutator relation of the amplitude and phase quadrature of the electromagnetic field is

$$[X_1, X_2] = 2i, \quad (3.14)$$

and thus the HUP is

$$\Delta X_1 \Delta X_2 \geq 1. \quad (3.15)$$

This relation shows that simultaneous measurements of phase and amplitude quadratures of the electromagnetic field cannot be done to arbitrary accuracy. This has widespread implications in quantum optics and quantum noise limited interferometry, such as in interferometric gravitational wave detectors. Simply put, it means that no matter how a measurement device is built, the signal to noise ratio of the measurement is ultimately limited by quantum noise of the electromagnetic field.

### 3.1.2 Important states of light

Experiments performed as part of this thesis, and in most quantum optics laboratories, use a combination of only a few states of light. Here we present some basic properties of only four: the coherent state, the vacuum state, the squeezed state, and the classically noisy state. Representations of these states are shown in the ‘ball on stick’ representation<sup>1</sup> in figure 3.1 (a)-(d). Important properties of these four states of light are introduced in the following sections.

#### The coherent state

The coherent state has non-zero coherent amplitude and quantum limited fluctuations, equally distributed in the amplitude and phase quadratures,

$$\Delta X_1 = \Delta X_2 = 1. \quad (3.16)$$

The coherent state, and the vacuum state described below, are examples of *minimum uncertainty states* which have the minimum allowable product of quadrature fluctuations. The quadrature fluctuations of the coherent state are constant amplitude at all frequencies and obey Poissonian statistics [80]. Note that, at high photon numbers, such as those emitted by continuous wave lasers, the Poissonian distribution of photons is well approximated by a Gaussian distribution. A frequency domain picture of a coherent state is shown in figure 3.2 (a). Here the carrier, at frequency  $\Omega_c$  is surrounded by a continuum of quantum sidebands each with  $\hbar/2$  energy. For

---

<sup>1</sup>This representation of the complex amplitude of each state of light is similar to the phasor diagram for classical fields. The amplitude of the vector represents the steady state amplitude of the field and the fuzzy ball represents time dependent fluctuations in the amplitude and phase quadratures.

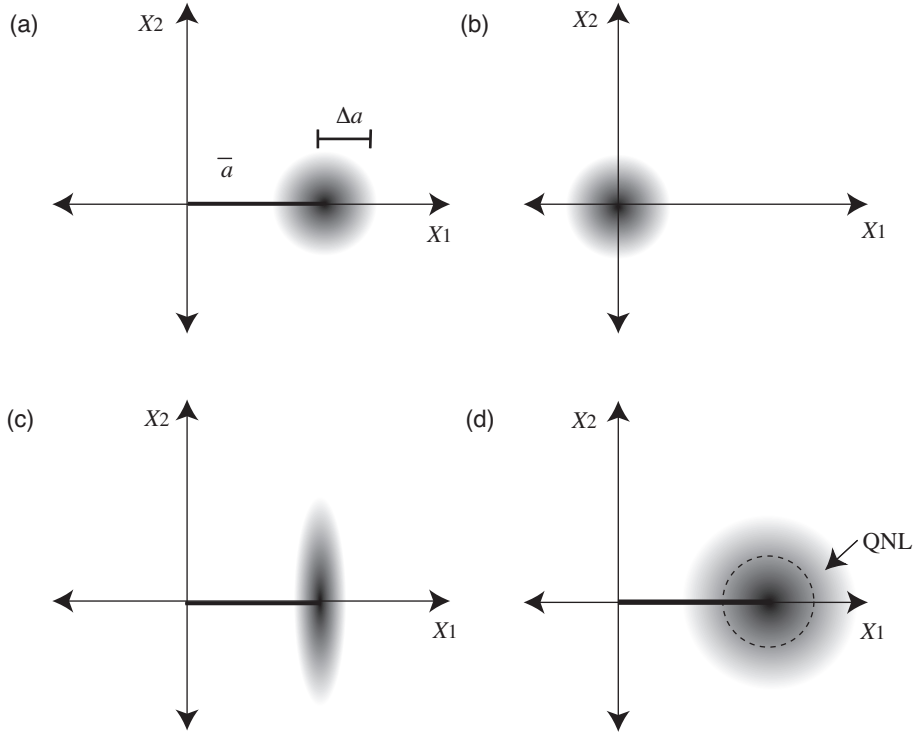


**Figure 3.1:** Ball and stick picture for four states of light: (a) The coherent state, (b) The vacuum state, (c) The amplitude squeezed states, and (d) The classically noisy state.

the coherent state, the sidebands are randomly distributed in phase, so equal noise is seen in the amplitude and phase quadrature.

The coherent state is particularly relevant to quantum noise limited interferometry because a well stabilised laser field is well approximated by the coherent state. When making interferometric measurements using a coherent state, the quantum noise that arises due to the fluctuations of the quadratures is called the quantum noise limit. For interferometric measurements, without the use of nonlinear devices or nonlinear interactions, the quantum noise limit represents the optimal sensitivity that can be obtained.

### The vacuum state

The vacuum state has the same noise statistics as the coherent state, but it has no coherent amplitude ( $\bar{a} = \langle a(t) \rangle = 0$ ). As its name suggests, the vacuum state exists in the optical vacuum, which is any region unoccupied by another state. It occupies all frequency, spatial, and polarization modes.

The vacuum state is extremely important in quantum optics experiments as it enters into optical systems in any unfilled ports of beamsplitters, cavities, and partially transmissive mirrors. Also, when an optical field experiences losses due to absorption or scattering events, the vacuum field replaces the fraction of optical field that is lost. As the optical losses of a field approach unity, its noise statistics approach that of the vacuum state. This concept is quantified in section 3.2.4 and is referred to throughout this thesis.

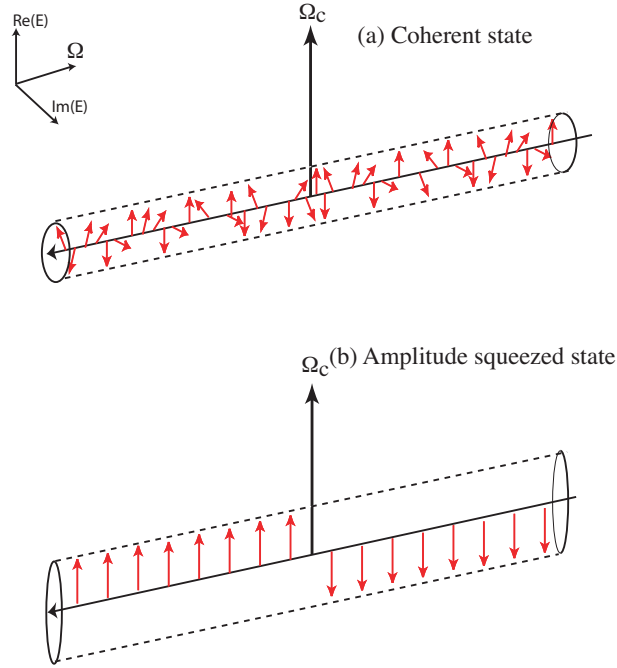


**Figure 3.2:** The frequency domain phasor diagram, or sideband picture of (a) the coherent state, and (b) the amplitude squeezed state. The coherent state has white noise distributed equally in all quadratures whereas the amplitude squeezed state has increased noise in the phase quadrature and reduced noise in the amplitude quadrature.

### The squeezed state

A squeezed state of light is a freely propagating field that has standard deviation in one quadrature less than the quantum noise limit<sup>2</sup>. In order to satisfy the HUP, the standard deviation of the orthogonal quadrature must be greater than the quantum noise limit and the product of the two quadratures greater than or equal to unity. Thus the minimum uncertainty amplitude squeezed state, for example, has

$$\Delta X_1 = 1/z \quad (3.17)$$

$$\Delta X_2 = z \quad (3.18)$$

where  $z$  is a real and positive number. The larger  $z$  is, the larger the magnitude of squeezing. A squeezed state with  $z = 2$  is shown in figure 3.1 (c). A squeezed state which has no coherent amplitude is called a *vacuum squeezed state*. A squeezed state with a coherent amplitude ( $\bar{a} \neq 0$ ) is called a *bright squeezed state*. The squeezed state is characterised by how far it is below the noise statistics of the quantum noise limit. In this thesis, the variance of the squeezed state is compared with the variance of the coherent or vacuum state, and is expressed in decibels (dB) (relative to the quantum noise limit). For example, the amplitude squeezed state with  $z = 2$  is written  $V_1 = -6\text{dB}$ . Sometimes the amplitude of the squeezed state is expressed by the parameter  $R$  where  $V = \exp(-2R)$ . For the amplitude squeezed state with  $z = 2$ , ( $V_1 = \frac{1}{4}$ ),  $R = -\frac{1}{2} \log_e(V_1) = 0.6931$ .

<sup>2</sup>A *squashed state* also has standard deviation less than the quantum noise limit in one quadrature, though it exists only *in loop* and therefore does not need satisfy the HUP [83].

The frequency domain picture of a bright squeezed state is shown in figure 3.2 (b). In a squeezed state, the quantum mechanical sidebands on either side of the carrier (at  $\pm\Omega$ ) are correlated. Here the sidebands are correlated so that there is almost no noise sideband beat terms in the amplitude quadrature but only in the phase quadrature.

In theory, squeezed states can be minimum uncertainty states. Experimentally, a minimum uncertainty squeezed state cannot be produced or measured, as finite optical loss replaces a fraction of the squeezed state statistics with those of the vacuum state. This changes the squeezed state to a non-minimum uncertainty state. Optical losses to the squeezed state limit the achievable quantum noise suppression.

### Classically noisy states

Most lasers produce optical fields not represented by any of the above states, but have excess noise of classical origin at sideband frequencies below a few MHz. The amplitude and frequency dependence of the technical noise depends on the type of laser. Solid state monolithic lasers, such as the Neodymium type non-planer ring oscillator [84], typically become quantum noise limited at sideband frequencies of  $\sim 10$  MHz, whereas diode lasers, for example have technical noise to much higher sideband frequencies. The fluctuations of a classically noisy state are often many times greater than quantum noise and generally in both quadratures

$$\Delta X_1 \geq 1, \quad \Delta X_2 \geq 1. \quad (3.19)$$

The excess noise of such a state can be reduced via: passive noise suppression using mode cleaner cavities (for example [85]); actively noise suppression using feedback to the laser (see for example [86]); or both. In this way the standard laser fields can be prepared for quantum noise limited interferometry and quantum optics experiments.

## 3.2 Mirrors, photodetection, and losses

This section gives an overview into the basic theory of the operation of mirrors and the detection of optical fields. The focus here is homodyne detection techniques that are used in experiments presented in this thesis.

### 3.2.1 A partially transmissive mirror

Figure 3.3 (a) shows two fields  $a$  and  $b$  incident on a partially transmissive (lossless) mirror with transmission  $\epsilon$ . The fields at the outputs of the mirror,  $c$  and  $d$ , can be related to the inputs by

$$\begin{pmatrix} c \\ d \end{pmatrix} = \begin{pmatrix} \sqrt{1-\epsilon} & \sqrt{\epsilon} \\ \sqrt{\epsilon} & -\sqrt{1-\epsilon} \end{pmatrix} \begin{pmatrix} a \\ b \end{pmatrix}, \quad (3.20)$$

where the phase relations of the ports of the beamsplitter are maintained by setting the reflectivity of the mirror to be  $-1 \times \sqrt{1-\epsilon}$  on the port on the right hand side (indicated by a minus sign). Another convention often used to maintain the phase relations of the four ports multiplies the field by  $i$  on each transmission. The output relations of the mirror at normal incidence also hold for the fields at with non-normal incidence, shown in figure 3.3 (b).

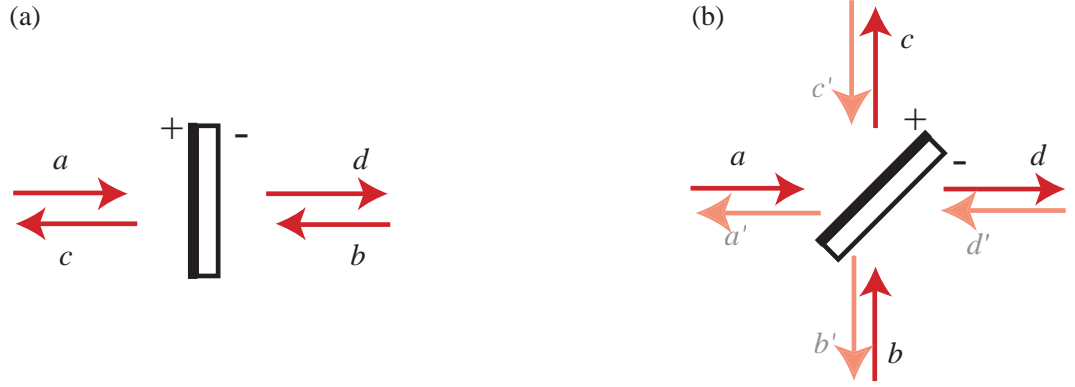


**Figure 3.3:** A partially transmissive mirror at normal incidence has two inputs and two outputs. The fields  $a, b, c, d$  are labeled for a partially transmissive mirror with fields at (a) normal incidence incident and (b) at  $45^\circ$ . The  $+$  and  $-$  signs indicates the side where the amplitude reflectivity receives a minus sign. Note that we have only considered half of the inputs and outputs of figure (b).

### 3.2.2 Direct photodetection

An ideal photodetector produces a photocurrent directly proportional to the power in the optical field. A field incident on an ideal photodetector with frequency  $\omega$  and power  $P(t)$  gives the photocurrent [4]

$$i(t) = \frac{eP(t)}{\hbar\omega}. \quad (3.21)$$

The power in the field is simply the number of photons per second times the energy of each photon

$$P(t) = \hbar\omega \langle a^\dagger a \rangle, \quad (3.22)$$

where the traveling field,  $\langle a^\dagger a \rangle$ , has units of 1/second. The photon number of an optical field is given by

$$n = a^\dagger a. \quad (3.23)$$

We will be interested in the average and time dependent photocurrent

$$i(t) = \bar{i} + \delta i(t) \quad (3.24)$$

where  $\bar{i} = \langle i(t) \rangle$  and  $\delta i(t) = i(t) - \bar{i}$ . To determine the average and fluctuating components of the photocurrent we need to determine the average and fluctuating components of the optical power. We start by writing the annihilation and creation operators in terms of a steady state and a time varying component

$$a = \bar{a} + \delta a, \quad (3.25)$$

$$a^\dagger = \bar{a}^* + \delta a^\dagger, \quad (3.26)$$

where

$$\bar{a} = \langle a \rangle, \quad \bar{a}^* = \langle a^\dagger \rangle, \quad (3.27)$$

$$\delta a = \bar{a} - a, \quad \delta a^\dagger = \bar{a}^* - a^\dagger. \quad (3.28)$$

The quadrature fluctuations of the amplitude and phase are then

$$\delta X_1 = \delta a + \delta a^\dagger, \quad (3.29)$$

$$\delta X_2 = -i(\delta a - \delta a^\dagger). \quad (3.30)$$

These quadrature operators satisfy the HUP. The HUP for the quadrature operators defined here can be found by replacing  $\Delta X_1$  with  $\delta X_1$  and  $\Delta X_2$  with  $\delta X_2$  in equation 3.15. Choosing  $\bar{a} = \bar{a}^*$ , without the loss of generality, the power in the optical field can be written in terms of the average power and power fluctuations

$$P(t) = \bar{P} + \delta P(t), \quad (3.31)$$

where

$$\bar{P} = \hbar\omega\bar{a}^2, \quad (3.32)$$

$$\delta P(t) = \hbar\omega(\bar{a}\delta X_1^{(a)} + \delta a^\dagger \delta a). \quad (3.33)$$

If the fluctuations of the field are much smaller than the steady state amplitude ( $\bar{a} \gg \delta a$ ) the linearisation approximation can be used [87]. The linearisation is performed by recognising that the second order fluctuating term is insignificant in comparison to terms containing the carrier beat ( $\delta a^\dagger \delta a \ll \bar{a}\delta X_1^{(a)}$ ). The linearised fluctuations of the field are

$$\delta P(t) = \hbar\omega\bar{a}\delta X_1^{(a)}. \quad (3.34)$$

The average and time dependent components of the photocurrent are

$$\bar{i} = \frac{e\bar{P}}{\hbar\omega} = e\bar{a}^2, \quad (3.35)$$

$$\delta i(t) = \frac{e\delta P(t)}{\hbar\omega} = e\bar{a}\delta X_1^{(a)}. \quad (3.36)$$

The variance of the photocurrent is

$$V^{(i)}(t) = \langle |\delta i(t)|^2 \rangle - \langle \delta i(t) \rangle^2, \quad (3.37)$$

$$= (e\bar{a})^2 V_1^{(a)}(t). \quad (3.38)$$

This shows that direct detection of the optical field gives a measurement of the amplitude quadrature and no phase information is obtained.

### 3.2.3 The two-ported homodyne detector

The signals or states measured in quantum optics and precision interferometry experiments are usually too low in power to be detected directly on a photodetector due to technical noise sources of the photodetector. Small signal measurements are instead performed by interfering a relatively strong local oscillator field with the signal and measuring the beat. Homodyne detection, where

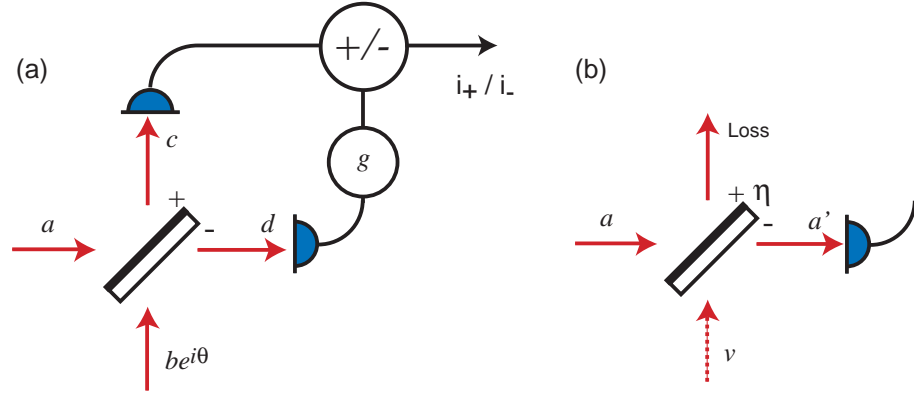


**Figure 3.4:** a) The two-ported homodyne detector. The small signal  $a$  is interfered on a beamsplitter with the local oscillator,  $b$ . The detected photocurrents can be either added or subtracted. (b) A model for inefficient detection where a mirror represents the loss introduced by a non-ideal photodetector.

the local oscillator is at the same optical frequency as the carrier of the signal beam, is a phase sensitive technique allowing an arbitrary quadrature of the signal to be measured. The two-ported homodyne detection system, shown in the figure 3.4 (a), is widely used because it offers common mode rejection of the local oscillator classical noise [88]. The two ported homodyne detector is used for the detection of squeezed states in the experiments presented in this thesis.

In figure 3.4 (a) the two fields  $a$ , and  $b$ , are combined on a beamsplitter of transmission  $\epsilon$ , and relative phase  $\theta$ . Both beamsplitter outputs are detected. The sum and difference of the photocurrents are then taken electronically. To calculate the sum/difference photocurrents we begin by calculating the fields at the beamsplitter output ports,  $c$ , and  $d$ , using equation 3.20, resulting in

$$c = \sqrt{1-\epsilon}a + \sqrt{\epsilon}be^{i\theta}, \quad (3.39)$$

$$d = \sqrt{\epsilon}a - \sqrt{1-\epsilon}be^{i\theta}, \quad (3.40)$$

the photon numbers at each detector are then

$$c^\dagger c = (1-\epsilon)a^\dagger a + \epsilon b^\dagger b + \sqrt{\epsilon(1-\epsilon)}(a^\dagger be^{i\theta} + b^\dagger ae^{-i\theta}), \quad (3.41)$$

$$d^\dagger d = \epsilon a^\dagger a + (1-\epsilon)b^\dagger b - \sqrt{\epsilon(1-\epsilon)}(a^\dagger be^{i\theta} + b^\dagger ae^{-i\theta}). \quad (3.42)$$

An electronic gain,  $g$ , is given to one of the photocurrents before the photocurrent difference is taken. The difference is given by

$$c^\dagger c - gd^\dagger d = [(1-\epsilon) - g\epsilon]a^\dagger a + [\epsilon - g(1-\epsilon)]b^\dagger b + \sqrt{\epsilon(1-\epsilon)}(1+g)(a^\dagger be^{i\theta} + b^\dagger ae^{-i\theta}). \quad (3.43)$$

The operators can be separated into steady state and time varying components,  $a = \bar{a} + \delta a$  and  $b = \bar{b} + \delta b$ . Because we have explicitly separated the relative phase of  $a$  and  $b$  we note that  $\bar{a} = \bar{a}^*$

and  $\bar{b} = \bar{b}^*$ . Rewriting the linearised difference photocurrent in terms of the quadratures gives

$$\begin{aligned} i_- &= c^\dagger c - g d^\dagger d \\ &\approx [(1 - \epsilon) - g\epsilon](\bar{a}^2 + a\delta X_1^{(a)}) + [\epsilon - g(1 - \epsilon)](\bar{b}^2 + b\delta X_1^{(b)}) + \\ &\quad \sqrt{\epsilon(1 - \epsilon)}(1 + g) \left( 2\bar{a}\bar{b}\cos\theta + \bar{a}(\delta X_1^{(b)}\cos\theta - \delta X_2^{(b)}\sin\theta) + \bar{b}(\delta X_1^{(a)}\cos\theta + \delta X_2^{(a)}\sin\theta) \right). \end{aligned} \quad (3.44)$$

Using the local oscillator condition, terms not containing  $\bar{b}$  can be neglected. The difference photocurrent becomes

$$i_- \approx [\epsilon - g(1 - \epsilon)](\bar{b}^2 + b\delta X_1^{(b)}) + \sqrt{\epsilon(1 - \epsilon)}(1 + g) \left( 2\bar{a}\bar{b}\cos\theta + \bar{b}(\delta X_1^{(a)}\cos\theta + \delta X_2^{(a)}\sin\theta) \right). \quad (3.45)$$

The two ported detector offers common mode rejection of the local oscillator intensity noise. The level of common mode rejection can be maximised by setting the electronic gain to  $g = \frac{\epsilon}{1 - \epsilon}$ . Experimentally this can be achieved very precisely, to the level of about 1 part in  $10^6$ . The difference photocurrent for a balanced homodyne is

$$i_- \approx \sqrt{\frac{\epsilon}{1 - \epsilon}} \left( 2\bar{a}\bar{b}\cos\theta + \bar{b}(\delta X_1^{(a)}\cos\theta + \delta X_2^{(a)}\sin\theta) \right), \quad (3.46)$$

therefore providing a measure of the signal beam quadratures, depending on the phase of the local oscillator. The sum photocurrent is approximately equal to that given by the direct detection of the local oscillator

$$i_+ \approx \bar{b}^2 + b\delta X_1^{(b)}. \quad (3.47)$$

### 3.2.4 The effect of optical losses

When an optical field encounters loss, a fraction of the field is replaced by the vacuum field. Mathematically, a loss of  $\mathcal{L}$  (in power) can be represented by a partially transmissive beamsplitter with transmission  $\eta = 1 - \mathcal{L}$ . This is shown schematically in figure 3.4 (b). At the source of loss, the vacuum mode is coupled into the outgoing field in exactly the same way as the combination of two beams on a beamsplitter. For an input field  $a$ , the field after the loss is  $a'$ , given by

$$a' = \sqrt{\eta}a + \sqrt{1 - \eta}v, \quad (3.48)$$

where  $v$  is the vacuum field coupled by the loss. The photon number of the field is

$$a'^\dagger a' = \eta a^\dagger a + 1 - \eta v^\dagger v + \sqrt{\eta(1 - \eta)}(a^\dagger v + v^\dagger a), \quad (3.49)$$

$$= \eta \bar{a}^2 + \sqrt{\eta}\bar{a}(\sqrt{\eta}\delta X_1^{(a)} + \sqrt{1 - \eta}\delta X_1^{(v)}), \quad (3.50)$$

where the second line here is the linearised photon number. The first term of the second line shows that the average power in the field  $a$  has been reduced by the amount of loss. The fluctuation term of the field  $a$  shows a similar result, the detected  $\delta X_1^{(a)}$  component is scaled by the amount of loss. The last term is the amount of vacuum fluctuations that enters into the measurement at the point of loss. This can be seen more explicitly in the variance of the photon number (relative to the

quantum noise limit)

$$V_1^{(a')} = \eta V_1^{(a)} + (1 - \eta), \quad (3.51)$$

since  $V_1^{(v)} = 1$ . It is clear from this equation that the noise statistics of the field after a lossy element are modified to approach the quantum noise limit. This simple expression has implications for making measurements at the quantum noise limit, something that is done routinely when measuring and characterising squeezed states.

### 3.3 Fabry-Perot interferometers

Fabry-Perot interferometers, often referred to as cavities, are based on two or more partially transmissive mirrors arranged to allow the electromagnetic field to resonate. An understanding of the workings of cavities is required for many of the experiments and concepts contained in this thesis. In this section the equation of motion for a cavity is introduced then used to solve for the reflected and transmitted fields.

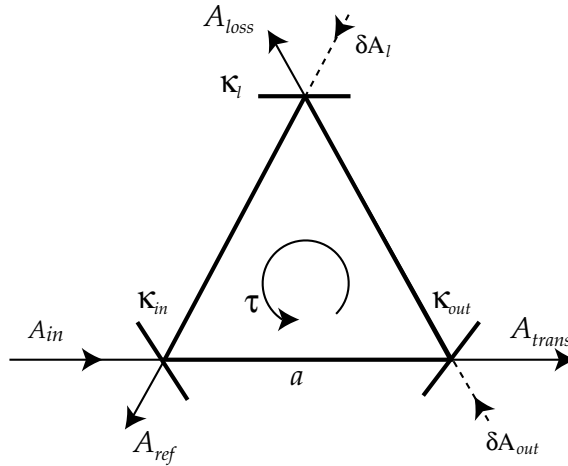


**Figure 3.5:** Layout of a ring cavity. The cavity is made from three mirrors: the input coupler, with decay rate,  $\kappa_{in}$ ; the output coupler, with decay rate,  $\kappa_{out}$ ; and a mirror to represent intra-cavity loss, with decay rate,  $\kappa_l$ . The cavity mode is labeled  $a$ . The extra-cavity fields are:  $A_{in}, A_{ref}, A_{trans}, \delta A_{out}, A_{loss}$ , and  $\delta A_l$ .

#### 3.3.1 Equation of motion for an optical resonator

Consider the empty cavity shown schematically figure 3.5. The cavity is made of three partially transmissive optics labeled  $in, out$ , and  $l$  referring to the input coupler, the output coupler, and the partially transmissive mirror used to simulate losses, respectively. The equation of motion for the cavity mode  $a$  is [80]

$$\dot{a} = -(\kappa + i\omega_0)a + \sqrt{2\kappa_{in}}A_{in}e^{-i\omega_A t} + \sqrt{2\kappa_{out}}A_{out} + \sqrt{2\kappa_l}A_l, \quad (3.52)$$

where the driving field  $A_{in}$  has coherent amplitude at frequency  $\omega_A$ , and the other fields,  $A_{out}$  and  $A_l$ , are assumed to be in the vacuum state. The cavity mode has resonant frequency  $\omega_0$ .

Note that the (lower case) cavity mode  $a$ , and the (uppercase) driving field  $A_j$  for  $j = in, out$ , and  $l$  have different units. The units of  $a$  are  $\sqrt{\text{photons}}$ , thus the photon number in the cavity can be given by

$$n = a^\dagger a \quad [\text{photons}], \quad (3.53)$$

whereas the units of the driving fields are  $\sqrt{\text{photons/s}}$ . Thus the number of photons per second in the driving field is

$$n_{in} = A_{in}^\dagger A_{in} \quad [\text{photons/s}]. \quad (3.54)$$

The equation of motion can be written in the rotating frame of reference by setting  $a \rightarrow ae^{i\omega_A t}$  and similarly for the driving fields

$$\dot{a} = -(\kappa + i\Delta)a + \sqrt{2\kappa_{in}}A_{in} + \sqrt{2\kappa_{out}}A_{out} + \sqrt{2\kappa_l}A_l, \quad (3.55)$$

where  $\Delta = \omega_0 - \omega_A$  is the cavity detuning. In the mean field approximation [89], the decay rates for each mirror are given by the (amplitude) transmissivity divided by the round trip time,  $\tau = \omega_0 p/c$ , where  $p$  is the perimeter of the cavity. That is,

$$\begin{aligned} \kappa_{in} &= \frac{\sqrt{T_{in}}}{\tau} \approx \frac{T_j}{2\tau}, \\ \kappa_{out} &\approx \frac{T_{out}}{2\tau}, \\ \kappa_l &\approx \frac{1 - \mathcal{L}_{RT}}{2\tau}, \end{aligned} \quad (3.56)$$

where  $\mathcal{L}_{RT}$  is the cavity round trip loss which for convenience we can write  $T_l = 1 - 1 - \mathcal{L}_{RT}$ . The total decay rate is a sum of the decay rates

$$\kappa = \kappa_{in} + \kappa_{out} + \kappa_l. \quad (3.57)$$

### 3.3.2 Compact matrix formalism for the equations of motion

In this section we introduce a matrix notation to solve for the equations of motion. This notation is useful for solving the complex equations of motion of a cavity which contains a nonlinear medium (see section 3.5 and chapter 5). We can start by writing the equation of motion for the cavity mode and its Hermitian conjugate as

$$\dot{a} = -(\kappa + i\Delta)a + \sqrt{2\kappa_{in}}A_{in} + \sqrt{2\kappa_{out}}A_{out} + \sqrt{2\kappa_l}A_l, \quad (3.58)$$

$$\dot{a}^\dagger = -(\kappa - i\Delta)a^\dagger + \sqrt{2\kappa_{in}}A_{in}^\dagger + \sqrt{2\kappa_{out}}A_{out}^\dagger + \sqrt{2\kappa_l}A_l^\dagger, \quad (3.59)$$

which can be rewritten in the compact form

$$\dot{\mathbf{a}} = \mathbf{M}_a \mathbf{a} + \mathbf{M}_{in} \mathbf{A}_{in} + \mathbf{M}_{out} \mathbf{A}_{out} + \mathbf{M}_l \mathbf{A}_l, \quad (3.60)$$

with the vectors

$$\dot{\mathbf{a}} = \begin{pmatrix} \dot{a} \\ \dot{a}^\dagger \end{pmatrix}, \quad \mathbf{a} = \begin{pmatrix} a \\ a^\dagger \end{pmatrix}, \quad \mathbf{A}_{in} = \begin{pmatrix} A_{in} \\ A_{in}^\dagger \end{pmatrix}, \quad \mathbf{A}_{out} = \begin{pmatrix} A_{out} \\ A_{out}^\dagger \end{pmatrix}, \quad \mathbf{A}_l = \begin{pmatrix} A_l \\ A_l^\dagger \end{pmatrix}. \quad (3.61)$$

The matrices are

$$\mathbf{M}_a = \begin{bmatrix} -\kappa - i\Delta & 0 \\ 0 & -\kappa + i\Delta \end{bmatrix}, \quad (3.62)$$

$$\mathbf{M}_{in} = \sqrt{2\kappa_{in}}\mathbf{I}, \quad \mathbf{M}_{out} = \sqrt{2\kappa_{out}}\mathbf{I}, \quad \mathbf{M}_l = \sqrt{2\kappa_l}\mathbf{I}, \quad (3.63)$$

where  $\mathbf{I}$  is the  $2 \times 2$  identity matrix.

The cavity mode in steady state can be found by setting  $\dot{\mathbf{a}} = 0$  and considering the time independent component  $\bar{a}$ . Given that the steady state amplitudes of the fields  $\bar{A}_{out} = \bar{A}_l = 0$ , the steady state cavity mode is

$$\bar{\mathbf{a}} = -\mathbf{M}_a^{-1}\mathbf{M}_{in}\bar{\mathbf{A}}_{in}, \quad (3.64)$$

thus

$$\bar{a} = \frac{\sqrt{2\kappa_{in}}}{\kappa + i\Delta}\bar{A}_{in}. \quad (3.65)$$

This result will be used to determine the reflected and transmitted fields as a function of detuning in the following section. We will also be interested in the Fourier components of the cavity mode. These can be found by Fourier transform of the operators

$$Q(\Omega) = \int_{-\infty}^{\infty} Q(t)e^{i\Omega t} dt, \quad (3.66)$$

for  $Q = a, A_{in}, A_{out}$ , and  $A_l$ . The equation of motion in the Fourier domain is

$$i\Omega\mathbf{a}(\Omega) = \mathbf{M}_a\mathbf{a}(\Omega) + \mathbf{M}_{in}\mathbf{A}_{in}(\Omega) + \mathbf{M}_{out}\mathbf{A}_{out}(\Omega) + \mathbf{M}_l\mathbf{A}_l(\Omega), \quad (3.67)$$

where  $\Omega$  is the sideband frequency. The cavity mode in the Fourier domain is

$$\mathbf{a}(\Omega) = (i\Omega\mathbf{I} - \mathbf{M}_a)^{-1} [\mathbf{M}_{in}\mathbf{A}_{in}(\Omega) + \mathbf{M}_{out}\mathbf{A}_{out}(\Omega) + \mathbf{M}_l\mathbf{A}_l(\Omega)]. \quad (3.68)$$

### 3.3.3 Reflected and transmitted fields

Using the cavity input-output relations [80], the reflected field  $A_{ref}$ , transmitted field  $A_{trans}$ , and the field lost to scatter and absorption  $A_{loss}$  can be determined

$$\mathbf{A}_{ref} + \mathbf{A}_{in} = \mathbf{M}_{in}\mathbf{a}, \quad (3.69)$$

$$\mathbf{A}_{trans} + \mathbf{A}_{out} = \mathbf{M}_{out}\mathbf{a}, \quad (3.70)$$

$$\mathbf{A}_{loss} + \mathbf{A}_l = \mathbf{M}_l\mathbf{a}, \quad (3.71)$$

which can be solved with some linear algebra. For the moment, consider the steady state reflected and transmitted fields

$$\bar{\mathbf{A}}_{trans} = \mathbf{M}_{out}\bar{\mathbf{a}} - \bar{\mathbf{A}}_{out}, \quad (3.72)$$

$$\bar{\mathbf{A}}_{ref} = \mathbf{M}_{in}\bar{\mathbf{a}} - \bar{\mathbf{A}}_{in}, \quad (3.73)$$

which give

$$\bar{A}_{trans} = \frac{2\sqrt{\kappa_{in}\kappa_{out}}}{\kappa + i\Delta} \bar{A}_{in}, \quad (3.74)$$

$$\bar{A}_{ref} = \frac{(2\kappa_{in} - \kappa - i\Delta)}{\kappa + i\Delta} \bar{A}_{in}. \quad (3.75)$$

The (amplitude) transmissivity and reflectivity of the cavity can be defined by the parameters

$$\mathcal{T}(\Delta) = \frac{\bar{A}_{trans}}{\bar{A}_{in}} = \frac{2\sqrt{\kappa_{in}\kappa_{out}}}{\kappa + i\Delta}, \quad (3.76)$$

$$\mathcal{R}(\Delta) = \frac{\bar{A}_{ref}}{\bar{A}_{in}} = \frac{(2\kappa_{in} - \kappa - i\Delta)}{\kappa + i\Delta}. \quad (3.77)$$

The functions  $|\mathcal{T}(\Delta)|^2$  and  $|\mathcal{R}(\Delta)|^2$  are shown in figure 3.6 (a), and their phase responses, given by  $\angle\mathcal{T}(\Delta)$  and  $\angle\mathcal{R}(\Delta)$  respectively, are shown in figure 3.6 (b). In quantum optics experiments

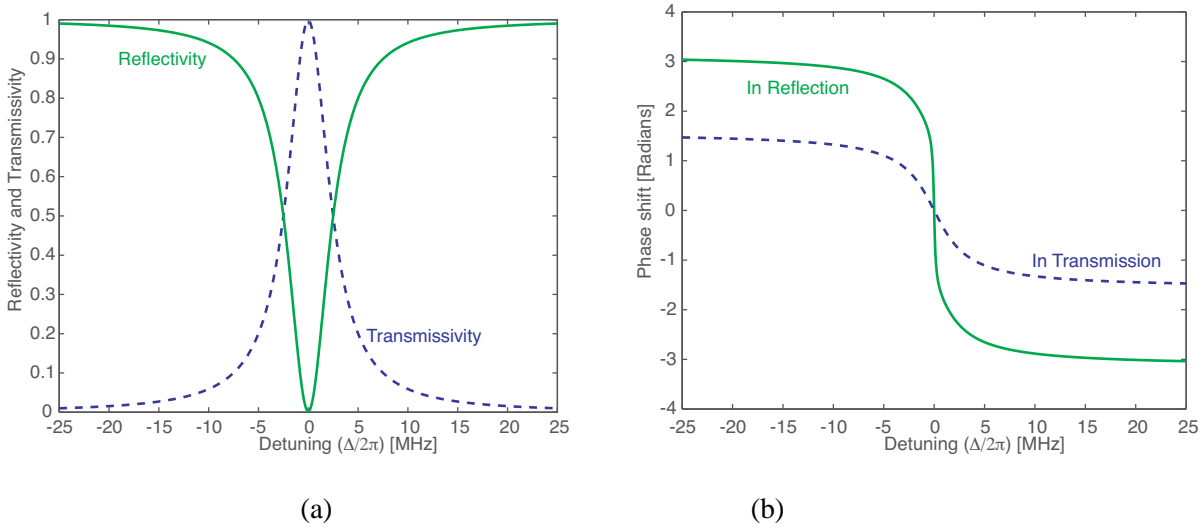


**Figure 3.6:** (a) The reflectivity and transmissivity and (b) the phase shift in reflection and transmission of an overcoupled cavity as a function of detuning. Parameters:  $L = 2\text{m}$ ,  $\lambda = 1\mu\text{m}$ ,  $T_{in} = 0.11$ ,  $T_{out} = 0.10$ , and  $T_{loss} = 0$ .

control techniques are typically used to force the laser frequency to match the cavity resonance frequency, or vice versa. The detuning parameter is thus forced to zero ( $\Delta = 0$ ). In this case we find

$$\mathbf{A}_{ref}(\Omega) = \frac{[2\kappa_{in} - \kappa - i\Omega]\mathbf{A}_{in}(\Omega) + 2\sqrt{\kappa_{in}\kappa_{out}}\mathbf{A}_{out}(\Omega) + 2\sqrt{\kappa_{in}\kappa_l}\mathbf{A}_l(\Omega)}{\kappa + i\Omega}, \quad (3.78)$$

$$\mathbf{A}_{trans}(\Omega) = \frac{2\sqrt{\kappa_{out}\kappa_{in}}\mathbf{A}_{in}(\Omega) + [2\kappa_{out} - \kappa - i\Omega]\mathbf{A}_{out}(\Omega) + 2\sqrt{\kappa_{out}\kappa_l}\mathbf{A}_l(\Omega)}{\kappa + i\Omega}, \quad (3.79)$$

$$\mathbf{A}_{loss}(\Omega) = \frac{2\sqrt{\kappa_l\kappa_{in}}\mathbf{A}_{in}(\Omega) + 2\sqrt{\kappa_l\kappa_{out}}\mathbf{A}_{out}(\Omega) + [2\kappa_l - \kappa - i\Omega]\mathbf{A}_l(\Omega)}{\kappa + i\Omega}. \quad (3.80)$$

The power at each port is then

$$P_k = \hbar\omega_d A_k^\dagger A_k \quad (3.81)$$

where  $k = ref, trans$ , and  $loss$ .

### 3.3.4 Noise variances of the reflected and transmitted fields

The fields  $A_k$  can be represented in terms of their steady state and fluctuating components

$$A_k(t) = \bar{A}_k + \delta A_k(t), \quad (3.82)$$

where  $\bar{A}_k = \langle A_k(t) \rangle$  and  $\langle \delta A_k(t) \rangle = 0$ . The quadratures operators relative to the frequency  $\omega_a$  are

$$\delta X_1^{(k)}(\Omega) = \delta A_k(\Omega) + \delta A_k^\dagger(-\Omega), \quad (3.83)$$

$$\delta X_2^{(k)}(\Omega) = -i(\delta A_k(\Omega) - \delta A_k^\dagger(-\Omega)). \quad (3.84)$$

The amplitude and phase quadratures are then

$$\begin{aligned} \delta \mathbf{X}^{(trans)} &= \frac{2\sqrt{\kappa_{in}\kappa_{out}}\delta \mathbf{X}^{(in)} + (2\kappa_{out} - i\Omega - \kappa)\delta \mathbf{X}^{(out)} + 2\sqrt{\kappa_l\kappa_{out}}\delta \mathbf{X}^{(l)}}{i\Omega + \kappa}, \\ \delta \mathbf{X}^{(ref)} &= \frac{(2\kappa_{in} - i\Omega - \kappa)\delta \mathbf{X}^{(in)} + 2\sqrt{\kappa_{out}\kappa_{in}}\delta \mathbf{X}^{(out)} + 2\sqrt{\kappa_l\kappa_{in}}\delta \mathbf{X}^{(l)}}{i\Omega + \kappa}, \end{aligned}$$

where

$$\delta \mathbf{X}^{(k)} = \begin{pmatrix} \delta X_1^{(k)} \\ \delta X_2^{(k)} \end{pmatrix}, \quad \delta \mathbf{X}^{(j)} = \begin{pmatrix} \delta X_1^{(j)} \\ \delta X_2^{(j)} \end{pmatrix}, \quad (3.85)$$

again with  $k = ref, trans$ , and  $loss$  and  $j = in, out$ , and  $l$ . The notation used here does not explicitly denote the dependence on the sideband frequency  $\Omega$ , for notational ease.

The variances of the fields are defined by  $V^{(k)} = \langle |\delta X^{(k)}|^2 \rangle$ . The transmitted and reflected variances are

$$\mathbf{V}^{(trans)} = \frac{4\kappa_{in}\kappa_{out}\mathbf{V}^{(in)} + ((2\kappa_{out} - \kappa)^2 + \Omega^2) + 4\kappa_l\kappa_{out}}{\Omega^2 + \kappa^2}, \quad (3.86)$$

$$\mathbf{V}^{(ref)} = \frac{((2\kappa_{in} - \kappa)^2 + \Omega^2)\mathbf{V}^{(in)} + 4\kappa_{in}\kappa_{out} + 4\kappa_l\kappa_{in}}{\Omega^2 + \kappa^2}, \quad (3.87)$$

where the substitution  $V_{1,2}^{(out)} = V_{1,2}^{(l)} = 1$  has been made given that these fields are in the vacuum state. Figure 3.7 shows the amplitude quadrature variances of the transmitted and reflected fields for an input field variance of  $V_1^{(in)} = 10$ , relative to the quantum noise limit. This was plotted for the cavity with parameters given in the caption of figure 3.6. The sideband frequency dependence of the variances in figure 3.7 shows that the cavity acts as a low pass filter on transmission and as a high pass filter on reflection.

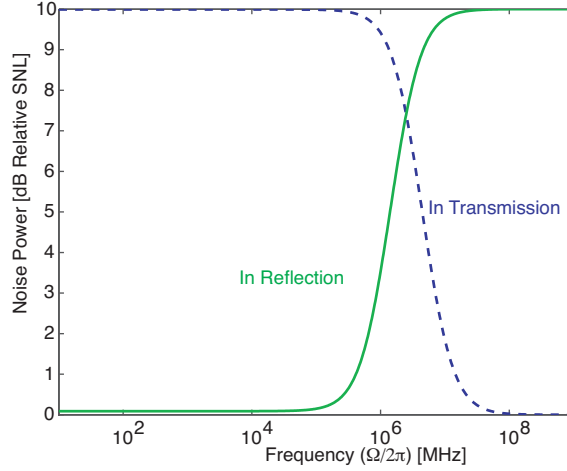


**Figure 3.7:** The amplitude quadrature noise variances of the reflected and transmitted fields relative to the shot noise limit (SNL) with 10dB of excess amplitude noise on the input field. Cavity parameters are the same as described in the caption of figure 3.6.

### 3.3.5 Useful cavity parameters

The *Free Spectral Range* (FSR) is a measure of the frequency separation between adjacent cavity modes<sup>3</sup>. The FSR is given by

$$\nu_{fsr} = \frac{c}{p} \quad (3.88)$$

where  $c$  is the speed of light and  $p$  the round trip optical path length. The *finesse* of a cavity is given by<sup>4</sup>

$$\mathcal{F} = \frac{\pi(R_{in}R_{out}R_l)^{\frac{1}{4}}}{1 - \sqrt{R_{in}R_{out}R_l}} \approx \frac{2\pi}{T_{in} + T_{out} + T_l}. \quad (3.89)$$

The *Full Width at Half Maximum* height (FWHM) is a measure of the linewidth of the cavity can be found from the FSR and the finesse

$$\delta\nu = \frac{\nu_{fsr}}{\mathcal{F}}. \quad (3.90)$$

The cavity quality factor, or  $Q$ , analogous to the quality factor of LC circuits is

$$Q = \frac{\omega\mathcal{F}}{2\pi\nu_{fsr}}. \quad (3.91)$$

<sup>3</sup>The equations of motion for the Fabry-Perot resonator presented here only considers one cavity mode (not adjacent FSRs).

<sup>4</sup>These equations for finesse are accurate for moderate to high reflectivity mirrors with  $R \geq 0.9$ . See p 428 of Lasers [90] for further information.

The circulating power in a cavity is given by

$$P_{circ} = \frac{\hbar\omega a^\dagger a}{\tau} = \frac{4T_{in}}{(T_{in} + T_{out} + T_l)^2} P_{in}, \quad (3.92)$$

where  $P_{in}$  is the input power. The *coupling* of the cavity is determined by the transmissivity of the mirror at the input port in relation to the total round trip loss. The three possible scenarios are

$$\begin{aligned} 2\kappa_{in} &> \kappa && \text{Overcoupled,} \\ 2\kappa_{in} &= \kappa && \text{Critically coupled,} \\ 2\kappa_{in} &< \kappa && \text{Undercoupled.} \end{aligned}$$

For the cavity parameters used in figure 3.6

$$\begin{aligned} \nu_{fsr} &= 150 \text{ MHz,} \\ \mathcal{F} &= 30, \\ \delta\nu &= 5 \text{ MHz,} \\ Q &= 5.6 \times 10^7, \end{aligned}$$

and the cavity is overcoupled.

### 3.4 Nonlinear interactions

As electromagnetic radiation passes through a dielectric medium, it induces a macroscopic polarization in the medium. The induced polarization is due to many loosely bound valence electrons being displaced by the electric field [4]. The polarized medium re-radiates the energy as an electric field. *Linear* dielectric media have a polarizability potential that is symmetric, so the polarization induced is directly proportional to the electric field inducing it. The re-radiated field is then a copy of the inducing field. Nonlinear media differ in that the polarizability potential is asymmetric and therefore the induced polarization is no longer directly proportional to the electric field. The polarization of the media can be written as the polynomial in the inducing electric field  $E$

$$\mathcal{P} = \epsilon_0(\chi^{(1)}E + \chi^{(2)}E^2 + \chi^{(3)}E^3 + \dots), \quad (3.93)$$

where  $\epsilon_0$  is the permittivity of free space and  $\chi^{(i)}$  represent the polarizability parameter for the  $i$ th order. In linear dielectrics  $\chi^{(1)}$  is the only non zero order of polarizability.

The experiments in this thesis use  $\chi^{(2)}$  nonlinear media to produce squeezed states. Here the  $\chi^{(2)}$  polarizability is the dominant higher order nonlinear coefficient. The  $\chi^{(2)}$  nonlinearity is responsible for three wave mixing effects like sum frequency generation and parametric down-conversion.

The  $\chi^{(3)}$  nonlinearity, also called the Kerr effect, includes such effects as intensity-dependent phase shifts. The mechanical Kerr effect is seen in interferometric gravitational wave detectors from the interaction of the laser field and the mirrors position via radiation pressure on the mirrors. The radiation pressure effects play a significant role in shaping the quantum noise limited sensitivity of gravitational wave detectors.

### 3.4.1 $\chi^{(2)}$ nonlinear interactions

$\chi^{(2)}$  nonlinear interactions can be separated into two regimes - up-conversion and down-conversion. Diagrams for the general up- and down-conversion processes are shown in figure 3.8. In up-conversion, two low energy photons are converted into one high energy photon. Down conversion is the complimentary process, a high energy photon is converted into two lower energy photons. For three interacting fields at frequencies  $\omega_1, \omega_2$  and  $\omega_3$  the conservation of energy requires that

$$\omega_3 = \omega_1 + \omega_2 \quad [\text{up-conversion}] \quad (3.94)$$

$$\omega_1 + \omega_2 = \omega_3 \quad [\text{down-conversion}] \quad (3.95)$$

Perhaps the simplest up-conversion process is second harmonic generation (SHG). In SHG the



**Figure 3.8:** A representation of different  $\chi^{(2)}$  nonlinear interactions. Left: Up-conversion; Two low energy photons (at  $\omega_1$  and  $\omega_2$ ) are converted into one higher photon (at  $\omega_3$ ). Right: Down-conversion; One high energy photon (at  $\omega_3$ ) is converted into two lower energy photons (at  $\omega_1$  and  $\omega_2$ ).

low energy photons have the same frequency ( $\omega_1 = \omega_2 = \omega_f$ ), which is often called the fundamental frequency. The up-converted field then is at the second harmonic frequency,  $2\omega_f$ . Second harmonic generation is widely used in research and commercial products to access optical frequencies where laser transitions may not be available or convenient. The complimentary process to SHG is degenerate optical parametric amplification (OPA). In degenerate OPA, a photon at frequency  $2\omega$  is converted into two photons at frequency  $\omega$ . Degenerate OPA and SHG are the degenerate cases of the  $\chi^{(2)}$  nonlinear interaction. In the non degenerate cases, sum frequency generation and non-degenerate OPA, the interacting fields have the frequency relations given in equations 3.94 and 3.95 as well as

$$\omega_1 = \omega_3/2 + \gamma, \quad \omega_2 = \omega_3/2 - \gamma; \quad (3.96)$$

where  $\gamma$  is a frequency offset.

### 3.4.2 Coupled wave equations and phase matching

Consider three fields with complex amplitudes  $A_1, A_2$ , and  $A_3$  propagating through a nonlinear medium. The field amplitudes will evolve as a function of distance. If this evolution is slow enough for the field amplitude to change little over the distance of an optical wavelength, the slowly varying envelope approximation can be invoked [91]. This simplifies the (classical) three-

wave mixing coupled equations to [91]

$$\frac{dA_1}{dz} = -i\Gamma A_3 A_2^* e^{-i\Delta kz}, \quad (3.97)$$

$$\frac{dA_2}{dz} = -i\Gamma A_3 A_1^* e^{-i\Delta kz}, \quad (3.98)$$

$$\frac{dA_3}{dz} = -i\Gamma A_1 A_2 e^{i\Delta kz}, \quad (3.99)$$

where  $\Gamma$  is proportional to the strength of the nonlinearity and  $\Delta k$  is called the phase matching parameter, given by

$$\Delta k = k_3 - k_2 - k_1, \quad (3.100)$$

where the wave vectors are given by  $k_1 = \omega_1 n(\omega_1)/c_0$  and  $n(\omega_1)$  is the refractive index at the frequency  $\omega_1$  and  $k_2$  and  $k_3$  are defined similarly. Consider the interaction over a length  $L$  in the degenerate case where  $\omega_1 = \omega_2$ . The fields amplitudes can be found by integrating from  $z = 0$  to  $L$

$$A_1(L) = A_1(0) - iL\Gamma g(\Delta kL) A_3(0) A_1^*(0), \quad (3.101)$$

$$A_3(L) = A_3(0) + iL\Gamma g^*(\Delta kL) A_1^2(0), \quad (3.102)$$

where the function  $g(\Delta kL)$ [4] is a complex function of the phase matching parameter

$$g(\Delta kz) = \text{sinc}(\Delta kz/2) e^{-i\Delta kz/2}. \quad (3.103)$$

The real and imaginary components of the phase matching function are shown in figure 3.9. The phase matching is crucial in determining the efficiency of the nonlinear interaction. The field evo-

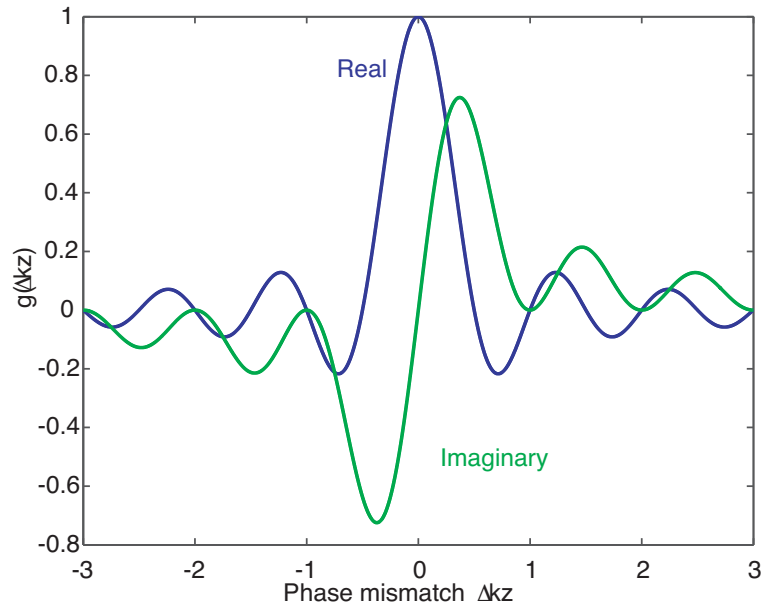


**Figure 3.9:** Real and imaginary components of the phase matching parameter,  $g(\Delta kL)$ .

lutions depends on the initial field amplitudes and relative phases as well as their phase velocities (the phase matching). It can be seen that, because the interaction of the fields depends on the

relative phase of the interacting waves, a phase mismatch changes the interaction as a function of length. In SHG, for example, a phase mismatch causes the direction of power flow from the fundamental to harmonic field to reverse at an interaction length called the *coherence length*. The coherence length is defined by

$$l_c = \frac{\pi}{k_3 - 2k_1}. \quad (3.104)$$

The net power flow returns to zero over an interaction length of  $2l_c$ . This is shown as a phasor diagram in figure 3.10 (a) and by curve (i) in figure 3.11. The phasor diagram show incremental components of produced second harmonic field adding up phasorially. Each incremental component represents the produced second harmonic field over a small length  $dl$ . As there is a phase mismatch in the process, the component of second harmonic field produced between  $dl$  and  $2dl$  has a phase shift with respect to the field produced between 0 and  $dl$ . As the process continues, the power flow into the second harmonic field becomes cyclical.

Second harmonic generation which is phase matched is shown phasorially in figure 3.10 (c) and by curve (iii) in figure 3.11. The power in the second harmonic field grows quadratically. Here the power flow is only one way (from the fundamental frequency field to the harmonic frequency field) as the interacting fields start in phase and maintain that phase relation.

Most dielectric materials are dispersive so the phase matching condition is not naturally satisfied. Techniques must be employed to enable phase matching to occur. There are two main techniques used in the field of dielectric nonlinear media: birefringent phase matching (BPM) (see for example [92, 93]) and quasi phase matching (QPM) [94, 95]. Both techniques were used (in different nonlinear media) in experiments presented in this thesis. In magnesium doped lithium niobate ( $\text{Mg}:\text{LiNbO}_3$ ) we used type I BPM, and in periodically poled potassium titanyl phosphate ( $\text{KTiOPO}_4$ ), or PPKTP for short, we used QPM.

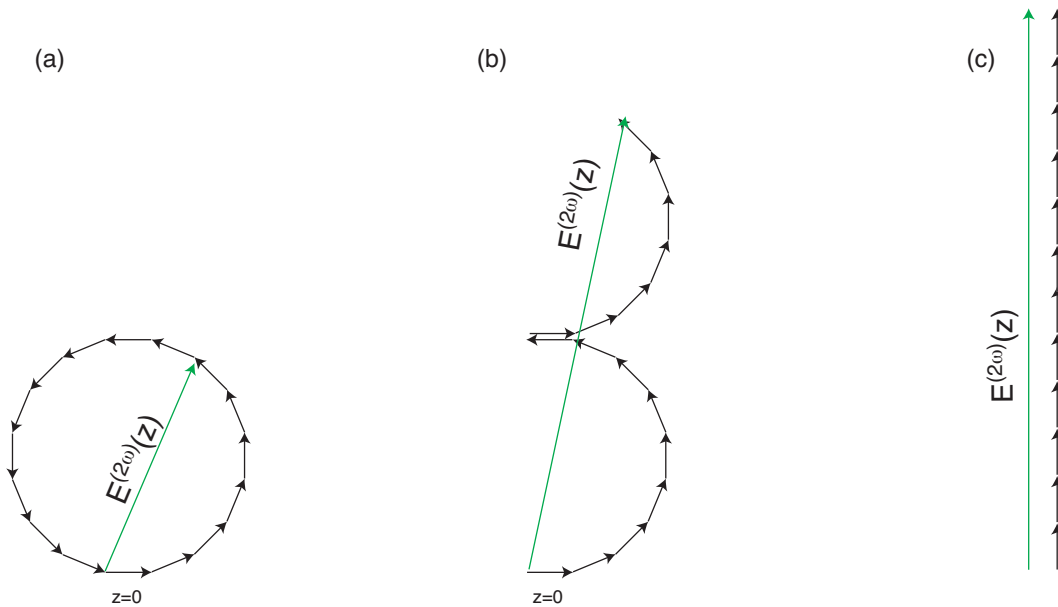


**Figure 3.10:** Phasor representation of the resultant second harmonic field ( $E^{2\omega}(z)$ ) for: (a) a phase mismatched material, (b) a quasi phase matched material, and (c) a phase matched material. (reproduced from [4] and [5])

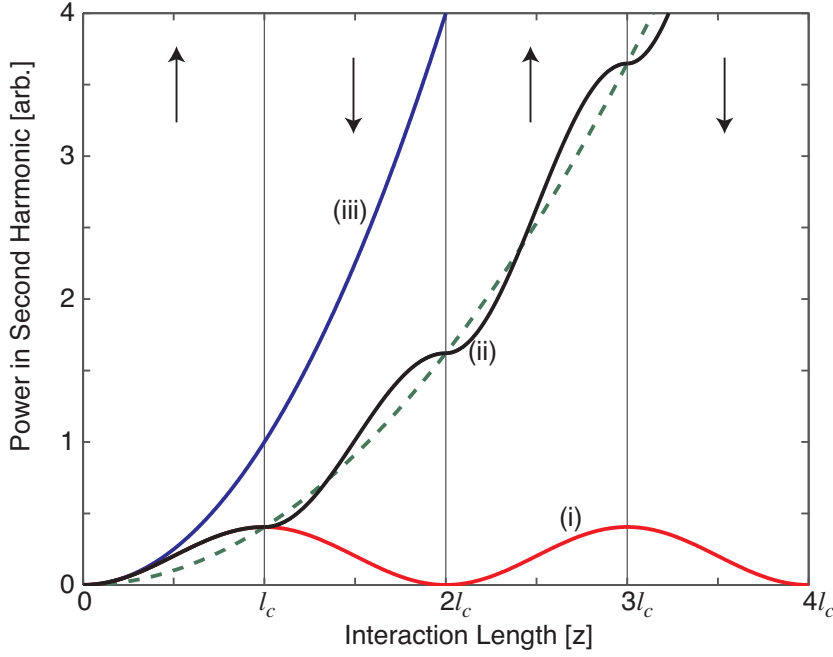


**Figure 3.11:** The power in the second harmonic vs the interaction length. Curve (i) shows a phase mismatched material with  $\Delta kz = \pi/2$ . Curve (ii) is the quasi phase matched material with  $\Delta kz = \pi/2$  and domain period  $\Lambda = l_c$ . Curve (iii) represents the phase matched case ( $\Delta kz = 0$ ).

### Birefringent phase matching

Phase matching can be achieved in birefringent media by polarizing the interacting waves along different axes of the medium. There are predominantly two ways to satisfy the phase matching condition using BPM called type I and type II phase matching.

#### Type I BPM

In type I phase matching in a uniaxial crystal, the high energy field is polarized along the extraordinary ( $z$ ) axis of the crystal and low energy modes along the ordinary axis ( $x$  or  $y$ ) ( $\uparrow_{\omega_3} = \rightarrow_{\omega_1} + \rightarrow_{\omega_2}$ ). Type I phase matching is often used in  $\text{LiNbO}_3$  which is a uniaxial crystal. The low energy modes can be polarized along either the  $x$  or  $y$  axes and maintain nonlinear interaction. This is called non-critical phase matching.

The temperature and wavelength dependence of the phase-matching condition for  $\text{MgO}:\text{LiNbO}_3$  is described by the Sellmeier equation [96], which can be approximated around the optimum temperature  $T_0$  and wavelength  $\lambda_0$  to

$$\Delta k = \varphi(T - T_0) - \psi\left(1 - \frac{\lambda}{\lambda_0}\right), \quad (3.105)$$

where  $\varphi$  and  $\psi$  are constants whose value depends on the crystal's properties,  $T$  is the crystal's temperature, and  $\lambda$  is the fundamental wavelength.

#### Type II BPM

In type II phase matching the high energy mode and one of the low energy modes are polarized along the extraordinary axis of the crystal, and the other low energy mode is polarised along the

ordinary axis. ( $\uparrow_{\omega_3} = \uparrow_{\omega_2} + \rightarrow_{\omega_1}$ ). Type II phase matching is often used in nonlinear media such as potassium titanyl phosphate (KTiOPO4 or KTP for short).

### Quasi-phase matching

Quasi-phase matching (QPM) is fundamentally different BPM. The *quasi* part of the name refers to the fact that the phase velocities of the interacting waves are not matched, rather the phase of the already generated field is approximately matched with newly created field. This is achieved by periodically modulating the nonlinear medium with an appropriate structure. The most common technique is periodic poling. A periodically poled crystal has the sign of the nonlinear susceptibility inverted periodically at a distance  $m$  times the coherence length, which is called the grating period

$$\Lambda_n = ml_c, \quad (3.106)$$

where  $m$  is called the QPM order. The diagram in figure 3.10 (b) shows the phasor representation of QPM in SHG. At the coherence length (where destructive interference starts in non-QPM materials), the sign of the nonlinear susceptibility of the medium is flipped so the newly created fields constructively interfere with the already generated fields. The power converted to second harmonic as a function of nonlinear medium length is plotted in figure 3.11 (ii). It can be seen that the power generated in the first coherence length matches that of the non phase matched case, curve (i).

For the same nonlinear susceptibility, QPM is not as efficient as a non-QPM systems. The efficiency for  $m$ th order QPM system relative to perfect phase matching is

$$\eta_{QPM}(m) = \frac{1}{m^2} \frac{4}{\pi^2}. \quad (3.107)$$

thus for first order QPM, the efficiency is reduced by  $4/\pi^2$ .

The use of QPM materials, which have advantages over BPM materials, has increased in the last two decades as the crystal production technologies improve. In QPM, the interacting modes can share the same polarization, thus nonlinear coefficients inaccessible to BPM can be used. Some of these nonlinear coefficients are much greater than those where different polarizations are used. QPM can also be used in isotropic media such as GaAs, in which BPM is not possible. Interestingly, the invention of QPM preceded BPM [94, 95], though BPM was the dominant technique until mid 1980's [97].

## 3.5 $\chi^{(2)}$ nonlinearity in an optical cavity

The efficiency of nonlinear interaction can be greatly enhanced by placing the nonlinear medium in an optical resonator. In this section the equations of motion for a cavity with  $\chi^{(2)}$  nonlinearity are presented and the classical and quantum properties of an optical parametric amplifier are introduced.

### 3.5.1 Equations of motion

The Hamiltonian for a degenerate  $\chi^{(2)}$  nonlinear interaction describes the swapping of photons between the fundamental and harmonic modes. The interaction Hamiltonian is [80]

$$H_{int} = \frac{i\hbar\epsilon}{2}(a^{\dagger 2}b - a^2b^{\dagger}), \quad (3.108)$$

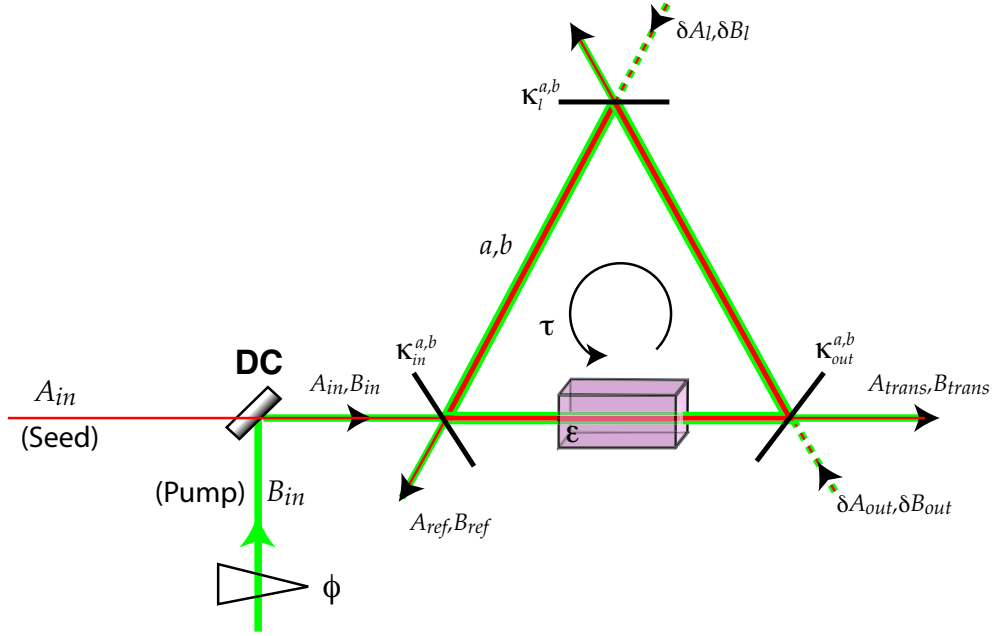


**Figure 3.12:** A schematic of an OPA. The fundamental and harmonic cavity modes are  $a$  and  $b$ . Extra-cavity fields are denoted with capital letters. DC is a dichroic mirror.

where the interacting fields  $a$  and  $b$  are at the fundamental frequency and harmonic frequency, respectively. The nonlinear coupling rate is given by  $\epsilon$ , which depends on the magnitude of the  $\chi^{(2)}$  nonlinearity as well as experimental parameters such as beam waist, phase matching, and medium length.

Consider a cavity which contains a  $\chi^{(2)}$  nonlinearity and resonates both  $a$  and  $b$ . The  $\chi^{(2)}$  nonlinearity couples the cavity fields. The equations of motion are [98]

$$\dot{a} = -(\kappa^a + i\Delta^a)a + \epsilon a^\dagger b + \sqrt{2\kappa_{in}^a}A_{in} + \sqrt{2\kappa_{out}^a}A_{out} + \sqrt{2\kappa_l^a}A_l, \quad (3.109)$$

$$\dot{b} = -(\kappa^b + i\Delta^b)b - \frac{\epsilon^* a^2}{2} + \sqrt{2\kappa_{in}^b}B_{in} + \sqrt{2\kappa_{out}^b}B_{out} + \sqrt{2\kappa_l^b}B_l, \quad (3.110)$$

where the terms proportional to  $\epsilon$  are responsible of the nonlinear dynamics. The parameters in equations 3.109 and 3.110 are defined similarly to the parameters in the empty cavity in section 3.3 and are shown in the schematic of the cavity in figure 3.12. The parameters are:  $\kappa^a$  and  $\kappa^b$  are the total resonator decay rates for each field;  $A_{in}, A_{out}, A_l$  and  $B_{in}, B_{out}, B_l$  are the driving fields with the respective coupling rates are  $\kappa_{in}^a, \kappa_{out}^a, \kappa_l^a$  and  $\kappa_{in}^b, \kappa_{out}^b, \kappa_l^b$  for the input, output, and roundtrip loss; and the detunings of the fundamental and harmonic cavities are given by  $\Delta^a$  and  $\Delta^b$ .

### 3.5.2 Optical parametric amplification: a semiclassical approach

In degenerate OPA, energy from the second harmonic field, which is referred to as the *pump field*, provides a phase dependent amplification of the fundamental field, which is referred to as the *seed field*. In this section, degenerate OPA is introduced using a semi-classical approach, where the pump field is taken to be a non-depletable classical field. Using this approximation, the underlying dynamics of the OPA process can be illuminated with simple equations. In chapter 5 a more complex analysis is presented and the noise couplings from the pump field, and other

sources, are studied.

The cavity fields can be calculated in the same manner as in section 3.3.1. With  $q = \varepsilon \bar{b}$  the equation of motion is

$$\dot{a} = -(\kappa^a + i\Delta^a)a + qa^\dagger + \sqrt{2\kappa_{in}^a}A_{in} + \sqrt{2\kappa_{out}^a}A_{out} + \sqrt{2\kappa_l^a}A_l. \quad (3.111)$$

In compact form we have

$$\dot{\mathbf{a}} = \mathbf{M}_a \mathbf{a} + \mathbf{M}_{in} \mathbf{A}_{in} + \mathbf{M}_{out} \mathbf{A}_{out} + \mathbf{M}_l \mathbf{A}_l, \quad (3.112)$$

where the vectors  $\dot{\mathbf{a}}$ ,  $\mathbf{a}$  and  $\mathbf{A}_j$  are given in equation 3.61 and the matrices are

$$\mathbf{M}_a = \begin{bmatrix} -\kappa^a - i\Delta & q \\ q^* & -\kappa^a + i\Delta \end{bmatrix}, \quad (3.113)$$

$$\mathbf{M}_{in} = \sqrt{2\kappa_{in}^a} \mathbf{I}, \quad \mathbf{M}_{out} = \sqrt{2\kappa_{out}^a} \mathbf{I}, \quad \mathbf{M}_l = \sqrt{2\kappa_l^a} \mathbf{I}, \quad (3.114)$$

where  $\mathbf{I}$  is the  $2 \times 2$  identity matrix.

### 3.5.3 Classical parametric gain

Using the equation of motion (equation 3.112) and the input-output relations (equations 3.69, 3.70 and 3.71), the OPA dynamics can be calculated. The parametric gain of the seed field is given by the ratio

$$\frac{P_{trans}(q)}{P_{trans}(q=0)} = \frac{((\kappa^a)^2 + |q|^2 + 2|q|\kappa_a \cos \phi)(\kappa^a)^2}{((\kappa^a)^2 - |q|^2)^2}, \quad (3.115)$$

where  $q = |q|e^{i\phi}$  with  $\phi$  the relative phase of the pump and seed fields, we have chosen  $A_{in} = A_{in}^*$  and the the cavity detuning is set to zero.

Optical parametric threshold occurs when the round trip nonlinear gain equals the round trip loss ( $|q| = \kappa^a$ ). At this point, the parametric gain goes to infinity (in the limit of no pump depletion). If the cavity is vacuum seeded, the light is produced. We can rewrite the parametric gain in with the substitution  $\left(\frac{q}{\kappa^a} \rightarrow \sqrt{\frac{P}{P_{thresh}}}\right)$

$$\frac{P_{trans}(q)}{P_{trans}(q=0)} = \frac{1 + \frac{P}{P_{thresh}} + 2 \cos \phi \sqrt{\frac{P}{P_{thresh}}}}{\left(1 - \frac{P}{P_{thresh}}\right)^2}, \quad (3.116)$$

where  $P$  is the pump power and  $P_{thresh}$  is the pump power required to reach the optical parametric oscillation threshold.

Equation 3.116 shows the phase dependence of the parametric process. The seed field can be amplified or de-amplified, depending on the phase relation of the pump and seed fields. The parametric gain is plotted in figure 3.13 for (i)  $\phi = 0$  and (ii)  $\phi = \pi$ , corresponding to amplification and deamplification of the seed field, respectively. Near threshold the gain approaches infinity for  $\phi = 0$  and  $1/4$  for  $\phi = \pi$ .

Here we have only considered the below threshold case ( $P < P_{thresh}$ ). There are many interesting dynamics seen in both threshold and above threshold operation, though they are not studied in this thesis. Below threshold operation offers favorable conditions for generating squeezed vacuum

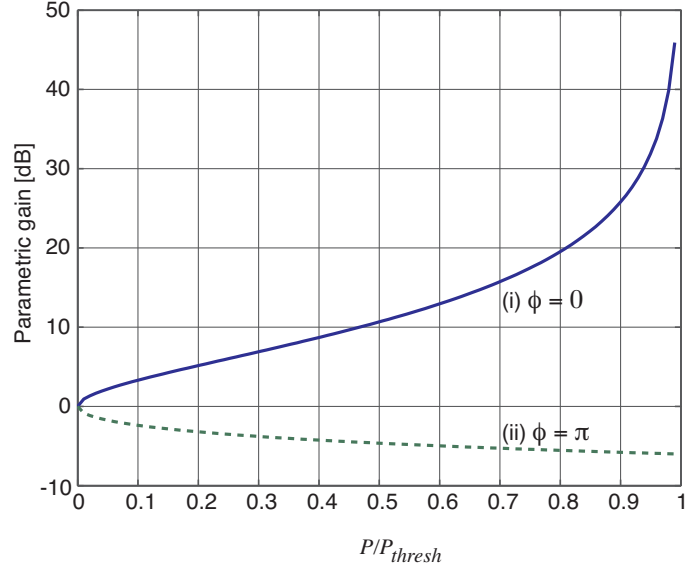


**Figure 3.13:** Parametric gain of the seed field given by equation 3.116. Amplification ( $\phi = 0$ ) and deamplification ( $\phi = \pi$ ) are shown in curves (i) and (ii).

states, which is done in experiments performed throughout this thesis.

### 3.5.4 Noise variances in parametric down-conversion

The quantum mechanical dynamics of the OPA mimic the classical dynamics. The phase sensitive amplification of OPA leads to the simultaneous squeezing of the fluctuations in one quadrature and anti-squeezing the fluctuations in the orthogonal quadrature. In this section the transmitted quadrature amplitudes  $\delta X_{1,2}^{(trans)}$ , and the corresponding variances  $V_{1,2}^{(trans)}$ , are determined to study the squeezing and anti-squeezing. Using equations 3.112, 3.68, and 3.84 the transmitted field amplitudes are given by

$$\begin{aligned} \mathbf{A}_{trans} &= \mathbf{M}_{out} \mathbf{a} - \mathbf{A}_{out}, \\ &= \mathbf{M}_{out} (i\Omega \mathbf{I} - \mathbf{M}_a)^{-1} [\mathbf{M}_{in} \mathbf{A}_{in}(\Omega) + \mathbf{M}_{out} \mathbf{A}_{out}(\Omega) + \mathbf{M}_l \mathbf{A}_l(\Omega)] - \mathbf{A}_{out}(\Omega). \end{aligned} \quad (3.117)$$

To start with, consider the simplest case: a single ported ( $T_{in}^a = 0$ ), lossless ( $T_l^a = 0$ ), cavity on resonance ( $\Delta^a = 0$ ) with a real gain parameter ( $q = q^*$ ). Using equations 3.117, 3.68, and 3.84 the transmitted amplitude and phase quadratures are found to be

$$\delta X_1^{(trans)} = \frac{\kappa^a + q - i\Omega}{\kappa^a - q + i\Omega} \delta X_1^{(out)}, \quad (3.118)$$

$$\delta X_2^{(trans)} = \frac{\kappa^a - q - i\Omega}{\kappa^a + q + i\Omega} \delta X_2^{(out)}. \quad (3.119)$$

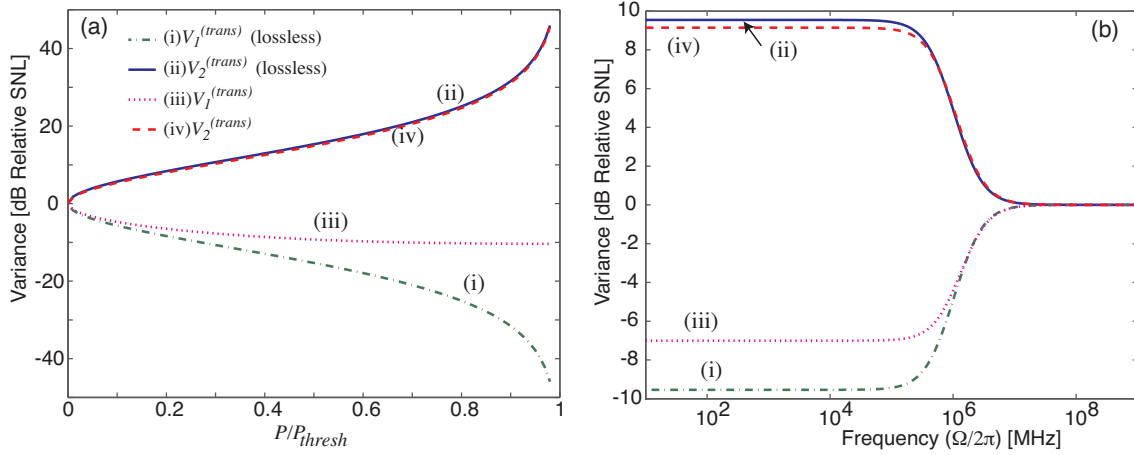


**Figure 3.14:** Variances of the transmitted field from an OPA plotted relative to the shot noise limit (SNL). Figure (a) is plotted as a function of pump power, and figure (b) as a function of sideband frequency. Curves (i) and (ii) show the variances neglecting intra-cavity losses and curves (iii) and (iv) show the variances calculated with intra-cavity losses. In both figures the variances of the input fields have been set in the vacuum state:  $V_{1,2}^{(in)} = V_{1,2}^{(out)} = V_{1,2}^{(l)} = 1$ . Cavity parameters:  $L = 2\text{m}$ ,  $\lambda = 1\mu\text{m}$ ,  $T_{out}^a = 0.10$ ,  $q = \kappa^a/2$ . In the lossless case:  $T_{in}^a = T_l^a = 0$ , with losses  $T_{in}^a = 0.001$ ,  $T_l^a = 0.01$ .

In general the extra-cavity field  $A_{out}$ , is the vacuum state. Thus  $V^{(out)} = 1$ , and the variances are simply

$$V_1^{(trans)} = \frac{1}{\mathcal{G}}, \quad (3.120)$$

$$V_2^{(trans)} = \mathcal{G}, \quad (3.121)$$

where

$$\mathcal{G} = \frac{(\kappa^a - q)^2 + \Omega^2}{(\kappa^a + q)^2 + \Omega^2} = \frac{\left(1 - \sqrt{\frac{P}{P_{thresh}}}\right)^2 + \Omega^2/(\kappa^a)^2}{\left(1 + \sqrt{\frac{P}{P_{thresh}}}\right)^2 + \Omega^2/(\kappa^a)^2}. \quad (3.122)$$

In this idealised case, the OPA produces a minimum uncertainty squeezed state. If  $q$  is positive this is an amplitude squeezed state. If  $q$  is negative this is a phase squeezed state. Curves (i) and (ii) in figure 3.14 (a) show  $V_1^{(trans)}$  and  $V_2^{(trans)}$  plotted as a function of pump power with positive  $q$  and  $\Omega = 0$ . In figure 3.14 (b)  $V_1^{(trans)}$  and  $V_2^{(trans)}$  are plotted in curves (i) and (ii), respectively, with and  $P = 0.25P_{thresh}$  as a function of sideband frequency. This is a minimum uncertainty amplitude squeezed state. The noise amplification (deamplification) is constant below the cavity pole and rolls-off above the cavity pole. Well above the cavity pole the noise variances approach the vacuum state.

Next we calculate the OPA output including intra-cavity losses. If we continue to assume  $\Delta^a = 0$  and  $q = q^*$ , the amplitude and phase quadratures can be found using equations 3.68 and

3.84

$$\delta X_1^{(trans)} = \frac{2\sqrt{\kappa_{in}^a \kappa_{out}^a} \delta X_1^{(in)} + (2\kappa_{out}^a - i\Omega - \kappa^a + q) \delta X_1^{(out)} + 2\sqrt{\kappa_l^a \kappa_{out}^a} \delta X_1^{(l)}}{i\Omega + \kappa^a - q}, \quad (3.123)$$

$$\delta X_2^{(trans)} = \frac{2\sqrt{\kappa_{in}^a \kappa_{out}^a} \delta X_2^{(in)} + (2\kappa_{out}^a - i\Omega - \kappa^a - q) \delta X_2^{(out)} + 2\sqrt{\kappa_l^a \kappa_{out}^a} \delta X_2^{(l)}}{i\Omega + \kappa^a + q}, \quad (3.124)$$

and the variances are

$$V_1^{(trans)} = \frac{4\kappa_{in}^a \kappa_{out}^a V_1^{(in)} + ((2\kappa_{out}^a - \kappa^a + q)^2 + \Omega^2) + 4\kappa_l^a \kappa_{out}^a}{\Omega^2 + (\kappa^a - q)^2}, \quad (3.125)$$

$$V_2^{(trans)} = \frac{4\kappa_{in}^a \kappa_{out}^a V_2^{(in)} + ((2\kappa_{out}^a - \kappa^a - q)^2 + \Omega^2) + 4\kappa_l^a \kappa_{out}^a}{\Omega^2 + (\kappa^a + q)^2}. \quad (3.126)$$

If the seed field is in the coherent state equations 3.125 and 3.126 can be written as

$$V_1^{(trans)} = 1 + \eta_{esc} \frac{4\kappa^a q}{\Omega^2 + (\kappa^a - q)^2}, \quad (3.127)$$

$$V_2^{(trans)} = 1 - \eta_{esc} \frac{4\kappa^a q}{\Omega^2 + (\kappa^a + q)^2}, \quad (3.128)$$

where  $\eta_{esc}$  is the cavity escape efficiency given by

$$\eta_{esc} = \frac{\kappa_{out}^a}{\kappa_a} = \frac{T_{out}}{T_{out} + T_{in} + T_l}. \quad (3.129)$$

The escape efficiency is a measure of the maximum obtainable quantum noise suppression from the OPA cavity. At the optical parametric oscillation threshold ( $q = \kappa^a$ ) the maximum squeezing is found and given by

$$V_{Sgz|Max}^{(trans)} = 1 - \eta_{esc}. \quad (3.130)$$

Curves (iii) and (iv) in figures 3.14 (a) and (b) show  $V_1^{(trans)}$  and  $V_2^{(trans)}$  calculated with losses. The figures show that the intra-cavity loss limits the magnitude of the squeezed that exits the cavity. This is a result of a fraction of the squeezed field being replaced by the vacuum field due to loss.

### 3.5.5 Optical parametric amplification verses optical parametric oscillation

In chapters 5, 6, and 7 an investigation into squeezing produced from parametric down conversion processes of optical parametric amplification and optical parametric oscillation is presented. Although the difference between the two modes of operation is subtle, the difference in the squeezing produced from the two processes is substantial. This short section is written to clarify the definition of optical parametric amplification and optical parametric oscillation used here.

- The seed field of an OPA contains optical power ( $\langle A_{in}^\dagger A_{in} \rangle \neq 0$ ). Thus the seed field can be amplified and it can be used as a classical device. The squeezed states produced from a OPA are bright squeezed states.
- The seed field an OPO contains *no* optical power ( $\langle A_{in}^\dagger A_{in} \rangle = 0$ ). That is, the seed field is the vacuum field. When operated below threshold, an OPO produces a squeezed vacuum state and has no classical output.

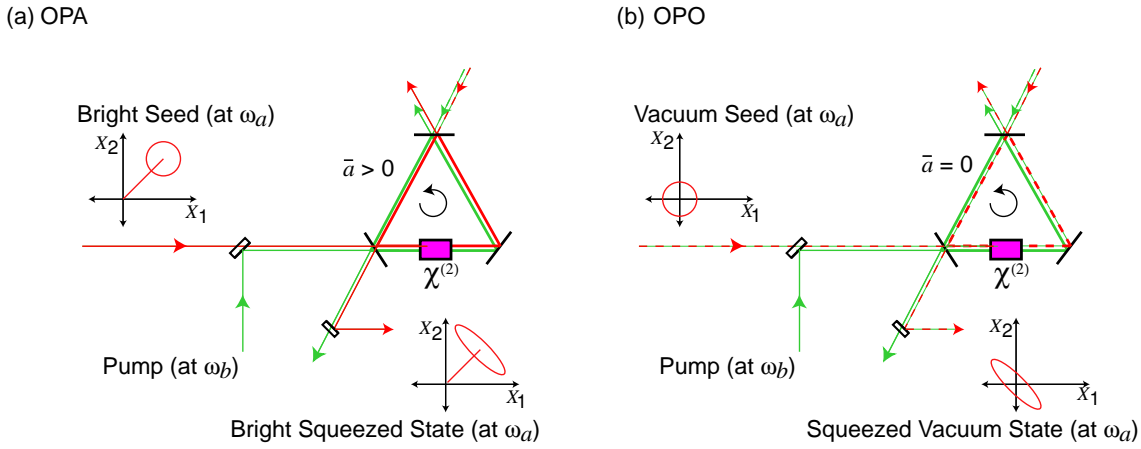


**Figure 3.15:** (a) Schematic of the OPA process. In OPA the seed field has a coherent amplitude and the squeezed state produced is a bright squeezed state. (b) Schematic of the OPO process operated below threshold. The seed field in OPO is the vacuum state and the squeezed state produced is a squeezed vacuum state.

These two processes are shown schematically in figure 3.15 (a) and (b). The definitions used here is used widely in the literature (for example, see [15, 21, 99]), but is not the exclusive definition. In references [100–105] a single pass parametric interaction is referred to as an ‘OPA’ and a parametric interaction in a cavity is called a ‘OPO’, with both generally consider to be vacuum seeded.

### 3.6 Chapter summary

This chapter has introduced some quantum optics notation, some devices used in quantum optics, and introduced the  $\chi^{(2)}$  nonlinearity. We have introduced

- states of light
- detection
- losses
- cavities
- the  $\chi^{(2)}$  nonlinearity
- phasematching
- optical parametric amplification

These are the basics needed to understand the theory and experiments in this thesis.

---

# Quantum noise and squeezing in interferometric gravitational wave detectors

---

This chapter provides background into the quantum noise limit in interferometric detectors and introduces possible squeezing enhancements. This provides context and motivation for the development of audio-frequency squeezed states. We show that squeezed states can improve the quantum noise limited strain (or displacement) sensitivity by up to  $1/\sqrt{e^{-2R}}$ , where  $R$  is the squeezing factor. For example, for a 10dB squeezed state ( $e^{-2R} = 0.1$ ), the strain sensitivity can be improved by a factor of 3.16 in the ideal lossless case.

## 4.1 Overview

In section 4.2 the quantum noise of a simple Michelson interferometer is introduced using the description and formalism of Kimble, Levin, Matsko, Thorne, and Levin from reference [38]. This calculation verifies that it is the vacuum fluctuations that enter the photodetector port, or antisymmetric port, of the Michelson interferometer that give rise to the quantum noise limit. In section 4.3 the discussion is then extended to include the injection of squeezed vacuum into antisymmetric port of the Michelson interferometer to illustrate the enhancement that squeezed states can provide. Following this, the quantum noise for the conventional interferometer, a power recycled Michelson interferometer with Fabry-Perot arm cavities, and the power and signal recycled interferometer with arm cavities are presented, along with the possible quantum noise enhancements that can be obtained using squeezed states.

## 4.2 Quantum noise limits

The Michelson interferometer is a natural choice for gravitational wave detection<sup>1</sup>. A perpendicular arm interferometer is ideal for detecting the quadrupole signal of gravitational waves. Operating the interferometer on a dark fringe, the Michelson interferometer offers considerable immunity to classical laser noise, reduces the power on the primary photodiodes, and offers the optimal shot noise performance [50]. For a lossless, ideal interferometer operating at a dark fringe, all of the laser light that enters the symmetric port reflects back towards the laser<sup>2</sup>. The same situation is

---

<sup>1</sup>Sagnac interferometers also offer many of the advantages of the Michelson interferometer, see for example [106], in addition they are naturally ‘speedmeter’ interferometers [107]

<sup>2</sup>Except for a very small component that couples to the asymmetric port due to the gravitational-wave signal.

true with the vacuum field that enters from the antisymmetric port - it too returns back towards the antisymmetric port photodetector with a phase shift, and with the electric field induced by the gravitational wave signal. Of course, if the laser classical amplitude and phase noise couple to the dark port only very weakly, so too does the quantum mechanical noise on the laser field. It can thus be seen that the quantum noise in gravitational wave detectors does not come from the laser. Caves published the first complete conceptual explanation of the origin of the quantum noise in interferometric gravitational wave detection [31], suggesting that the quantum noise (radiation pressure noise and shot noise) originates from the vacuum field that enters the interferometer from the antisymmetric port. More recently, Braginsky *et al.* confirmed that the quantum noise limits in gravitational wave detectors lies *solely in the quantum noise of the electromagnetic field* and not in the test mass quantization [32].

#### 4.2.1 Input-output relations of a Michelson interferometer

A derivation of the the input-output relation of a lossless Michelson interferometer is presented in Appendix A, following the derivation presented in the Appendix B of reference [38] and in the diploma thesis of Harms [108]. In this chapter we simply present the results. For the Michelson

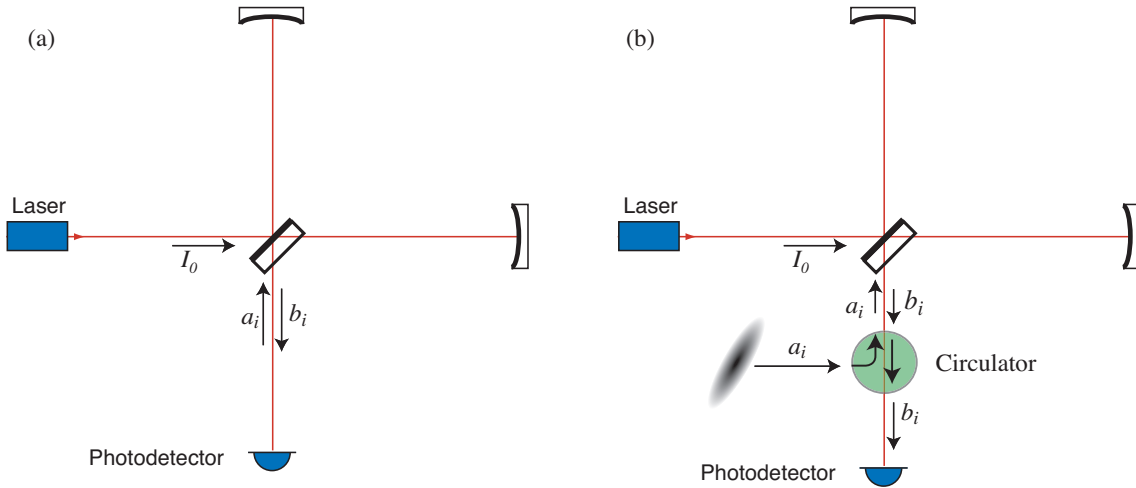


**Figure 4.1:** (a) A Michelson interferometer. The asymmetric port input and output fields are denoted  $a_i$  and  $b_i$ . The laser power at the symmetric port is  $I_0$ . (b) A Michelson interferometer with a squeezed state injected into the asymmetric port.

interferometer shown in figure 4.1 (a), and the more detailed figure A.1, the outgoing field of the asymmetric port,  $b$ , can be written terms of the ingoing field,  $a$ , and the gravitational wave strain,  $h$ . The formalism in this chapter uses the two photon formalism [109, 110]. The amplitude quadrature,  $b_1$ , and phase quadrature,  $b_2$ , of the outgoing fields are [38]

$$b_1 = \Delta b_1, \quad \Delta b_1 = a_1 e^{2i\beta}, \quad (4.1)$$

$$b_2 = \Delta b_2 + \sqrt{2\mathcal{K}} \frac{h}{h_{SQL}} e^{i\beta}, \quad \Delta b_2 = (a_2 - \mathcal{K}a_1) e^{2i\beta}, \quad (4.2)$$

where  $\Delta b_1$  and  $\Delta b_2$  are the fluctuating terms of the outgoing quadratures which arise due to quantum noise and  $a_1$  and  $a_2$  are the amplitude and phase quadratures of the field that enter the dark port. The single pass phase shift that the field at sideband frequency  $\Omega$  experience relative to the

carrier frequency  $\omega_0$ , is given by  $\beta = \Omega L/c$ , with  $L$  the arm length. Here

$$\mathcal{K} = \frac{4I_0\omega_0}{mc^2\Omega^2}, \quad (4.3)$$

is the radiation pressure coupling parameter, which has dependence on the input laser power at the beamsplitter,  $I_0$ , and the mass,  $m$ , of the cavity mirrors, which are considered as free masses. The (single sided) strain sensitivity standard quantum limit (SQL) of a Michelson interferometer is

$$h_{SQL} = \sqrt{\frac{4\hbar}{m\Omega^2 L^2}}. \quad (4.4)$$

The standard quantum limit is the optimal sensitivity achievable without the use of quantum non demolition (QND) techniques [33]. Here  $h_{SQL}$  is  $\sqrt{2}$  larger than the SQL for an individual test mass [33] because the difference of the Michelson interferometer test masses behaves like a free particle with reduced mass  $m \rightarrow m/2$  (see footnote 3 in reference [38]).

The outgoing amplitude quadrature,  $b_1$ , (equation 4.1) is simply the ingoing amplitude quadrature,  $a_1$ , with an uninteresting phase shift due to propagation. The outgoing phase quadrature,  $b_2$ , (equation 4.2) contains a term due to quantum noise plus the gravitational wave signal. The quantum noise term,  $\Delta b_2$ , has two components: one originating from the ingoing phase quadratures fluctuations,  $a_2$ , which gives rise to shot noise; and one from the ingoing amplitude quadratures fluctuations,  $a_1$ , which gives rise to radiation pressure fluctuations. The radiation pressure noise is driven by the amplitude quadrature fluctuations that enter from the dark port,  $a_1$ , and scaled by  $-\mathcal{K}$ . Note that the amplitude quadrature fluctuations from the laser port are common in both arms (see equation A.21 and A.22 in the Appendix A) and as such drives a common-mode radiation pressure which does not couple to the photodetector port. The shot noise contribution is frequency independent whereas the radiation pressure term scales as  $1/\Omega^2$  due to the mechanical susceptibility of the mirror suspensions.

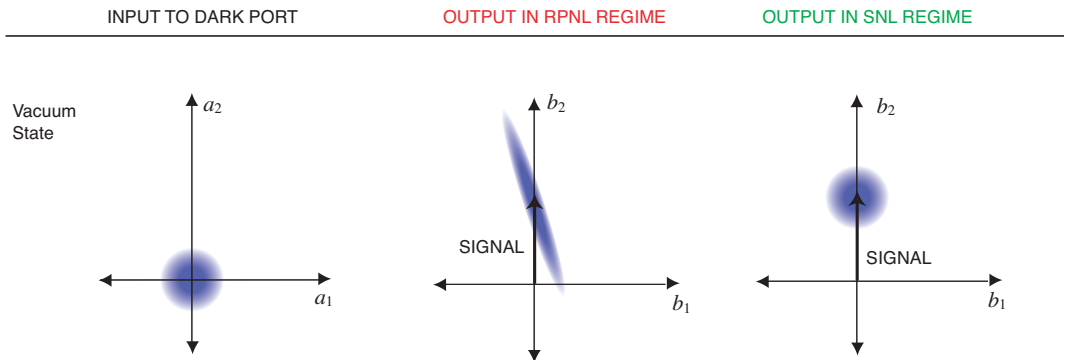


**Figure 4.2:** Phasor representation of the input-output relations of a Michelson interferometer. The input field is shown in the leftmost column, and the outputs in the middle column and the rightmost column. The output contains a classical gravitational wave signal and the fluctuations of the outgoing field. In the radiation pressure noise limited (RPNL) regime, the output phase noise is dominated by the amplitude induced phase fluctuations, whereas in the shot noise limited (SNL) regime, it is simply the phase fluctuations of the vacuum input field.

The transfer function from input vacuum field,  $a$ , to output field,  $b$ , of the Michelson interferometer is illustrated in figure 4.2. This shows the vacuum field input to the dark port (leftmost col-

umn) and the output in two frequency bands corresponding to the radiation pressure noise limited (RPNL) frequency band (middle column) and the shot noise limited (SNL) frequency band (right column). The output shows a classical (gravitational wave) signal vector in the phase quadrature and the superimposed noise ellipse. The relative size of the signal to the noise ellipse in the measured quadrature is proportional to the quantum-limited signal to noise ratio of the interferometer. The ball on stick representation in figure 4.2 shows that the magnitude of the fluctuations in the amplitude quadrature remains unchanged from the input to output (equation 4.1). However, in the RPNL regime, the magnitude of the phase quadrature fluctuations is increased due to radiation pressure noise (equation 4.2). In the SNL regime, the magnitude of the phase quadrature fluctuations is unchanged from the input.

### 4.2.2 Quantum noise limited sensitivity

The quantum noise limited sensitivity of the interferometer can be found by looking at the signal to noise ratio, given by

$$h = \frac{h_{SQL}}{\sqrt{2}\mathcal{K}} \Delta b_{\zeta} e^{-i\beta}, \quad (4.5)$$

where  $\Delta b_{\zeta} = \Delta b_1 \sin \zeta + \Delta b_2 \cos \zeta$ , with  $\zeta$  the detection phase. The power spectral density for the phase quadrature measurement ( $\zeta = \pi/2$ ) is then [38],

$$S_h = \frac{h_{SQL}^2}{2} \left( \frac{1}{\mathcal{K}} + \mathcal{K} \right), \quad (4.6)$$

and the strain sensitivity is  $\sqrt{S_h}$ .

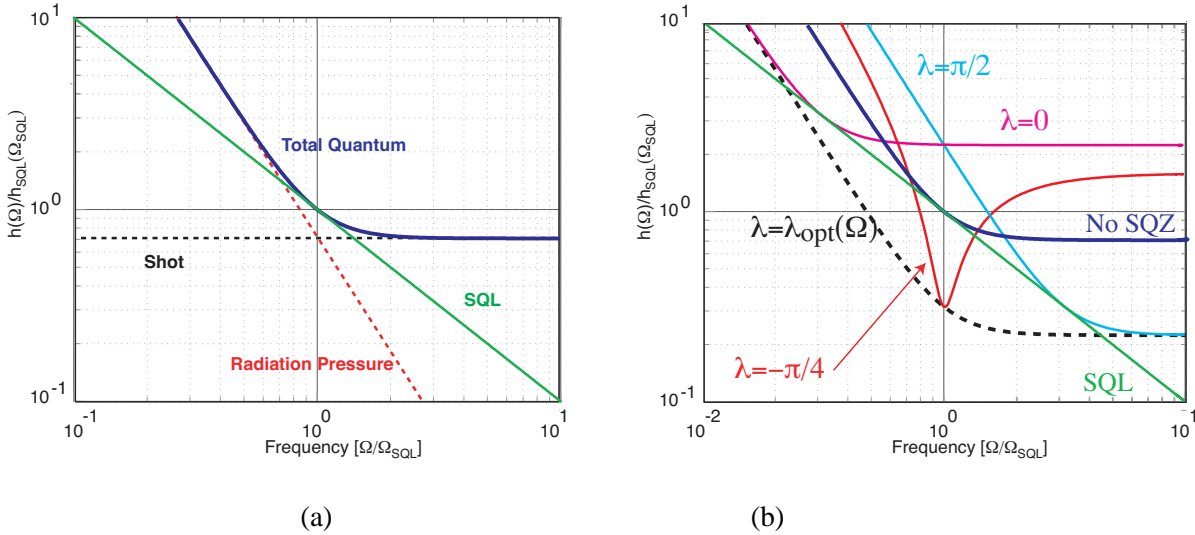


**Figure 4.3:** (a) Quantum noise limited strain sensitivity of a Michelson interferometer. (b) Michelson interferometer strain sensitivity with 10dB of squeezing injected into the dark port, with different squeezing angles.

The strain sensitivity normalized to the SQL,  $h_{SQL}(\Omega_{SQL})$ , is plotted in figure 4.3 (a). Shot noise and radiation pressure noise are shown as well as the total quantum noise and the SQL. Modifying the input laser power affects the sensitivity in the shot noise and radiation pressure noise

regimes inversely. The shot noise limited sensitivity improves as square root of the power, whereas radiation pressure noise limited sensitivity degrades as the square root of the power. Without QND schemes, the optimal sensitivity for each sideband frequency is reached when the shot noise and radiation pressure noise are equal - the SQL. Raising or lowering the laser power maps out the SQL at different sideband frequencies.

### 4.3 Gravitational wave detectors with quantum correlations

The quantum noise limited sensitivity of gravitational wave interferometers can be improved by using QND schemes. Examples are speed-meter designs [111–113], variational output detection [38, 114], and the injection of squeezed states into the interferometer’s dark port, first proposed by Caves [34]. Caves showed that the shot noise (or radiation pressure noise) could be reduced by the replacement of vacuum state that enters the asymmetric port by a phase (or amplitude) squeezed state. Unruh [35], and later Jaekel and Reynaud [36], built on this proposal, showing that a squeezed state with an intermediate quadrature (neither phase nor amplitude) could reduce the quantum noise below the SQL.

The injection of a squeezed state into the asymmetric port can be achieved using an optical circulator (for example, see [115, 116]) as illustrated in figure 4.1 (b). The spectral density of the quantum noise of a simple Michelson with squeezing is given by [38]

$$S_{SQZ} = \frac{h_{SQL}^2}{2} \left( \frac{1}{\mathcal{K}} + \mathcal{K} \right) [\cosh 2R - \cos(2\lambda + 2\Phi)] \sinh 2R, \quad (4.7)$$

where  $R$  is the squeeze factor,  $\lambda$  the squeeze angle, and  $\Phi = \text{arccot}(\mathcal{K})$ . The quantum noise of a simple Michelson interferometer with 10dB of squeezing ( $e^{-2R} = 0.1$ ) at various squeeze angles is shown in figure 4.3 (b). A phase squeezed state ( $\lambda = \pi/2$ ) offers quantum noise reduction in the shot noise limited regime and increased noise in the radiation pressure noise limited regime. An amplitude squeezed state ( $\lambda = 0$ ) has the opposite effect, radiation pressure noise is reduced whereas shot noise is increased. The input-output transfer functions of the squeezed states is illustrated in figure 4.4.

In the lossless case, injecting a phase squeezed state with  $e^{-2R} = x$  into the asymmetric port gives the same quantum noise performance improvement as an increase in the laser power by  $\sqrt{x}$ . Similarly, an amplitude squeezed state improves noise performance by the same factor a reduction in the laser power by  $\sqrt{x}$ .

Orienting the squeeze ellipse at  $45^\circ$  ( $\lambda = -\pi/4$ ) correlates the amplitude and phase quadratures and enables sub-SQL performance to be achieved [35, 36], but degrades performance in the shot noise and amplitude noise limited regimes. It can be seen that for an interferometer that is limited by radiation pressure at low frequencies and shot noise at high frequencies, a frequency dependent squeezed state is required to give the optimal noise reduction over all sideband frequencies. For a simple Michelson the optimal frequency dependent squeezed state would have a phase rotation such that it would be amplitude squeezed at low frequencies, where radiation pressure noise is dominant, squeezed at  $45^\circ$  degrees at the SQL, and phase squeezed at high frequencies, where shot noise is dominant. The optimal phase rotation of the squeezed state is given by [38]

$$\lambda_{opt}(\Omega) = -\text{arccot} \mathcal{K}(\Omega). \quad (4.8)$$

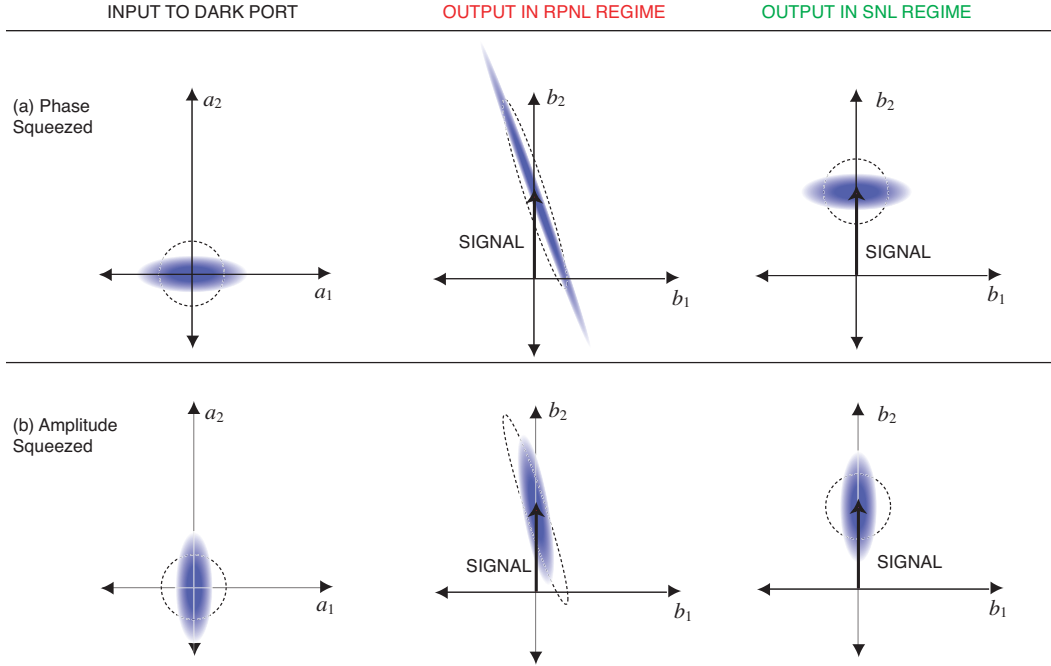


**Figure 4.4:** Phasor representation of the input-output relations of a Michelson interferometer with (a) phase squeezing and (b) amplitude squeezing. For comparison, the input-output relations are also plotted for the vacuum state, indicated by the circle and ellipses with dashed lines.

With  $\lambda = \lambda_{opt}(\Omega)$  equation 4.7 reduces to

$$S_{SQZ|OPT} = \frac{h_{SQL}^2}{2} \left( \frac{1}{\mathcal{K}} + \mathcal{K} \right) e^{-2R}, \quad (4.9)$$

which is equivalent to equation 4.6 multiplied by  $e^{-2R}$ . Thus, with an optimal frequency dependent squeezed state, the quantum noise limited strain sensitivity of an interferometer is shifted down by  $e^{-R}$ . This result is also shown in figure 4.3 (b).

The reader may wonder if there is something suspect about improving the quantum noise limited sensitivity in the amplitude and phase quadratures simultaneously. There is no violation of Heisenberg uncertainty relation since frequency dependent squeezed states satisfies the HUP at each frequency.

### 4.3.1 Quantum noise of conventional interferometers

‘Conventional interferometers’ are Michelson interferometers with arm cavities (without squeezed states), the configuration of TAMA, LIGO and VIRGO<sup>3</sup>. The input-output relations of a conventional interferometer are identical to equations 4.1 and 4.2, except the radiation pressure coupling parameter and standard quantum limit are different. In a conventional interferometer the radiation

<sup>3</sup>Recall that GEO has signal recycling and no arm cavities.

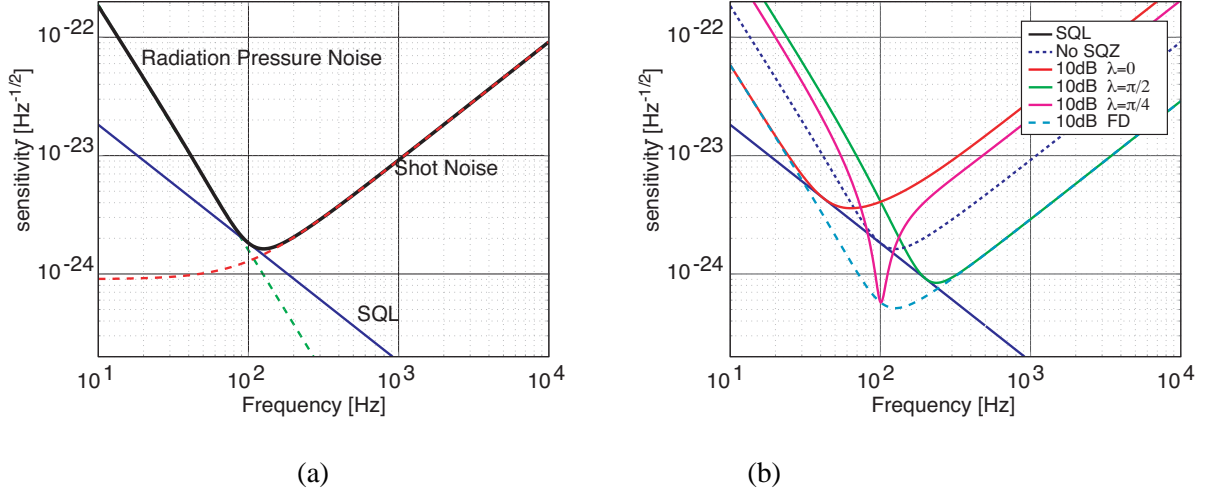


**Figure 4.5:** (a) Strain sensitivity of a conventional interferometer. (b) Strain sensitivity of a conventional interferometer with 10dB of squeezing injected into the dark port, with different squeezing angles.  $m = 40\text{kg}$ ,  $L = 3995\text{m}$ ,  $T = 0.033$ ,  $\omega_0 = 1.77 \times 10^{15}\text{rads}$  and  $I_0 = I_{SQL}$ .

pressure coupling parameter is

$$\mathcal{K}_c = \frac{2(I_0/I_{SQL})\gamma^4}{\Omega^2(\gamma^2 + \Omega^2)}, \quad (4.10)$$

where the arm cavity half bandwidth is  $\gamma = Tc/(4L)$  and  $T$  is the transmission of the input test mass mirror.  $I_{SQL}$  is the input laser power required for a conventional interferometer to reach the standard quantum limit.

$$I_{SQL} = \frac{mL^2\gamma^4}{4\omega_0}. \quad (4.11)$$

The (single sided) SQL of a conventional interferometer is

$$h_{SQL}^c(\Omega) = \sqrt{\frac{8\hbar}{m\Omega^2L^2}}. \quad (4.12)$$

The quantum noise limited strain sensitivity of a (lossless) conventional interferometer is given by the square root of equation 4.6, with the radiation pressure coupling constant and SQL strain replaced by equations 4.10 and 4.12 ( $\mathcal{K} \rightarrow \mathcal{K}_c$ ,  $h_{SQL} \rightarrow h_{SQL}^c$ ). Figure 4.5 (a) shows the strain sensitivity of the conventional interferometer with  $\zeta = \pi/2$ . With the parameters used in the figure (listed in the figure caption), below 100Hz, the sensitivity is limited by radiation pressure noise, whereas above 200Hz it is limited by shot noise. The shot noise limited sensitivity is shaped by the frequency response of the arm cavities. Above the arm cavity linewidth the signal response decreases, and so the shot noise limited strain sensitivity is degraded.

Figure 4.5 (b) shows the sensitivity modification to quantum noise of a the conventional interferometer when injecting 10dB of squeezing at various squeeze angles. The improvement is identical to the simple Michelson case and the optimal frequency dependent squeeze angle is given by equation 4.8 with the radiation pressure coupling  $\mathcal{K}_c$  substituted for  $\mathcal{K}$ .

**Table 4.1:** Signal recycled Michelson interferometer parameters

Parameter	Symbol	Value	Units
Laser frequency	$\omega_0$	$1.77 \times 10^{15}$	radians/s
Mirror mass	$m$	40	kg
Laser power at beamsplitter <sup>5</sup>	$I_0$	2100	W
ITM transmittance (power)	$T$	0.005	-
Arm length	$L$	3995	m
Transmission of signal recycling mirror (amplitude)	$\tau$	$\sqrt{0.07}$	-
Reflectivity of signal recycling mirror (amplitude)	$\rho$	$1 - \tau^2$	-
Sideband frequency	$\Omega$		
Signal recycling cavity length	$l$	10	m
Signal recycling cavity detuning	$\phi$	$(\pi - 0.08)/2$	radians
Signal recycling cavity single pass phase shift	$\Theta$	$\text{mod}_{2\pi}(l\Omega/c)$	radians

### 4.3.2 Signal recycled gravitational wave detectors

Buonanno and Chen [117] showed that the quantum noise of detuned signal recycled interferometers could be lower than the free mass SQL without additional input or output optics. This is because the correlations in the quantum noise of the amplitude and phase quadratures created by radiation pressure coupling are recycled in the signal recycling cavity. The free mass SQL no longer applies to this system and sub SQL sensitivity can be obtained. An additional sensitivity peak to the optical resonance is created, called the opto-mechanical resonance, in reference to its origin from radiation pressure coupling<sup>4</sup>.

The quantum noise power spectral density of a (lossless) signal recycled Michelson interferometer with arm cavities is given by [117]

$$S_{h_{SR}}^{\zeta} = \frac{h_{SQL}^2 (C_{11}^{(1)} \sin \zeta + C_{21}^{(1)} \cos \zeta)^2 + (C_{12}^{(1)} \sin \zeta + C_{22}^{(1)} \cos \zeta)^2}{2\mathcal{K}_c \tau^2 |D_1^{(1)} \sin \zeta + D_2^{(1)} \cos \zeta|^2}, \quad (4.13)$$

with

$$C_{11}^{(1)} = (1 + \rho^2) \left( \cos 2\phi + \frac{\mathcal{K}_c}{2} \sin 2\phi \right) - 2\rho \cos[2\beta + 2\Theta], \quad (4.14)$$

$$C_{22}^{(1)} = C_{11}^{(1)}, \quad (4.15)$$

$$C_{12}^{(1)} = -\tau^2 (\sin 2\phi + \mathcal{K}_c \sin^2 \phi), \quad (4.16)$$

$$C_{21}^{(1)} = \tau^2 (\sin 2\phi - \mathcal{K}_c \cos^2 \phi), \quad (4.17)$$

$$D_1^{(1)} = -(1 + \rho e^{2i(\beta+\Theta)}) \sin \phi, \quad (4.18)$$

$$D_2^{(1)} = -(-1 + \rho e^{2i(\beta+\Theta)}) \cos \phi, \quad (4.19)$$

where  $\tau$  and  $\rho$  are the (amplitude) reflectivity and transmission of the signal recycling mirror, respectively, and  $\phi$  and  $\Theta$  are the microscopic signal recycling cavity detuning and macroscopic single pass phase shift of the signal recycling cavity. Figure 4.6 (a) shows the quantum noise limited sensitivity of a lossless SR interferometer with parameters similar to those expected in

<sup>4</sup>Another way of looking at this is the optical spring effect [118]

<sup>5</sup>This number is derived using 125W laser power times the recycling gain of 16.8.

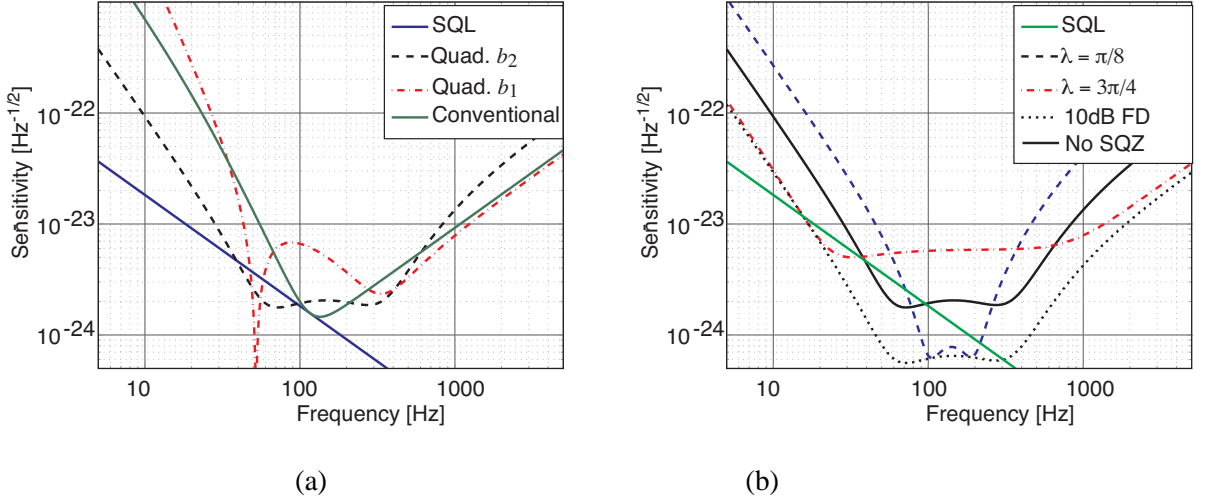


**Figure 4.6:** (a) Quantum noise of a signal recycled Michelson interferometer with arm cavities. (b) Quantum noise with 10dB ( $R = 1.15$ ) and  $\zeta = \pi/2$  for different  $\lambda$ . Interferometer parameters can be found in Table 8.1

Advanced LIGO, as detailed in Table 4.1. Both the amplitude and phase quadrature sensitivities are shown, labeled Quadrature  $b_1$  and  $b_2$ , respectively, along with the quantum noise of a conventional interferometer and the free mass SQL. Unlike conventional interferometers the gravitational wave signal is not entirely in a single quadrature in a signal recycled interferometer.

### 4.3.3 Squeezing in a signal recycled interferometer

The QND schemes such as variational readout and squeezed states can also be applied to signal recycled interferometers. The use of squeezed states to improve the quantum noise limited sensitivity of signal recycled interferometers has been examined in [37, 39, 40]. The lossless spectral density of a quantum noise limited signal recycled interferometer is given by [40]

$$S_{h_{SQZ}}^{\zeta} = \frac{h_{SQL}^2}{2\mathcal{K}_c} \frac{e^{-2R}(C_{11}^{\lambda} \sin \zeta + C_{21}^{\lambda} \cos \zeta)^2 + e^{2R}(C_{12}^{\lambda} \sin \zeta + C_{22}^{\lambda} \cos \zeta)^2}{\tau^2 |D_1^{(1)} \sin \zeta + D_2^{(1)} \cos \zeta|^2}, \quad (4.20)$$

with

$$C_{11}^{\lambda} = C_{11}^{(1)} \cos \lambda + C_{12}^{(1)} \sin \lambda, \quad (4.21)$$

$$C_{12}^{\lambda} = C_{12}^{(1)} \cos \lambda - C_{11}^{(1)} \sin \lambda, \quad (4.22)$$

$$C_{21}^{\lambda} = C_{21}^{(1)} \cos \lambda + C_{22}^{(1)} \sin \lambda, \quad (4.23)$$

$$C_{22}^{\lambda} = C_{22}^{(1)} \cos \lambda - C_{21}^{(1)} \sin \lambda, \quad (4.24)$$

recall  $R$  is the squeeze factor and  $\lambda$  the squeeze angle. Figure 4.6 (b) shows the quantum noise limited strain sensitivity of a signal recycled interferometer with squeezing at different, frequency independent squeeze angle  $\lambda$ , and the readout quadrature set to  $b_2$  ( $\zeta = \pi/2$ ). Like conventional interferometers the optimal squeeze angle is a function of frequency. The frequency dependence of the signal recycled interferometer is more complex than the conventional interferometer. If a squeezed state with the optimal frequency dependence ( $\lambda = \lambda_{opt}(\Omega)$ ) is injected into a lossless

signal recycled interferometer, the spectral density is the unsqueezed spectral density multiplied by a factor  $e^{-2R}$  [39].

## **4.4 Chapter summary**

We have discussed the origin of quantum noise and how it couples to interferometric measurements. The possible improvements obtainable with the injection of squeezed states has been presented assuming a lossless interferometer.

This chapter concludes the background materials of this thesis. Next, we describe the development of audio-frequency squeezed states.

**Part II**

**Development of Audio Frequency  
Squeezing**





---

tinually held the record for the largest amount of quantum noise reduction, except for a period between 1991-1992. In the period 1991-1992 the record was held by Bergman and Haus [120] who produced 5dB (68%) noise suppression from a pulsed  $\chi^{(3)}$  nonlinearity experiment in optical fibre. OPO or OPA are natural choices for producing large squeeze magnitude because, in theory, they can produce perfect quantum noise suppression (at threshold) and produces a minimum uncertainty state. This is unlike singly resonant SHG, for example, which produces a non-minimum uncertainty state and is limited in theory to 9.5dB (89%) of quantum noise suppression [89]. In this thesis an OPO operated below threshold is used to generate squeezed states.

The point labeled McKenzie *et al.* (1) in Figure 4.7 is the quantum noise reduction demonstrated in this thesis. The measured noise suppression of 5.5dB (72%)<sup>6</sup> can be compared with other the locked squeezing of similar magnitude at 1064nm of 6.5dB (78%) by Vahlbruch *et al.* [17] and 7.4dB (82%) by Goda *et al.* [19].

### The development of audio frequency squeezed states

In 1981 Caves [34] proposed the use of squeezed states to improve the quantum noise limited noise performance of gravitational wave detectors. To offer quantum noise reduction at the gravitational wave signal frequencies (10Hz-10kHz), as Caves envisaged, squeezing is required at the same sideband frequencies. The task of producing squeezed states at these frequencies differs significantly from producing it at RF frequencies, where squeezing was initially produced. The reason for the difference between producing squeezing at audio and RF frequencies is purely technical, there is no fundamental reason to expect nonlinear processes, such as the  $\chi^{(2)}$  processes, to not produce squeezed states in the audio band. Generally, at audio frequencies, classical noise sources are large enough to obscure the quantum noise properties and squeezing is ‘buried’. For this reason, until recently, squeezed states were generally measured at sideband frequencies of a few MHz or higher. Figure 4.8 shows the lowest reported sideband frequency of squeezed states as a function of time. It shows that only in the last few years have squeezed states been measured in the audio gravitational wave detection band.

The noise sources that limit the production of squeezed states to RF sideband frequencies are: the classical amplitude and phase fluctuations of the laser [100, 103, 104]; acousto-mechanical noise coupled via cavity length fluctuations; and photothermal noise [121]. There were thought to be two solutions to overcome these classical noise limitations, to enable production of squeezed states at low sideband frequencies [89]. These were:

- Reduce the limiting noise sources. This is the brute force method of working to eliminate any noise sources that limits the production of a squeezed state. This means stabilizing the laser amplitude and phase fluctuations to near the quantum noise limit and reducing environmental noise sources.
- Recover buried squeezing. The underlying squeezed state statistics are recovered by canceling the classical noise by either optical or electronic means.

Reduction of the limiting noise sources to produce squeezing has not yet been attempted at audio sideband frequencies, perhaps due to the enormity of the task. It has been proven to be successful in the MHz regime. For example, in an SHG squeezing experiment by White *et al.* [122], the lowest sideband frequency squeezing was observed at moved from  $\sim 15$ MHz without any

---

<sup>6</sup>Without electronic noise subtraction. If the effect of electronic noise is taken into account 6.5dB of quantum noise reduction could be inferred.

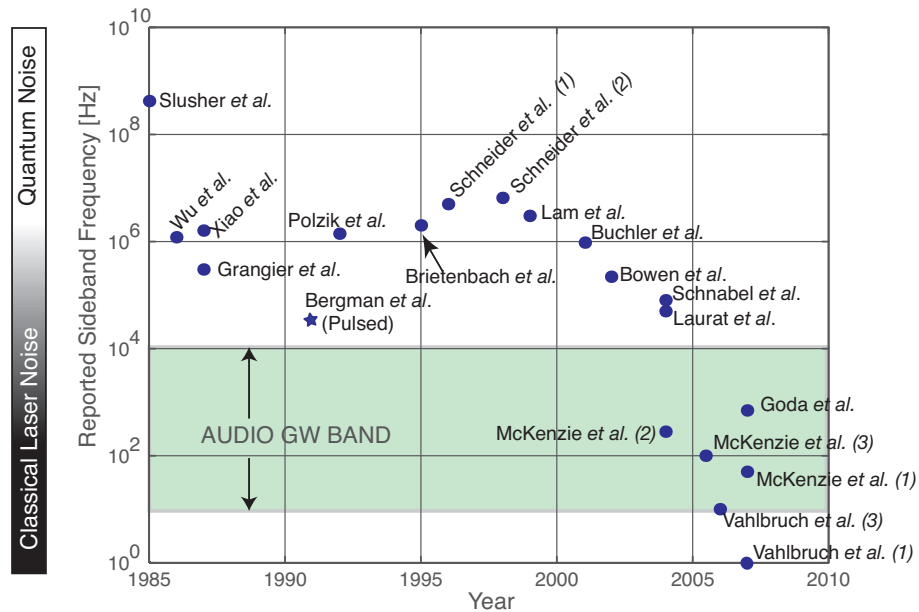


**Figure 4.8:** Reported sideband frequency vs time. (Left) is a depiction of classical laser noise as a function of frequency. References (some are given in the caption of figure 4.7.), Bowen *et al.* [21], Schnabel *et al.* [22] Laurat *et al.* [23] McKenzie *et al.* (2) [24],(3) [25], Vahlbruch *et al.* (3) [26].

noise reduction, to  $\sim 5$  MHz by using a mode cleaner cavity for passive noise reduction of pump field.

Recovery of buried squeezing was proposed and proven effective in 1991 by Bergman and Haus [120], who recovered pulsed squeezing down to 35 kHz, in the same experiment that held the record for squeezing amplitude at that time. They generated squeezed states in the counter-propagating directions of a Sagnac interferometer. The idea was that the common classical noise of the squeezed states would interfere destructively toward the dark port, leaving only squeezed vacuum to exit the dark port. They commented that below 35 kHz, the laser noise no longer cancelled. It is hard to know why the laser noise did not cancel at low frequencies, but it would seem likely to be due to one of two reasons: either the level of cancellation was not sufficient to cancel the noise at those frequencies or other uncorrelated noise sources were present which did not cancel. After this experimental demonstration, a proposal to recover buried squeezing was made by Lai *et al.* [123] from bright amplitude squeezed states produced by diode lasers and a similar one by Ralph and White [124] from squeezed states using the SHG process.

Recovery of buried squeezing was extended to bright squeezed states produced from two near identical OPA's by Bowen *et al.* [21]. They recovered continuous wave squeezing at 220 kHz. When measured individually, the spectra of the two squeezed states showed classical intensity noise (much greater than the quantum noise limit) at frequencies below a few MHz, and squeezing only above 1.9 MHz. The technique to obtain low frequency squeezing was to combine the two states on a beamsplitter, cancel the correlated classical noise sources in one output, and leave a squeezed vacuum state in the other. In 2004, a similar classical noise cancellation experiment by Schnabel *et al.* [22] resulted in squeezing to 80 kHz. The main difference was that only one OPA was used.

The concept of the recovering buried squeezing seemed to work well down to a few tens of kHz. The two apparent limitations to this technique are: firstly, only the correlated classical

---

noise in the squeezed beam could be cancelled, so uncorrelated noise would always remain; and secondly, the level of cancellation of correlated noise is limited by experimental parameters such as mode-matching, usually to about a factor of 100. To produce (low frequency) vacuum squeezing from intensity dependent processes such as Kerr media and SHG classical noise cancellation seems like the only option. However, optical parametric down-conversion has an important difference: vacuum squeezing can be produced readily, without requiring any post processing. An OPO operated below threshold produces a squeezed vacuum state, which, as we detail over the next few chapters, is naturally immune to classical noise sources.

### Sub-threshold OPO for low frequency squeezing

In a 2004 paper [24] we presented the first measurement of squeezing in the audio gravitational wave detection band using an alternate technique to the two described above. Our technique *prevents classical noise sources from coupling to the squeezed field*. This was achieved by operating the parametric down-converter as a vacuum seeded sub-threshold OPO. It was shown that the vacuum squeezed state produced from a sub-threshold OPO was immune to classical noise sources to first-order, enabling broadband vacuum squeezing to be measured from 280Hz to 100kHz. Also shown was that, in OPA experiments, it was the beating with the coherent amplitude of the intra-cavity field at the fundamental frequency which coupled the classical noise sources into the squeezed state, thereby obscuring the squeezing. By operating the parametric down-conversion as a sub-threshold OPO, the coupling mechanism in the down-conversion process was removed, and low frequency squeezing could be obtained. We note that our work was not the first time that below threshold OPO has been used to produce squeezed states. It is therefore possible that squeezing has been produced at low frequencies before now, even if it wasn't measured.

In an experiment also performed in 2004, Laurat *et al.* [23] measured squeezing down to 50kHz from a type II OPO system operating below threshold. The authors of the paper do not mention if they knew of the cause of the the low frequency limit.

Since this first demonstration of low frequency squeezing from an OPO, this mode of operation has been the standard of all low frequency squeezing experiments OPO [17, 25, 26, 125, 126]<sup>7</sup>.

### Current status of audio frequency squeezing

The first report of locked audio frequency squeezed states was by McKenzie *et al.* [25] using a doubly resonant OPO<sup>8</sup>. Squeezing was measured down to 100Hz. The low frequency limit was thought to be imposed by excess noise in the homodyne detection system. Since then the Valhbruch *et al.* measured locked squeezing down to 10Hz [26]. More recently, Vahlbruch *et al.* were able to identify and mitigate the low frequency limiting noise source in their homodyne detection system and measure squeezing at 1 Hz [17]. This is the current low frequency record.

In 2007, Goda *et al.* [128] measured squeezing enhancement in a suspended, signal-recycled Michelson at the Caltech 40m prototype interferometer [129]. This was the first measurement of

---

<sup>7</sup>Recently McCormick *et al.* [127] produced squeezing down to 5kHz from a four wave mixing experiment.

<sup>8</sup>In this thesis 'singly resonant' is defined to mean the nonlinear medium is placed in an optical cavity for the fundamental frequency field (lower frequency mode), but not for the harmonic frequency field (higher frequency mode), which is single passed or double passed through the nonlinear medium. A doubly resonant OPO then would have both the the nonlinear medium in a cavity where both the fields at the fundamental and harmonic frequencies are resonant. In this thesis only degenerate OPO considered, hence we refer to SROPO and DROPO. In a non degenerate OPO, where signal and idler frequencies have the relation:  $f_s = f_0 + \Delta$ ,  $f_i = f_0 - \Delta$  singly resonant may mean resonant for only the signal, idler or pump, doubly resonant for two of the three and a triply resonant optical parametric oscillator (TROPO) would be resonant for all three different frequencies.

---

squeezing enhancement of a suspended interferometer, and represents a significant step toward squeezing enhancement in a long baseline interferometric detector.

---

---

# Noise couplings in parametric down-conversion

---

In this chapter noise couplings in the optical parametric down-conversion processes of optical parametric oscillation and optical parametric amplification are analysed theoretically. Transfer functions for different noise sources are derived with a view to understanding how they couple into the squeezed field produced in the parametric down-conversion processes. The calculation in this chapter is similar to that in the journal article

*Photothermal Fluctuations as a Fundamental Limit to Low-Frequency Squeezing in a Degenerate Optical Parametric Amplifier.*

K. Goda, K. McKenzie, E. E. Mikhailov, P. K. Lam, D. E. McClelland and N. Mavalvala, Phys. Rev. A **72**, 043819 (2005)

## 5.1 Introduction

Though the production of squeezed states using OPO or OPA<sup>1</sup> is now standard practice in many quantum optics laboratories, there have been relatively few investigations into the coupling of noise sources that can limit the production of squeezing. The reason is partially because experimentalists have often chosen to operate at RF sideband frequencies, where lasers are quantum noise limited and there is negligible environmental noise. There have been theoretical investigations into the limits imposed by fluctuations of the pump field, in single pass parametric amplifiers [100–103] and in OPO's [104, 105]<sup>2</sup>. These investigations show that both amplitude and phase fluctuations provide a limit to the level of vacuum squeezing, and that the effect of amplitude fluctuations is generally small compared to those of phase fluctuations [103–105]. In both single pass and resonant systems, amplitude fluctuations of the pump field impose a limit to squeezing because they modulate the nonlinear gain. The simplest manifestation of pump phase noise is to cause the squeezed quadrature to fluctuate. If the detection phase were to be held constant, the apparent squeezing will be reduced as the detected quadrature will be a time dependent mixture of the squeezed and anti-squeezed quadratures. This effect can be negated if the detected quadrature is locked to the squeezed quadrature, which is done in most squeezing experiments. Gea-Banachloche and Zubairy [104] pointed out that when the nonlinear medium is placed in a cavity, the quadrature mixing due to pump phase noise happens in the cavity and this effect cannot

---

<sup>1</sup>Recall the subtle difference of the OPO and OPA processes is that the OPA has a coherent seed field, whereas the OPO process has only a vacuum field as a seed field.

<sup>2</sup>Note that references [100–105] call a single pass parametric interaction an 'OPA' and a parametric interaction in a cavity an 'OPO' and generally consider both to be vacuum seeded.

be negated by controlling the detected quadrature. These theoretical investigations ([100–105]) show that pump noise represents a fundamental limit to vacuum squeezing, but, in practice, it is a second order effect. To the best of our knowledge, pump noise has not limited vacuum squeezing in any OPO experiment. Instead the limit to the amount of quantum noise reduction has been linear absorption and nonlinear absorption, such as blue light induced infrared absorption (BLIIRA) [130]; the green light counterpart, GRIIRA [131]; and grey tracking [132, 133].

In OPA experiments, squeezing has often been limited to high frequencies by first order coupling of classical noise sources. An example of a first order noise coupling is seed noise, which couples to the squeezed beam via a simple cavity transfer function (cf. equations 3.125, 3.126). There exists a similar transfer function for the pump noise, and other environmental noise sources. The aim in this chapter is to derive these transfer functions in an effort to understand how to minimise or decouple these noise sources from the squeezed state. Noise sources that are important at low frequencies are: amplitude and phase noise in the pump and seed fields; the fluctuations in the nonlinearity; and cavity detuning. It is shown that noise in the pump field, the nonlinear coupling, and the cavity detuning all couple to the squeezed field via a beat with the mean intra-cavity field at the fundamental wavelength,  $\bar{a}$ . It follows that, by operating a below threshold OPO, where  $\bar{a} = 0$ , there is no first order coupling of these noise sources. This is an important result, which provides a path to produce squeezed states at low frequencies without requiring laser or environmental noise stabilization, or noise cancellation techniques. This result is contained in the standard equations of motion and, perhaps surprisingly, has not been studied in this context prior to this work.

The calculation in this chapter follows the framework laid out in reference [121]. In section 5.2, the linearized equations of motion are used to calculate the fluctuations of the intra-cavity fields in terms of: the extra-cavity fields; the fluctuations in the cavity detuning; and fluctuations in the nonlinear coupling. In section 5.3 the amplitude and phase quadrature fluctuations of the transmitted field are determined. These quadratures contain any squeezing and anti-squeezing, plus classical noise sources. In section 5.4 the variances of the transmitted fields are calculated. Finally, in section 5.5, noise budgets of the for the squeezed field are presented using parameters similar to those in experiments detailed in later chapters.

## 5.2 Equations of motion and cavity fields

For convenience, the equations of motion for degenerate  $\chi^{(2)}$  nonlinear interactions presented in section 3.5 are rewritten here. The cavity modes at the fundamental frequency,  $a$ , and harmonic frequency,  $b$ , are

$$\dot{a} = -(\kappa^a + i\Delta^a)a + \varepsilon a^\dagger b + \sqrt{2\kappa_{in}^a}A_{in} + \sqrt{2\kappa_{out}^a}A_{out} + \sqrt{2\kappa_l^a}A_l, \quad (5.1)$$

$$\dot{b} = -(\kappa^b + i\Delta^b)b - \frac{\varepsilon^* a^2}{2} + \sqrt{2\kappa_{in}^b}B_{in} + \sqrt{2\kappa_{out}^b}B_{out} + \sqrt{2\kappa_l^b}B_l, \quad (5.2)$$

where  $\kappa^a$  and  $\kappa^b$  are the total resonator decay rates for each field and  $\varepsilon$  is the nonlinear coupling parameter.  $A_{in}, A_{out}, A_l$  and  $B_{in}, B_{out}, B_l$  are the driving fields with the respective coupling rates are  $\kappa_{in}^a, \kappa_{out}^a, \kappa_l^a$  and  $\kappa_{in}^b, \kappa_{out}^b, \kappa_l^b$  for the input, output and roundtrip loss (see figure 5.1). The angular frequency detuning of the fundamental and harmonic cavities with respect to the driving field frequencies are given by  $\Delta^a$  and  $\Delta^b$ . The equations of motion can be solved using a linearized approach [87]. Each operator can be separated into average and fluctuating parts. That is

$$s = \bar{s} + \delta s, \quad s^\dagger = \bar{s}^* + \delta s^\dagger, \quad (5.3)$$

for  $s = a, b, A_{in}, A_{out}, A_l, B_{in}, B_{out}, B_l, \Delta^a, \Delta^b, \epsilon$ .<sup>3</sup>

The fluctuations of the extra-cavity fields can be of classical or quantum mechanical origin. Fluctuations in cavity detuning are often due to such sources as acousto-mechanical noise and photothermal noise and fluctuations of the nonlinearity maybe due to fluctuations in the phase matching condition. Unlike the calculation in [121], the photothermal noise is not explicitly included, though the fluctuations in cavity detuning and nonlinearity strength could be from photothermal noise.

Equations 5.1 and 5.2 with expanded operators become

$$\begin{aligned} \frac{d}{dt}(\bar{a} + \delta a) &= -(\kappa_a + i(\bar{\Delta}^a + \delta\Delta^a))(\bar{a} + \delta a) + (\bar{\epsilon} + \delta\epsilon)(\bar{a}^* + \delta a^\dagger)(\bar{b} + \delta b) \\ &\quad + \sqrt{2\kappa_{in}^a}(\bar{A}_{in} + \delta A_{in}) + \sqrt{2\kappa_{out}^a}\delta A_{out} + \sqrt{2\kappa_l^a}\delta A_l, \end{aligned} \quad (5.4)$$

$$\begin{aligned} \frac{d}{dt}(\bar{b} + \delta b) &= -(\kappa_b + i(\bar{\Delta}^b + \delta\Delta^b))(\bar{b} + \delta b) - \frac{1}{2}(\bar{\epsilon}^* + \delta\epsilon^*)(\bar{a} + \delta a)^2 \\ &\quad + \sqrt{2\kappa_{in}^b}(\bar{B}_{in} + \delta B_{in}) + \sqrt{2\kappa_{out}^b}\delta B_{out} + \sqrt{2\kappa_l^b}\delta B_l, \end{aligned} \quad (5.5)$$

where we have made the assumption that the cavity loss and output ports have vacuum state inputs so  $\bar{A}_{out} = \bar{A}_l = \bar{B}_{out} = \bar{B}_l = 0$ .

The classical amplitudes of equations 5.4 and 5.5 are given by

$$\frac{d\bar{a}}{dt} = -(\kappa_a + i\bar{\Delta}^a)\bar{a} + \bar{\epsilon}\bar{a}^*\bar{b} + \sqrt{2\kappa_{in}^a}\bar{A}_{in}, \quad (5.6)$$

$$\frac{d\bar{b}}{dt} = -(\kappa_b + i\bar{\Delta}^b)\bar{b} - \frac{\bar{\epsilon}\bar{a}^2}{2} + \sqrt{2\kappa_{in}^b}\bar{B}_{in}. \quad (5.7)$$

In the experiments performed as part of this thesis, the parametric process is operated below threshold in a regime where the pump field is not significantly depleted by down-conversion ( $\bar{\epsilon}\bar{a}^2/2 \ll \sqrt{2\kappa_{in}^b}\bar{B}_{in}$ ). The steady state intra-cavity field amplitudes are found by setting  $\frac{d\bar{a}}{dt} = 0, \frac{d\bar{b}}{dt} = 0$ ,

$$\bar{a} = \frac{\sqrt{2\kappa_{in}^a}(\kappa^a - i\Delta^a + \bar{\epsilon}b)}{(\kappa^a)^2 + (\Delta^a)^2 - |\bar{\epsilon}b|^2}\bar{A}_{in}, \quad \bar{b} \approx \frac{\sqrt{2\kappa_{in}^b}}{\kappa^b + i\Delta^b}\bar{B}_{in}, \quad (5.8)$$

where, without the loss of generality,  $\bar{A}_{in}$  has been chosen to be real.

The linearised fluctuating components of equations 5.4 and 5.5 along with their Hermitian conjugates are given by

$$\delta\dot{a} = -\kappa_a\delta a - i(\bar{\Delta}^a\delta a + \bar{a}\delta\Delta^a) + \bar{\epsilon}\bar{b}\delta a^\dagger + \bar{\epsilon}\bar{a}^*\delta b + \bar{a}^*\bar{b}\delta\epsilon + \sum_j \sqrt{2\kappa_j^a}\delta A_j, \quad (5.9)$$

$$\delta\dot{a}^\dagger = -\kappa_a\delta a^\dagger + i(\bar{\Delta}^a\delta a^\dagger + \bar{a}^*\delta\Delta^a) + \bar{\epsilon}^*\bar{b}^*\delta a + \bar{\epsilon}^*\bar{a}\delta b^\dagger + \bar{a}\bar{b}^*\delta\epsilon^* + \sum_j \sqrt{2\kappa_j^a}\delta A_j^\dagger, \quad (5.10)$$

$$\delta\dot{b} = -\kappa_b\delta b - i(\bar{\Delta}^b\delta b + \bar{b}\delta\Delta^b) - \bar{\epsilon}^*\bar{a}\delta a - \frac{1}{2}\bar{a}^2\delta\epsilon^* + \sum_j \sqrt{2\kappa_j^b}\delta B_j, \quad (5.11)$$

$$\delta\dot{b}^\dagger = -\kappa_b\delta b^\dagger + i(\bar{\Delta}^b\delta b^\dagger + \bar{b}^*\delta\Delta^b) - \bar{\epsilon}\bar{a}^*\delta a^\dagger - \frac{1}{2}\bar{a}^{*2}\delta\epsilon + \sum_j \sqrt{2\kappa_j^b}\delta B_j^\dagger, \quad (5.12)$$

where the equations and the fluctuating components of the extra-cavity fields have been denoted

<sup>3</sup>Note: the detuning parameters,  $\Delta^a$  and  $\Delta^b$ , are real numbers and  $\epsilon$  is a complex number.

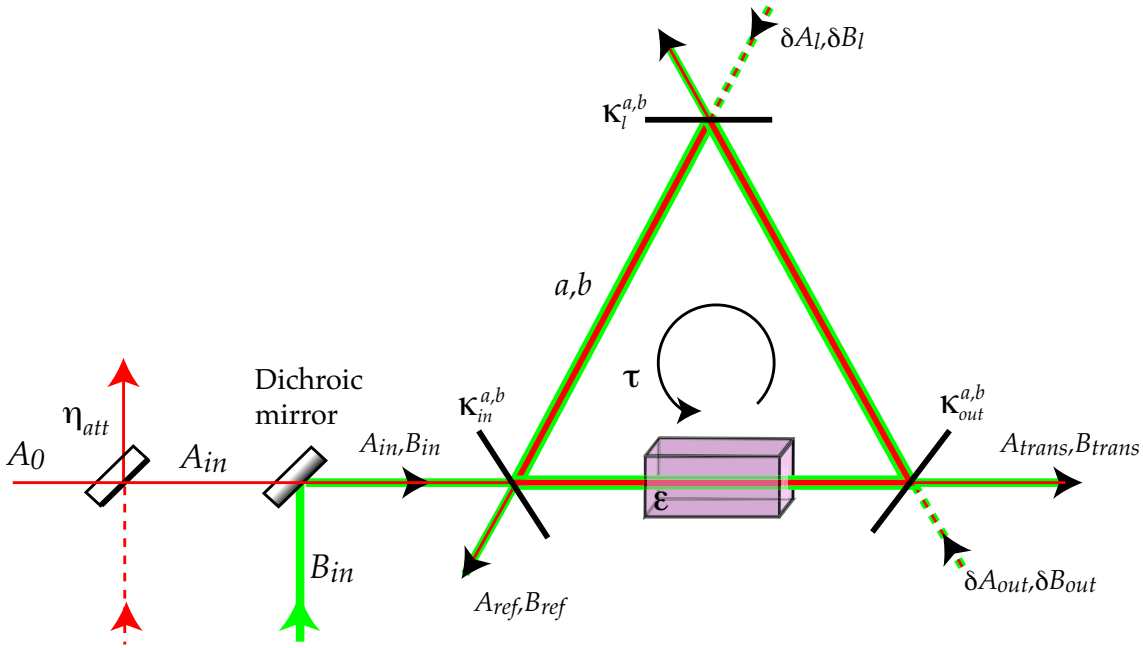


**Figure 5.1:** A schematic of the parametric down-converter. The fundamental and harmonic cavity modes are  $a$  and  $b$ , respectively. Cavity inputs and output are denoted with capital letters.

by the sum over  $j$ , with  $\{j = in, out, \text{ and } l\}$ . That is

$$\sum_j \sqrt{2\kappa_j^a} \delta A_j = \sqrt{2\kappa_{in}^a} \delta A_{in} + \sqrt{2\kappa_l^a} \delta A_l + \sqrt{2\kappa_{out}^a} \delta A_{out}, \quad (5.13)$$

$$\sum_j \sqrt{2\kappa_j^b} \delta B_j = \sqrt{2\kappa_{in}^b} \delta B_{in} + \sqrt{2\kappa_l^b} \delta B_l + \sqrt{2\kappa_{out}^b} \delta B_{out}. \quad (5.14)$$

The system of four differential equations 5.9-5.12 can be rewritten in a more succinct form

$$\dot{\mathcal{X}}_c = \mathbf{M}_c \mathcal{X}_c + \mathbf{M}_{in} \mathcal{X}_{in} + \mathbf{M}_{out} \mathcal{X}_{out} + \mathbf{M}_l \mathcal{X}_l + \mathcal{X}_\Delta + \mathcal{X}_\epsilon, \quad (5.15)$$

which will allow a solution for the fluctuations of the cavity fields to be found with relative ease. The vectors for the fluctuating terms in equation 5.15 are

$$\mathcal{X}_{in} = \begin{pmatrix} \delta A_{in} \\ \delta A_{in}^\dagger \\ \delta B_{in} \\ \delta B_{in}^\dagger \end{pmatrix}, \quad \mathcal{X}_{out} = \begin{pmatrix} \delta A_{out} \\ \delta A_{out}^\dagger \\ \delta B_{out} \\ \delta B_{out}^\dagger \end{pmatrix}, \quad \mathcal{X}_l = \begin{pmatrix} \delta A_l \\ \delta A_l^\dagger \\ \delta B_l \\ \delta B_l^\dagger \end{pmatrix}, \quad (5.16)$$

$$\mathcal{X}_c = \begin{pmatrix} \delta a \\ \delta a^\dagger \\ \delta b \\ \delta b^\dagger \end{pmatrix}, \quad \mathcal{X}_\Delta = \begin{pmatrix} -i\bar{a}\delta\Delta^a \\ i\bar{a}^*\delta\Delta^a \\ -i\bar{b}\delta\Delta^b \\ i\bar{b}^*\delta\Delta^b \end{pmatrix}, \quad \mathcal{X}_\epsilon = \begin{pmatrix} \bar{a}^*\bar{b}\delta\epsilon \\ \bar{a}\bar{b}^*\delta\epsilon^* \\ -\frac{1}{2}\bar{a}^2\delta\epsilon^* \\ -\frac{1}{2}\bar{a}^2\delta\epsilon \end{pmatrix}, \quad (5.17)$$

and the matrices are

$$\mathbf{M}_c = \begin{pmatrix} -\kappa - i\bar{\Delta}^a & \bar{\epsilon}b & \bar{\epsilon}a^* & 0 \\ \bar{\epsilon}^*b^* & -\kappa^a + i\bar{\Delta}^a & 0 & \bar{\epsilon}^*a \\ -\bar{\epsilon}^*a & 0 & -\kappa^b - i\bar{\Delta}^b & 0 \\ 0 & -\bar{\epsilon}a^* & 0 & -\kappa^b + i\bar{\Delta}^b \end{pmatrix}, \quad \mathbf{M}_j = \text{diag} \begin{pmatrix} \sqrt{2\kappa_j^a} \\ \sqrt{2\kappa_j^a} \\ \sqrt{2\kappa_j^b} \\ \sqrt{2\kappa_j^b} \end{pmatrix}, \quad (5.18)$$

where ‘‘diag’’ represents the diagonal matrix. Equation 5.15 can be solved for the cavity fields by taking the Fourier transform and rearranging. The Fourier transform of equation 5.15 is

$$i\Omega\tilde{\mathcal{X}}_c = \mathbf{M}_c\tilde{\mathcal{X}}_c + \mathbf{M}_{in}\tilde{\mathcal{X}}_{in} + \mathbf{M}_{out}\tilde{\mathcal{X}}_{out} + \mathbf{M}_l\tilde{\mathcal{X}}_l + \tilde{\mathcal{X}}_\Delta + \tilde{\mathcal{X}}_\epsilon, \quad (5.19)$$

where  $\Omega$  is the sideband frequency and the tildes on the vectors indicate frequency domain operators ( $\tilde{\mathcal{X}}_c \Leftarrow \mathcal{X}_c$ , etc.). The solution for the fluctuations on the intra-cavity fields is

$$\tilde{\mathcal{X}}_c = (i\Omega\mathbf{I} - \mathbf{M}_c)^{-1} (\mathbf{M}_{in}\mathcal{X}_{in} + \mathbf{M}_{out}\mathcal{X}_{out} + \mathbf{M}_l\mathcal{X}_l + \tilde{\mathcal{X}}_\Delta + \tilde{\mathcal{X}}_\epsilon), \quad (5.20)$$

where  $\mathbf{I}$  is the  $4 \times 4$  identity matrix. We now have the fluctuations of the intra-cavity fields in terms of the fluctuations of the extra-cavity fields, the cavity detuning, and the nonlinear coupling.

### 5.3 Quadratures of the transmitted fields

The fluctuations of the transmitted fields are found by applying the cavity boundary conditions to equation 5.20. The transmitted field is

$$\begin{aligned} \tilde{\mathcal{X}}_{trans} &= \mathbf{M}_{out}\tilde{\mathcal{X}}_c - \tilde{\mathcal{X}}_{out}, \\ &= \mathbf{M}_{out}(i\Omega\mathbf{I} - \mathbf{M}_c)^{-1}\mathbf{M}_{in}\tilde{\mathcal{X}}_{in} + [\mathbf{M}_{out}(i\Omega\mathbf{I} - \mathbf{M}_c)^{-1}\mathbf{M}_{out} - \mathbf{I}]\tilde{\mathcal{X}}_{out} + \\ &\quad \mathbf{M}_{out}(i\Omega\mathbf{I} - \mathbf{M}_c)^{-1}\mathbf{M}_l\tilde{\mathcal{X}}_l + \mathbf{M}_{out}(i\Omega\mathbf{I} - \mathbf{M}_c)^{-1}\tilde{\mathcal{X}}_\Delta + \mathbf{M}_{out}(i\Omega\mathbf{I} - \mathbf{M}_c)^{-1}\tilde{\mathcal{X}}_\epsilon, \end{aligned} \quad (5.21)$$

where

$$\tilde{\mathcal{X}}_{trans} = \begin{pmatrix} \delta\tilde{A}_{trans} \\ \delta\tilde{A}_{trans}^\dagger \\ \delta\tilde{B}_{trans} \\ \delta\tilde{B}_{trans}^\dagger \end{pmatrix}. \quad (5.22)$$

The amplitude and phase quadratures of the transmitted field can be calculated from equation 5.21 in the standard way. This can be done by conveniently by writing

$$\delta\tilde{\mathbf{X}}^{trans} = \Lambda\tilde{\mathcal{X}}_{trans}, \quad (5.23)$$

where

$$\delta\tilde{\mathbf{X}}^{trans} = \begin{pmatrix} \delta\tilde{X}_1^{(A_{trans})} \\ \delta\tilde{X}_2^{(A_{trans})} \\ \delta\tilde{X}_1^{(B_{trans})} \\ \delta\tilde{X}_2^{(B_{trans})} \end{pmatrix}, \quad \Lambda = \begin{pmatrix} 1 & 1 & 0 & 0 \\ i & -i & 0 & 0 \\ 0 & 0 & 1 & 1 \\ 0 & 0 & i & -i \end{pmatrix}. \quad (5.24)$$

Similarly, the quadratures of the other extra-cavity fields can be found by

$$\delta\tilde{\mathbf{X}}^{in} = \Lambda\tilde{\chi}_{in}, \quad \delta\tilde{\mathbf{X}}^{out} = \Lambda\tilde{\chi}_{out}, \quad \delta\tilde{\mathbf{X}}^l = \Lambda\tilde{\chi}_l, \quad (5.25)$$

where

$$\delta\tilde{\mathbf{X}}^{in} = \begin{pmatrix} \delta\tilde{X}_1^{(A_{in})} \\ \delta\tilde{X}_2^{(A_{in})} \\ \delta\tilde{X}_1^{(B_{in})} \\ \delta\tilde{X}_2^{(B_{in})} \end{pmatrix}, \quad \delta\tilde{\mathbf{X}}^{out} = \begin{pmatrix} \delta\tilde{X}_1^{(A_{out})} \\ \delta\tilde{X}_2^{(A_{out})} \\ \delta\tilde{X}_1^{(B_{out})} \\ \delta\tilde{X}_2^{(B_{out})} \end{pmatrix}, \quad \delta\tilde{\mathbf{X}}^l = \begin{pmatrix} \delta\tilde{X}_1^{(A_l)} \\ \delta\tilde{X}_2^{(A_l)} \\ \delta\tilde{X}_1^{(B_l)} \\ \delta\tilde{X}_2^{(B_l)} \end{pmatrix}. \quad (5.26)$$

The solution for the quadratures of the transmitted fields is

$$\delta\tilde{\mathbf{X}}^{trans} = \Theta_{in}\delta\tilde{\mathbf{X}}^{in} + \Theta_{out}\delta\tilde{\mathbf{X}}^{out} + \Theta_l\delta\tilde{\mathbf{X}}^l + \Theta_\Delta + \Theta_\varepsilon, \quad (5.27)$$

where  $\Theta_{in}, \Theta_{out}, \Theta_l$  are given by the following  $4 \times 4$  matrices

$$\Theta_{in} = \Lambda\mathbf{M}_{out}(i\Omega - \mathbf{M}_c)^{-1}\mathbf{M}_{in}\Lambda^{-1}, \quad (5.28)$$

$$\Theta_{out} = \Lambda[\mathbf{M}_{out}(i\Omega - \mathbf{M}_c)^{-1}\mathbf{M}_{out} - \mathbf{I}]\Lambda^{-1}, \quad (5.29)$$

$$\Theta_l = \Lambda\mathbf{M}_{out}(i\Omega - \mathbf{M}_c)^{-1}\mathbf{M}_l\Lambda^{-1}. \quad (5.30)$$

$\Theta_\Delta$  and  $\Theta_\varepsilon$  are  $1 \times 4$  column vectors given by

$$\Theta_\Delta = \Lambda\mathbf{M}_{out}(i\Omega - \mathbf{M}_c)^{-1}\tilde{\chi}_\Delta, \quad (5.31)$$

$$\Theta_\varepsilon = \Lambda\mathbf{M}_{out}(i\Omega - \mathbf{M}_c)^{-1}\tilde{\chi}_\varepsilon. \quad (5.32)$$

The equation 5.27 is a complete solution for the quadratures of the transmitted fields from an OPO or OPA.

## 5.4 Variances of the transmitted fields

The variances of the transmitted fields are given by,

$$\begin{aligned} \tilde{V}_1^{(A_{trans})} &= \left\langle \left| \delta\tilde{X}_1^{(A_{trans})} \right|^2 \right\rangle, & \tilde{V}_2^{(A_{trans})} &= \left\langle \left| \delta\tilde{X}_2^{(A_{trans})} \right|^2 \right\rangle, \\ \tilde{V}_1^{(B_{trans})} &= \left\langle \left| \delta\tilde{X}_1^{(B_{trans})} \right|^2 \right\rangle, & \tilde{V}_2^{(B_{trans})} &= \left\langle \left| \delta\tilde{X}_2^{(B_{trans})} \right|^2 \right\rangle. \end{aligned} \quad (5.33)$$

Here, we consider all fluctuating components to be of independent origin<sup>4</sup>, thus, all cross terms of fluctuating components vanish. The variances of the transmitted fields are then

$$\tilde{\mathbf{V}}^{trans} = |\Theta_{in}|^2\tilde{\mathbf{V}}^{in} + |\Theta_{out}|^2 + |\Theta_l|^2 + |\Theta_\Delta|^2 + |\Theta_\varepsilon|^2, \quad (5.34)$$

<sup>4</sup>The noise terms of the detuning and nonlinear coupling can be correlated if the same mechanism is driving them both, as is the case is photothermal noise in the nonlinear crystal, see reference [121].

where

$$\tilde{\mathbf{V}}^{trans} = \begin{pmatrix} \tilde{V}_1^{(A_{trans})} \\ \tilde{V}_2^{(A_{trans})} \\ \tilde{V}_1^{(B_{trans})} \\ \tilde{V}_2^{(B_{trans})} \end{pmatrix}, \quad \tilde{\mathbf{V}}^{in} = \begin{pmatrix} \tilde{V}_1^{(A_{in})} \\ \tilde{V}_2^{(A_{in})} \\ \tilde{V}_1^{(B_{in})} \\ \tilde{V}_2^{(B_{in})} \end{pmatrix}, \quad (5.35)$$

and we have set:  $\tilde{V}_1^{(A_{out})} = \tilde{V}_2^{(A_{out})} = \tilde{V}_1^{(B_{out})} = \tilde{V}_2^{(B_{out})} = \tilde{V}_1^{(A_i)} = \tilde{V}_2^{(A_i)} = \tilde{V}_1^{(B_i)} = \tilde{V}_2^{(B_i)} = 1$ , since the fields due to intra-cavity loss and from the output port are vacuum states. The variances of the transmitted fundamental field (first and second columns of equation 5.34) contain the squeezing/anti-squeezing plus any classical noise. These are given by

$$\begin{aligned} V_1^{(A_{trans})} &= |\Theta_{in}^{(11)}|^2 \tilde{V}_1^{(A_{in})} + |\Theta_{in}^{(12)}|^2 \tilde{V}_2^{(A_{in})} + |\Theta_{in}^{(13)}|^2 \tilde{V}_1^{(B_{in})} + |\Theta_{in}^{(14)}|^2 \tilde{V}_2^{(B_{in})} \\ &+ \sum_{m=1}^4 \left[ |\Theta_l^{(1m)}|^2 + |\Theta_{out}^{(1m)}|^2 \right] + |\Theta_\Delta^{(1)}|^2 + |\Theta_\varepsilon^{(1)}|^2, \end{aligned} \quad (5.36)$$

$$\begin{aligned} V_2^{(A_{trans})} &= |\Theta_{in}^{(21)}|^2 \tilde{V}_1^{(A_{in})} + |\Theta_{in}^{(22)}|^2 \tilde{V}_2^{(A_{in})} + |\Theta_{in}^{(23)}|^2 \tilde{V}_1^{(B_{in})} + |\Theta_{in}^{(24)}|^2 \tilde{V}_2^{(B_{in})} \\ &+ \sum_{m=1}^4 \left[ |\Theta_l^{(2m)}|^2 + |\Theta_{out}^{(2m)}|^2 \right] + |\Theta_\Delta^{(2)}|^2 + |\Theta_\varepsilon^{(2)}|^2. \end{aligned} \quad (5.37)$$

Here, the  $|\Theta_j^{(\cdot)}|^2$  are the transfer functions of the noise terms. The transmitted quadratures of the harmonic field (third and fourth columns of equation 5.34) are not of interest here, though they too can be squeezed, and even entangled with the fundamental field [134].

### 5.4.1 A simplified case

The dynamics of equations 5.36 and 5.37 are hidden in the  $\Theta$  matrix elements, which are too large to write in full here. To provide some insight to the dynamics, a simplified case can be considered. In section 5.5.3 the case without simplifying assumptions is considered.

The first assumption made is that the fundamental and harmonic field cavities are held on resonance. That is

$$\bar{\Delta}^a = \bar{\Delta}^b = 0, \quad (5.38)$$

Secondly, the nonlinear coupling is assumed to be real

$$\bar{\varepsilon}^* = \bar{\varepsilon}, \quad (5.39)$$

which corresponds to operating at the phase matched condition. Finally, the interacting field are assumed to be real

$$\bar{a}^* = \bar{a}, \quad \bar{b}^* = \bar{b}. \quad (5.40)$$

If the first two assumptions are met and the relative phase of the input fields  $\bar{A}_{in}, \bar{B}_{in}$  locked to amplify or deamplify the coherent seed field, setting  $\bar{B}_{in} = \pm |\bar{B}_{in}|$  (+ for amplification, – for deamplification) the fields  $a$  and  $b$  will be real.

With the three above assumptions, the calculation for the variances is vastly simplified. As the fluctuations well within the cavity linewidth are of interest we assume  $\Omega \ll \kappa^a$ . The coefficients

for the  $\Theta_j$  for the amplitude quadrature are then

$$\Theta_{in}^{(11)} = \frac{2\sqrt{\kappa_{out}^a \kappa_{in}^a}}{\kappa^a - \bar{\varepsilon}b + \frac{\bar{\varepsilon}^2 \bar{a}^2}{\kappa^b}}, \quad \Theta_{in}^{(12)} = 0, \quad \Theta_{in}^{(13)} = \frac{2\bar{\varepsilon}a\sqrt{\kappa_{out}^a \kappa_{in}^b}}{\kappa^b \left( \kappa^a - \bar{\varepsilon}b + \frac{\bar{\varepsilon}^2 \bar{a}^2}{\kappa^b} \right)}, \quad \Theta_{in}^{(14)} = 0, \quad (5.41)$$

$$\Theta_{out}^{(11)} = \frac{2\kappa_{out}^a - \kappa^a + \bar{\varepsilon}b - \frac{\bar{\varepsilon}^2 \bar{a}^2}{\kappa^b}}{\kappa^a - \bar{\varepsilon}b + \frac{\bar{\varepsilon}^2 \bar{a}^2}{\kappa^b}}, \quad \Theta_{out}^{(12)} = 0, \quad \Theta_{out}^{(13)} = \frac{2\bar{\varepsilon}a\sqrt{\kappa_{out}^a \kappa_{out}^b}}{\kappa^b \left( \kappa^a - \bar{\varepsilon}b + \frac{\bar{\varepsilon}^2 \bar{a}^2}{\kappa^b} \right)}, \quad \Theta_{out}^{(14)} = 0, \quad (5.42)$$

$$\Theta_l^{(11)} = \frac{2\sqrt{\kappa_{out}^a \kappa_l^a}}{\kappa^a - \bar{\varepsilon}b + \frac{\bar{\varepsilon}^2 \bar{a}^2}{\kappa^b}}, \quad \Theta_l^{(12)} = 0, \quad \Theta_l^{(13)} = \frac{2\bar{\varepsilon}a\sqrt{\kappa_{out}^a \kappa_l^b}}{\kappa^b \left( \kappa^a - \bar{\varepsilon}b + \frac{\bar{\varepsilon}^2 \bar{a}^2}{\kappa^b} \right)}, \quad \Theta_l^{(14)} = 0, \quad (5.43)$$

and there is no coupling of fluctuations in the detuning or nonlinearity to the amplitude quadrature

$$\Theta_{\Delta}^{(1)} = 0, \quad \Theta_{\varepsilon}^{(1)} = \frac{\sqrt{2\kappa_{out}^a} \bar{a} \left( 2\bar{b} - \frac{\bar{\varepsilon}^2 \bar{a}^2}{\kappa^b} \right) \Re[\delta\varepsilon]}{\kappa^a - \bar{\varepsilon}b + \frac{\bar{\varepsilon}^2 \bar{a}^2}{\kappa^b}} \approx 0, \quad (5.44)$$

where  $\Re[\delta\varepsilon]$  is the real part of  $\delta\varepsilon$ , which is negligible when  $\varepsilon = \varepsilon^*$ .

The coefficients for the  $\Theta_j$  for the phase quadrature are

$$\Theta_{in}^{(21)} = 0, \quad \Theta_{in}^{(22)} = \frac{2\sqrt{\kappa_{out}^a \kappa_{in}^a}}{\kappa^a + \bar{\varepsilon}b + \frac{\bar{\varepsilon}^2 \bar{a}^2}{\kappa^b}}, \quad \Theta_{in}^{(23)} = 0, \quad \Theta_{in}^{(24)} = \frac{2\bar{\varepsilon}a\sqrt{\kappa_{out}^a \kappa_{in}^b}}{\kappa^b \left( \kappa^a + \bar{\varepsilon}b + \frac{\bar{\varepsilon}^2 \bar{a}^2}{\kappa^b} \right)}, \quad (5.45)$$

$$\Theta_{out}^{(21)} = 0, \quad \Theta_{out}^{(22)} = \frac{2\kappa_{out}^a - \kappa^a - \bar{\varepsilon}b - \frac{\bar{\varepsilon}^2 \bar{a}^2}{\kappa^b}}{\kappa^a + \bar{\varepsilon}b + \frac{\bar{\varepsilon}^2 \bar{a}^2}{\kappa^b}}, \quad \Theta_{out}^{(23)} = 0, \quad \Theta_{out}^{(24)} = \frac{2\bar{\varepsilon}a\sqrt{\kappa_{out}^a \kappa_{out}^b}}{\kappa^b \left( \kappa^a + \bar{\varepsilon}b + \frac{\bar{\varepsilon}^2 \bar{a}^2}{\kappa^b} \right)}, \quad (5.46)$$

$$\Theta_l^{(21)} = 0, \quad \Theta_l^{(22)} = \frac{2\sqrt{\kappa_{out}^a \kappa_l^a}}{\kappa^a + \bar{\varepsilon}b + \frac{\bar{\varepsilon}^2 \bar{a}^2}{\kappa^b}}, \quad \Theta_l^{(23)} = 0, \quad \Theta_l^{(24)} = \frac{2\bar{\varepsilon}a\sqrt{\kappa_{out}^a \kappa_l^b}}{\kappa^b \left( \kappa^a + \bar{\varepsilon}b + \frac{\bar{\varepsilon}^2 \bar{a}^2}{\kappa^b} \right)}, \quad (5.47)$$

and the coupling of fluctuations in the detuning and nonlinearity into the phase quadrature are given by

$$\Theta_{\Delta}^{(2)} = \frac{2\bar{a} \left( \delta\Delta^a + \frac{\bar{\varepsilon}b}{\kappa^b} \delta\Delta^b \right) \sqrt{2\kappa_{out}^a}}{\kappa^a + \bar{\varepsilon}b + \frac{\bar{\varepsilon}^2 \bar{a}^2}{\kappa^b}}, \quad \Theta_{\varepsilon}^{(2)} = \frac{\sqrt{2\kappa_{out}^a} \bar{a} \left( 2\bar{b} + \frac{\bar{\varepsilon}^2 \bar{a}^2}{\kappa^b} \right) \Im[\delta\varepsilon]}{\kappa^a + \bar{\varepsilon}b + \frac{\bar{\varepsilon}^2 \bar{a}^2}{\kappa^b}}, \quad (5.48)$$

where  $\Im[\delta\varepsilon]$  is the imaginary part of  $\delta\varepsilon$ .

The features to note from this simplified case are:

1. Noise from the seed field couples to the squeezed beam via the simple cavity transfer functions:  $|\Theta_{in}^{(11)}|^2$  for the amplitude quadrature;  $|\Theta_{in}^{(22)}|^2$  for the phase quadrature.
2. There is no cross quadrature coupling. i.e.  $\Theta_j^{(12)} = \Theta_j^{(14)} = \Theta_j^{(21)} = \Theta_j^{(23)} = 0$ . This means that phase noise does not couple to the amplitude quadrature, and vice versa.
3. Fluctuations in the cavity detuning do not couple to the amplitude quadrature to first order ( $\Theta_{\Delta}^{(1)} = 0$ ). This is because the amplitude response of a cavity goes through a turning point at resonance.
4. Fluctuations in the nonlinear coupling do not couple to the amplitude quadrature ( $\Theta_{\varepsilon}^{(1)} = 0$ ).

At the phase matched condition the real part of the phase matching curve is a turning point (see figure 3.9).

5. The fluctuations of the pump field, cavity detuning, and the nonlinearity all couple to the squeezed state proportional to  $\bar{a}^2$  in variance<sup>5</sup>.

Points 3,4 and 5 indicate that amplitude quadrature squeezing offers advantages over phase squeezing in terms of noise performance. The amplitude quadrature is not sensitive to fluctuations in cavity detuning and nonlinearity (points 3 and 4). Also, in amplitude squeezing, the coherent part of the seed field is de-amplified, so  $\bar{a}^2$  is less than in the case of phase squeezing, where it is amplified.

Point 5 is the most important for the work in this thesis. It shows that vacuum squeezing, where  $\bar{a} = 0$ , is optimal in terms of minimising noise coupling. With  $\bar{a} = 0$  all classical noise sources do not couple to first order, which is a remarkable result. To re-emphasize the dependence of  $\bar{a}^2$  on the coupling of noise sources, equations 5.36 and 5.37 can be rewritten with the assumptions in equations 5.38, 5.39, and 5.40. They are

$$V_1^{(A_{trans})} = \underbrace{|\Theta_{in}^{(11)}|^2 \tilde{V}_1^{(A_{in})} + |\Theta_{out}^{(11)}|^2 + |\Theta_l^{(11)}|^2}_{(\star)} + \underbrace{|\Theta_{in}^{(13)}|^2 \tilde{V}_1^{(B_{in})} + |\Theta_l^{(13)}|^2 + |\Theta_{out}^{(13)}|^2}_{(\star\star)}, \quad (5.49)$$

$$V_2^{(A_{trans})} = \underbrace{|\Theta_{in}^{(22)}|^2 \tilde{V}_2^{(A_{in})} + |\Theta_{out}^{(22)}|^2 + |\Theta_l^{(22)}|^2}_{(\star)} + \underbrace{|\Theta_{in}^{(24)}|^2 \tilde{V}_2^{(B_{in})} + |\Theta_l^{(24)}|^2 + |\Theta_{out}^{(24)}|^2 + |\Theta_{\Delta}^{(2)}|^2 + |\Theta_{\epsilon}^{(2)}|^2}_{(\star\star)}. \quad (5.50)$$

where, the terms which have no dependence on  $\bar{a}$  are denoted by  $(\star)$  and the terms that scale proportional to  $\bar{a}^2$  are denoted by  $(\star\star)$ . Thus, the  $(\star\star)$  noise couplings (pump noise, detuning, and nonlinear coupling fluctuations) can be switched off by setting  $\bar{a} = 0$ .

## 5.5 Noise budget of a OPA

In this section the variances of the transmitted fields are plotted as a function of seed power with model parameters similar to those found in experiments in the following two chapters. The total noise of the squeezed field is plotted along with the individual noise sources that make a noise budget.

### 5.5.1 Model parameters

Before the noise budgets are plotted, it is useful to examine the parameters used in the model.

---

<sup>5</sup>The terms  $\frac{\bar{\epsilon}^2 \bar{a}^2}{\bar{\kappa}^2}$  are much smaller than the rest of the parameters at the type of seed powers used here, and can be ignored.

### Cavity parameters

The parameters used in the models here were chosen to be similar to the experimental values of the experiments presented in chapter 7. The cavity is a doubly resonant cavity with mirror reflectivities, nonlinear gain, and cavity losses were chosen to be close as possible to the experimental parameters.

### Cavity detuning

The variance of the cavity detuning can be written in terms a cavity length change,  $\delta\tilde{x}$ , via a conversion factor [90]

$$\langle |\delta\tilde{\Delta}^a|^2 \rangle = \left( \frac{2\pi c}{\lambda_a L} \right)^2 \langle |\delta\tilde{x}_{(a)}|^2 \rangle, \quad \langle |\delta\tilde{\Delta}^b|^2 \rangle = \left( \frac{2\pi c}{\lambda_b L} \right)^2 \langle |\delta\tilde{x}_{(b)}|^2 \rangle, \quad (5.51)$$

where  $\lambda_a$  is the wavelength of the fundamental field,  $\lambda_b$  the wavelength of the harmonic field, and  $L$  the cavity optical path length. Here, the assumption  $\delta\tilde{x}_{(a)} = \delta\tilde{x}_{(b)}$  is made since the fundamental and harmonic cavities share the same physical path.

### Nonlinear coupling

The noise in the nonlinear coupling strength considered here comes from deviation from the phase matching condition due to temperature fluctuations of the nonlinear medium. To derive  $\delta\epsilon$  we first write the nonlinear coupling constant,  $\epsilon$ , as a function of the phase mismatch parameter,  $\Delta k$ ,

$$\epsilon = \gamma_0 z e^{i\frac{\Delta k z}{2}} \text{sinc} \frac{\Delta k z}{2}, \quad (5.52)$$

where  $\gamma_0$  is a constant depending on the crystal properties, the beam waist, etc., and  $z$  is the crystal length. Around the optimal phase matching temperature,  $T_0$ , the phase matching parameter can be written as

$$\Delta k = \varphi(T - T_0), \quad (5.53)$$

where  $T$  is the crystal's temperature and  $\varphi$  is a constant whose value depends on the crystal's properties. Fluctuations in the crystal's temperature,  $\delta T$ , cause fluctuations in the nonlinearity,  $\delta\bar{\epsilon}$ , via the photo-refractive effect

$$\begin{aligned} \delta\bar{\epsilon} &= \frac{\partial\bar{\epsilon}}{\partial\Delta k} \delta\Delta k, \\ &= \left( \frac{\partial\bar{\epsilon}}{\partial\Delta k} \frac{d\Delta k}{dT} \right) \delta T, \\ &= \left( \frac{\partial\bar{\epsilon}}{\partial\Delta k} \right) \varphi \delta T, \end{aligned} \quad (5.54)$$

where the substitution  $\frac{d\Delta k}{dT} = \varphi$  has been made. In reference [121]  $\delta\epsilon$ ,  $\delta\Delta^{(a)}$ , and  $\delta\Delta^{(b)}$  are considered to originate only due to the photothermal effect and are therefore correlated with each other and with the intra-cavity fields. Here, a more general case is considered, where  $\delta\epsilon$  is not correlated with the detuning parameters. This is the case in typical experiments, because the fluctuating detuning will be dominated by acousto-mechanical sources.

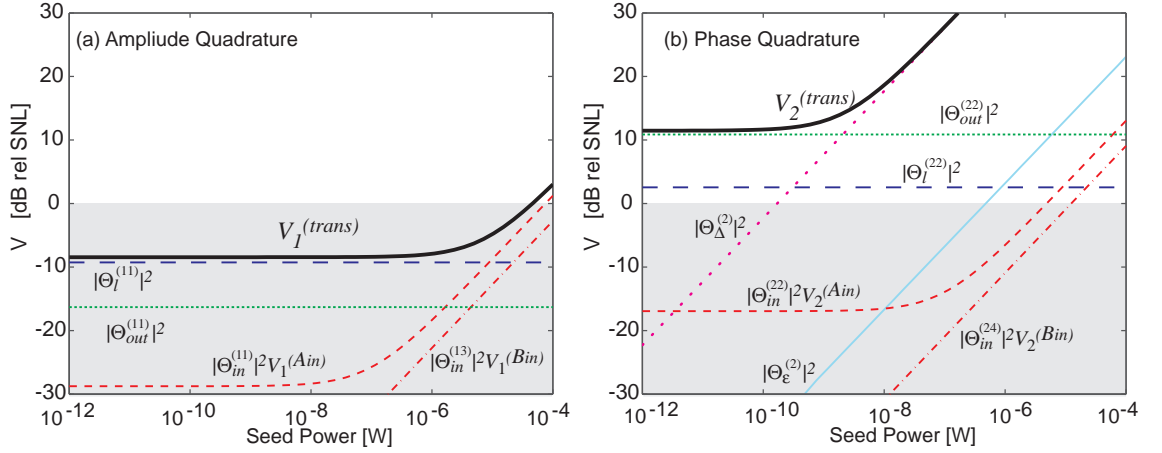


**Figure 5.2:** The noise budget of an amplitude squeezed state, plotted as a function seed power. (a) shows the amplitude quadrature, and (b) the phase quadrature.

### Variable seed power

To vary the seed power in the model (and in the experiments) a variable transmission optic is used which has transmission  $\eta_{att}$ , as shown in figure 5.1. The seed power,  $\bar{P}_{A_{in}}$ , and the variance of the seed field  $\tilde{V}_{1,2}^{(A_{in})}$  vary according to

$$\bar{P}_{A_{in}} = \eta_{att} \bar{P}_{A_0}, \quad (5.55)$$

$$\tilde{V}_{1,2}^{(A_{in})} = \eta_{att} \tilde{V}_{1,2}^{(A_0)} + 1 - \eta_{att}. \quad (5.56)$$

The variance of the input seed field is set to  $\tilde{V}_{1,2}^{(A_0)} = 10^3$  (relative to the quantum noise limit) for  $\bar{P}_{A_0} = 0.1\text{mW}$ .

### Other parameters

In general, the variances of the fields  $\tilde{V}^{(A_{in})}, \tilde{V}^{(B_{in})}$  and  $\langle |\delta\tilde{\Delta}^a|^2 \rangle, \langle |\delta\tilde{\Delta}^b|^2 \rangle, \langle |\delta\tilde{\epsilon}|^2 \rangle$  will have frequency dependence. For simplicity, a single sideband frequency (say  $\Omega/2\pi = 100\text{Hz}$ ) is considered with typical values of the parameters for this frequency.

Also set is  $\tilde{V}_1^{(B_{in})} = \tilde{V}_2^{(B_{in})} = 5 \times 10^5$  (relative to the quantum noise limit),  $\delta x = 10^{-12}\text{m}$ ,  $\delta T = 10^{-5}\text{K}$ , and a parametric gain of 12dB ( $P = 0.35P_{thres}$ ). All parameters used in the model are listed in table 5.1.

### 5.5.2 A simplified case

To begin with, consider the noise budget of the amplitude and phase quadratures with the assumptions used for equations 5.49 and 5.50. Figure 5.2 shows the noise budget of (a) the amplitude quadrature and (b) the phase quadrature as a function of seed power for an amplitude squeezed state. The solid black curve indicates the variance of the transmitted field, whereas the coloured dashed curves indicate the noise contributions of individual terms of equations 5.49 and 5.50.

For seed power less than  $10^{-6}\text{W}$ , the squeezing level (figure (a)) is limited by intra-cavity losses (dashed blue curve). At higher seed powers the squeezed quadrature becomes degraded

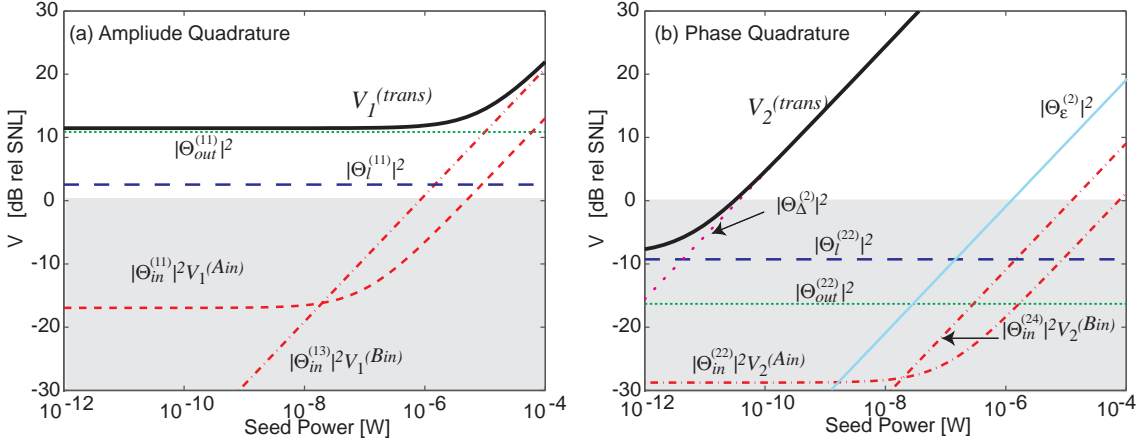


**Figure 5.3:** Noise budget of an phase squeezed state, plotted as a function seed power. (a) shows the amplitude quadrature, and (b), the phase quadrature.

by classical noise on the seed field (dashed red curve, the first term in equation 5.49) and the pump field (dot-dashed red line, the fourth term in equation 5.49). With the assumptions made in equations 5.49 and 5.50 there is no coupling of detuning noise or nonlinear coupling noise into the amplitude quadrature.

At very low seed powers (less than  $10^{-10}$ W) the anti-squeezed quadrature, figure 5.2 (b), is limited by the quantum noise from the output port. At these low powers the squeezed state is a near minimum uncertainty state. At larger seed powers, the detuning noise (dotted pink curve) dominates all other noise sources in the phase quadrature, whilst the amplitude quadrature remains squeezed. Large anti-squeezing is not desirable as the requirements for the locking and measurement stability are increased.

Figure 5.3 (a) and (b) shows the amplitude and phase quadrature with the pump set to squeeze the phase quadrature. The phase quadrature is below the shot noise limit for only very low seed powers as the detuning noise (dotted pink curve) degrades the squeezing as the seed power increases. A comparison of the noise budgets figures 5.2 and 5.3 shows that producing amplitude squeezing rather than phase squeezing has advantages. Also, very low seed power is optimal because the coupling of classical noise sources into the squeezed beam is minimised.

### 5.5.3 Including cavity detuning

Amplitude squeezing is now studied without the simplifying assumptions from the previous section. That is we consider the case where

$$\begin{aligned} \bar{\Delta}^a &\neq 0, & \bar{\Delta}^b &\neq 0, \\ \epsilon &\neq \epsilon^*, \\ \bar{a}^* &\neq \bar{a}, & \bar{b}^* &\neq \bar{b} \end{aligned}$$

Figure 5.4 (a) and (b) shows the noise budget of an amplitude squeezed state with a constant

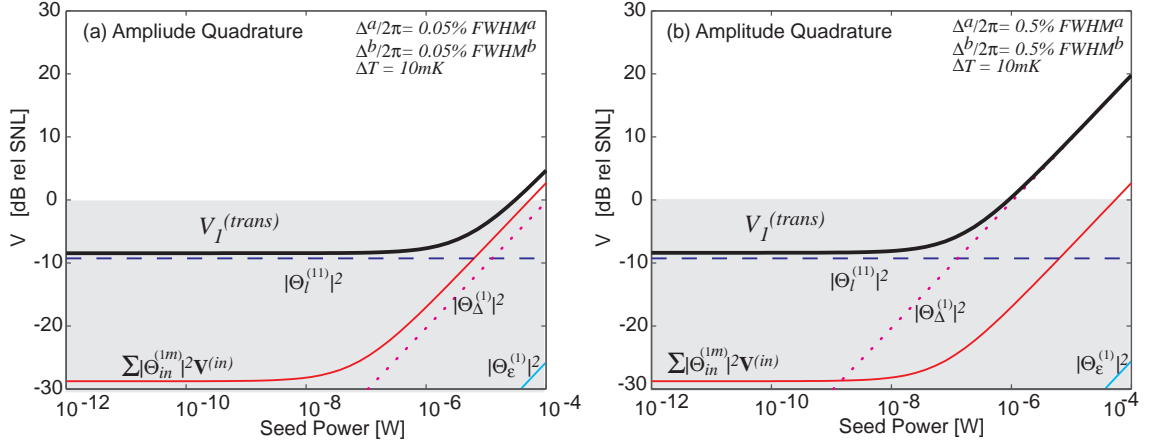


**Figure 5.4:** The noise budget of an amplitude squeezed state plotted as a function seed power with different cavity detunings. In (a)  $\bar{\Delta}^a/(2\pi) = \bar{\Delta}^b/(2\pi) = 0.05\%$  FWHM, in (b)  $\bar{\Delta}^a/(2\pi) = \bar{\Delta}^b/(2\pi) = 0.5\%$  FWHM.

offset in the cavity detuning at both frequencies. The values used were

$$\begin{aligned} \bar{\Delta}^a/(2\pi) = \bar{\Delta}^b/(2\pi) &= 0.05\% \text{ FWHM} \quad [\text{in figure 5.4 (a)}], \\ \bar{\Delta}^a/(2\pi) = \bar{\Delta}^b/(2\pi) &= 0.5\% \text{ FWHM} \quad [\text{in figure 5.4 (b)}]. \end{aligned}$$

These are typical values that might be expected in a laboratory due to residual offsets in the cavity error signal. Also included is an offset from phase matching by setting<sup>6</sup>

$$\Delta T = 10\text{mK}.$$

Figures 5.4 (a) and (b) show that a constant offset in detuning causes the detuning noise to couple to the amplitude (squeezed) quadrature. The phase quadratures are not plotted here but they closely resemble the noise budget of figure 5.2. With the cavities detuned by 0.05% of their respective FWHM's, the detuning noise (dotted pink curve) is similar magnitude to noise due to the input fields (solid red curve). With the cavity detuned by 0.5% of their respective FWHMs, the cavity detuning fluctuations increase to become the dominant classical noise source, limiting the squeezing at seed powers above  $10^{-8}\text{W}$ . Thus, although amplitude quadrature squeezing offers some immunity to detuning fluctuations, they can be significant and may still limit squeezing.

## 5.6 Discussion of the squeezing from a parametric down-converter

The noise budgets in figures 5.2 and 5.3 show that amplitude quadrature squeezing is easier to obtain in the presence of classical noise than phase quadrature squeezing, but given realistic conditions, amplitude quadrature squeezing can still be degraded by laser noise in the seed field, and pump field (figure 5.4). More importantly, the coupling of the classical noise sources into the squeezed beam can be *turned off* by setting  $\bar{a}^2$  to 0.  $\bar{a}^2 = 0$  can be readily achieved experimentally by ensuring the input seed field has zero coherent amplitude ( $\bar{A}_{in} = 0$ ) and operating below the

<sup>6</sup>Note that, in this chapter we consider the effect of cavity detuning and phase mismatch separately. In chapter 10 phase mismatch is considered to be a source of detuning.

OPO threshold. Below threshold OPO quadrature variances given in equations 5.36 and 5.37 reduce to those given by the semi-classical analysis of an OPA presented in the background chapter, i.e. equations 3.125 and 3.126. In this case, the only fluctuations that enter the squeezed field are from the input port, the intra-cavity loss, and the output port. Since these three fields are all the vacuum fluctuations with  $V_{1,2}^{(j)} = 1$ , the quadrature variances become much simpler

$$V_1^{(A_{trans})} = |\Theta_{in}^{(11)}|^2 + |\Theta_{out}^{(11)}|^2 + |\Theta_l^{(11)}|^2, \quad (5.57)$$

$$V_2^{(A_{trans})} = |\Theta_{in}^{(22)}|^2 + |\Theta_{out}^{(22)}|^2 + |\Theta_l^{(22)}|^2. \quad (5.58)$$

The result that the classical noise sources can be prevented from coupling into the squeezed state, to first order, is important. It essentially means that the classical noise sources such as pump noise and cavity detuning, which are typically large at low frequencies, do not need to be reduced in order to produce low frequency squeezed states as long as  $\bar{a}^2 = 0$  is maintained. In the following chapters experimental evidence is presented that confirms this result.

In this simple study, relatively small values for cavity detunings were chosen and only very low seed powers were plotted. In many experiments seed powers are on the order of 10-60mW (e.g. [22, 135]). It can be seen that for 10mW seed power, and the values chosen for  $\delta\epsilon, \delta\Delta^{(a)}, \delta\Delta^{(b)}, V_{1,2}^{(A_{in})}, V_{1,2}^{(B_{in})}$ , there will be no squeezing produced at 100Hz. One other point to note from the noise budgets is that often more than one noise source degrades the squeezed state. This may be why the classical noise cancellation techniques in experiments [21, 22, 120] were not able to recover squeezing below 10kHz.

**Table 5.1:** Parametric down converter parameters

Parameter	Symbol	Value	Units
Fundamental Wavelength	$\lambda_a$	1064	nm
Harmonic Wavelength	$\lambda_b$	532	nm
Input mirror Transmission (at $\lambda_a$ )	$T_{in}^a$	0.0005	-
Input mirror Transmission (at $\lambda_b$ )	$T_{in}^b$	0.025	-
Output mirror Transmission (at $\lambda_a$ )	$T_{out}^a$	0.1	-
Output mirror Transmission (at $\lambda_b$ )	$T_{out}^b$	0.0005	-
Round Trip Loss (at $\lambda_a$ )	$T_l^a$	0.0085	-
Round Trip Loss (at $\lambda_b$ )	$T_l^b$	0.022	-
Average detuning (at $\lambda_a$ )	$\bar{\Delta}^a / (2\pi)$	0 – 0.5%	FWHM <sub>a</sub>
Average detuning (at $\lambda_b$ )	$\bar{\Delta}^b / (2\pi)$	0 – 0.5%	FWHM <sub>b</sub>
Seed power	$P_{(A_0)}$	0.1	mW
Pump power	$P_{(B_{in})}$	$0.35P_{thres}$	W
Transmission of Attenuator	$\eta_{att}$	$1 - 10^{-8}$	-
Variance of seed field before att.	$V_{1,2}^{(A_0)}$	$10^3$	rel SNL
Variance of pump field	$V_{1,2}^{(B_{in})}$	$5 \times 10^5$	rel SNL
Nonlinear coupling parameter	$\bar{\epsilon}$	150	1/s
Optical Path Length	$L$	0.67	m
Cavity length Fluctuation	$\delta x$	$10^{-12}$	m
Phase mismatch constant	$\xi$	150	1/m/K
Offset From phase matched temp	$\Delta T$	0 – 10	mK
Crystal Temperature Fluctuations	$\delta T$	10	$\mu$ K

## 5.7 Summary

A calculation of noise sources that can limit the production of squeezing has been presented. The calculation showed that noise on the pump field; the cavity detuning; and the nonlinear coupling are all coupled to the squeezed field via a beat term with the average intra-cavity field  $\bar{a}$ , and as such can be decoupled from the squeezed beam by setting  $\bar{a} = 0$ . Thus, vacuum squeezing in an OPO is decoupled from these major noise sources.



---

# Squeezing in the audio gravitational wave detection band

---

In this chapter presents an experimental comparison of the squeezing produced from an optical parametric amplifier, and from an optical parametric oscillator operated below threshold. The results confirm the linear dependence of noise coupling on the intra-cavity power of the fundamental field and that sub-threshold OPO offers advantages in terms of producing squeezing at low frequencies. This chapter culminates with the demonstration of squeezing measured over much of the audio gravitational wave detection band. This chapter is based on the work presented in the paper:

*Squeezing in the audio gravitational wave detection band*

K. McKenzie, N. Grosse, W. P. Bowen, S. E. Whitcomb, M. B. Gray, D. E. McClelland and P. K. Lam.

Phys. Rev. Lett. **93**, 161105 (2004).

## 6.1 Introduction

Many previous experiments and proposals to produce squeezed states at low sideband frequencies were based on cancellation of classical noise to recover buried squeezing [21–23, 120, 123, 124]. In this chapter an alternate technique, the suppression of the coupling of classical noise sources, is shown to be extremely effective. We compare OPO and OPA operation of the parametric down-converter and confirm that the presence of a coherent seed field (OPA operation) leads to dramatic degradation of the squeezing at low sideband frequencies due to classical noise coupling. The system operating as a sub-threshold OPO displays immunity to the same technical noise that degrades OPA squeezing. This result is the experimental demonstration of the theory described in chapter 5. We report the generation of high purity broad-band squeezing from a sub-threshold OPO at sideband frequencies from 280Hz to well above 100kHz, covering a large fraction of the audio gravitational wave detection band. The squeezing level measured at 11kHz was  $4.0\text{dB} \pm 0.6\text{dB}$  below the shot noise limit.

This chapters is laid out as follows: section 6.2 details the experimental setup; sections 6.3 and 6.4 present and compare measurements of squeezed states from OPA and sub-threshold OPO; and section 6.5 presents the conclusions drawn from this experiment.

## 6.2 Experiment Details

The experimental setup is shown in figure 6.1. The laser was a 1.5 Watt continuous-wave Nd:YAG Non planar ring oscillator operating at 1064nm. This is the same type of laser and wavelength cur-

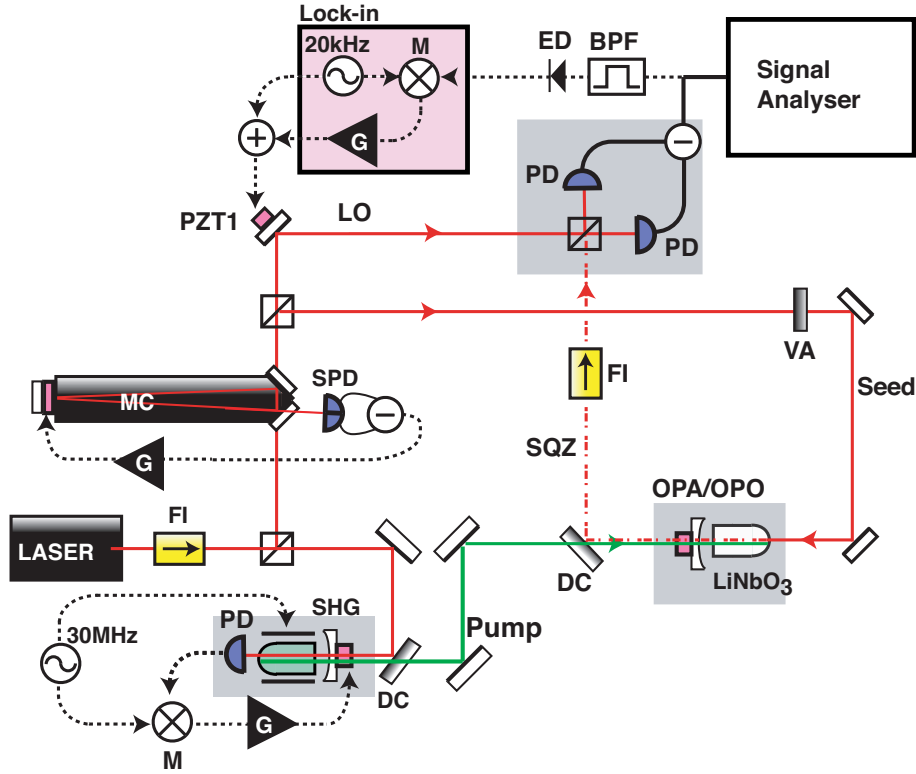


**Figure 6.1:** Schematic of the experiment. The parametric down-converter (labeled OPA/OPO) was pumped with light from the SHG and was seeded with a bright field/vacuum field. The squeezed state (SQZ) was detected on a homodyne detection by interfering it with the local oscillator (LO). The control electronics are indicated with dashed lines. VA-variable attenuator, MC-Modecleaner cavity, PZT-Peizo-electric transducer, BPF-band pass filter, ED-envelope detector, G-gain stage, PM-phase modulator, M-mixer, DC-dichroic mirror, PD-Photodetector, SPD-Split photodetector, FI-Faraday isolator.

rently used in all gravitational wave detectors, though they use amplified versions to give higher power. The majority of the laser power was frequency doubled in a second harmonic generator (SHG) to produce a pump beam of up to 350 mW for the parametric down conversion processes. The SHG was constructed from a type-I phase-matched, 5% doped MgO:LiNbO<sub>3</sub> hemilithic crystal and an external mirror of reflectivity  $R_a = 96\%$  at 1064nm and  $R_b < 4\%$  at 532nm. The curved surface of the crystal was coated for high reflectivity (HR) and the flat surface coated for anti-reflectivity (AR) at both 532nm and 1064nm. A small fraction of the laser field was split-off and spatially filtered using a mode-cleaner cavity [85], to provide a local oscillator field for the homodyne detection system, and to use as a seed beam when required. Though the laser, modecleaner and SHG are essential components, the details of these devices were not critical for the success of this experiment. Further details on the SHG can be found in [135].

The cavity of the parametric down-converter had similar construction to the SHG. The nonlinear medium was a type-I phase-matched, 5% doped MgO:LiNbO<sub>3</sub> hemilithic crystal. The curved surface of the crystal was coated for HR and the flat surface AR coated at both 532nm and 1064nm. A singly resonant standing-wave cavity was formed at 1064nm between the HR surface of the crystal and an external mirror of reflectivity  $T_{in}^a = 4\%$ ,  $T_{in}^b = 96\%$ . The parametric down-converter was pumped with 100mW of 532nm light that double passed through the crystal, resulting in para-

**Table 6.1:** Experimental parameters of the parametric down-converter

Parameter	Value	Parameter	Value
$\lambda_a$	1064nm	Seed power	1-6000nW
$\lambda_b$	532nm	Pump power	100mW
Cavity type	Linear - Standing Wave	$T_{out}^a$	4%
Resonance condition	Singly Resonant	$L_{RT}^a$	0.7%
Nonlinear medium	MgO:LiNbO <sub>3</sub> 5%	$\eta_{esc}$	85%
Crystal dimensions	7.5×2.5×5 mm	$\eta_{hom}$	93%
Crystal geometry	Hemilithic	$\eta_{det}$	93(±2)%
Finesse (at 1064nm)	133	$\eta_{tot}$ (without FI)	73(±2)%
FSR	3718MHz	$\eta_{tot}$ (with FI)	66(±2)%

metric gain of 7dB. Results were taken in OPA operation with seed powers varying between 1nW and 6 $\mu$ W and in sub-threshold (unseeded) OPO operation. The cavity was not actively controlled during the measurements presented in this chapter. The broad cavity linewidth and stability of the laboratory environment was such that, once tuned to resonance manually, the cavity would stay on resonance for approximately 10 seconds, which was sufficient time to take results.

The squeezed state was detected using a balanced homodyne detection system which had a common mode rejection of 55dB. The homodyne photodetectors were built around ETX 500 photodiodes with quantum efficiency  $\eta_{det} = 93(\pm 2)\%$ <sup>1</sup>. The cavity escape efficiency was  $\eta_{esc} = 85\%$ . The homodyne fringe visibility was  $vis = 96.5\%$ , giving  $\eta_{hom} = vis^2 = 93\%$ . The total detection efficiency was therefore  $\eta_{tot} = \eta_{esc}\eta_{hom}\eta_{det} = 73(\pm 2)\%$ . Whilst in OPO operation, a Faraday isolator (FI) was inserted between the OPO cavity and the photodetectors to reduce local oscillator backscattered light. The Faraday isolator introduced an additional 9% loss and so the total detection efficiency with the Faraday isolator was  $\eta_{tot} = 66(\pm 2)\%$ . A summary of the parameters used in the experiment is contained in table 6.1.

The control electronics in the experiment are indicated by dashed lines in figure 6.1. The Tilt Locking technique [136] was used to lock the modecleaner cavity, and transmission dither locking to lock the SHG. The dither for the SHG control loop was imposed by applying electro-optic modulation to the SHG nonlinear crystal. Quantum noise locking (see chapter 9) was used to lock the homodyne detection phase. The quantum noise locking error signal was generated by dithering the local oscillator phase and demodulating the difference photocurrent noise power. The noise power was detected using a spectrum analyzer (Agilent-E4407B, zero span at 2MHz, RBW=300kHz, VBW=30kHz) then demodulated with a lock-in amplifier (Stanford Research Systems (SRS)-SR830) and filtered before being fed back to PZT1. The stability of the homodyne detection phase enabled results to be taken without locking the parametric down-converter cavity. All spectra were taken on a SRS SR785 signal analyser and time domain data were taken on an Agilent-E4407B spectrum analyser.

<sup>1</sup>Errors for the detection efficiency were estimated from the power meter calibration uncertainty. Recently, Vahlbruch *et al.* [18] inferred the detection efficiency of the ETX500 photodiodes to be  $95\pm 2\%$  using a measurement of squeezing. In the the Vahlbruch *et al.* measurement the protective window of the photodiode had been removed, unlike this experiment.

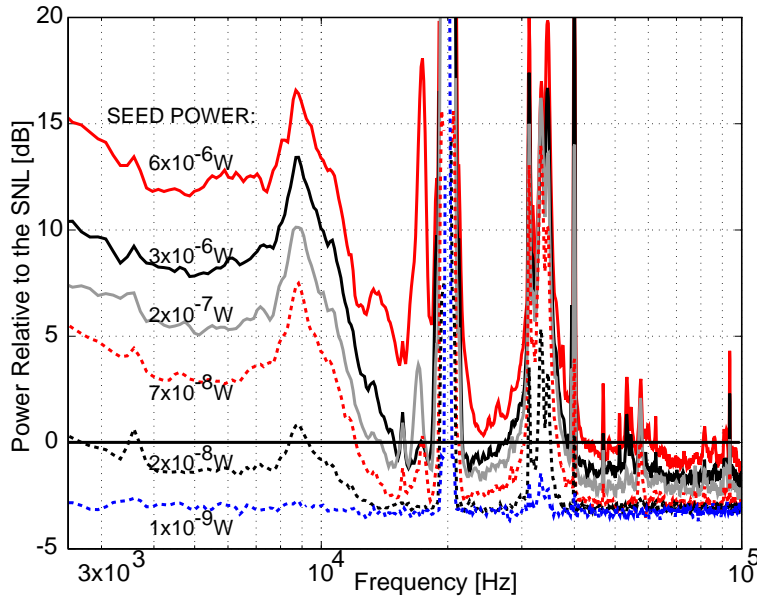


**Figure 6.2:** (Best viewed in colour) The OPA spectrum 2kHz-100kHz with different seed powers. The variance of the seed beam with power  $6\mu\text{W}$  was less than 4dB above the SNL across the spectrum. RBW=128Hz. Electronic noise (at -12dB) was subtracted from all traces.

### 6.3 Squeezing from an OPA

Spectra of the squeezed states generated from the experiment operated as an OPA are shown in figure 6.2. Spectra were taken for six different seed powers between 1nW and  $6\mu\text{W}$ , and are plotted relative to the shot noise limit (SNL). At seed power of 1nW the spectrum is essentially flat at -3.5dB with the exception of a feature at 34kHz and a peak at 20kHz which was due to the quantum noise locking modulation. At the seed power of 80nW, the spectrum shows the feature at 34kHz has increased in amplitude and additional noise is present below 15kHz, degrading the squeezing amplitude to modest levels below 10kHz. The new feature in the spectrum at 8kHz was also present in the pump intensity noise spectrum and was expected to have coupled into the squeezed field via the nonlinear interaction with the intra-cavity fundamental field. As the seed power was increased further, the noise floor and features in the spectra continued to increase. By  $6\mu\text{W}$  of seed power, squeezing below 40kHz was no longer observable. These results clearly show contamination of the squeezed state by classical noise sources at high seed power. Whilst this data was taken, no experimental parameters other than the input seed power were varied, indicating it was the noise coupling that was changing with seed power, rather than the noise sources.

The noise power increase of the squeezed state in proportion to the seed power is evident in figure 6.3, which shows the integrated noise power of the data in figure 6.2 between 5-6kHz as a function of seed power. The experimental points indicated by 'x' can be compared with: a fitted line which is the sum of classical and quantum noise, curve (i); squeezed quantum noise, curve (ii), and a classical noise source which has linear dependence on seed power, curve (iii). Large uncertainties in the experimental data were expected for a number of reasons. Firstly, the OPA cavity length was not actively controlled because the seed power was insufficient to obtain a cavity error signal. Instead the cavity was simply tuned to resonance manually, and left there whilst data was taken. Secondly, the seed power had uncertainties. The seed power was inferred

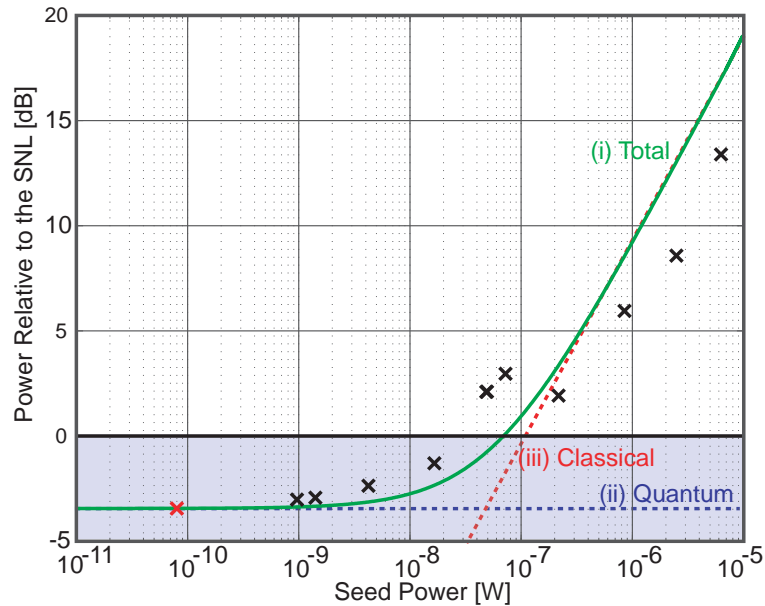


**Figure 6.3:** The average noise power from 5-6kHz as a function of seed power, experimental data indicated by ‘x’, model fit given by curve (i). Electronic noise (at -12dB) was subtracted from all data.

by attenuating a beam of known power (measurable on a power meter) using a neutral density filter wheel (New Focus 5214-B). As the neutral density filters were changed, misalignment of the seed beam to the cavity could occur, which changes the amount of seed light that is coupled into the cavity. Finally, the relative phase of the seed and pump field was not controlled. This meant that the intra-cavity power of the fundamental field could vary significantly depending if the seed field was amplified or deamplified. Even with the large uncertainties expected, the data roughly follows the linear trend predicted by the theory in equations 5.49 and 5.50.

Further evidence of the seed field enabling contamination of the squeezed state can be seen from the data in figure 6.4. Curve (i) was taken with the seed field blocked in an attempt to operate the experiment as a sub-threshold OPO, to produce vacuum squeezing. Large peaks between 300Hz and 700Hz were observed. This low frequency contamination was attributed to light from the local oscillator field backscattered from the photodetectors and seeding the OPO cavity. Note that even with the photodetectors tilted at an angle to prevent retro-reflection, the scattering from the front face of the detectors, which was estimated to be of the order of  $1\text{pW}^2$ , was sufficient to seed the parametric process and cause parametric amplification and interaction with classical noise sources. A Faraday isolator was placed between the cavity and the detection system to reduce the backscattered light. With the isolator in place the noise coupling via in the parametric amplification process was reduced to an immeasurable level, as shown by curve (ii). The residual peaks at 150Hz and 250Hz in both the detection system noise floor and the squeezed spectra were due to pick up from the electronic mains (not shown in this figure).

In figure 6.3, a single red ‘x’ has been placed to indicate the data point where the OPA cav-

<sup>2</sup>The power of the backscattered light could be quantified by tuning the OPO cavity off resonance, so it acted like a HR mirror reflecting the backscattered seed to the homodyne detection system, then measuring the interference of the backscattered seed with the local oscillator. From the fringe visibility and known local oscillator power the backscattered seed power could be obtained.

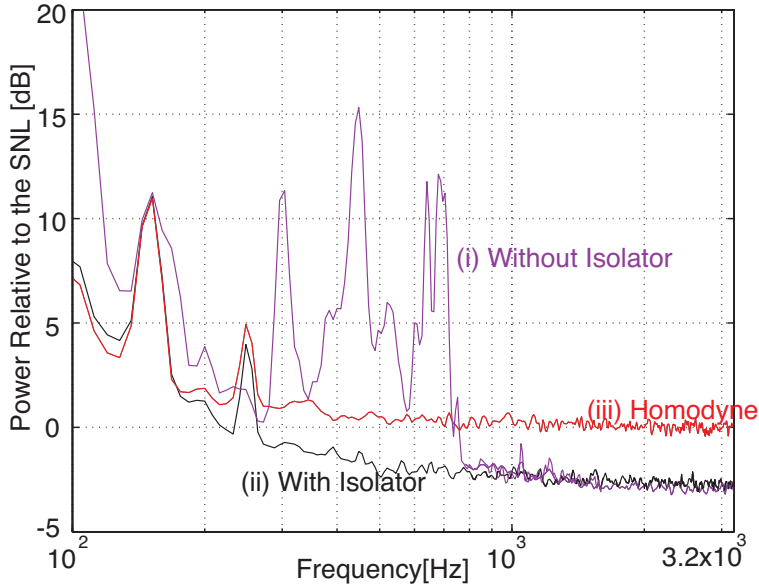


**Figure 6.4:** The OPO spectrum from 100Hz to 3.2kHz without (i) and with (ii) the Faraday isolator between the OPO cavity and homodyne detector. RBW=8Hz. Electronic noise (not shown) was not subtracted

ity was (unintentionally) seeded through the output coupler by backscattered light from the photodetector of order 1pW. The power value of the red x has been scaled to accommodate for the difference in coupling from the HR side of the cavity (black x's) and the output coupler (red x).

## 6.4 Squeezing from an OPO

The spectrum of the squeezed state produced using an OPO is shown by curve (ii) in figure 6.5. Squeezing continues to tens of MHz, as reported in [135]. Curve (i) shows the spectrum of the homodyne detection system<sup>3</sup> without squeezed input. This indicates that the measurement is shot noise limited at frequencies above 1kHz and is contaminated at frequencies below 1kHz. Curve (iii) is the electronic noise of the detection system. Broadband squeezing was measured from 280Hz to 100kHz, with the exception of a locking signal peak at 20kHz. Squeezing could not be measured at 150Hz and 250Hz due to power supply harmonics. Squeezing data at frequencies lower than 100Hz could not be taken since the stability of the squeezing was insufficient for measurements on the required time scale (because the OPO cavity length was not actively controlled) and because the homodyne detection noise floor was above the shot noise limit. The roll-up in noise power in the homodyne and squeezed light traces below 1kHz was due to excess noise in the homodyne detector system. This is likely due to noise sources such as scattered light [17]. A detailed investigation into these noise sources is presented in section 7.5.

Evidence that classical noise is not coupling to the squeezed vacuum state can be obtained by comparing the measured purity to the purity calculated taking into account the parametric gain and the losses. If no classical noise sources are present then the squeezed and anti-squeezed

<sup>3</sup>In this thesis we have chosen to use the term 'homodyne detection noise floor' or 'detection noise' rather than the more common 'shot noise' for describing the noise power as measured by the homodyne detector. This is because although at high frequencies the detection system is indeed shot noise limited, at low frequencies the noise deviates away from the calculated shot noise.

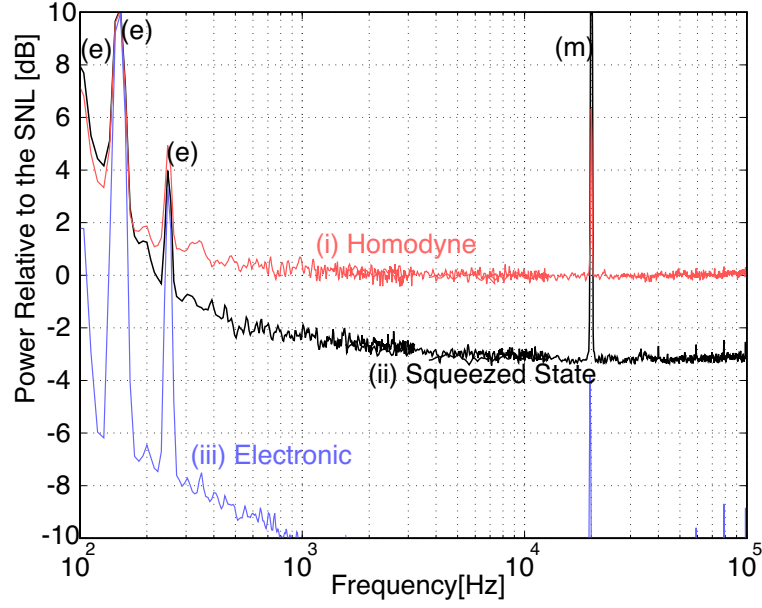


**Figure 6.5:** Measured noise spectra for the homodyne, curve (i), the squeezed light, curve (ii), and the electronic noise of the homodyne detection system, curve (iii). The traces are pieced together from three FFT frequency windows: 100Hz-3.2kHz, 1.6kHz-12.8kHz, and 3.8kHz-100kHz. Each point is the averaged RMS value of 500, 1000 and 2000 measurements made in the respective ranges. The RBW of the three windows was 8Hz, 32Hz and 128Hz, respectively. The electronic noise was -12dB below the quantum noise from 10kHz-100kHz. The 20kHz peak arises from the homodyne modulation locking signal and is labeled (m). Peaks at 50Hz harmonics are due to electrical mains supply, labeled (e).

quadratures are given by

$$V_{sqz} = \frac{\eta_{tot}}{\mathcal{G}} + 1 - \eta_{tot}, \quad (6.1)$$

$$V_{asqz} = \eta_{tot} \mathcal{G} + 1 - \eta_{tot}, \quad (6.2)$$

where the gain parameter,  $\mathcal{G}$ , is given in equation 3.122. The purity of the squeezed state is given by the product

$$V_{sqz} V_{asqz} = \left[ \left( \frac{1}{\mathcal{G}} + \mathcal{G} \right) - 2 \right] \eta_{tot} (1 - \eta_{tot}) + 1, \quad (6.3)$$

Figure 6.6 shows the OPO squeezed state at 11.2kHz as the detection phase was varied. This data was taken without the Faraday Isolator between the OPO cavity and detection system. The measured and calculated squeezed state purities are

$$V_{sqz} V_{asqz} = 1.6(\pm 0.2) \quad (\text{Measured}), \quad (6.4)$$

$$V_{sqz} V_{asqz} = 1.6(\pm 0.1) \quad (\text{Calculated}). \quad (6.5)$$

which agree, confirming that there is no excess noise at this measurement frequency.

For the above measured value we have used  $V_{sqz} = 0.43(\pm 0.04)$ ,  $V_{asqz} = 4.55(\pm 0.04)$  (with errors due to standard deviation of noise), and calculated value we used  $\mathcal{G} = 5$  (i.e. 7dB),  $\eta_{tot} =$

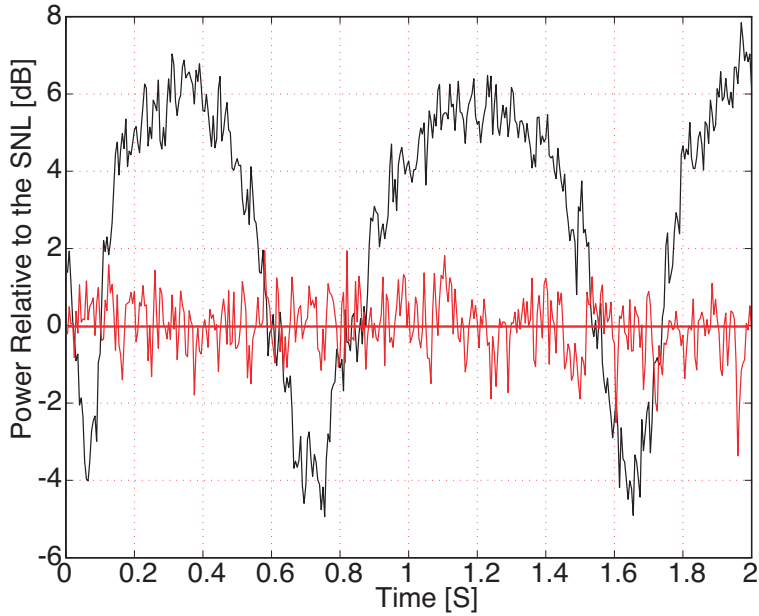


**Figure 6.6:** The squeezed state at 11.2kHz as the phase of the homodyne is varied. RBW=1kHz, VBW=30Hz. Electronic noise (9dB below SNL) was subtracted from the data.

73( $\pm 2$ )%.

## 6.5 Chapter summary

In this chapter the parametric down conversion process of OPA and sub-threshold OPO were compared experimentally. It was shown that excess noise coupled to the squeezed field in direct proportion to the seed field power, agreeing with the result derived in chapter 5. By eliminating the seed field from the parametric down conversion process, the coupling of the excess noise could be ‘switched off’. This resulted in broadband squeezing down to 280Hz.

The experiment presented here was not suited to producing squeezing at very low sideband frequencies, or over long time scales, because the OPO cavity length was not actively controlled. In the following chapter we introduce an experiment that produced stable squeezed states.

---

# Stable audio frequency squeezing from a doubly resonant OPO

---

This chapter documents the production of stable, low frequency squeezing from a doubly resonant OPO experiment, and examines the limitations of squeezing measurement imposed by the detection system. Much of the work presented in this chapter was published in the journal articles:

*Squeezed State Generation for Interferometric Gravitational-Wave Detection*

K. McKenzie, M. B. Gray, S. Goßler, P. K. Lam, and D. E. McClelland,  
Class. Quant. Grav. **23**, S245 (2006)

*Technical limitations to homodyne detection at audio frequencies*

K. McKenzie, M. B. Gray, P. K. Lam, and D. E. McClelland,  
Appl. Opt. **46**, 3389 (2007)

## 7.1 Introduction

The first experimental demonstration of squeezing in the audio gravitational wave detection band was presented in the previous chapter. That work showed that the OPO intra-cavity power at the fundamental frequency was the coupling mechanism for many noise sources into the squeezed field. By eliminating the seed field, vacuum squeezing at low sideband frequencies could be obtained. That simple insight has been the cornerstone of all subsequent low frequency OPO squeezing experiments [17, 25, 26, 125, 126].

Elimination of the intra-cavity power at the fundamental frequency meant removing the coherent seed field and reducing backscattered light, which could act as a spurious seed field. By removing the coherent seed field, the only coherent phase reference for the singly resonant OPO cavity resonance was also removed and therefore no cavity length control signal could be obtained. Without active cavity length control, the squeezing was stable for only tens of seconds, insufficient length of time for low frequency applications. Two solutions were proposed to allow stable, low frequency squeezing to be produced from OPO's without a coherent seed field<sup>1</sup>. These are:

1. Add a frequency shifted sub-carrier field to sense the singly resonant OPO cavity resonance condition.
2. Use a doubly resonant OPO cavity and the pump field to sense the cavity resonance condition.

---

<sup>1</sup>The quantum noise locking technique could also be used to obtain a cavity error signal, however it may be difficult to obtain the required stability using this technique.

Both of the above techniques have proven successful. The use of frequency shifted subcarrier field for cavity control in singly resonant OPO has been demonstrated by Vahlbruch *et al.* [26, 137] and Goda *et al.* [19]. Using the pump field in a doubly resonant OPO to obtain a cavity control signal has also been successfully demonstrated previously by Laurat [23]. This was the method chosen for the experiment described here.

## 7.2 OPO design considerations

### 7.2.1 Doubly resonant OPO vs. singly resonant OPO

The primary advantage of doubly resonant OPOs over singly resonant OPOs for producing (low frequency) vacuum squeezing is the simplicity of obtaining a cavity error signal. The pump field can be used to readout the cavity length error signal and no sub-carrier field is required. There are also other advantages of doubly resonant OPOs, three important ones are:

- The pump field amplitude is resonantly enhanced, giving a higher nonlinear gain for the same input pump power. This allows the possibility of increasing the transmission of the output coupler at the fundamental frequency to increase the escape efficiency.
- The doubly resonant cavity naturally assures perfect mode matching of the interacting fields. Since the harmonic and fundamental fields share the same optical cavity, the ratio of the waist sizes is  $\sqrt{2}$  (the fundamental waist is larger than the harmonic) which is exactly the optimal relative waist sizes for  $\chi^{(2)}$  nonlinear interaction [138].
- Any spatial component of the pump field that is not matched to the cavity mode will be rejected from the cavity. This means photothermal effects induced by the pump light and nonlinear effects like GRIIRA [131] are minimised because only interacting light enters.

There are also disadvantages associated with doubly resonant OPO, which require mitigation to operate effectively. These are:

- The intra-cavity dispersion of the fundamental and harmonic fields causes the resonance frequencies to be offset. In this case, when co-resonance does not occur, nonlinear interaction is interferometrically suppressed. There are two sources of dispersion that need to be considered: dispersion from the dichroic mirror coatings and dispersion introduced from phase mismatch in the nonlinear medium. Dispersion from mirror coatings has a static value and can be negated using a tunable dispersive element, as shown in appendix C.2. The dispersion introduced by phase mismatch is the more problematic. A doubly resonant cavity modifies the temperature dependence of the phase matching curve from the single pass non-linearity, significantly narrowing the phase matching FWHM temperature, see chapter 10 and figure 10.2. This means there are more stringent temperature stability requirements<sup>2</sup>.
- The photothermal effect [76] associated with absorption of the pump field in the nonlinear crystal. This can cause length instabilities such as optical bi-stability.

---

<sup>2</sup>Dispersion of the interacting fields is also seen in singly resonant systems where the pump field makes double pass through the nonlinear medium and dispersion is present as is detailed in Andrew White's thesis [89], however this effect is generally much smaller.

## 7.2.2 Traveling-wave vs. standing-wave cavity

Another design consideration is whether to use a traveling- or standing-wave cavity. A traveling-wave cavity offered an advantage for producing low frequency squeezed states: the traveling-wave OPO has inherent isolation to backscattered light from the local oscillator of the detection system (or light from the gravitational wave detector dark port), which can spuriously seed the OPO. The isolation of the traveling-wave cavity to backscattered light occurs as the backscattered light occupies the mode which propagates in the opposite direction to the squeezed beam. In low frequency squeezing experiments that use standing wave cavities, Faraday isolators were required to reduce backscatter and prevent spurious seeding of the OPO (see section 6.3 and also [24, 26, 128]). The use of Faraday isolators can add considerable optical loss, typically 5-10% single pass [139]. With some effort, considerably less loss ( $\sim 1\%$ ) should be achievable [140].

With the above design considerations in mind, a bow-tie traveling-wave doubly resonant OPO cavity was chosen for this experiment. Details of the experiment are presented in section 7.3. In section 7.4 we present measurements of stable, audio frequency vacuum squeezing with up to  $5.5 \pm 0.2$  dB of quantum noise reduction. In section 7.5 an investigation into excess low frequency noise in homodyne detection systems is presented.

## 7.3 The experiment

The experimental setup is shown in figure 7.1. The basic setup for the experiment was similar to that presented in chapter 6, although details of the laser, SHG, and mode-cleaner were different. Details of these three devices can be found in appendix C. The doubly resonant OPO was a bow-tie cavity with an optical path length of 756mm. The geometry is shown in detail in figure 7.2. The cavity was formed from a flat input/output mirror, a flat HR/HR (at 532nm/1064nm) mirror and two concave HR/HR mirrors with ROC = -150mm. The two cavity waists were located midway between the flat mirrors and midway between the concave mirrors with sizes at 532nm of  $\omega_1 = 150\mu\text{m}$  and  $\omega_2 = 50\mu\text{m}$ , respectively. The nonlinear medium was a periodically poled (quasi-phase matched) potassium titanyl phosphate (KTiOPO4) (called PPKTP hereafter) crystal from Raicol Crystals [141] which was placed at the smaller of the two waists. This was a rectangular prism 10mm in length with end faces polished and AR coated at both wavelengths. The crystal was housed in custom built peltier (thermo-electric cooler) driven oven, which was held at  $35.0^\circ\text{C}$  using a commercial temperature controller (Newport 3040).

Both MgO:LiNbO<sub>3</sub> and PPKTP crystals were trialed in the doubly resonant OPO. PPKTP was chosen for these experiments due to the higher nonlinearity, broader phase matching temperature, and smaller photothermal effect. A comparison of the performance of the doubly resonant OPO with two nonlinear media is presented in appendix B.

The cavity input/output coupling mirror (input coupler for the pump field, output coupler for the squeezed field) had transmission  $T_{in}^b = 3\%$ ,  $T_{out}^a = 10\%$ . Transmissivities were chosen to: maximise the circulating pump power, by matching the transmission at the pump wavelength to the expected round trip loss and impedance match the pump cavity; and to give high escape efficiency for the squeezed field. The round trip losses of the cavity were  $L_{RT}^a = 0.9(\pm 0.1)\%$ ,  $L_{RT}^b = 2.2(\pm 0.1)\%$  determined by measurements of the cavity linewidths. The linear loss at 1064nm is consistent with the losses expected from the AR coatings and non unity reflectivities of the HR mirrors, plus the linear absorption of PPKTP measured in previous experiments (0.1-0.3% per cm) [19]. The round trip losses with output coupler transmission gave the cavity escape efficiency of  $\eta_{esc} = 92(\pm 1)\%$ .

An additional optic was placed in the cavity to compensate for dispersion introduced by the dichroic mirror and crystal coatings, labeled DCW for dispersion compensation window. This

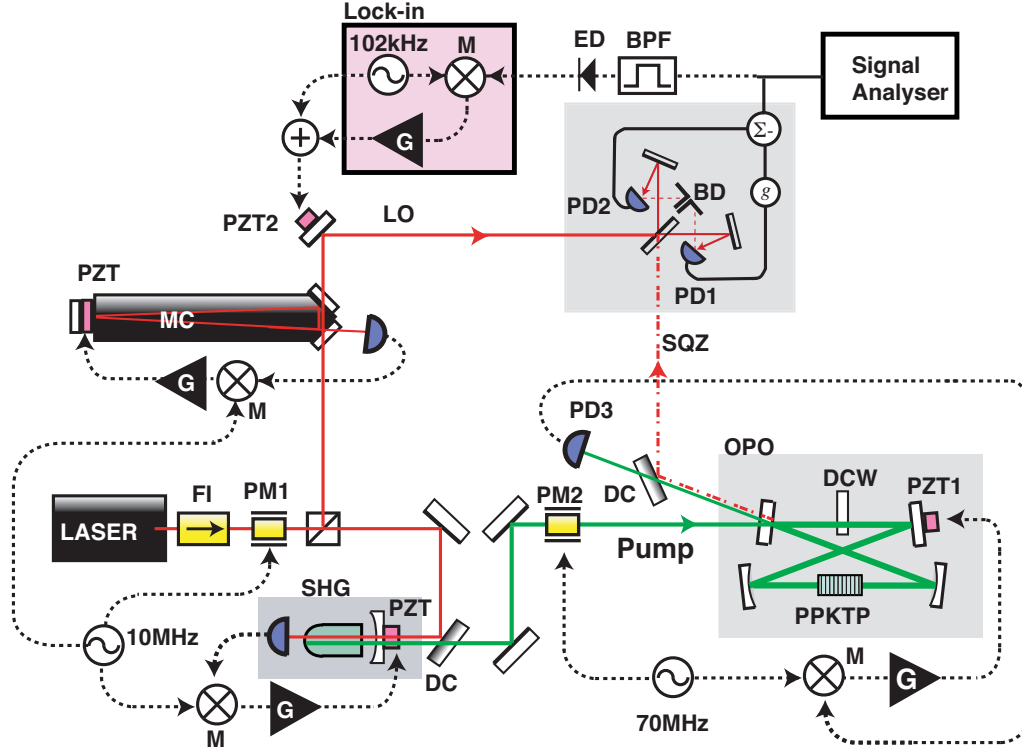


**Figure 7.1:** Schematic of the experiment. The OPO was pumped with the SHG and was seeded with vacuum. The bow-tie OPO cavity was resonant for both fundamental and harmonic frequencies, containing a PPKTP crystal and a dispersion compensation window (DCW). Control electronics are indicated with dashed lines. SQZ- squeezed state, LO-local oscillator, MC-Modecleaner, PZT-piezo-electric transducer, BPF-band pass filter, ED-envelope detector, G-gain stage, SHG-second harmonic generator, PM-phase modulator, PZT-piezo electric transducer, DC-dichroic mirror, PD-Photodetector, M-mixer. Modematching optics are not shown.

was a 1/4 inch thick, flat-flat AR/AR coated BK7 optic. The round trip cavity dispersion was nulled (to the nearest  $2\pi$  integer) by varying the angle of the DCW, which due to the dispersion in glass, gives a differential phase shift between the fundamental and harmonic frequencies. This ensured both fundamental and harmonic cavities were resonant simultaneously, giving the optimal nonlinear gain. See appendix C.2 for additional details.

The cavity was locked using the PDH technique [142, 143], with the error signal derived from the reflected pump field. The error signal was fed back to a PZT bonded to a cavity mirror, to stabilize the cavity length. The PZT was single layer element which was glued on a custom built mount and reaction mass. The primary piston-mode resonance frequency was approximately 200kHz, enabling a unity gain frequency of approximately 50kHz in the length control loop. The design and characteristics of the PZT mounted mirror are detailed in section C.3. The OPO was pumped with approximately 75mW of 532nm light which, due to the cavity enhancement, gave an effective pump power of  $\sim 2.8$ W, resulting in a parametric gain of 15dB. The OPO cavity was vacuum seeded and operated below threshold for reasons previously described, thus a squeezed vacuum field was produced.

The squeezed vacuum was steered to a balanced homodyne detector using four dichroic beam-splitters which separated it from the reflected pump field. We estimate the small loss ( $\approx 1\%$ )

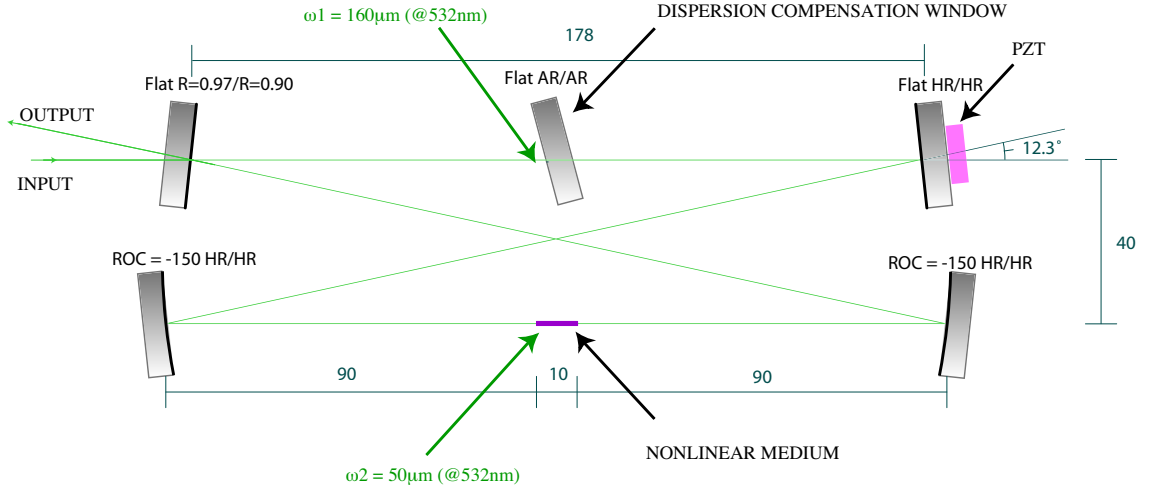


**Figure 7.2:** OPO cavity design. Length dimension are millimeters, angles in degrees.

from the dichroic beamsplitters to give a transmission efficiency of  $\eta_{opt} = 99(\pm 0.5)\%$ . The local oscillator power was  $380\mu\text{W}$  and fringe visibility was  $98.5(\pm 0.5)\%$ . The photodetectors used ETX500T photodiodes which had the protective windows removed. The common mode rejection of the homodyne detector was over 60dB. The detection phase was controlled using the quantum noise locking technique, with the error signal generated by dithering the local oscillator phase and demodulating the homodyne photocurrent noise power. This error signal was fed back to PZT2.

The values of the experimental efficiencies:  $\eta_{esc} = 92(\pm 1)\%$ ,  $\eta_{opt} = 99(\pm 0.5)\%$ ,  $\eta_{hom} = 97(\pm 1)\%$ , and  $\eta_{det} = 93(\pm 2)\%$ , give an estimate for the total efficiency:  $\eta_{tot} = 84(\pm 2)\%$ .

**Table 7.1:** Experimental parameters of the doubly resonant OPO

Parameter	Value	Parameter	Value
Nonlinear medium	PPKTP	Cavity type	Traveling-wave
$\lambda_a$	1064nm	$\lambda_b$	532nm
Seed power	-	Pump power	<70mW
$T_{out}^a$	10%	$T_{in}^b$	3%
Finesse (at 1064nm)	55	Finesse (at 532nm)	117
$L_{RT}^a$	$0.9(\pm 0.1)\%$	FSR	397MHz
$\eta_{esc}$	$92(\pm 2)\%$	$\eta_{hom}$	$97(\pm 1)\%$
$\eta_{det}$	$93(\pm 2)\%$	$\eta_{tot}$	$84(\pm 2)\%$

## 7.4 Squeezed state measurements

Curve (i) in figure 7.3 is a measurement of the squeezed vacuum spectra. Curve (ii) shows the noise power of the homodyne detection system, which coincides with the calculated shot noise limit (curve (iii)) at high frequencies and has additional noise below 1kHz. Curve (iv) is the measured electronic noise floor of the detection system. Broadband quantum noise reduction can be seen, with the maximum reduction of  $5.3(\pm 0.3)\text{dB}$  in the 2kHz-100kHz band. The squeezed

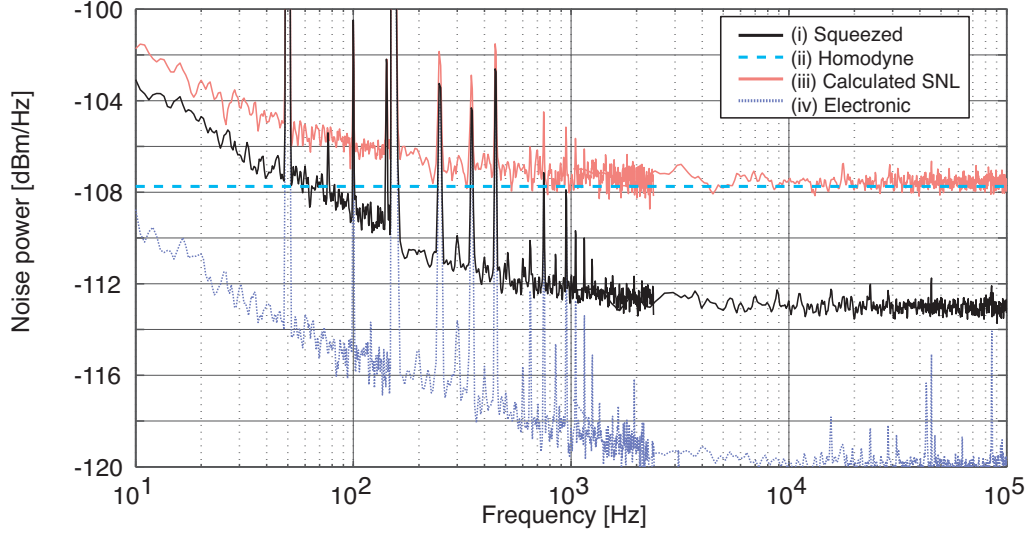


**Figure 7.3:** Measured noise spectra for the homodyne noise limit; the squeezed light; the electronic noise of the homodyne detection system; and the calculated shot noise limit (SNL). The curves are pieced together from three FFT frequency windows 100kHz-1.024kHz, 3.2kHz-160Hz, and 200Hz-10Hz. The RBW of the three windows was 128Hz, 4Hz, and 1/2Hz, respectively. Peaks at 50Hz harmonics are due to electrical mains supply.

vacuum curve is below the calculated shot noise limit at sideband frequencies above 70Hz, with the exception of the power supply harmonics in the electronic noise (at 50Hz multiples). The roll-up in noise power in the detection and squeezed spectra below 1kHz is partly attributable the increase of the electronic noise at these frequencies, but is also a result of excess noise sources in the detection system. Noise sources in the homodyne detection system are discussed in section 7.5.

Figure 7.4 shows spectra of the squeezed state, curve (i), and homodyne detector, curve (ii), with electronic noise subtracted and plotted relative to the calculated shot noise limit. At frequencies above 1kHz, the squeezed curve is  $6.3(\pm 0.2)$ dB below the shot noise limit, and below 1kHz the squeezed amplitude reduces with reducing frequency. The squeezed curve is below the calculated shot noise limit at frequencies above 50Hz. Over the entire measurement band, the noise power of the squeezed curve is lower than that of the detection system, though the separation between the two curves reduces at low frequencies. It may be thought that this is a measurement of squeezing across this entire frequency band. This is not necessarily the case, since classical correlations or a reduction in the excess noise of the homodyne detector could be responsible for a reduction in the noise power. Thus we consider the measurement of squeezing to be below the calculated shot noise limit, not the noise limit of the detection system.

The high frequency spectra of squeezed and anti-squeezed quadratures are shown in figure 7.5 (a). The magnitude of the squeezed and anti-squeezed quadratures reduces at high frequencies due to the cavity pole (FWHM=7.2MHz). At frequencies approaching 10MHz, the quadratures tend to the vacuum state. This data shows that the relatively low OPO cavity linewidth does not suit high frequency squeezing measurements. In the gravitational wave detection band the attenuation due to the cavity pole is negligible (less than 0.01%).

Figure 7.5 (b) shows a measurement of the squeezed state at 100kHz as a function of time. Here the shot noise, curve (i), the locked squeezed noise, curve (ii), and the electronic noise, curve

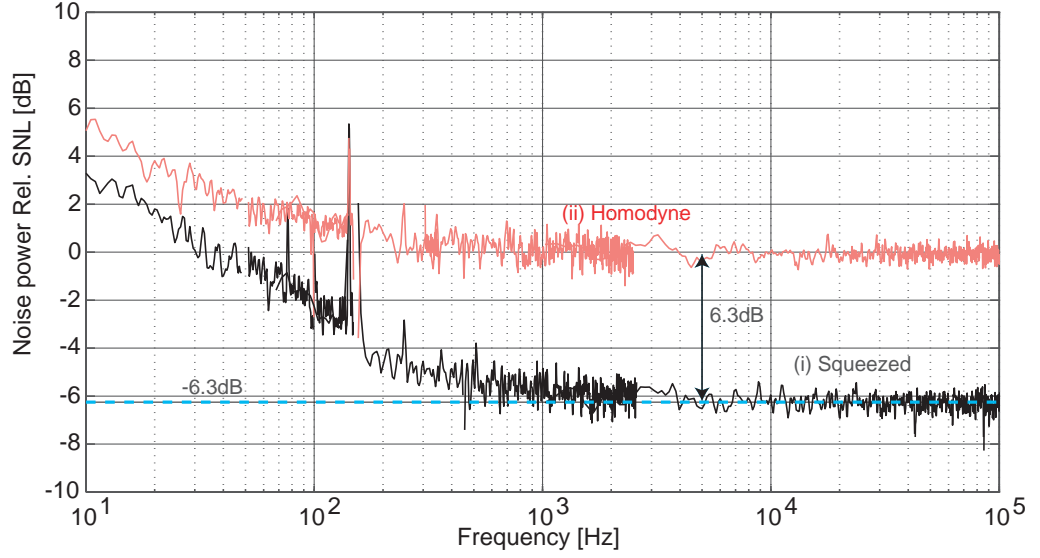


**Figure 7.4:** Measured noise spectra for: (i) the squeezed state; (ii) the homodyne detection noise limit; (iii) the calculated shot noise limit; and (iv) the electronic noise of the detection system. The curves are pieced together from three FFT frequency windows 100kHz-1.024kHz, 3.2kHz-160Hz, and 200Hz-10Hz. The RBW of the three windows was 128Hz, 4Hz, and 1/2Hz, respectively.

(iii), have been averaged 10 times. The locked squeezed curves is an average of  $5.4(\pm 0.2)$ dB below the shot noise limit. Curve (iv) shows the noise power of the squeezed state as the detection phase was varied. This shows that the anti-squeezed quadrature is approximately 14dB above the shot noise limit, and the squeezed quadrature at  $6.2(\pm 0.5)$ dB below the shot noise limit. The difference between the magnitude of the squeezed quadrature in the locked and unlocked curves may be due to phase noise added to the system when using quantum noise locking, or statistical variation.

With the electronic noise floor subtracted from all of the curves, the measured magnitude of squeezing can be compared with that expected from the nonlinear gain and the total detection efficiency. The measured squeezing (taken from the locked data) and calculated values are

$$6.5 \pm 0.2\text{dB}, \quad (\text{Measured}) \quad (7.1)$$

$$7.3 \pm 0.4\text{dB}, \quad (\text{Calculated}) \quad (7.2)$$

where the calculated value was obtained from equation 6.1. The difference in these values could be explained by an either an extra 3% loss. or by an rms phase jitter in the detection phase of 0.035 radians, which couples a fraction of the anti-squeezed quadrature noise into the measurement [20]. The measured and calculated (equation 6.3) squeezed state purity was

$$V_{sqz}V_{asqz} = 5.6 \pm 0.3, \quad (\text{Measured}) \quad (7.3)$$

$$V_{sqz}V_{asqz} = 4.7 \pm 0.3. \quad (\text{Calculated}) \quad (7.4)$$

The squeezing at the output of the OPO can be inferred by taking into account the photodetection and homodyne efficiencies and optics loss. The inferred magnitude of the squeezing out of the OPO is of interest when modeling the squeezing enhancement of interferometers, such as in

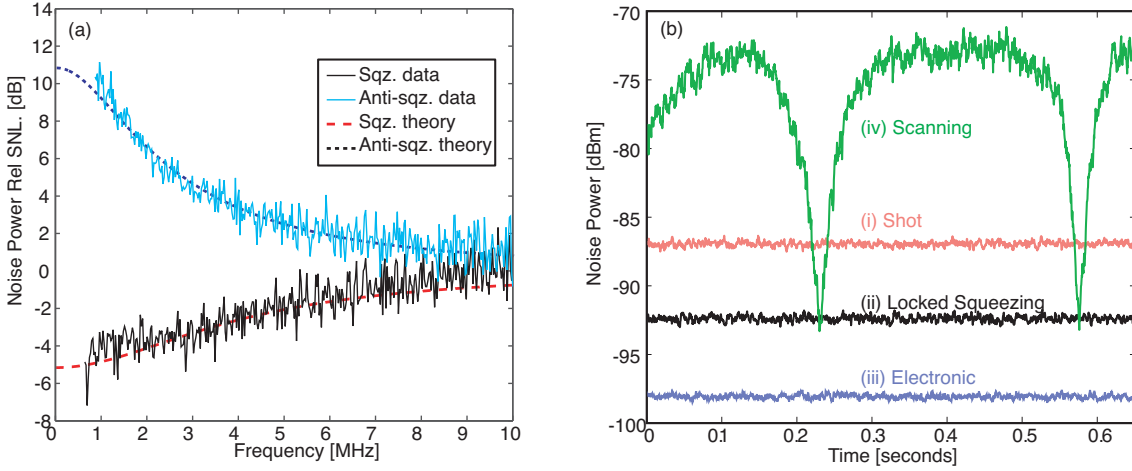


**Figure 7.5:** (a) The frequency dependence of the squeezed and anti-squeezed quadratures from the OPO. This shows the reduction of squeezing and anti-squeezing amplitude outside the cavity linewidth. Also shown are theory curves with parametric gain of 12dB, and total detection efficiency of  $\eta_{tot} = 0.74$ . Experimental parameters:  $\eta_{hom} = 0.89$ , RBW = 100kHz, VBW = 1kHz. (b) The time domain measurement taken at 100kHz of: (i) the shot noise limit, (ii) the squeezed state with detection phase locked, (iii) the electronic noise of the detection system, and (iv) the squeezed state with the detection phase varied. RBW=1kHz, VBW=30Hz.

chapter 8, since this is the value that would be injected into the interferometer and the losses of the interferometer and detection can be taken into account explicitly. The inferred squeezing out of the OPO cavity can be found from

$$V_{inf} = \frac{V_{meas} + \eta_{opt}\eta_{hom}\eta_{det} - 1}{\eta_{opt}\eta_{hom}\eta_{det}}, \quad (7.5)$$

$$= 9.2(\pm 0.4)\text{dB}, \quad (7.6)$$

where  $V_{meas}$  is the measured squeezing level (with electronic noise subtracted).

The long term stability of the production of squeezing is crucial for application to gravitational wave detectors. Squeezing data taken over 34 minutes is shown in figure 7.6 to demonstrate the stability of the experiment. The data was taken at 100kHz. The average noise power level was  $5.5(\pm 0.2)\text{dB}$  below the shot noise floor (curve (i)) over this time, not taking into account data at the 18 minute mark, where the PZT used to lock the detection phase ran out of range, requiring re-locking to an adjacent fringe. The OPO cavity, and all degrees of freedom except the detection phase, maintained lock for many hours at a time. Although only a quarter of an hour of continuous measurement was obtained, the squeezing magnitude was consistent. It is thought that an actuator with larger range and/or a more accurately temperature controlled environment would yield lock times on the order of many hours.

## 7.5 Limits to balanced homodyne detection at low frequencies

The low frequency measurements of squeezing in this thesis were impeded by excess noise in the homodyne detection system. This excess noise can be seen at the low frequency end of the spectra in figures 7.3 and 7.4. In this section seven potential candidates of the excess noise are discussed

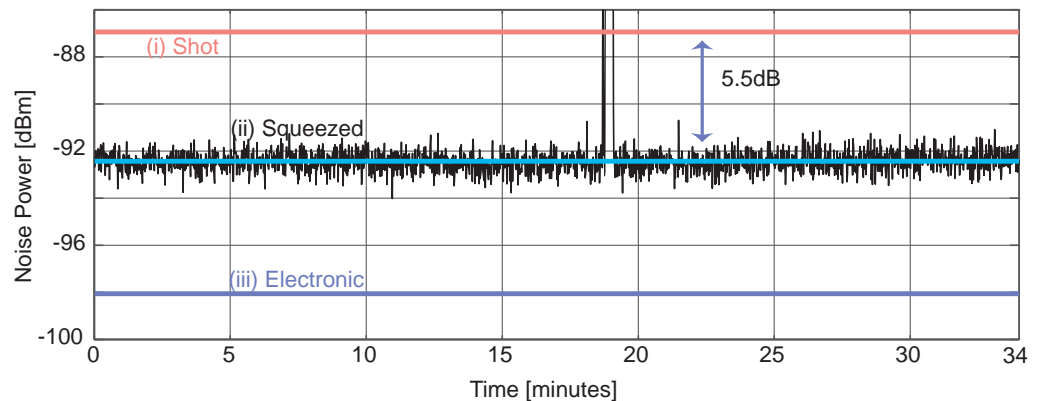


**Figure 7.6:** Measurement of squeezing at 100kHz, curve (ii), as a function of time. Also shown: (i) the average value of the shot noise and (iii) the average value of the electronic noise. RBW = 10kHz, VBW = 30Hz.

in an attempt to understand the mechanisms responsible. The candidates for excess noise are:

1. Local oscillator intensity noise
2. Beam jitter noise
3. Photodetector electronic noise
4. Scattered light
5.  $1/f$  photodiode noise
6. Temperature noise of the photodiode
7. Non-stationary noise

### 7.5.1 Balanced homodyne detector noise budget

The contribution of some of the noise sources in the above list to the homodyne detection spectra could be measured directly or inferred. Figure 7.7 shows the inferred contribution of three noise sources: curve (i) is derived from the local oscillator intensity noise; curve (ii) from beam jitter noise; and curve (iii) from electronic noise of the homodyne detection system. Also shown is the measured homodyne spectrum, curve (iv), and the sum of the local oscillator intensity noise, electronic noise, beam jitter noise and shot noise, curve (v), which is labeled ‘total’.

The total noise curve is significantly lower than the measured spectrum at frequencies below 100Hz. This indicates the three noise sources included in the noise budget are not sufficient to explain the measured spectrum. Thus, an additional noise source, or noise sources, need to be taken into account to understand the measured spectrum fully. In the following sections we detail each noise source, starting with the three that could be quantified.

#### 1. Local oscillator intensity noise

The balanced homodyne detector delivers immunity to local oscillator intensity noise to the level of the common mode rejection. The local oscillator intensity noise and common mode rejection

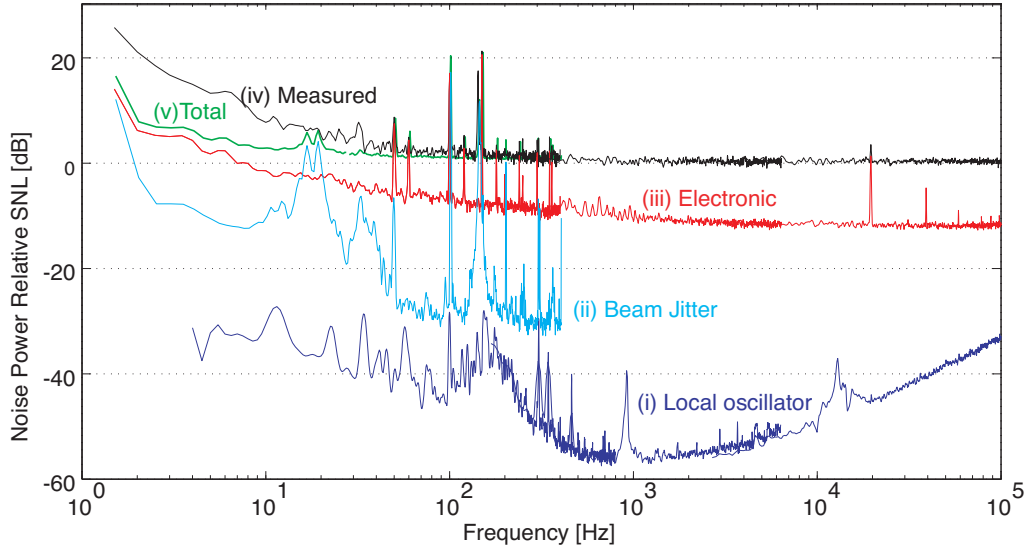


**Figure 7.7:** An incomplete noise budget for the homodyne detector. Shown are contributions due to: (i) local oscillator intensity noise, (ii) beam jitter noise, (iii) photodetector electronic noise, and (iv) the measured homodyne spectrum. The ‘total’ noise, curve (v), is the quadrature sum of curves (i), (ii), (iii) and the calculated shot noise.

were measured individually (see figures D.2 (a) and (b)) and their product was taken to give the local oscillator intensity noise curve in the noise budget. The intensity noise of the local oscillator field was measured by direct detection and found to be  $\sim 40$ dB above the SNL at 100Hz. The common mode rejection was found by measuring the transfer function of amplitude modulation from the local oscillator field to the homodyne photocurrent. With the variable electronic gain optimized we found up to 80dB of common mode rejection. This was sufficient to require no intensity noise stabilization.

## 2. Beam-jitter noise

Beam jitter of the local oscillator beam can couple into the photocurrent via spatial inhomogeneities of photodiode efficiency. Beam jitter is generally largest at low frequencies due to air currents and acousto-mechanical coupling. Spatial variations in the photodiode efficiency arise in the manufacturing process and also from dust particles that land on the diode or the protecting window [144]. The spatial variations in efficiency of silicon diodes have been previously measured to be between 0.1% rms [144] and 1.3% rms [145]. Up to a 1.5% deviation from peak sensitivity was measured and attributed to dust particles on the photodiode window [144].

The beam jitter curve plotted in figure 7.7 was found by measuring the beam jitter displacement spectrum,  $\Delta x(f)$ , on a quad-photodiode (see figure D.3 (a)) and inferring its contribution to the homodyne detector photocurrent. The beam jitter can be converted to equivalent relative intensity noise (RIN) by

$$\sqrt{RIN_{BJ}(f)} = A\Delta x(f), \quad (7.7)$$

where the coupling constant,  $A$ , has units 1/m, and  $\Delta x(f) = \sqrt{\Delta x_H(f)^2 + \Delta x_V(f)^2}$ , where  $\Delta x_H(f)$ , is the horizontal displacement spectrum and  $\Delta x_V(f)$  is the vertical displacement spectrum. The

constant  $A$  was found by fitting  $RIN_{BJ}$  to common features in the measured RIN of the photocurrent. This process was done with the laboratory air conditioning on, which increased the low frequency beam jitter, and gave rise to noise peaks in the homodyne photocurrent spectrum that could be matched to the beam jitter spectrum. For details see Appendix D.1.2.

### 3. Photodetector electronic noise

Photodetector electronic noise typically has the spectral properties of  $1/f$  noise at low frequencies due to the capacitive nature of PIN photodiodes and broadband Johnson noise. The electronic noise of the detection system came primarily from the photodetectors. It was largest at low frequencies, being 2dB below the calculated shot noise limit at 10Hz then rolling down to -12dB at 10kHz (for  $380\mu\text{W}$  local oscillator power). The peaks at 50Hz and harmonics were pickup from the mains. Below 100Hz electronic noise was a significant noise source, but as figures 7.4 and 7.7 demonstrate, not the major source of excess noise.

### 4. Scattered light

Recently Vahlbruch *et al.* [17] made a measurement of squeezing across the entire gravitational wave detection band and down to 1Hz, the current record for low frequency squeezing. Instrumental to this measurement was a homodyne detection system which was shot noise limited down to 1Hz. They determined that scattered light [71, 146] had been the limiting noise source in their balanced homodyne detection system below 100Hz in previous work [26]. Scattered light from beam dumps and dust on the optics was thought to contaminate the homodyne measurement by interfering with the local oscillator at the beamsplitter and the photodiode. Henning Vahlbruch suggested that, in their experiment, diffuse scattering from dust on the optics was the larger source of scattered light [147] and that the optics had to be cleaned extremely well to reduce the scatter. The frequency dependence of the scattered light noise source comes from movement of scattering centres at audio and sub-audio frequencies, due to thermal expansion, seismic motion and acoustic noise, thus creating modulation sidebands at these frequencies and higher harmonics [17].

Similar measures were applied to this experiment. All unused laser beams and reflections from AR coatings were carefully dumped. Lenses were tilted from normal incidence and optics were carefully cleaned. However, even with this considerable effort, no low frequency improvement in the noise spectrum was obtained. We were unable to verify if scattered light was a source of the excess low frequency noise seen in the homodyne spectrum.

### 5. $1/f$ Photodiode noise

$1/f$  photodiode noise [148] was thought to be a low frequency limit to a measurement near the shot noise of the laser intensity, in a laser stabilization experiment performed by Seifert *et al.* [149]. This noise scales proportional to the photocurrent [150], thus, if the electronic noise of the photodetector is measured (by blocking the incident light)  $1/f$  photodiode noise is not seen. Because the optical power detected, and therefore the photocurrent, in the experiment of Seifert *et al.* (110mW) was vastly different to that detected in this experiment ( $190\mu\text{W}$  per photodiode) we expect it to be insignificant in the measurements here.

### 6. Temperature noise of the photodiode

The quantum efficiency of photodiodes is temperature dependent. Thus photodiode temperature fluctuations results in photocurrent noise. A typical temperature dependence of InGaAs photodi-

odes is  $\Delta\eta_{det}=0.039\% / \text{K}$  [151]. Thus a temperature fluctuation of  $\Delta T \approx \frac{RIN_{SNL}}{\Delta\eta_{det}} \approx 10\mu\text{K}$  would result in photocurrent noise equivalent to shot noise. It is unknown if this was a limiting noise source in this experiment.

### 7. Non-stationarity of the photocurrent

The difference photocurrent behaved in a non-stationary manner, resulting in excess noise at low frequencies. A separate balanced homodyne experiment was setup to characterize the contribution of the non-stationary noise<sup>3</sup>. Non-stationary noise was not included in the noise budget as it does not have a spectral distribution in the traditional sense.

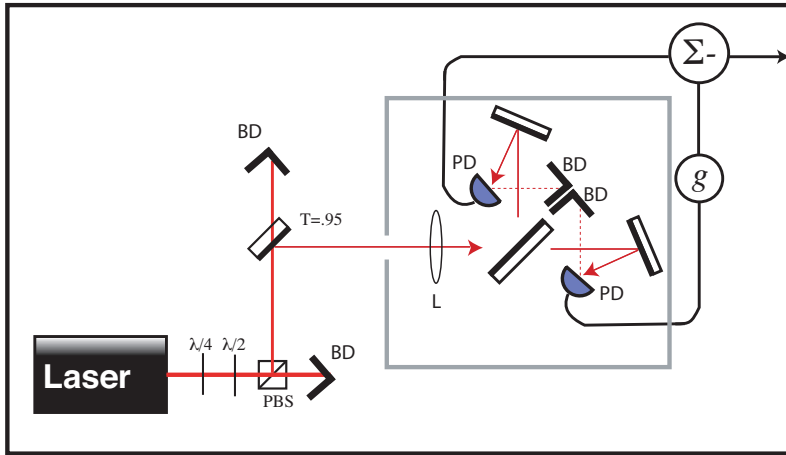


**Figure 7.8:** Schematic of the non-stationary noise characterisation experiment. PD - photodetector, BD - beam dump, L - lens

The mechanism driving the non stationarity of the photocurrent was thought to be dust particles passing through the beam path in the homodyne detector arms. This would scatter light out of the beams in the two arms in an uncorrelated manner, causing an impulse signal to the difference photocurrent.

A schematic of the experiment setup to characterize this noise is shown figure 7.8. The 300mW laser was attenuated to provide a local oscillator field with power of  $300\mu\text{W}$ . The homodyne detector was similar to that described in section 7.3 and beam dumps were used to minimize scattered light. The entire experiment was enclosed in a sealed black perspex box to reduce air currents and external stray light. A second, smaller black perspex box enclosed the homodyne detector to isolate it from scattered light from the beam-dumps.

To investigate if dust was a cause of non-stationary noise two sets of measurements of the homodyne photocurrent were taken and compared. Measurements were taken with the lids of the boxes open so the experiment was exposed to the laboratory environment. These were compared with measurements taken with the boxes closed and then left for two days so that the dust in the air could settle. The non-stationary events that occurred in the ‘open’ experiment did not occur in the ‘closed’ experiment. The spectra from the measurements are shown in figure 7.9. Both spectra

<sup>3</sup>The author would like to acknowledge Sheon Chua who took the experimental results in this section as part of his Honours thesis [152].

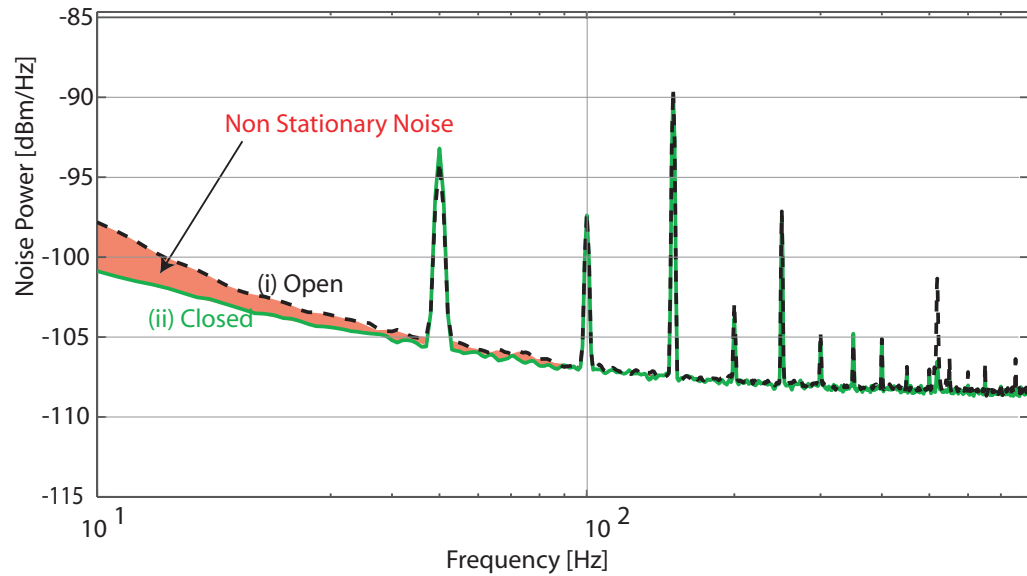


**Figure 7.9:** Spectra from the balanced homodyne with the experiment; (i) open to the laboratory environment; and (ii) sealed in a black perspex box. The large peaks at 50Hz and harmonics were due to pick-up of the mains power.

are the average of 100 curves, each with 20 rms averages. The noise floor of the open and closed measurements have the same noise power at frequencies above 100Hz, but below 100Hz the open measurement shows excess noise, thought to be due to non-stationary events. The excess noise is largest at 10Hz and reduces at frequencies approaching 100Hz. Note that, in the closed experiment spectra, a low frequency roll-up is still present, indicating that the non-stationary noise is not the only excess noise source.

To show the non-stationary nature of the photocurrent in the experiment open to the laboratory environment, data from the spectra in figure 7.9 were plotted as the histograms, shown in figure 7.10 (a) and (b). Each count in the histograms is the noise power of one frequency bin. The data is made up from 30 different, 1Hz wide frequency bins from 60-90Hz, for the 100 different curves, resulting in 3000 data points in each histogram. If the photocurrent were stationary, the histogram would be expected to follow a Gamma distribution. The histograms for the open and closed experiments have a Gamma distribution probability density function fitted to them using a Matlab [153] distribution fitting tool. A Gamma distribution is expected because the noise power of a gaussian photocurrent is a Rayleigh squared distribution [154], and a sum of independent Rayleigh squared distributions (taken in the rms averaging process) is a Gamma distribution [155].

The fit of the closed experiment appears to be better than the open experiment. The closed experiment had smaller standard deviation,  $\sigma_C = 5.3\text{pW}$ , than the open experiment, which had  $\sigma_O = 6.4\text{pW}$ . The closed experiment also had a lower mean power of 22.2pW than the open experiment, which had 24.1pW. One clear point of difference in the two histograms is the number of counts at bin powers above 50pW (shown by the inset in figures 7.10 (a) and (b)): 0 counts in the closed experiment versus 26 counts in the open experiment. The large number of counts at high bin power in the open experiment is an indication of non-stationary noise.

To quantify the excess of counts at high bin power, the percentage of the counts in the wings of the distribution can be compared to the value expected from the probability density function of the Gamma distribution. We chose a value at a noise power of mean +  $4\sigma$  and compare this

to the expected value of 0.1%. In the closed experiment there were 6 counts (0.2%) above the  $\text{mean}_C + 4\sigma_C$  (43pW) compared to 28 counts (0.9%) above the  $\text{mean}_O + 4\sigma_O$  (49pW) in the open experiment.

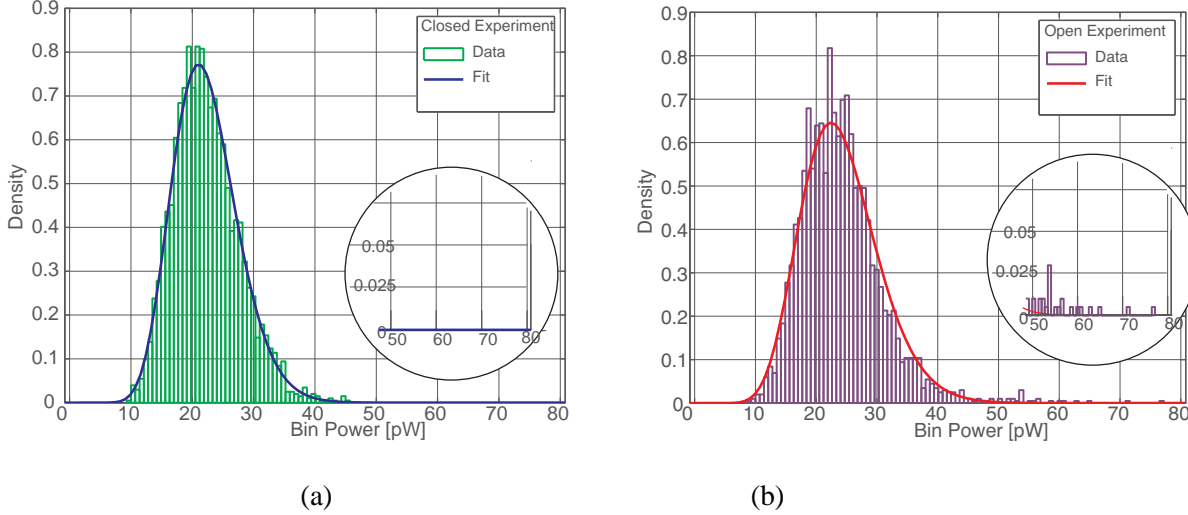


**Figure 7.10:** Histograms of the homodyne photocurrent with the experiment (a) closed to the laboratory environment and (b) open to the laboratory environment. The insets are a zoomed look at the histogram at high bin power.

### 7.5.2 Discussion of candidates for the low frequency excess noise

Noise from the local oscillator intensity, photodetector electronics, and beam jitter are insufficient to explain the measured low frequency roll-up of the homodyne photocurrent. We expect that non-stationary noise is likely to partly reconcile the difference between the ‘measured’ and ‘total’ noise spectra in the homodyne noise budget presented in figure 7.7. However, with non-stationary noise removed (c.f. figure 7.9), the photocurrent spectra still showed excess noise at low frequency. At least one additional noise source must therefore be present.

From the experiment performed by Vahlbruch *et al.*, it seems likely that scattered light is the excess noise source. Without further research,  $1/f$  photodiode noise and photodiode temperature noise can not be excluded as limiting noise sources.

## 7.6 Chapter summary

In this chapter we detailed an experiment designed to produce stable low frequency squeezing. Quantum noise suppression down to sideband frequencies of 70Hz was measured with up to  $5.5(\pm 0.2)$ dB of locked suppression at higher frequencies. The stability of the experiment was demonstrated by a measurement of squeezing over a 30 minute period. The limit to the low frequency measurement of squeezing was attributed to excess noise in the homodyne detection system. Measurements of different noise sources in the homodyne detection system were carried out, including electronic, beam jitter, local oscillator intensity, and non-stationary noise. Of these measured noise sources, electronic noise and non-stationary noise were responsible for a significant component of the excess noise. We speculate that scattered light was responsible for the remaining excess noise, as Vahlbruch *et al.* found to be the case in a similar system.

---

# Squeezing in second generation gravitational wave detectors

---

In this chapter a short theoretical investigation is undertaken into sensitivity enhancements to the Advanced LIGO detector with the injection of squeezed states. Current best estimates of the interferometer classical noise sources are used, obtained from the interferometer noise modeling program Bench 6.2 [1]. Quantum noise of the interferometer is then calculated, including the expected optical losses in the interferometer and photodetection process.

## 8.1 Introduction

In chapter 4 squeezing enhanced gravitational wave interferometer configurations were introduced. An idealised case was considered, where the losses in the interferometer and the detection process were neglected. Furthermore, the interferometers classical noise sources, which we labeled hardware and facility noise were neglected (see section 2.4.1). With such assumptions, a squeezed state with optimal frequency dependence was shown to improve the quantum noise limited strain sensitivity by  $e^{-R}$ .

In this chapter, a more realistic case is considered. An investigation into the sensitivity enhancements that could be made to a second generation interferometric detector with the injection of squeezed states is presented. Specifically, possible squeezing enhancements to Advanced LIGO are considered quantitatively<sup>1</sup>. Included in the investigation are: the hardware and facility noise sources; losses in the interferometer; and losses in the photodetection process.

A similar type of study has been performed by Buonanno and Chen in reference [40]. They calculated improvements in the signal to noise ratio of specific gravitational wave sources using squeezed states and a frequency dependent readout scheme, with the combination of the two called the ‘fully optimal’ scheme. They included two estimates of coating thermal noise: the coating thermal noise expected in Advanced LIGO, similar to that used here; and coating thermal noise using ‘mesa beams’ [156], instead of TEM<sub>00</sub> Gaussian beams, in the arm cavities. The use of mesa beams offers lower coating thermal noise, but requires an upgrade of Advanced LIGOs mirrors to ‘Mexican hat’ shaped mirrors.

Here we analyze the improvement to strain sensitivity that can be made using only squeezed states (i.e. we don’t consider a frequency dependent readout scheme or Buonanno and Chen’s fully optimal scheme [40]). Two operating conditions of Advanced LIGO are considered: the ‘wideband’ configuration [157], where a high input laser power is used and a signal recycling

---

<sup>1</sup>Similar analysis would be interesting for the other next generation detectors: Advanced VIRGO [56], GEO HF [66], and LCGT [67].

cavity detuning is chosen to give good broadband sensitivity; and the ‘narrowband’ configuration, where a low input laser power is used and the signal recycling cavity detuning is set to optimize low frequency sensitivity.

We start by writing down the total strain equivalent noise of the interferometer,  $h_{tot}(\Omega)$ , which is given by the quadrature sum of the strain equivalent hardware and facility noise,  $h_{hf}(\Omega)$ , and the strain equivalent quantum noise,  $h_{qn}(\Omega)$ . That is

$$h_{tot}(\Omega) = \sqrt{h_{hf}^2(\Omega) + h_{qn}^2(\Omega)}. \quad (8.1)$$

Both  $h_{hf}(\Omega)$  and  $h_{qn}(\Omega)$  will be defined shortly. The methodology of the investigation is to consider the improvements to  $h_{tot}(\Omega)$  by modifying  $h_{qn}(\Omega)$  with the injection of squeezed states.

In section 8.2 models of the hardware and facility noise and the quantum noise are presented. In section 8.3 we present results showing squeezing enhancements. We consider improvements to the total noise with different squeezing magnitudes and different optical losses. Also considered is the use of squeezed states with an intermediate input laser power. In section 8.4 we discuss the parameters used in the models.

## 8.2 Models for noise

### 8.2.1 Hardware and facility noise

The hardware and facility noise is the quadrature sum of all the noise sources presented in section 2.4.1, except the quantum noise component. The strain equivalent noise of the hardware and facility sources is given by

$$h_{hf}(\Omega) = \frac{\sqrt{x_s^2(\Omega) + x_{gg}^2(\Omega) + x_{rg}^2(\Omega) + x_{st}^2(\Omega) + x_{mt}^2(\Omega)}}{L}, \quad (8.2)$$

where  $L$  is the interferometer arm length. The displacement noise sources are:  $x_s(\Omega)$  from seismic origin;  $x_{gg}(\Omega)$  from gravity gradient;  $x_{rg}(\Omega)$  from residual gas;  $x_{st}(\Omega)$  from suspension thermal; and  $x_{mt}(\Omega)$  from mirror thermal. These displacement noise sources were calculated using Bench 6.2.

### 8.2.2 Quantum noise

The quantum noise of the signal-recycled Michelson interferometer including losses is similar to the lossless case (equation 4.13). Included are losses in the arm cavities, signal recycling cavity, and the photodetection process. These are shown schematically in figure 8.1. The parameters used to represent the losses are:

- $\mathcal{L}_{ac}$ , which is the round trip loss in an arm cavity. The model assumes quantum noise from this loss enters from the end test mass mirror. In the below equations,  $\mathcal{L}_{ac}$  is contained in the parameter  $\varepsilon = 2\mathcal{L}_{ac}/T$ , where  $T$  is the transmission of the input cavity mirror.
- $\lambda_{SR}$ , which is the loss parameter for the signal recycling cavity. The model assumes that all of the loss, including beamsplitter loss, is all located on the signal recycling mirror.
- $\lambda_{PD}$ , which is the loss parameter for the photodetection process.

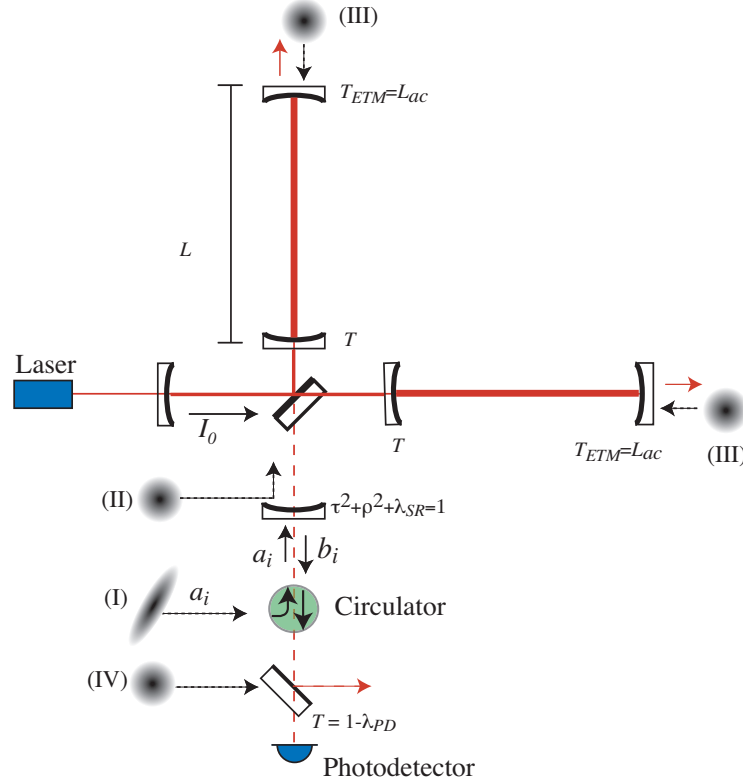


**Figure 8.1:** Layout of the Advanced LIGO detector with squeezing injection. Also shown is the sources of quantum noise considered in the model. They are labeled: (I) from the dark port, which is either a vacuum state or a squeezed state; (II) vacuum noise due to loss on the signal recycling mirror; (III) vacuum noise due to loss in the arm cavities; and (IV) vacuum noise due to photodetector loss.

The quantum noise spectral density with optical losses is derived in section V of reference [117]. We do not re-derive this here, as it is not the focus of the investigation. The quantum noise limited strain is given by the square root of the spectral density (equation 5.13 in [117])

$$h_{qn}(\Omega) = \sqrt{S_L^\zeta}, \quad (8.3)$$

where

$$S_L^\zeta = \frac{(h_{SQL}^\zeta)^2}{2\mathcal{K}_c\tau^2|D_1^L \sin \zeta + D_2^L \cos \zeta|^2} \times \left[ \underbrace{|C_{11}^L \sin \zeta + C_{21}^L \cos \zeta|^2 + |C_{12}^L \sin \zeta + C_{22}^L \cos \zeta|^2}_{(I)} + \underbrace{|P_{11} \sin \zeta + P_{21} \cos \zeta|^2 + |P_{12} \sin \zeta + P_{22} \cos \zeta|^2}_{(II)} + \underbrace{|N_{11} \sin \zeta + N_{21} \cos \zeta|^2 + |N_{12} \sin \zeta + N_{22} \cos \zeta|^2}_{(III)} + \underbrace{|Q_{11} \sin \zeta + Q_{21} \cos \zeta|^2 + |Q_{12} \sin \zeta + Q_{22} \cos \zeta|^2}_{(IV)} \right], \quad (8.4)$$

where the parameters  $\mathcal{K}_c$  and  $h_{SQL}^c$  and are given by equations 4.10 and 4.12 respectively and interferometer parameters are summarized in table 8.1. Note that the phase gained by the sidebands in the signal recycling cavity has been set to zero ( $\Phi = 0$ ). In equation 8.4, terms of similar origin have been grouped together. These are: (I) due to the quantum fluctuations that enter the dark port of the interferometer; (II) due to losses in the signal recycling cavity; (III) due to losses in Fabry-Perot arm cavities; and (IV) due to losses in the photodetection process. These noise sources are also labeled in figure 8.1.

Coefficients in equation 8.4 denoted by capital letters:  $C_{ij}^L, D_{ij}^L, P_{ij}, N_{ij}$ , and  $Q_{ij}$  are given by equations 5.8 to 5.12 in reference [117]. The terms in the denominator of equation 8.4 are

$$D_1^L = \sqrt{1 - \lambda_{PD}} \left\{ -(1 + \rho e^{2i\beta}) \sin \phi + \frac{\epsilon}{4} [3 + \rho + 2\rho e^{4i\beta} + e^{2i\beta}(1 + 5\rho)] \sin \phi + \frac{\lambda_{SR}}{2} e^{2i\beta} \rho \sin \phi \right\}, \quad (8.5)$$

$$D_2^L = \sqrt{1 - \lambda_{PD}} \left\{ (1 - \rho e^{2i\beta}) \cos \phi + \frac{\epsilon}{4} [-3 + \rho + 2\rho e^{4i\beta} - e^{2i\beta}(1 - 5\rho)] \cos \phi + \frac{\lambda_{SR}}{2} e^{2i\beta} \rho \cos \phi \right\}. \quad (8.6)$$

The coefficients for the quantum noise that enters the dark port are

$$C_{11}^L = C_{22}^L = \sqrt{1 - \lambda_{PD}} \left\{ (1 + \rho^2) \left( \cos 2\phi + \frac{\mathcal{K}_c}{2} \sin 2\phi \right) - 2\rho \cos 2\beta - \frac{1}{4} \epsilon [-2(1 + e^{2i\beta})^2 \rho + 4(1 + \rho^2) \cos^2 \beta \cos 2\phi + (3 + e^{i2\beta}) \mathcal{K}_c (1 + \rho^2) \sin 2\phi] + \lambda_{SR} \left[ e^{2i\beta} \rho - \frac{1}{2} (1 + \rho^2) \left( \cos 2\phi + \frac{\mathcal{K}_c}{2} \sin 2\phi \right) \right] \right\}, \quad (8.7)$$

$$C_{12}^L = \sqrt{1 - \lambda_{PD}} \tau^2 \left( -(\sin 2\phi + \mathcal{K}_c \sin^2 \phi) + \frac{1}{2} \epsilon \sin \phi [(3 + e^{2i\beta}) \mathcal{K}_c \sin \phi + 4 \cos^2 \beta \cos \phi] + \frac{1}{2} \lambda_{SR} (\sin 2\phi + \mathcal{K}_c \sin^2 \phi) \right), \quad (8.8)$$

$$C_{21}^L = \sqrt{1 - \lambda_{PD}} \tau^2 \left( (\sin 2\phi - \mathcal{K}_c \sin^2 \phi) + \frac{1}{2} \epsilon \cos \phi [(3 + e^{2i\beta}) \mathcal{K}_c \cos \phi - 4 \cos^2 \beta \sin \phi] + \frac{1}{2} \lambda_{SR} (-\sin 2\phi + \mathcal{K}_c \cos^2 \phi) \right). \quad (8.9)$$

Coefficients for the vacuum fluctuation that enter the signal recycled cavity due to loss are

$$P_{11} = P_{22} = \frac{1}{2} \sqrt{1 - \lambda_{PD}} \sqrt{\lambda_{SR}} \tau (-2\rho e^{2i\beta} + 2 \cos 2\phi + \mathcal{K}_c \sin 2\phi), \quad (8.10)$$

$$P_{12} = -\sqrt{1 - \lambda_{PD}} \sqrt{\lambda_{SR}} \tau \sin \phi (2 \cos \phi + \mathcal{K}_c \sin \phi), \quad (8.11)$$

$$P_{21} = \sqrt{1 - \lambda_{PD}} \sqrt{\lambda_{SR}} \tau \cos \phi (2 \sin \phi - \mathcal{K}_c \cos \phi). \quad (8.12)$$

Coefficients for the vacuum fluctuation that enter the arm cavities due to loss are

$$N_{11} = \sqrt{1 - \lambda_{PD}} \sqrt{\frac{\epsilon}{2}} \tau (\mathcal{K}_c (1 + \rho e^{2i\beta}) \sin \phi + 2 \cos \beta [e^{-i\beta} \cos \phi - \rho e^{i\beta} (\cos \phi + \mathcal{K}_c \sin \phi)]), \quad (8.13)$$

$$N_{22} = -\sqrt{1 - \lambda_{PD}} \sqrt{2\epsilon} \tau (-e^{-i\beta} + \rho e^{i\beta}) \cos \beta \cos \phi, \quad (8.14)$$

$$N_{12} = -\sqrt{1-\lambda_{PD}}\sqrt{2\varepsilon\tau}(e^{-i\beta} + \rho e^{i\beta})\cos\beta\sin\phi, \quad (8.15)$$

$$N_{21} = \sqrt{1-\lambda_{PD}}\sqrt{\frac{\varepsilon}{2}}\tau(-\mathcal{K}_c(1+\rho)\cos\phi + 2\cos\beta(e^{-i\beta} + \rho e^{i\beta})\cos\beta\sin\phi). \quad (8.16)$$

Finally, coefficients for the vacuum fluctuation that enter at the photodetector due to imperfect detection efficiency are

$$\begin{aligned} Q_{11} = Q_{22} = & \sqrt{\lambda_{PD}}\left\{e^{-2i\beta} + \rho^2 e^{2i\beta} - \rho(2\cos 2\phi + \mathcal{K}_c \sin 2\phi) + \frac{\varepsilon}{2}\rho[e^{-2i\beta}\cos 2\phi \right. \\ & + e^{2i\beta}(-2\rho - 2\rho\cos 2\beta + \cos 2\phi + \mathcal{K}_c \sin 2\phi) + 2\cos 2\phi + 3\mathcal{K}_c \sin 2\phi] \\ & \left. - \frac{\lambda_{SR}}{2}\rho(2\rho e^{2i\beta} - 2\cos 2\phi - \mathcal{K}_c \sin 2\phi)\right\}, \end{aligned} \quad (8.17)$$

$$Q_{12} = Q_{21} = 0. \quad (8.18)$$

The spectral density of quantum noise with squeezing can be derived as it was in section 4.3.2. The quantum noise with squeeze parameter  $R$  and angle  $\lambda$  is given by

$$\begin{aligned} S_{hsQZ}^{\zeta} = & \mathcal{D}\left[e^{-2R}|C_{11}^{L[\lambda]}\sin\zeta + C_{21}^{L[\lambda]}\cos\zeta|^2 + e^{2R}|C_{12}^{L[\lambda]}\sin\zeta + C_{22}^{L[\lambda]}\cos\zeta|^2 + \right. \\ & |P_{11}\sin\zeta + P_{21}\cos\zeta|^2 + |P_{12}\sin\zeta + P_{22}\cos\zeta|^2 + |N_{11}\sin\zeta + N_{21}\cos\zeta|^2 + \\ & \left. |N_{12}\sin\zeta + N_{22}\cos\zeta|^2 + |Q_{11}\sin\zeta + Q_{21}\cos\zeta|^2 + |Q_{12}\sin\zeta + Q_{22}\cos\zeta|^2\right], \end{aligned} \quad (8.19)$$

with

$$\mathcal{D} = \frac{(h_{sQL}^{\zeta})^2}{2\mathcal{K}_c\tau^2|D_1^L\sin\zeta + D_2^L\cos\zeta|^2}, \quad (8.20)$$

and

$$C_{11}^{L[\lambda]} = C_{11}^{(L)}\cos\lambda + C_{12}^{(L)}\sin\lambda, \quad (8.21)$$

$$C_{12}^{L[\lambda]} = C_{12}^{(L)}\cos\lambda - C_{11}^{(L)}\sin\lambda, \quad (8.22)$$

$$C_{21}^{L[\lambda]} = C_{21}^{(L)}\cos\lambda + C_{22}^{(L)}\sin\lambda, \quad (8.23)$$

$$C_{22}^{L[\lambda]} = C_{22}^{(L)}\cos\lambda - C_{21}^{(L)}\sin\lambda. \quad (8.24)$$

With optimal frequency dependence, equation 8.19 reduces to

$$\begin{aligned} S_L^{\zeta}|_{OPT} = & \mathcal{D}\left[ (|C_{11}^L\sin\zeta + C_{21}^L\cos\zeta|^2 + |C_{12}^L\sin\zeta + C_{22}^L\cos\zeta|^2)e^{-2R} + \right. \\ & |P_{11}\sin\zeta + P_{21}\cos\zeta|^2 + |P_{12}\sin\zeta + P_{22}\cos\zeta|^2 + |N_{11}\sin\zeta + N_{21}\cos\zeta|^2 + \\ & \left. |N_{12}\sin\zeta + N_{22}\cos\zeta|^2 + |Q_{11}\sin\zeta + Q_{21}\cos\zeta|^2 + |Q_{12}\sin\zeta + Q_{22}\cos\zeta|^2 \right], \end{aligned} \quad (8.25)$$

### 8.3 Results

The hardware and facility noise,  $h_{hf}(\Omega)$ , is the dotted line in figure 8.2 (a) and (b), plotted using values from Bench 6.2. The quantum noise,  $h_{qn}(\Omega)$ , and total noise,  $h_{tot}(\Omega)$ , are shown in figures 8.2 (a) for the ‘wideband’ and in (b) the ‘narrowband’ operations of Advanced LIGO respectively. Without squeezed input the quantum noise and total noise are given by  $h_{qn}$  and  $h_{tot}$  labeled ‘No Sqz’. The parameters used in this calculation were taken from Bench 6.2. A summary of the interferometer parameters that relate to the quantum noise are given in table 8.1. The

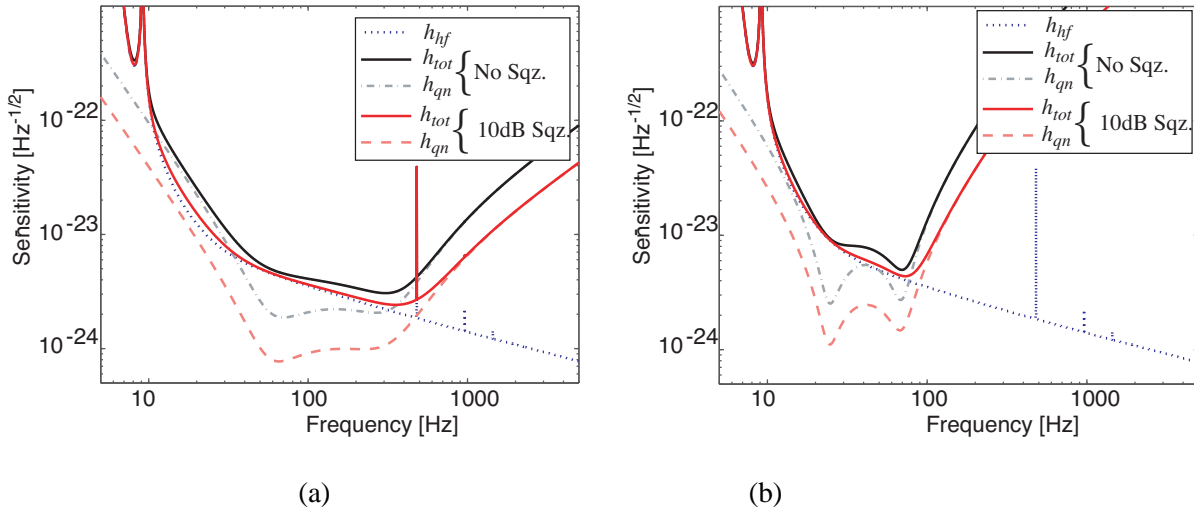


**Figure 8.2:** The hardware and facility noise,  $h_{hf}$ , the quantum noise,  $h_{qn}$ , and the total noise,  $h_{tot}$ , for the unsqueezed case (No Sqz.) and with squeezed input of  $e^{-2R} = 0.1$ ,  $\lambda = \lambda_{opt}$  (10dB Sqz.). The parameters used are those expected for Advanced LIGO. (a) Shows Advanced LIGO ‘wideband’ operation and (b) narrowband operation.

wideband and narrowband operations differ in two parameters only: the input laser power and the signal recycling cavity detuning. Wideband operation uses high input laser power of 125W and a signal recycling cavity detuning of  $\phi = \pi/2 - 0.04$ , set to optimize the broadband response. The narrowband operation is set to optimize low frequency sensitivity. This is done using a lower input laser power of 5W (to reduce radiation pressure noise) and a detuning of  $\phi = \pi/2 - 0.2$ . Figure 8.2 also shows quantum and total noise curves with squeezed state injection. The squeezing injected has optimal frequency dependence ( $\lambda = \lambda_{opt}$ ), 10dB magnitude ( $e^{-2R} = 0.1$ ), and is labeled ‘10dB Sqz’. The total noise in both the wideband and narrowband operation is reduced significantly with the squeezed input. The gains are most significant where the quantum noise is a substantial contributor to the total noise curve. With squeezed input, both the wideband and narrowband operations become dominated by hardware and facility noise below the signal recycling cavity optical resonance.

The proportion of quantum noise to total noise, the ratio ( $h_{qn}^2(\Omega)/h_{tot}^2(\Omega)$ ), is plotted in figure 8.3 for both the unsqueezed case (solid line) and squeezed case (dashed line). In the wideband case, figure 8.3 (a), the quantum noise improvement with squeeze input is particularly substantial between 10Hz and 30Hz, where the proportion of quantum noise reduces from a maximum of 80% to less than 40%. The integrated proportion of quantum noise between the sideband frequencies of  $\Omega/2\pi = 5\text{Hz}$  and 1kHz was 47.8% of the total noise for the unsqueezed wideband case and 24.0% of the total noise for the squeezed wideband case. For the narrowband case, between  $\Omega/2\pi = 5\text{Hz}$

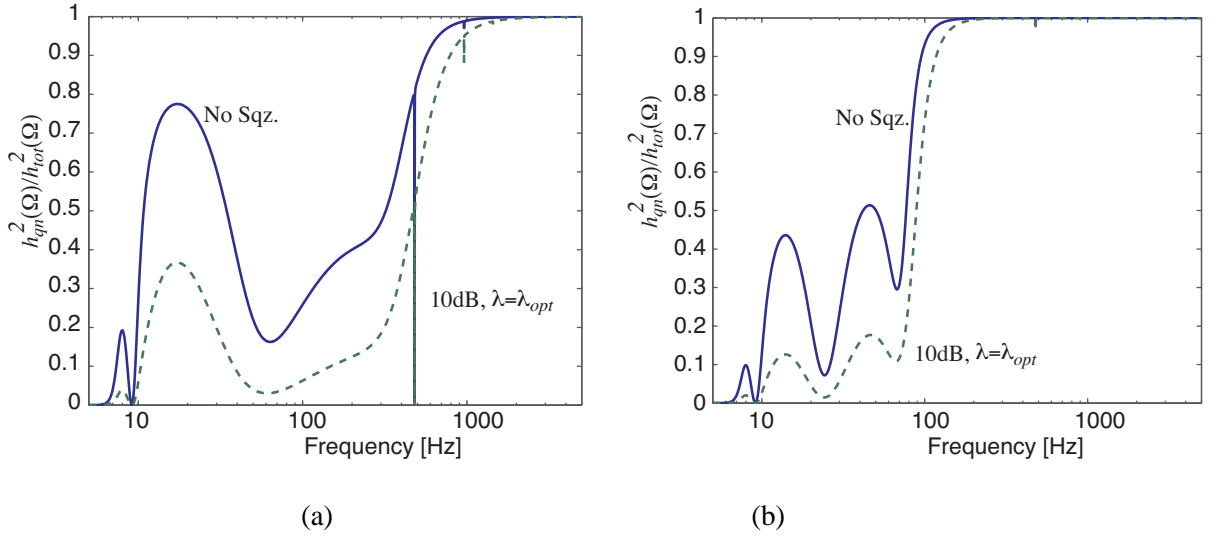


**Figure 8.3:** The proportion of quantum noise in the total noise for the Advanced LIGO configuration with unsqueezed input (No Sqz.) and squeezed input (10dB,  $\lambda = \lambda_{opt}$ ). (a) Shows is the Advanced LIGO wideband operation and (b) the narrowband operation.

and 100Hz, the proportion of quantum noise was 30.3% for the unsqueezed case and 11.1% with squeezed state injection.

A comparison of the sensitivities in figure 8.2 (a) and (b) shows that the low frequency sensitivity of the squeezed wideband interferometer is very similar to the (squeezed or unsqueezed) narrowband interferometer, however wideband operation retains and enhances the broadband sensitivity. Thus, if Advanced LIGO were to operate wideband with squeezed input, the narrowband operation would become redundant.

Only the wideband case is considered henceforth. Two parameters are varied: firstly, the amplitude of the squeezed input; and secondly, the optical losses in the interferometer and detection process. In figure 8.4 (a), the quantum noise and total noise curves are plotted for the frequency dependent squeezed inputs of: 6dB, 10dB, and 20dB. We see that the total noise curves for the three squeeze inputs are very similar below 300Hz, where the facility and hardware noise dominates the total noise. Above 300Hz, the total noise curves differ as the total noise curve is dominated by quantum noise. The difference between the quantum noise curves for the three squeeze magnitude is less than the difference in squeeze magnitude at the input, because the larger squeeze magnitude are more sensitive to loss.

Figure 8.4 (b) shows quantum and total noise curves for 10dB squeezed input for three different loss scenarios. The first case, labeled ‘Losses (a)’, the losses are those expected in Advanced LIGO, as described previously. In the second case, labeled ‘Losses (b)’, the losses are a more optimistic set of losses: the same arm cavity and signal recycling cavity losses, but a loss of 5% in photodetection instead of 10%. The final case, for comparison, is the ‘Lossless’ case, which has no losses in the interferometer or photodetection process. The total noise curves for the three different losses are similar below 300Hz, where the hardware and facility noise dominates, and differ most substantially above 300Hz.

For the final part of this investigation we examine a case with lower input laser power. We assume the input laser power is  $I_0 = 25\text{W}$ , one fifth of the baseline for Advanced LIGO. It is likely that

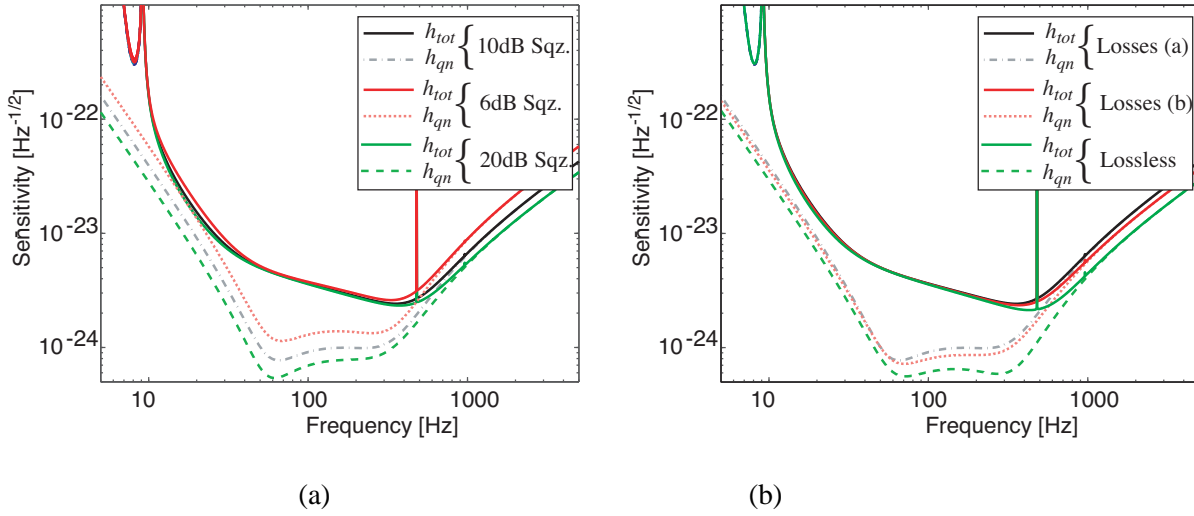


**Figure 8.4:** The squeezing enhancement of Advanced LIGO operated in wideband mode for: (a) different squeezed state amplitudes; and (b) different interferometer and detection losses.

the full baseline laser power will be available for Advanced LIGO, given the high laser power demonstrations from the Hannover University and Laser Zentrum Hannover [158]. However, difficulties associated with high circulating powers, such as thermal lensing [159] and parametric instabilities [160, 161], may initially prevent the use of full laser power. An input of  $I_0 = 25\text{W}$  is similar to that expected in Enhanced LIGO [162, 163]. Figure 8.5 shows baseline wideband Advanced LIGO and wideband Advanced LIGO with lower input laser power, with and without squeezed input. Above 50Hz, the total noise for the squeezed input with lower laser power is slightly higher than baseline wideband Advanced LIGO, whereas below 50Hz it is significantly lower. It seems that with lower input power and squeeze input, near baseline sensitivity can be retained in the mid to high sideband frequencies, and better sensitivity is obtained in the low sideband frequencies.

## 8.4 Discussion of assumptions and values

### 8.4.1 Squeezing magnitude and frequency dependence

In the above calculations a 10dB squeezed state input with the optimal frequency dependent squeezed quadrature has been assumed. A 10dB squeezed state magnitude seems realistic given 6 to 7dB of noise reduction is routinely measured at audio frequencies at 1064nm (see [17, 19] and the results in chapter 7), and up to 10dB has been measured at RF sideband frequencies [18]. Note that these measured squeezed state levels include the loss of at least 5% associated with non-unity quantum efficiency of the photodiode, so the squeezing magnitude before measurement is actually higher. It seems that less than 5% total injection loss should be achievable for Advanced LIGO. Kimble *et al.* [38] suggest that the loss could conceivably be as low as 0.1% each for the circulator and for the mode-matching. Fabry-Perot cavities used to apply a frequency dependent phase shift, as proposed by Kimble *et al.*, could also be made to have a similar level of loss if the filter cavities were to be long enough.

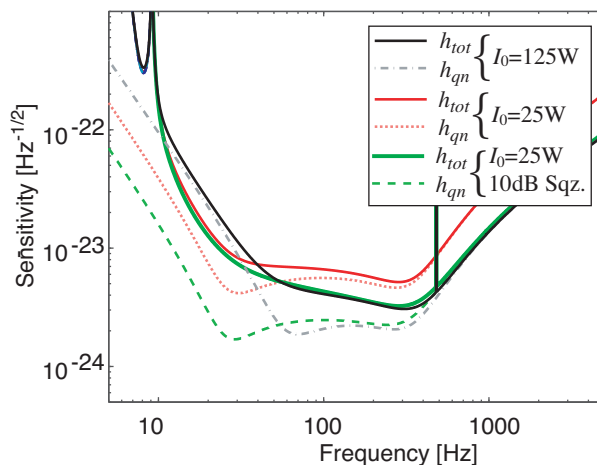


**Figure 8.5:** Quantum and total noise curves for wideband Advanced LIGO with baseline input laser power ( $I_0=125\text{W}$ ) and lower input power ( $I_0=25\text{W}$ ). Also shown is lower input laser power Advanced LIGO with squeezed input of 10dB, optimally frequency dependent squeezing ( $I_0=25\text{W}$ , 10dB).

### 8.4.2 Levels of optical losses in the interferometer and detection

In this investigation we have used the interferometer losses expected for Advanced LIGO. These numbers (recall that we assume  $\mathcal{L}_{PD} = 0.1$  for the photodetection process,  $\mathcal{L}_{SR} = 0.0035$  (per pass) in the SR cavity and  $\mathcal{L}_{AC} = 75 \times 10^{-6}$  (per round trip)) seem realistic and possibly conservative. Better than 90% detection efficiency is routinely achieved in quantum optics labs<sup>2</sup>. One difference that Advanced LIGO will have is an output modecleaner. In figure 8.4 (b), we also looked at the lower level of photodetector loss of 5%. This may be achievable for Advanced LIGO given that it can be achieved in benchtop experiments now.

### 8.4.3 Laser power

This short investigation has included two Advanced LIGO configurations - wideband and narrow-band and three laser powers. Wideband configuration assumes that full laser power can be used: resulting in arm cavity circulating power of  $\sim 0.5\text{MW}$  (compared with 10kW for initial LIGO). Initially, this may not be possible due to thermal lensing issues and parametric instabilities. A better idea of the operating capabilities should be known in the upgrade to Enhanced LIGO. Figure 8.5 showed that with lower laser power and squeezed states, Advanced LIGO may reach its design sensitivity.

### 8.4.4 Hardware and facility noise

Current hardware and facility noise predictions have been used. More development and testing will show if these prediction are accurate. Broadly speaking, higher hardware and facility noise would reduce the improvements that squeezed states could offer, whereas lower hardware and facility noise would increase the improvements. Techniques such as the ‘Mexican Hat’ mirrors with the ‘Mesa’ beams open the possibility of a reduction in coating thermal noise, which would

<sup>2</sup>In chapter 7 the product of our homodyne efficiency and photodiode efficiency was 90( $\pm 2$ )%. The authors in Reference [18] report detection efficiency of 95( $\pm 2$ )%.

**Table 8.1:** Advanced LIGO interferometer parameters

Parameter	Symbol	Value	Units
Laser Frequency	$\omega_0$	$1.77 \times 10^{15}$	radians/s
Mirror mass	$m$	40	kg
Laser Power at BS (wideband)	$I_0$	2100	W
Laser Power at BS (narrowband)	$I_0$	84	W
ITM transmittance (power)	$T$	0.005	—
Transmission of signal recycling mirror (amplitude)	$\tau$	$\sqrt{0.07}$	—
Reflectivity of signal recycling mirror (amplitude)	$\rho$	$1 - \tau^2 - \mathcal{L}_{SR}$	—
Sideband frequency	$\Omega$		
Arm Length	$L$	3995	m
Signal recycling cavity length	$l$	10	m
Signal recycling cavity detuning (wideband)	$\phi$	$(\pi - 0.08)/2$	radians
Signal recycling cavity detuning (narrowband)	$\phi$	$(\pi - 0.4)/2$	radians
Efficiency of photodetection	$1 - \lambda_{PD}$	.9	—
Round Trip Arm Cavity loss	$\lambda_{ac}$	$75 \times 10^{-6}$	—
Signal recycling cavity loss	$\mathcal{L}_{SR}$	0.0035	—
Detection phase	$\zeta$	$\pi/2$	radians

allow the more benefits of squeezed states to be obtained and higher squeeze factors would be useful.

## 8.5 Chapter summary

We have presented a simple study into possible improvements in sensitivity obtainable with the injection of squeezed states into Advanced LIGO. Realistic levels of classical noise and optical loss were included in these calculations, which show that Advanced LIGO might significantly improve in sensitivity or power-handling requirements with the addition of squeezed light.

**Part III**

**Locking Techniques**



---

# Quantum noise locking

---

In this chapter we present a detailed analysis of quantum noise locking, a technique that uses the quantum noise of an optical field to derive a phase reference for control purposes. This chapter is based on the work presented in the publication

*Quantum Noise Locking*

K. McKenzie, E. E. Mikhailov, K. Goda, P. K. Lam, N. Grosse, M. B. Gray, N. Mavalvala, and D. E. McClelland.

J. Opt. B **7**, S421-S428 (2005)

## 9.1 Introduction

Squeezed states of light can offer quantum noise reduction to interferometric measurements [34] and give rise to quantum mechanical phenomena such as entanglement [164, 165]. To be of practical use in these experiments, the squeeze angle must be actively controlled. For example, to reduce the shot noise of an interferometric measurement, the squeezed angle needs to be actively controlled to coincide with the phase quadrature of the measurement. Control of the squeeze angle of ‘bright’ squeezed states has routinely been achieved using standard techniques such as dither locking or PDH locking [12, 13, 15, 21]. Controlling the squeeze angle of a squeezed vacuum state is more difficult. Standard locking techniques cannot be used as the squeezed vacuum state has no carrier amplitude that can be used as a phase reference.

Vacuum squeezed states offer considerable advantages over bright squeezed states, particularly at low sideband frequencies; a requirement for applications such as interferometric gravitational wave detection (at sideband frequencies of 10Hz-10kHz) and atomic systems (at sideband frequencies  $< 500\text{kHz}$ ) [43, 125]. Squeezed vacuum states have inherent immunity to classical noise, allowing squeezed states to be created across the audio frequency band (see references [24–26] and chapters 5 and 7), whereas bright squeezed states typically exhibit squeezing only at high frequencies ( $\sim \text{MHz}$  and above).

One solution to this apparent dichotomy would be to create a vacuum squeezed state over the sideband frequency band of interest (say DC-100kHz) which had a ‘bright’ frequency shifted sideband (at say, a few MHz) for use as a phase reference. Vahlbruch *et al.* [26] and Goda *et al.* [166] have successfully demonstrated this type of operation. Vahlbruch *et al.* used two orthogonally polarized frequency shifted sidebands; one to control the OPO cavity length, the other to control the squeezed vacuum phase. To control the vacuum squeezed state, the phase of the frequency shifted sideband was first locked to the squeezed quadrature, achieved by locking the phase of the frequency shifted sideband and the pump field. It was then locked to the local oscillator phase, thereby enabling stable measurement of the squeezed state.

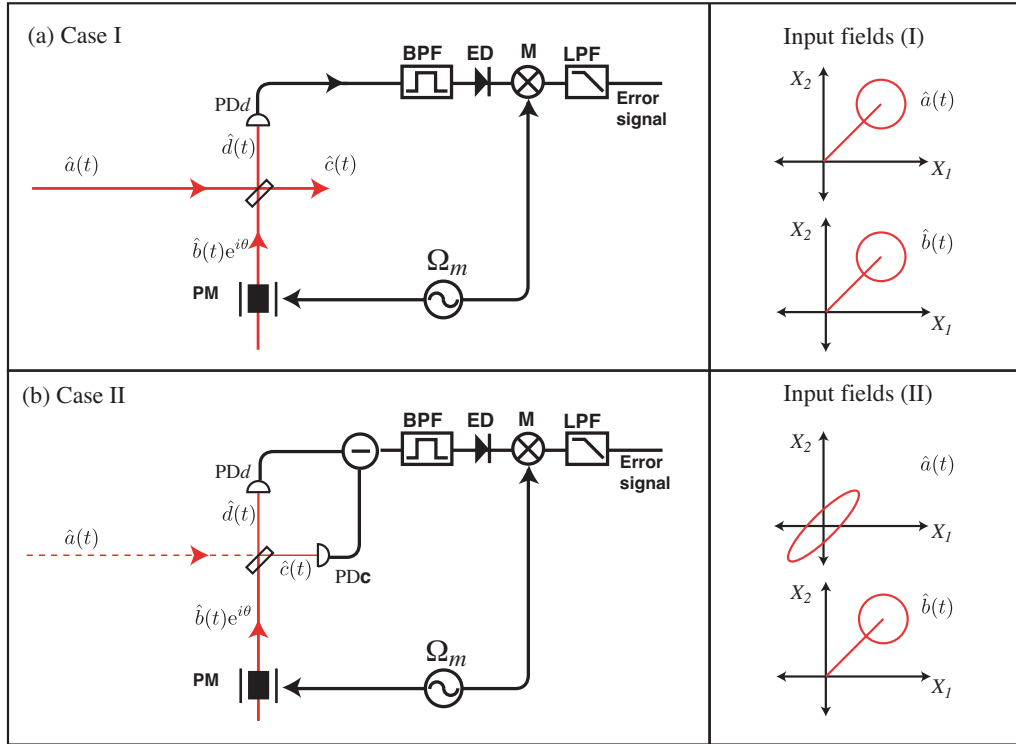


**Figure 9.1:** Setup of a balanced homodyne detector with input fields,  $\hat{a}(t)$  and  $\hat{b}(t)$ , interfering with relative phase,  $\theta$ , on a balanced beamsplitter. Here the local oscillator beam  $\hat{b}(t)$  passes through a phase modulator (PM) with applied sinusoidal modulation at frequency  $\Omega_m$ . The output fields,  $\hat{d}(t)$  and  $\hat{c}(t)$ , are incident on the photodetectors,  $\text{PD}_d$  and  $\text{PD}_c$ . To derive the quantum noise locking error signal, the output of the homodyne is bandpass filtered (BPF) then envelope detected (ED). The output of the envelope detector is demodulated and low pass filtered (LPF).

An alternative solution to the frequency shifted sideband scheme is to use the *quantum noise locking* technique. To obtain a phase-sensitive readout, quantum noise locking relies on asymmetry in the noise of the squeezed and anti-squeezed quadratures. A schematic of a homodyne detector using the quantum noise locking technique is shown in figure 9.1 (b). Here the field  $\hat{a}(t)$  represents a squeezed vacuum state and  $\hat{b}(t)$  the local oscillator field for the balanced homodyne detector. The quantum noise locking error signal can be derived by dithering the squeeze angle (at a frequency  $\Omega_m$ ) and demodulating the *noise power* of the homodyne detector photocurrent. This is analogous to the more standard dither locking technique, where the relative phase of two coherent fields is modulated and the photocurrent demodulated to obtain an error signal.

Quantum noise locking has been used to enable stable measurements of quantum correlations by Schori *et al.* [167] and Laurat *et al.* [23], and in the work presented in this thesis (first published in [24] and [25]). Recently, Goda *et al.* [128] used quantum noise locking to lock the squeeze angle for a squeezing-enhanced signal-recycled Michelson interferometer at the Caltech 40m prototype gravitational wave detector [129]. Quantum noise locking is simpler experimentally than a frequency shifted sideband scheme for two reasons. Firstly, no frequency shifted sidebands are required, so the complexity of adding an extra phase locked laser or an acoustic optic modulator is avoided. Secondly, two length degrees of freedom degenerate into one. In quantum noise locking, the only important degree of freedom is the squeeze angle at detection, as there is no other

phase reference. For a squeezed vacuum state, the squeeze angle can be actuated with either the pump phase or the detection phase, reducing the quantum noise locking control scheme to a single degree of freedom. When using a coherent locking technique to control a squeezed state phase, there are two degrees of freedom that must be controlled: the phase between the pump and the frequency shifted sideband phase, and the detection phase.

Quantum noise locking is appealing due to its experimental simplicity. Here it is compared with standard locking techniques in terms of robustness and noise performance. We show that quantum noise locking provides a robust and stable lock, however, its noise performance was found to be inferior to the standard dither locking technique. We investigated quantum noise locking in two different systems shown schematically in figure 9.1. The system we investigate first is case I, shown in figure 9.1 (a). Case I is the control of the relative phase of two coherent beams interfered on a beamsplitter. The quantum noise locking error signal for case I is derived by demodulation of the noise power of a single photodetector. Case I shares quadrature dependent noise power with case II, since the interference condition of the fields  $\hat{a}(t)$  and  $\hat{b}(t)$  determines the optical power at each beamsplitter port and the associated shot noise varies accordingly. There is maximum shot noise at a bright fringe (analogous to the anti-squeezed quadrature in case II) and minimum shot noise at the dark fringe (analogous to the squeezed quadrature in case II). The purpose of the ‘coherent’ quantum noise locking experiment (case I) was threefold: to enable the testing and ‘shaking down’ of electronics that were designed for use in quantum noise locking in a simple experimental system; to provide an out of loop readout of the noise performance of quantum noise locking, which was done by using the other port of the beamsplitter to readout a dither locking error signal concurrently; and for a direct comparison of the displacement noise in quantum noise locking and the standard dither locking technique.

The chapter is laid out as follows: in section 9.2 the quantum noise locking error signals for cases I and II are derived; in section 9.3 an experimental demonstration of quantum noise locking in case I and II is presented; in section 9.4 the quantum noise limited noise performance of quantum noise locking is calculated; finally, in section 9.5 the experimental limitations of quantum noise locking are discussed.

## 9.2 Derivation of the noise locking error signal

In this section an overview of the derivation of the quantum noise locking error signal is given. The general experimental setup is the same for both cases I and II, however the input fields  $\hat{a}(t)$  and  $\hat{b}(t)$ , and the photodetection processes are different. After detection the electronics used to derive the error signal are identical (see figure 9.1). The photocurrent (from either the single photodetector, or balance detector) is passed through a bandpass filter (BPF), then sent to an envelope detector (see, for example [168]) which gives an output proportional to the real envelope of the input photocurrent. In both cases, the BPF low frequency cut-off,  $\Omega_{lf}$ , is set such that  $\Omega_m \ll \Omega_{lf}$ , so that any coherent beats (between the PM sidebands and the carrier for example) are not passed. Figure 9.2 shows a phasor diagram of the frequency distribution of the optical fields and the BPF. The envelope detector LPF corner frequency was set higher than the modulation frequency. The output of the envelope detector is demodulated and low pass filtered to give the quantum noise locking error signal.

The fields  $\hat{a}(t)$  and  $\hat{b}(t)$  have relative phase,  $\theta$ , and interfere on a balanced beamsplitter. The fields at the output ports of the beamsplitter are labeled  $\hat{d}(t)$  and  $\hat{c}(t)$ . The field operators can be decomposed into average (dc) and fluctuating (time-dependent) components,  $\hat{s}(t) = \bar{s} + \delta\hat{s}(t)$ , for  $s = a, b, c, d$ . The operators satisfy the standard commutation relations as laid out in chapter 3. Average components are assumed to be real. The linearized photocurrents of  $PD_d$  and  $PD_c$  are

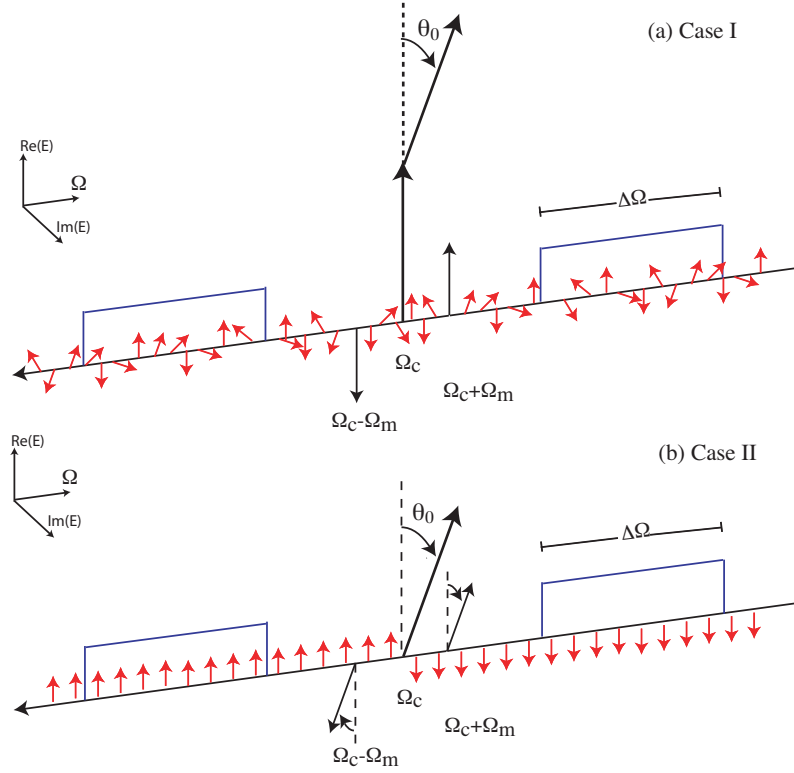


**Figure 9.2:** Phasor diagram of the fields incident on the detectors showing the carrier at  $\Omega_C$  modulation sidebands at  $\Omega_m$ , the quantum noise (small red vectors) and the frequency relation of the bandpass filter frequencies (which has bandwidth  $\Delta\Omega$ ). Top figure shows the fields for case I, here the quantum noise is shot noise, and the two carrier fields at  $\Omega_C$  represent the field amplitudes of  $a$  and  $b$  with relative (dc) phase of  $\theta_0$ . The bottom figure shows fields for case II. Here the quantum noise is squeezed vacuum and the phase  $\theta_0$  determines the measured quadrature.

proportional to (see equation 3.42)

$$i_{\theta}^{(d,c)}(t) = \frac{h\nu}{2} \left( \bar{a}^2 + \bar{b}^2 \pm 2\bar{a}\bar{b} \sin \theta + \delta X_1^{(b)}(\bar{b} \pm \bar{a} \sin \theta) + \delta X_1^{(a)}(\bar{a} \pm \bar{b} \sin \theta) \pm (\bar{a}\delta X_2^{(b)} + \bar{b}\delta X_2^{(a)}) \cos \theta \right), \quad (9.1)$$

where the photocurrent  $i_{\theta}^{(d)}(t)$  is given by the top sign and  $i_{\theta}^{(c)}(t)$  the lower sign. We have assumed unity detection efficiency for simplicity.

### 9.2.1 Case I: Locking the phase of coherent fields

In case I the quantum noise locking error signal comes from the variation of shot noise as a function of  $\theta$ . In this section, the variance of the detected power is calculated on a single photodetector. Once demodulated, this is the error signal<sup>1</sup>. The magnitude of the error signal depends on the BPF

<sup>1</sup>Either the output voltage or output power of the envelope detector can be demodulated to obtain a quantum noise locking error signal. In this section we assume it is the noise power of the photocurrent which is demodulated. The variance of the photocurrent is directly proportional to the noise power.

bandwidth, However, this dependence is neglected here. The dependence on the BPF bandwidth is taken into account when the signal to noise ratio is calculated, in section 9.4.

The output noise power of the envelope detector is proportional to the variance of the photocurrent detected at  $PD_d$

$$\begin{aligned} V(i_\theta^{(d)}) &= \langle |\delta i_\theta^{(d)}|^2 \rangle, \\ &= \frac{h^2 \nu^2}{4} \left( V_1^{(b)} (\bar{a}^2 + \bar{b}^2 \sin^2 \theta + 2\bar{a}\bar{b} \sin \theta) + V_1^{(a)} (\bar{b}^2 + \bar{a}^2 \sin^2 \theta + 2\bar{a}\bar{b} \sin \theta), \right. \\ &\quad \left. + (\bar{a}^2 V_2^{(b)} + \bar{b}^2 V_1^{(a)}) \cos^2 \theta \right), \end{aligned} \quad (9.2)$$

where  $V_{1,2}^{(a)}$  and  $V_{1,2}^{(b)}$  are the quadrature variances of the fields  $a$  and  $b$ . Since these are shot noise limited the substitution  $V_1^{(a)} = V_2^{(a)} = V_1^{(b)} = V_2^{(b)} = 1$  can be used. The variance of the photocurrent becomes

$$V(i_\theta^{(d)}) = \frac{h^2 \nu^2}{2} (\bar{a}^2 + \bar{b}^2 + 2\bar{a}\bar{b} \sin \theta). \quad (9.3)$$

In the experimental demonstration of case I presented in section 9.3.1, the fields  $a$  and  $b$  are the fields in the two arms of a Mach-Zehnder interferometer. Consider that the input beamsplitter of the Mach-Zehnder interferometer has amplitude reflectivity,  $r$ , and amplitude transmissivity,  $t$ . In the lossless case where ( $r^2 + t^2 = 1$ )

$$\bar{a}^2 = r^2 \frac{P_{in}}{h\nu}, \quad \bar{b}^2 = t^2 \frac{P_{in}}{h\nu}, \quad (9.4)$$

where  $P_{in}$  is the power at the Mach-Zehnder input. Equation 9.3 can be rewritten

$$V(i_\theta^{(d)}) = \frac{1}{2} h\nu P_{in} (1 + \mathcal{V} \sin \theta), \quad (9.5)$$

where  $\mathcal{V} = 2rt$  is the Mach-Zehnder fringe visibility. For later calculations it is convenient to introduce a dc phase shift of  $\pi/2$  to  $\theta$ . Thus equation 9.5 becomes

$$V(i_\theta^{(d)}) = \frac{1}{2} h\nu P_{in} (1 + \mathcal{V} \cos \theta). \quad (9.6)$$

The generation of noise locking error signals requires relative phase modulation of the input fields. This is included by letting the phase difference of the input fields vary as a function of time,  $\theta = \theta_0 + \beta \sin \Omega_m t$ , where  $\theta_0$  is the average phase,  $\beta$  is the modulation depth, and  $\Omega_m$  is the modulation frequency. For small modulation depth ( $\beta \ll \theta_0$ ) we make the approximation  $e^{i\beta \sin \Omega_m t} \simeq J_0(\beta) + J_1(\beta) e^{i\Omega_m t} - J_1(\beta) e^{-i\Omega_m t}$ . Expanding the phase  $\theta$  and neglecting the  $J_1(\beta)^2$  terms, we find

$$V(i_\theta^{(d)}) = \frac{1}{2} h\nu P_{in} (1 + \mathcal{V} J_0(\beta) \cos \theta_0 - 2\mathcal{V} J_1(\beta) \sin \theta_0 \sin \Omega_m t). \quad (9.7)$$

The error signal can be found by demodulation of equation 9.7. The demodulation process can be described mathematically by multiplication by a sinusoid at the modulation frequency. The error signal for case I is

$$\begin{aligned} \xi_I &\propto V(i_\theta^{(d)}) \times \sin(\Omega_m t + \phi_D), \\ &\propto -\frac{1}{2} h\nu P_{in} \mathcal{V} J_1(\beta) \sin \theta_0, \end{aligned} \quad (9.8)$$

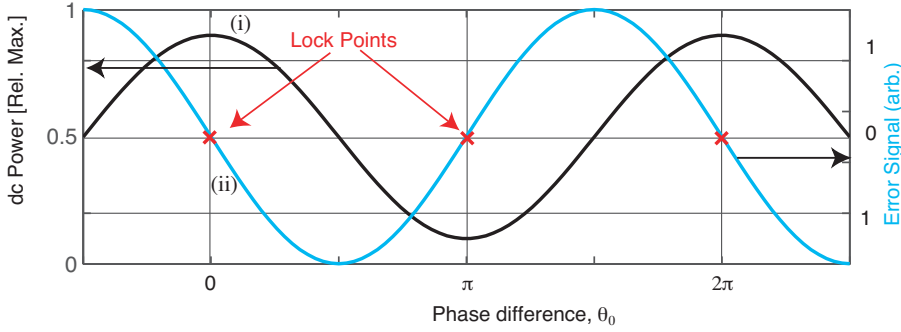


**Figure 9.3:** (i) The power at  $PD_d$  of a Mach-Zehnder interferometer with fringe visibility 0.8 and (ii) the error signal as the relative phase is varied. The error signal's zero crossing points indicate that the homodyne angle can be locked to either a dark or bright fringe by choosing the appropriate feedback sign.

where we have discarded terms at frequency  $\Omega_m$  or higher and chosen the demodulation phase  $\phi_D = 0$ . Equation 9.8 reveals that the quantum noise locking error signal has zero crossings at  $\theta_0 = 0$  and  $\theta_0 = \pi$  corresponding to the dark and bright fringes of the Mach-Zehnder interferometer. Either the dark or bright fringes can be locked to by selecting the appropriate feedback sign. The lock points are shown on the quantum noise locking error signal by  $\times$ 's in figure 9.3, curve (ii). The magnitude of the error signal depends linearly the fringe visibility,  $\mathcal{V}$ . Of course, if  $\mathcal{V} = 0$  there is no quadrature dependent noise and the error signal vanishes.

### 9.2.2 Case II: Locking a squeezed vacuum state

The quantum noise locking error signal is calculated in a similar manner to that of case I. Here the input fields are considered to be a squeezed vacuum<sup>2</sup> and a local oscillator field. The difference photocurrent from the balanced homodyne detector is given by  $i_{\theta}^{-}(t) = i_{\theta}^{(d)}(t) - i_{\theta}^{(c)}(t)$ . The fluctuating component is

$$\delta i_{\theta}^{-}(t) = hv \left( \bar{a} \delta X_1^{(b)} \sin \theta + \bar{a} \delta X_2^{(b)} \cos \theta + \bar{b} \delta X_1^{(a)} \sin \theta - \bar{b} \delta X_2^{(a)} \cos \theta \right). \quad (9.9)$$

The variance of the difference photocurrent is

$$\begin{aligned} V(i_{\theta}^{-}) &= \langle |\delta i_{\theta}^{-}|^2 \rangle, \\ &= h^2 v^2 \left( \bar{a}^2 (V_1^{(b)} \sin^2 \theta + V_2^{(b)} \cos^2 \theta) + \bar{b}^2 (V_1^{(a)} \sin^2 \theta + V_2^{(a)} \cos^2 \theta) \right), \end{aligned} \quad (9.10)$$

The local oscillator condition implies  $\bar{a} \ll \bar{b}$ , so the variance in equation 9.10 can be written

$$\begin{aligned} V(i_{\theta}^{-}) &\simeq h^2 v^2 \bar{b}^2 (V_1^{(a)} \sin^2 \theta + V_2^{(a)} \cos^2 \theta), \\ &= hv \bar{P}_{LO} V_{\theta}, \end{aligned} \quad (9.11)$$

where  $\bar{P}_{LO} = hv \bar{b}^2$  is the power of the local oscillator and  $V_{\theta}$  is the variance relative to the shot noise limit

$$V_{\theta} = V_1^{(a)} \sin^2 \theta + V_2^{(a)} \cos^2 \theta. \quad (9.12)$$

<sup>2</sup>bright squeezing can also be locked using quantum noise locking.

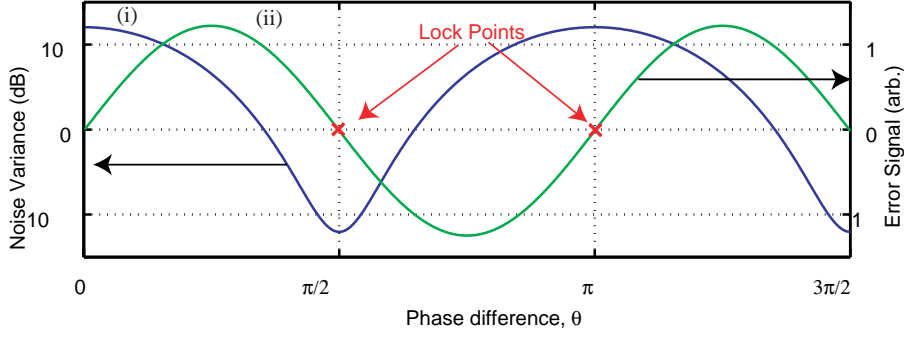


**Figure 9.4:** The noise variance of a phase squeezed beam relative to the shot noise limit and the quantum noise locking error signal as the relative phase is varied. The error signal's zero crossing points indicate that the homodyne angle can be locked to observe both squeezing and anti-squeezing. The scale of the error signal is arbitrary.

We can write  $V_\theta$  as a function of time ( $\theta \rightarrow \theta(t)$ ) and in a similar form to equation 9.6

$$\begin{aligned} V_\theta &= V_1^{(a)} \sin^2 \theta(t) + V_2^{(a)} \cos^2 \theta(t), \\ &= \frac{1}{2} \left( V_1^{(a)} (1 - \cos 2\theta(t)) + V_2^{(a)} (1 + \cos 2\theta(t)) \right), \\ &= (V_1^{(a)} + V_2^{(a)})/2 (1 + \gamma \cos \theta'(t)), \end{aligned} \quad (9.13)$$

where

$$\gamma = \frac{|V_2^{(a)} - V_1^{(a)}|}{V_1^{(a)} + V_2^{(a)}}, \quad (9.14)$$

is a parameter which plays a similar roll to the fringe visibility in the Mach-Zehnder interferometer. Here

$$\theta'(t) = 2\theta(t). \quad (9.15)$$

Expanding  $\theta'(t) = 2\theta_0 + 2\beta \sin \Omega_m t$  to first order and discarding  $J_1(2\beta)^2$  terms we find

$$V_\theta \simeq \frac{1}{2} (V_1^{(a)} + V_2^{(a)}) (1 + \gamma J_0(2\beta) \cos 2\theta_0 - 2\gamma J_1(2\beta) \sin 2\theta_0 \sin \Omega_m t). \quad (9.16)$$

$V_\theta$  can be substituted back into equation 9.11 to find the quantum noise locking error signal

$$\begin{aligned} \xi_{II} &= V(i_{\bar{\theta}}^-) \times \sin(\Omega_m t + \phi_D), \\ &= -\frac{1}{2} h\nu P_{LO} (V_1^{(a)} + V_2^{(a)}) \gamma J_1(2\beta) \sin 2\theta_0, \\ &= -\frac{1}{2} h\nu P_{LO} (V_2^{(a)} - V_1^{(a)}) J_1(2\beta) \sin 2\theta_0. \end{aligned} \quad (9.17)$$

Again we have chosen the demodulation phase  $\phi_D = 0$ . The quantum noise locking error signal for squeezed vacuum has zero crossings at  $\theta_0 = 0$  and  $\theta_0 = \pi/2$  corresponding to the anti-squeezed and squeezed quadratures. The lock points are shown on the error signal by  $\times$ 's in figure 9.4 curve (ii) along with  $V_\theta$ , curve (i), for a minimum uncertainty phase squeezed state. Equation 9.17 also reveals that the amplitude of the error signal depends the asymmetry of the quadrature variances

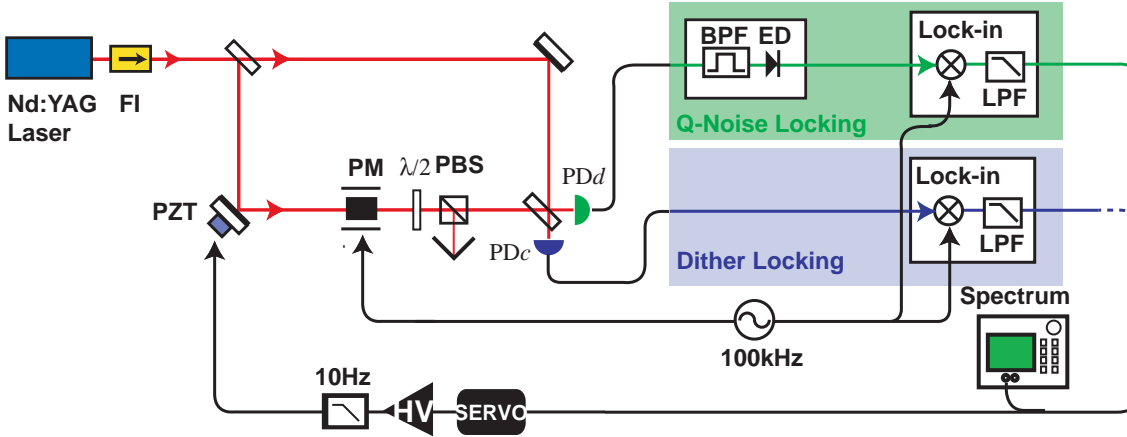


**Figure 9.5:** An experimental schematic of the setup used to analyze noise locking. In the optics section: FI - Faraday isolator; PM - Phase modulator;  $\lambda/2$  - half-wave plate; PBS - Polarizing beam splitter; PZT - piezo electric transducer bonded onto a mirror;  $PD_d, PD_c$  - photodetectors. In the electronics section; Lock-in - Lock-in amplifier; BPF - Band pass filter; ED - envelope detector; LPF - Low pass filter; and HV amp - High voltage amplifier.

via the parameter  $\gamma$  or  $(V_2^{(a)} - V_1^{(a)})$ , which plays the same roll as the fringe visibility  $\mathcal{V}$  in case I. If there is no asymmetry in the quadrature variances, the phase reference is lost and the error signal vanishes.

### 9.3 Experimental demonstration of quantum noise locking

In this section we present two experimental demonstrations of the quantum noise locking technique. Firstly, we demonstrate case I, the locking of two coherent fields. Secondly, we present case II, the locking of the detection phase of a squeezed state.

#### 9.3.1 Experimental analysis of case I: Locking of coherent fields

Figure 9.5 shows a schematic of the quantum noise locking experiment. Approximately 2mW from a Nd:YAG laser operating at 1064nm was injected into a Mach-Zehnder interferometer. Contained in the lower arm of the Mach-Zehnder was a phase modulator (New-Focus 4004); used to dither the interference condition of the Mach-Zehnder and a mirror mounted on a piezoelectric transducer (PZT). The dither frequency was  $\Omega_m/2\pi=100\text{kHz}$  with a modulation depth of  $\beta \approx 0.045$  radians. A variable attenuator consisting of a  $\lambda/2$  plate and a polarizing beam-splitter (PBS) was placed in the lower arm to allow the fringe visibility to be adjusted - to mimic changing the level of squeezing and anti-squeezing. The fringe visibility was set to  $\mathcal{V} = 0.6$  to have 6dB noise power variation on the fringe. Both output ports of the beamsplitter were detected on matched photodetectors ( $PD_d$  and  $PD_c$ ) with ETX500 photodiodes, but only one photodetector ( $PD_d$ ) was used to derive the quantum noise locking error signal. A standard dither locking error signal was derived from photodetector ( $PD_c$ ).

The quantum noise locking error signal was produced as follows: The output of  $PD_d$  was bandpass filtered, with low frequency cutoff of  $\Omega_{lf}/2\pi = 2\text{MHz}$  and a high frequency cutoff of  $\Omega_{hf}/2\pi = 20\text{MHz}$ , giving a detection bandwidth of  $\Delta\Omega = 18\text{MHz}$ . The low frequency corner was designed to cut out any component of the coherent modulation signal at 100kHz by employing

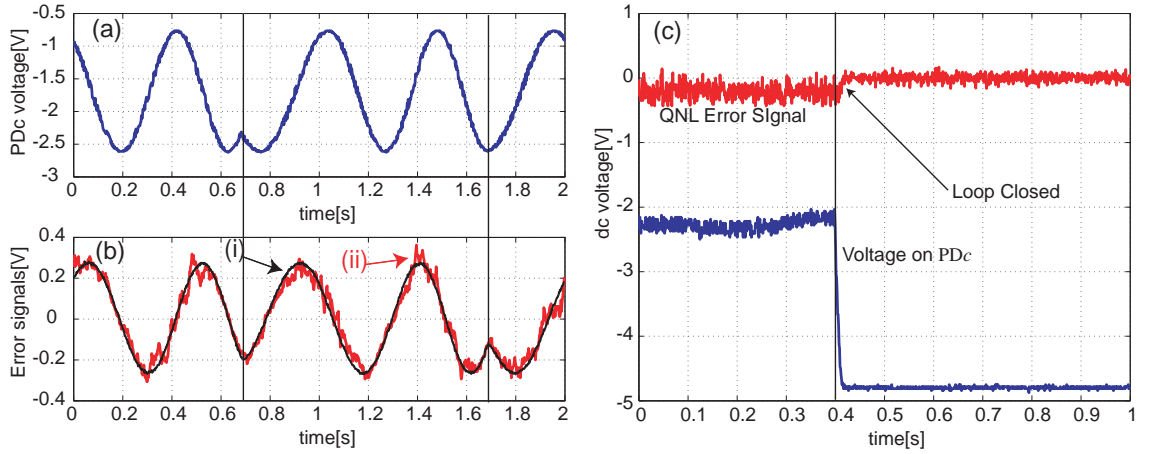


**Figure 9.6:** (a) The DC voltage on  $PD_c$  as the fringe is scanned (the photodetector is negatively coupled, thus lower voltage corresponds to higher incident power). (b) (i) The corresponding dither locking error signal and (ii) the quantum noise locking error signal. (c) Lock acquisition curve showing the quantum noise locking error signal and the voltage on  $PD_c$ . Initially, the control loop is open. At 0.4 seconds the control loop is closed and the interferometer is locked to a bright fringe on  $PD_c$  (dark fringe on  $PD_d$ ). Lock-in amplifier settings; LPF Time constant = 10ms, 6dB/octave for the both dither locking techniques.

a low frequency corner with  $f^3$  roll up. Over the BPF frequency range, most of the spectrum (5MHz - 20MHz) was shot noise limited, however below 5MHz there was some classical intensity noise present. The BPF output was sent to an envelope detector, which had a series of amplifying stages before a diode stage, giving an output voltage proportional to real envelope of the input below the cut-off frequency, which in our case was 200kHz. The output of the envelope detector was then demodulated using a low frequency lock-in amplifier (SRS-SR830) to give the quantum noise locking error signal. The error signal was then low pass filtered (to remove components at frequencies of  $\Omega_m$  and higher) sent to the servo, then to the PZT actuator. The dither locking error signal was derived from  $PD_c$  using an identical lock-in amplifier where it was demodulated and low pass filtered.

### Demonstration of locking using the quantum noise locking technique

Figure 9.6 shows: (a) the detected optical power on  $PD_c$  (the photodetector is negatively coupled) and (b) the error signals from (i) the standard dither locking technique and (ii) the quantum noise locking error signal as the fringe was scanned. Note that the demodulation phase of the two techniques has a 180 degree difference to give the error signals the same sign in the figure, because the signals are derived from different beamsplitter ports. It can be seen that both error signals have zero crossing points at the bright and dark fringes. The noise of the quantum noise locking error signal is noticeably larger than that of the dither locking technique, which is not visible on this scale. Also, the noise on the quantum noise locking error signal varies significantly over the fringe. The noise on the quantum noise locking error signal is minimized at the dark fringe for  $PD_d$  (bright fringe for  $PD_c$ ) and maximum at the bright fringe for  $PD_d$  (dark fringe for  $PD_c$ ).

Lock acquisition using quantum noise locking is shown in figure 9.6 (c). The bottom curve is the optical power on  $PD_c$  and the top curve is the quantum noise locking error signal. Initially, the control loop is open. At 0.4 seconds the control loop was closed. Here the quantum noise

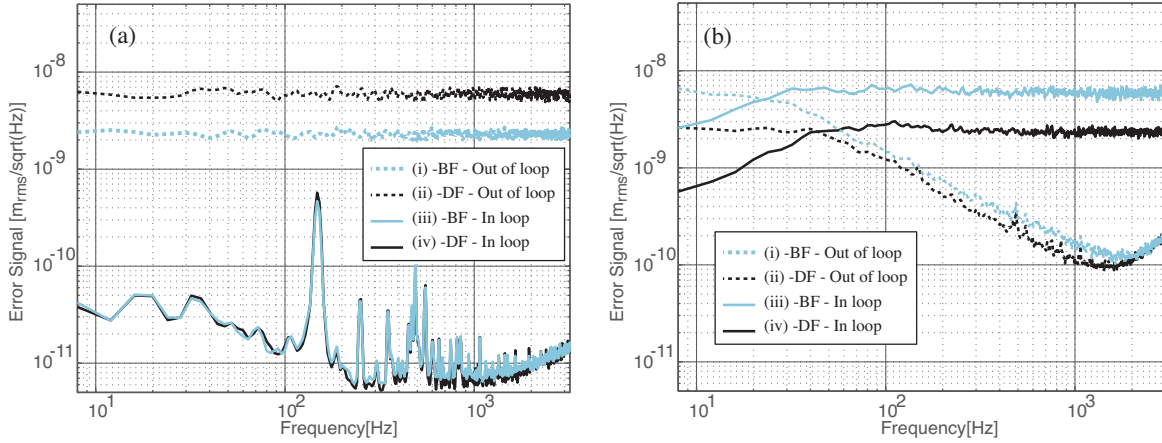


**Figure 9.7:** (a) Spectral densities of the error signals whilst the interferometer was locked using the dither locking technique. Curves (i) and (ii) are the out-of-loop quantum noise locking error signal spectra of the bright and dark fringes (on  $PD_d$ ). Curves (iii) and (iv) are the in-loop dither locking error signal spectra of the bright and dark fringes (on  $PD_c$ ). (b) Spectral densities of the error signals whilst the interferometer was locked using the quantum noise locking technique. Curves (i) and (ii) are the out-of-loop dither locking error signal spectra of the bright and dark fringes (on  $PD_d$ ). Curves (iii) and (iv) are the in-loop quantum noise locking error signal spectra of the bright and dark fringes (on  $PD_c$ ). The excess noise of the quantum noise locking readout can be seen from the different amplitudes of the dither locking and quantum noise locking error signal spectra. DF = dark fringe, BF = bright fringe.

locking error signal was quickly zeroed and the fringe on  $PD_c$  reaches the maximum value. The quantum noise locking system was found to provide a robust lock comparable to the dither locking technique and was able to maintain lock indefinitely.

### Noise performance of the quantum noise locking technique

The noise performance of quantum noise locking was able to be measured by, and compared with, the dither locking technique. This comparison can be seen in the spectral density of the error signals recorded on a signal analyzer (SRS-SR785), shown in the figure 9.7 (a) and (b). The data in figure 9.7 (a) was taken with the Mach-Zehnder locked using the dither locking technique, and in (b) when using the quantum noise locking technique. The data was calibrated from volts/ $\sqrt{\text{Hz}}$  to m/ $\sqrt{\text{Hz}}$  by using the slope of the error signal in volts/m measured from the data in figure 9.6 (b).

The solid curves in figure 9.7 (a) are the in-loop dither locking error signals spectra whilst locked to the dark (dark solid line) and bright fringes (light solid line). The dither locking control loop had a unity gain frequency  $\sim 40\text{Hz}$ . The dashed curves are the corresponding out-of-loop quantum noise locking error signal spectra taken for the dark fringe (on  $PD_c$  - dark dashed line) and the bright fringe (on  $PD_c$  - light dashed line). The spectral densities of the in-loop dither locking error signal show little difference for the dark and bright fringe, with a noise of approximately  $1.5 \times 10^{-11} \text{m}/\sqrt{\text{Hz}}$  at 100Hz. Many acousto-mechanical noise sources in the interferometer couple into the readout and can be seen in the structure shown in the dither locking error signal spectra. The out-of-loop quantum noise locking error signal show white noise approximately 2 orders of magnitude larger. These spectra bear no resemblance to the dither locking error signal spectra, indicating the quantum noise locking technique has a much higher noise floor that buries the interferometer noise source. The noise of the bright fringe quantum noise locking readout is

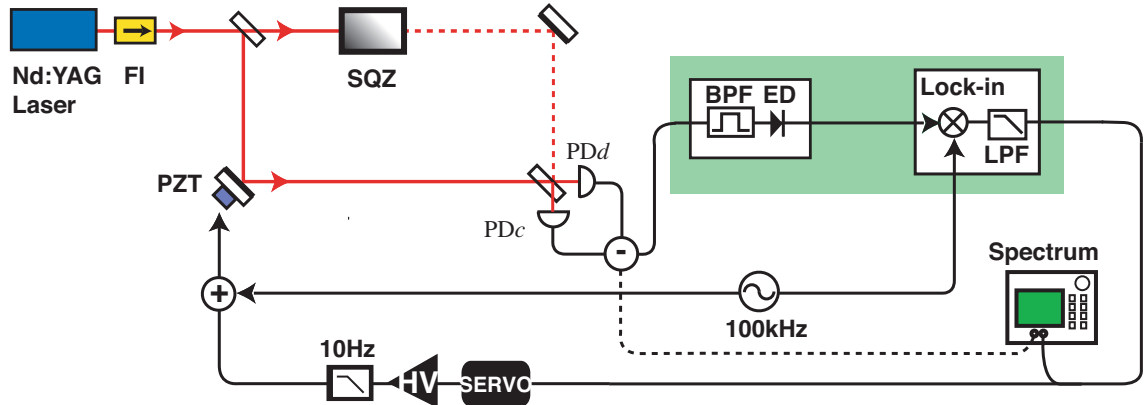


**Figure 9.8:** An schematic of the experiment to quantum noise lock a squeezed vacuum state. The box labeled ‘SQZ’ represents the squeezing apparatus.

approximately a factor of 2 larger than the dark fringe quantum noise locking readout.

Because the dither locking technique was at least two orders of magnitude more sensitive than the quantum noise locking technique it could be used to make out-of-loop measurements of the displacement noise of the quantum noise locking technique. Figure 9.7 (b) shows the spectral densities of the error signals whilst the interferometer was locked using quantum noise locking. The solid curves are the in-loop quantum noise locking error signals whilst locked to the dark fringe (dark solid line) and bright fringe (light solid line). The dashed curves are the corresponding out-of-loop dither locking error signal spectra used to readout the displacement noise of the quantum noise locking technique. Below the unity gain frequency ( $\sim 40\text{Hz}$ ) the in-loop error signals show some suppression of noise, due to the loop gain. The out-of-loop (dither locking) signals at  $10\text{Hz}$  show displacement noise of  $2.5 \times 10^{-9} \text{m}/\sqrt{\text{Hz}}$  and  $5.5 \times 10^{-9} \text{m}/\sqrt{\text{Hz}}$  for the dark and bright fringe locking signals, respectively. The displacement noise above the unity gain frequency can be seen to roll off as  $1/f$  which is the filter shape of the control loop. The origin of the noise peaking in the dither locking spectra above  $2\text{kHz}$  was thought to be a feature of the digital filters in the lock-in amplifier.

The difference in the noise whilst locked to the bright and dark fringes shown here can also be seen qualitatively in figure 9.6 (b). The factor of two difference in the noise floor is predicted by the calculation of the noise performance presented in section 9.4.

The comparison of the error signal spectra of the dither locking and quantum noise locking techniques indicates that, in this bench-top experiment, the noise performance of quantum noise locking is significantly poorer than dither locking. The quantum noise locking error signal had broadband white noise which increased the interferometer noise over the frequency band measured here. The white noise of the quantum noise locking technique suggests that low control bandwidth would be desirable, to limit the amount of displacement noise imposed by the quantum noise locking control loop into the system. The white noise of the quantum noise locking technique is analogous to the shot noise limit of dither locking techniques, however it is many orders of magnitude larger.

### 9.3.2 Experimental analysis of case II: Locking of a squeezed vacuum state

Figure 9.8 shows a simplified schematic of experimental demonstration of quantum noise locking of a squeezed vacuum state. Here the box labeled ‘SQZ’ in the upper arm of the Mach-Zehnder indicates the experiment used to generate the squeezed vacuum state (SHG, doubly resonant OPO, etc.) described in detail in chapter 7. Up to 6.5dB of squeezing was detected on a balanced homodyne detector with a local oscillator power of  $380\mu\text{W}$ . The photocurrent of the balanced homodyne detector was demodulated to provide the quantum noise locking error signal and was simultaneously monitored on a signal or spectrum analyzer to measure quantum noise properties. The electronics and processes used to derive the quantum noise locking error signal in this experiment were identical to those in case I.

#### Demonstration of locking a squeezed vacuum state using the quantum noise locking technique

Figure 9.9 (a) shows the noise power out of the homodyne detector as the local oscillator phase was scanned. The corresponding quantum noise locking error signal can be seen in figure 9.9 (b)<sup>3</sup>. The error signal has zero crossings coinciding with the squeezed and anti-squeezed quadratures. Figure 9.9 (c) shows curves of the locked squeezed and anti-squeezed quadratures as well as the shot noise limit and electronic noise.

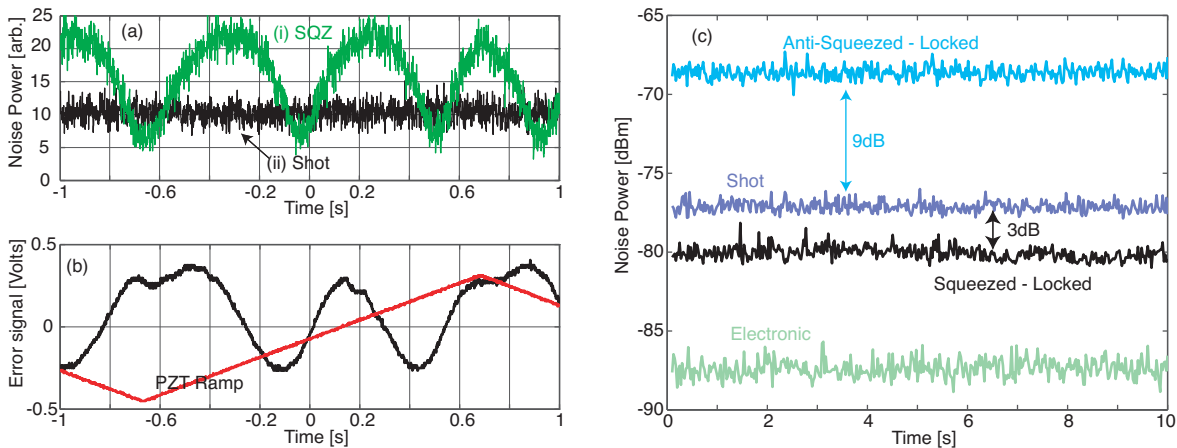


**Figure 9.9:** (a) The noise power of squeezed field (i) and noise power of shot noise (ii). The noise power units here are arbitrary, however the squeezed quadrature is approximately 3dB below the shot noise limit and the anti-squeezed quadrature is approximately 9dB above the shot noise limit. (b) The corresponding quantum noise locking error signal and PZT ramp. (c) Noise power of the squeezed and anti-squeezed quadratures using quantum noise locking. The measured shot noise and electronic noise are also shown. Measurements taken with zero span at 1MHz, RBW = 100kHz, VBW = 3kHz.

<sup>3</sup>The quantum noise locking signal here was viewed with a low pass filter (with corner frequency  $f_c = .5\text{Hz}$ ) immediately before the oscilloscope. This reduces the error signal amplitude and offsets the zero crossing point of the error signal. In the calibration of the spectra of the in-loop error signal in figure 9.9, the low pass filter was accounted for.

### The noise performance of quantum noise locking a squeezed vacuum on a homodyne detector

Figure 9.10 (a) shows the in-loop quantum noise locking error signal spectrum when the detection phase was locked to the squeezed quadrature (solid line) and the anti-squeezed quadrature (dashed line). The unity gain frequency of the control loop was approximately 20Hz. Though an out-of-loop measurement for the displacement noise was not recorded, it is reasonable to expect that displacement noise spectrum of locked the squeeze angle would behave in the same fashion as the coherent field quantum noise locking shown in figure 9.7. The displacement noise is expected to be  $1.3 \times 10^{-9} \text{m}/\sqrt{\text{Hz}}$  for the squeezed quadrature and  $2.7 \times 10^{-9} \text{m}/\sqrt{\text{Hz}}$  for the anti-squeezed quadrature, at frequencies below the unity gain frequency, and to roll off as  $1/f$  above the unity gain frequency.

The displacement noise difference for squeezed quadrature and anti-squeezed quadrature locking was a factor of two, as it was in case I. However, as shown in figure 9.9 (c), the noise power variation (at 1MHz) on the fringe is 12dB, compared to 6dB in case I. If the displacement noise limit scales in the same way for both cases (proportional to the square root of the noise power difference), one may expect a factor of four difference in displacement on the squeezed and anti-squeezed quadratures. The displacement noise sensitivity calculation presented in section 9.4, shows that the displacement noise does indeed scale proportional to the square root of noise power, so there seems to be a discrepancy in the displacement noise measured in figure 9.10 (a). This discrepancy can be accounted for by the frequency dependence of the magnitude of the squeezed and anti-squeezed quadratures over the detection band, as shown in figure 7.5 (a). The difference of the squeezed and anti-squeezed quadratures averaged over the detection band was  $\sim 6\text{dB}$ .

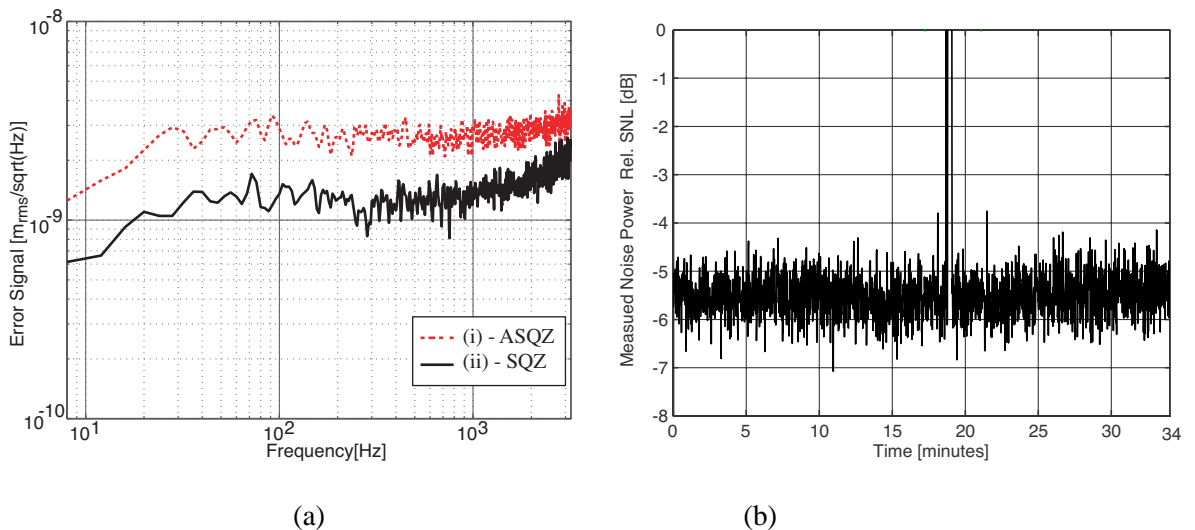


**Figure 9.10:** (a) The quantum noise locking error signal spectra whilst locked to the squeezed quadrature, curve (ii) and anti squeezed quadrature, curve (i). (b) Measurement of the squeezed quadrature over 34 minutes. The electronic noise at -11dB was not subtracted. Measurements taken with zero span at 100kHz, RBW = 10kHz, VBW = 30Hz. ASQZ = anti-squeezed quadrature, SQZ = squeezed.

## Long term measurement

Squeezing data taken over 34 minutes is shown in figure 9.10 (b) to demonstrate the stability of the apparatus and the quantum noise locking technique<sup>4</sup>. The figure shows the measured noise power at 100kHz over 34 minutes. The average measured noise power level was 5.5dB below the measured homodyne noise floor over this time, except for a short period starting at the 18 minute mark, where the PZT actuator for the homodyne phase ran out of range, and was re-locked to an adjacent fringe.

## 9.4 Analysis of the noise performance of quantum noise locking

In this section a theoretical calculation of the noise performance of quantum noise locking is presented.

### 9.4.1 Case II: A squeezed vacuum state

Since it is the variance, or noise power of the detected squeezed state which is used to derive the error signal, the noise performance of the lock depends on the variance of the variance, or the *noise on the noise* of the state. This can be found by taking the kurtosis<sup>5</sup>, which we label  $\Delta V_a^\theta$ . For the amplitude quadrature of the field,  $a$ , in the squeezed vacuum state, with variance in the squeezed quadrature of  $e^{-2R}$  and in the anti-squeezed quadrature of  $e^{2R}$ , the kurtosis is given by

$$\begin{aligned}\Delta V_1^{(a)} &= \sqrt{\left\langle \left( \delta X_1^{(a)} - \langle \delta X_1^{(a)} \rangle \right)^4 \right\rangle - \left\langle \left( \delta X_1^{(a)} - \langle \delta X_1^{(a)} \rangle \right)^2 \right\rangle^2}, \\ &= \sqrt{2}V_1^{(a)},\end{aligned}\tag{9.18}$$

and similarly for the phase quadrature,  $\Delta V_2^{(a)} = \sqrt{2}V_2^{(a)}$ . Note that the kurtosis is a factor of  $\sqrt{2}$  larger than the variance. As a measure of locking noise performance, the kurtosis of the photocurrent,  $\Delta V_\theta$  is expressed in terms of phase fluctuations,  $\Delta\theta$ . The kurtosis is equated with the variance due to phase fluctuation. Using a Taylor expansion of  $\tilde{V}_\theta^{(a)}$  to second order around  $\theta = \theta_0$

$$\Delta \tilde{V}_\theta^{(a)}(\theta_0) \simeq \left. \frac{d\tilde{V}_\theta^{(a)}}{d\theta} \right|_{\theta_0} \Delta\theta + \frac{1}{2} \left. \frac{d^2\tilde{V}_\theta^{(a)}}{d\theta^2} \right|_{\theta_0} (\Delta\theta)^2.\tag{9.19}$$

Expanding both sides, the equation becomes

$$\sqrt{2}(\tilde{V}_1^{(a)} \sin^2 \theta_0 + \tilde{V}_2^{(a)} \cos^2 \theta_0) = \left| (\tilde{V}_1^{(a)} - \tilde{V}_2^{(a)}) \sin 2\theta_0 \Delta\theta + (\tilde{V}_1^{(a)} - \tilde{V}_2^{(a)}) \cos 2\theta_0 (\Delta\theta)^2 \right|,\tag{9.20}$$

<sup>4</sup>This data is reproduced from chapter 7 for convenience.

<sup>5</sup>The kurtosis is the fourth order moment of the distribution.

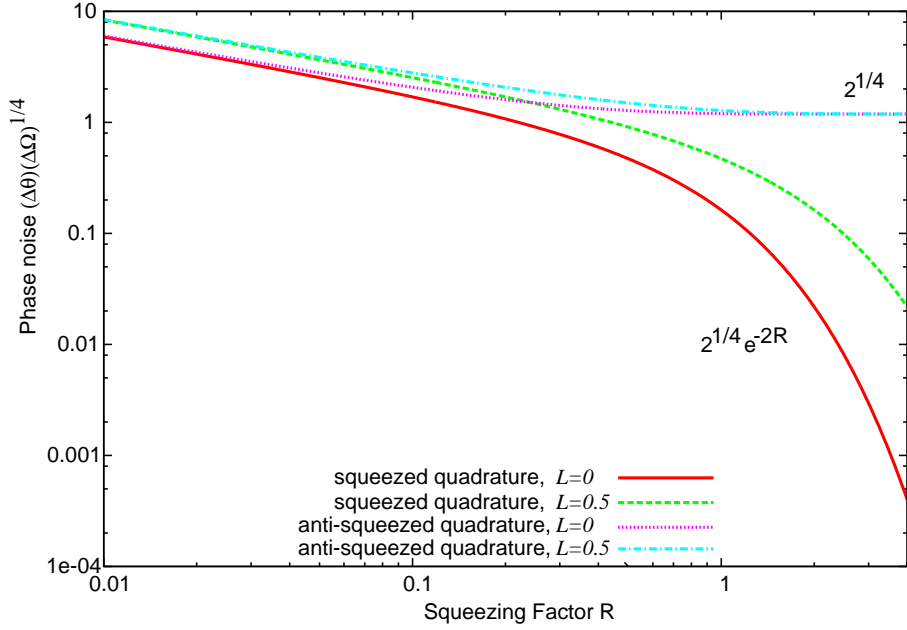


**Figure 9.11:** Squeezing angle stability vs squeezing factor,  $R$ , for the cases of quantum noise locking to the squeezed and anti-squeezed quadrature, for various levels of detection loss,  $\mathcal{L}$ .

which can be solved for the phase fluctuations,  $\Delta\theta$ , at the two lock points ( $\theta_0 = 0, \pi/2$ ). We find the phase fluctuations are

$$\Delta\theta|_{\theta_0=\pi/2} = \sqrt{\frac{\sqrt{2}\tilde{V}_1^{(a)}}{\tilde{V}_2^{(a)} - \tilde{V}_1^{(a)}}}, \quad (9.21)$$

$$\Delta\theta|_{\theta_0=0} = \sqrt{\frac{\sqrt{2}\tilde{V}_2^{(a)}}{\tilde{V}_2^{(a)} - \tilde{V}_1^{(a)}}}. \quad (9.22)$$

Equations 9.21 and 9.22 can be rewritten in terms of squeezing factor,  $R$ , detection loss,  $\mathcal{L}$ ; and detection bandwidth,  $\Delta\Omega$ . With detection loss included the variance is degraded and vacuum fluctuations are introduced, i.e.  $V_{1,2}^{(a)'} \rightarrow (1 - \mathcal{L})V_{1,2}^{(a)} + \mathcal{L}$ . The dependence on detection bandwidth can be included by noting that the variance, which provides the signal for quantum noise locking, is proportional to the detection bandwidth,  $\Delta\Omega$ . The associated noise, which is proportional to the kurtosis, is proportional to the square root of the detection bandwidth,  $(\Delta\Omega)^{1/2}$ . The phase noise of the squeezed and anti-squeezed quadratures are given by

$$\Delta\theta|_{\theta_0=\pi/2} \sim \sqrt{\frac{1 + \frac{\mathcal{L}}{1-\mathcal{L}}e^{2R}}{e^{4R} - 1}} \left(\frac{2}{\Delta\Omega}\right)^{1/4}, \quad (9.23)$$

$$\Delta\theta|_{\theta_0=0} \sim \sqrt{\frac{1 + \frac{\mathcal{L}}{1-\mathcal{L}}e^{-2R}}{1 - e^{-4R}}} \left(\frac{2}{\Delta\Omega}\right)^{1/4}, \quad (9.24)$$

where we have taken the case of amplitude quadrature squeezing. The stability of the two lock points are plotted as a function of squeezing factor in figure 9.11 (the detection bandwidth has been normalised out). The noise performance of the squeezed and anti-squeezed quadratures improves as the squeezing factor is increased. This is not surprising since it is from the quadrature

asymmetry that the error signal is derived. Perhaps more surprising is the different behavior of the two quadratures. The noise performance of the squeezed quadrature lock becomes perfect in the limit of perfect squeezing, since the noise of the variance becomes infinitely small. Note that losses and detector inefficiency mean that this will never be produced experimentally. The residual phase noise of the anti-squeezed quadrature lock point approaches  $2^{1/4}$  at high squeezing factor, and is always worse than the squeezed quadrature lock stability. The noise performance of the lock for both quadratures improves as the detection bandwidth is increased, albeit with a weak dependence ( $\Delta\Omega^{(1/4)}$ ).

To compare the predictions of equations 9.23 and 9.24 to the experimental measurements, we converted the phase noise to displacement noise with units of  $\text{m/Hz}^{1/2}$ . This is done using

$$\frac{\Delta\theta}{\Delta x} = \frac{2\pi}{\lambda/2}, \quad (9.25)$$

so

$$\Delta x = \frac{\lambda}{4\pi} \Delta\theta, \quad (9.26)$$

Using the experimental values ( $R = 0.46$ ,  $\mathcal{L} = 1 - \eta_{tot} = 0.26$ ,  $\Delta\Omega/2\pi = 18\text{MHz}$ , and  $\lambda = 1064\text{nm}$ ) the displacement noise is predicted to be

$$\Delta x|_{\theta_0=\pi/2} \sim 1.2 \text{ nm/Hz}^{1/2}, \quad (9.27)$$

$$\Delta x|_{\theta_0=0} \sim 2.3 \text{ nm/Hz}^{1/2}, \quad (9.28)$$

which are very close to the measured values of  $1.3 \text{ nm/Hz}^{1/2}$  and  $2.6 \text{ nm/Hz}^{1/2}$  for the squeezed and anti-squeezed quadrature, respectively. Here we have used the average squeeze factor over the detection band.

### 9.4.2 Case I: Locking coherent fields

The calculation of the noise performance of the locking of coherent fields can be calculated in similar fashion to case II. The phase fluctuations when locking to the dark ( $\theta_0 = \pi$ ) and bright ( $\theta_0 = 0$ ) fringes are

$$\Delta\theta|_{\theta_0=\pi} \sim \sqrt{\frac{\sqrt{2}(a-b)^2}{ab}} \left(\frac{1}{\Delta\omega}\right)^{1/4}, \quad (9.29)$$

$$\Delta\theta|_{\theta_0=0} \sim \sqrt{\frac{\sqrt{2}(a+b)^2}{ab}} \left(\frac{1}{\Delta\omega}\right)^{1/4}. \quad (9.30)$$

Note that kurtosis in this case has the same dependence on variance as in case of squeezed state. Equations 9.29 and 9.30 can be rewritten in terms of fringe visibility of the Mach-Zehnder.

$$\Delta\theta|_{\theta_0=\pi} \sim \sqrt{\frac{1-\mathcal{V}}{\sqrt{2}\mathcal{V}}} \left(\frac{1}{\Delta\omega}\right)^{1/4}, \quad (9.31)$$

$$\Delta\theta|_{\theta_0=0} \sim \sqrt{\frac{1+\mathcal{V}}{\sqrt{2}\mathcal{V}}} \left(\frac{1}{\Delta\omega}\right)^{1/4}. \quad (9.32)$$

The functional form is the same for the dark fringe stability and the squeezed quadrature stability, equations 9.31 and 9.23, respectively. Similarly for the bright fringe and anti-squeezed quadrature stabilities, equations 9.30 and 9.24 respectively. The dependence on detection bandwidth is found to be identical in the two cases.

Again, to compare the predictions of equations 9.31 and 9.32 to the experimental measurements, we convert the phase noise to displacement noise with units of  $\text{m/Hz}^{1/2}$ . This is done using

$$\frac{\Delta\theta}{\Delta x} = \frac{2\pi}{\lambda}, \quad (9.33)$$

so

$$\Delta x = \frac{\lambda}{2\pi} \Delta\theta. \quad (9.34)$$

Note the factor of two difference between equations 9.26 and 9.34. This factor two difference arises because the required change in optical path length to cycle dark and bright fringes is  $\Delta x = \lambda$ , whereas the change in path length required to cycle squeezed and anti-squeezed quadratures is  $\Delta x = \lambda/2$ . Using the experimental values ( $\mathcal{V} = 0.6$ ,  $\Delta\Omega/2\pi = 18\text{MHz}$ , and  $\lambda = 1064\text{nm}$ ) we predict

$$\Delta x|_{\theta=\pi} \sim 2.3 \text{ nm/Hz}^{1/2}, \quad (9.35)$$

$$\Delta x|_{\theta=0} \sim 4.6 \text{ nm/Hz}^{1/2}, \quad (9.36)$$

which is again close to the measured values of  $2.5 \text{ nm/Hz}^{1/2}$  and  $5.5 \text{ nm/Hz}^{1/2}$  of the dark and bright fringes.

## 9.5 Discussion

Although the noise performance of quantum noise locking was found to be inferior to dither locking in this experiment, in the absence of coherent fields, the quantum noise locking technique remains a good candidate for extracting error signals to control quadrature phases. With moderate detection bandwidth ( $\Delta\Omega/2\pi = 18\text{MHz}$  and fringe visibility ( $\mathcal{V} = 0.6$ ), the noise performance of quantum noise locking was on the order of 100 times worse than dither locking technique. The noise floor for locking squeezed vacuum had similar performance. From a theoretical point of view, the noise performance of quantum noise locking a squeezed vacuum can be improved by two avenues. The first is to increase the detection bandwidth, the second is to increase the squeezing amplitude. The detection bandwidth dependence of the noise performance is weak, it goes as  $(1/\Delta\Omega)^{1/4}$ . The detection bandwidth used here was  $\Delta\Omega/2\pi = 18\text{MHz}$ , it would be difficult to make this significantly larger. The best way to improve the noise performance of this experiment would be to increase the squeeze factor. The squeeze factor averaged over the detection band was just  $R = 0.46$  (4dB). This was low because the squeezing/anti-squeezing magnitude reduced as a function of frequency due to the cavity pole. An OPO with a larger linewidth would translate readily into an increase the squeeze factor and stability. For example if the squeeze factor was to increase the value measured at 1MHz  $R = 1.15$  (10dB) the stability would improve by a factor of 2.6.

## **9.6 Chapter summary**

In this chapter we have analyzed the quantum noise locking technique and compared it with dither locking. Quantum noise locking was found to have inferior noise performance to dither locking. The stability of quantum noise locking was analyzed and it was found the stability improves with squeezing amplitude and detection bandwidth and the squeezed quadrature lock stability is always superior to the anti-squeezed quadrature lock stability. Detector inefficiencies and losses were found to degrade the stability of quantum noise locking, since uncorrelated vacuum fluctuations are coupled into the signal.

---

# Phase matching locking via optical readout

---

In this chapter a technique developed to readout the phase matching condition of a nonlinear medium is introduced. In this technique, the phase matching condition is readout interferometrically using the interacting fields. We describe this technique theoretically and demonstrated it in an experiment. This research is based on the publication:

*Nonlinear phase matching locking via optical readout.*

K. McKenzie, M. B. Gray, P. K. Lam, and D. E. McClelland  
Optics Express **14**, 11256-11264 (2006).

## 10.1 Introduction

An elementary requirement for efficient  $\chi^{(2)}$  nonlinear interaction is the conservation of momentum, also referred to as the phase matching condition (see section 3.4). In birefringent materials phase matching can be achieved using *type I*, *type II* or *quasi* phase matching (see section 3.4.2). Consider the example of a SHG or degenerate OPA that is type I phase matched. In SHG or degenerate OPA's the low energy interacting fields have the same optical frequency,  $\omega_a = \omega_{a'}$ , and the high energy interacting field has twice that frequency  $\omega_b = 2\omega_a$ . Henceforth, we shall refer to the field with frequency  $\omega_a$  as the fundamental field, and to  $\omega_b$  as the harmonic field. The phase matching condition in this type I degenerate system is achieved by matching the refractive indices for the two frequencies:  $n_b = n_a$ . To match these indices the polarization of the fundamental field is set to the crystal's ordinary axis, the harmonic to the extraordinary axis, and the crystal temperature is tuned. Temperature tuning changes the ordinary and extraordinary refractive indices differentially according to the Sellmeier equation [96], until they become equal at the phase matched temperature.

In most experiments that use type I phase matched media, the nonlinear medium must be temperature controlled to maintain the phase matching condition. Typically, the temperature of the nonlinear medium is sensed by a nearby thermister and actuated by a peltier (thermo-electric) element or resistive heater. Stabilizing the phase matching condition using a temperature sensor on the exterior of the nonlinear medium has inherent disadvantages. An external sensor reads out the external temperature, rather than temperature of the optical path through the crystal where the nonlinear interaction occurs. Therefore, temperature change in the nonlinear interaction region, say due to absorbed laser power, will not necessarily be sensed or suppressed by the temperature control loop. Instead a temperature gradient will arise between the interaction region and the boundary of the nonlinear medium. Thus, if an external temperature readout and control system

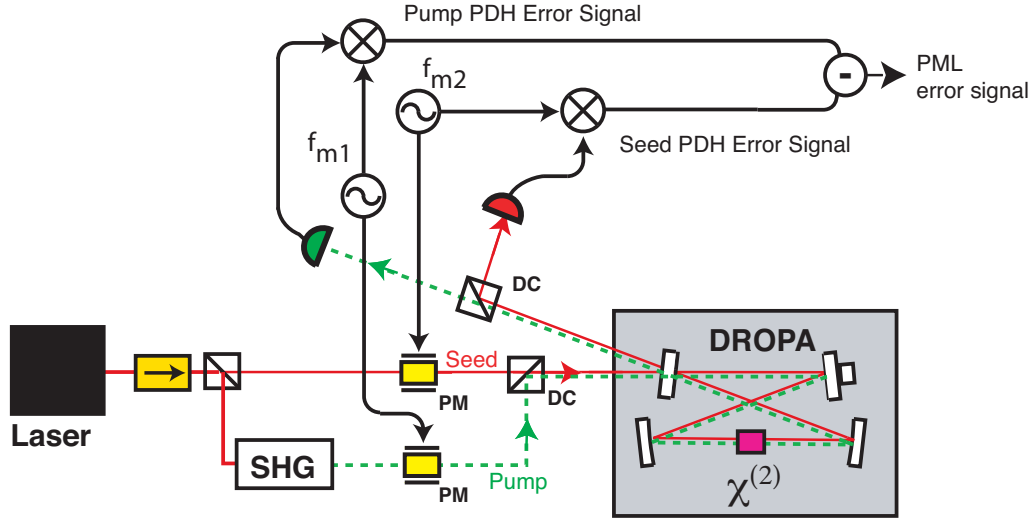


**Figure 10.1:** Schematic of an experiment to derive phase matching locking error signal from a doubly-resonant optical parametric amplifier (DROPA). The red (unbroken) lines indicate the fundamental (seed) field and the green (dashed) lines indicate the harmonic (pump) field. PDH error signals are derived for both cavities and differenced to give the phase-matching locking error signal. SHG - second harmonic generator, PM - phase modulator, DC1 & DC2- dichroic mirrors used to separate the fundamental and harmonic frequencies.  $\chi^{(2)}$  indicates the nonlinear medium.

is used, the temperature may require manual adjustment for each laser power. This is a problem because lasers have inherent power fluctuations over both short and long time scales.

Here we present an alternative to a temperature sensor readout, which we call phase matching locking. The phase-matching locking technique works in a radically different way to standard temperature sensors. Phase-matching locking uses the optical fields that interact in the nonlinear medium in a doubly-resonant OPA to derive an error signal for the phase matching condition of the nonlinear medium. Using the optical fields enables fast readout of the phase matching condition, exactly where the nonlinear process is occurring. The phase-matching readout involves monitoring the cavity resonance conditions at both the fundamental and harmonic frequencies of the doubly-resonant OPA using a standard locking technique, for example the Pound-Drever-Hall (PDH) technique [142]. A schematic of an experiment to derive a phase-matching error signal is shown in figure 10.1. The doubly-resonant OPA has input fields at the harmonic (the pump field) and fundamental frequencies (the seed field). Both input fields receive phase modulation, at different modulation frequencies, and the reflected fields are detected and demodulated to derive the PDH error signals for each cavity. The phase-matching error signal is obtained by differencing the PDH error signals. Mathematically, this can be represented by

$$\mathcal{E}_{pml} = \mathcal{E}_b - \mathcal{E}_a, \quad (10.1)$$

where  $\mathcal{E}_b$  is the cavity error signal of the harmonic field,  $\mathcal{E}_a$  is the cavity error signal of the fundamental field, and  $\mathcal{E}_{pml}$  is the phase-matching error signal. The mathematical detail and derivation of the phase-matching error signal is in section 10.3. For now, consider a doubly-resonant OPA that is phase matched ( $n_b = n_a$ ). If the doubly-resonant OPA cavity is held on resonance for the harmonic frequency, then because the two fields have the same optical path length, the fundamental field will also be resonant<sup>1</sup>. With both cavities on resonance, both PDH

<sup>1</sup>Actually, having the harmonic cavity on resonance does not guarantee co-resonance, only every second FSR re-

error signals, and subsequently, the phase-matching error signal, will read zero. If a phase mismatch is introduced, the refractive indices in the nonlinear medium are no longer equal ( $n_b \neq n_a$ ) for the two fields and so the optical path length of the cavities will be different, and co-resonance no longer occurs. The fundamental field will still be on resonance, since the control system is forcing it to be so, but the harmonic field will no longer be on resonance. The PDH error signal of the harmonic field will have a non-zero value, and therefore so will the phase-matching signal.

In this chapter we describe the phase-matching locking technique theoretically and demonstrate it experimentally. We start by deriving the nonlinear gain of a doubly-resonant OPA as a function of temperature offset from phase matching in section 10.2. Our model shows that the FWHM temperature of the nonlinear gain is significantly smaller than in the singly-resonant- or single-pass OPA, motivating the requirement for precision phase matching control. In section 10.3 we derive a phase-matching error signal, starting with error signals from the PDH technique. In section 10.4, an experimental demonstration of phase-matching locking is presented. Readout of the phase-matching error signal is shown and the active control of the phase matching temperature is implemented. Fast actuation of the crystal temperature is achieved using the photothermal effect [76, 121, 169, 170]. The phase matching error signal was used to modulate the harmonic (pump) field amplitude, which is partially absorbed in the nonlinear medium. This actuation can be extremely fast ( $\sim 100\text{kHz}$ ) compared to using an external temperature actuator, which has bandwidth limitations due to the time delay associated with thermal conductivity of the nonlinear medium.

## 10.2 Nonlinear gain in a doubly-resonant OPA

In this section we derive the nonlinear gain in a doubly-resonant OPA as a function of phase mismatch. This gives the reader some insight into the effect of phase mismatch in doubly-resonant OPA. The results show the enhanced nonlinearity of a doubly-resonant system and the narrowing of the phase matching condition, motivating better phase matching control.

The classical  $\chi^{(2)}$  nonlinear optic equations of motion are (see section 3.5)

$$\dot{a} = -(\kappa^a + i\Delta^a)a + \varepsilon^* a^* b + \sqrt{2\kappa_{in}^a} A_{in}, \quad (10.2)$$

$$\dot{b} = -(\kappa^b + i\Delta^b)b - \frac{\varepsilon a^2}{2} + \sqrt{2\kappa_{in}^b} B_{in}, \quad (10.3)$$

where  $a$  and  $b$  are proportional to the the intra-cavity fundamental and second harmonic fields, respectively;  $\kappa^a$  and  $\kappa^b$  are the total resonator decay rates for each field;  $\varepsilon$  is the nonlinear coupling parameter; and  $A_{in}$  and  $B_{in}$  are the driving fields with the respective input coupling rates  $\kappa_{in}^a$  and  $\kappa_{in}^b$ . The angular frequency detuning of the fundamental and harmonic cavities with respect to the driving field frequencies are given by  $\Delta^a$  and  $\Delta^b$ . In this calculation we consider all of the optical fields to be classical fields, in contrast to most of the work in this thesis where the quantum noise properties are important.

The nonlinear coupling parameter dependence on temperature is due to the phase mismatch,  $\Delta k$ , in the following form [4]

$$\varepsilon = \varepsilon_0 L_c e^{i\frac{\Delta k L_c}{2}} \text{sinc} \frac{\Delta k L_c}{2}, \quad (10.4)$$

---

sults in co-resonance. Also this is only the case if we assume no differential phase shift between the harmonic and fundamental frequencies on the mirror coatings. In practice, we use the dispersion compensation window to null the effect of a differential phase shift, as described in appendix C.3.

where  $\varepsilon_0$  is a constant. The Sellmeier equation at the fundamental frequency is  $\Delta k = \xi(\delta T)$ , where  $\xi$  is a constant whose value depends on the crystal's properties, and  $\delta T$  is the crystal's temperature offset from the phase matched temperature. We limit the calculation to the non-pump depleted regime where  $\varepsilon a^2/2 \ll \sqrt{2\kappa_{in}^b B_{in}}$ . The steady state intra-cavity field amplitudes are found by setting  $\dot{a} = \dot{b} = 0$

$$a = \frac{\sqrt{2\kappa_{in}^a} A_{in} ((\kappa^a - i\Delta^a) + \varepsilon^* b^*)}{(\kappa^a)^2 + (\Delta^a)^2 - |\varepsilon b|^2}, \quad b \approx \frac{\sqrt{2\kappa_{in}^b} B_{in}}{\kappa^b + i\Delta^b}. \quad (10.5)$$

As described in equation 10.4, deviation from the phase matching condition results in reduced nonlinear gain. In a doubly-resonant OPA, where the interacting fields share the same optical cavity, a phase mismatch also results in relative detuning of the two cavity resonances. The cavity detunings are due to change in the optical path length at the fundamental frequency,  $\delta p^a$ , and at the harmonic frequency,  $\delta p^b$ , are given by the following equations [90],

$$\Delta^a = -2\pi v_{fsr} \frac{\delta p^a}{\lambda^a}, \quad (10.6)$$

$$\Delta^b = -2\pi v_{fsr} \frac{\delta p^b}{\lambda^b}, \quad (10.7)$$

where  $v_{fsr} = c_0/p$  is the cavity FSR with the total optical path length;  $p = L + n^j L_c$ , with  $L$  the round trip length in free space,  $L_c$  the length of the crystal, and  $c_0$  is the speed of light in vacuum. The refractive index of the crystal is  $n^j$  for  $j = \{a, b\}$  and wavelengths of the fields in vacuum are  $\lambda^j$ .  $\delta p$  can come from change to the free space optical path length,  $\delta L_{fs}$ , and from change in the crystal optical path length,  $\delta L_{cr}^j$ . The crystal optical path length is a function of crystal temperature change,  $\delta T$ , arising from two mechanisms, thermal expansion and refractive index change

$$\begin{aligned} \delta p^j &= \delta L_{fs} + \delta L_{cr}^j, \\ &= \delta L_{fs} + n L_c \left( \frac{1}{n} \frac{dn_j}{dT} + \alpha_j \right) \delta T, \end{aligned} \quad (10.8)$$

where  $dn^j/dT$  are the crystal's photorefractive constants and  $\alpha_j$  are the crystal's thermal expansion constants. Since the operation point is close to the phase-matched condition, the refractive indices are set to  $n^a = n^b = n$ . Using equation 10.8, the total cavity detuning can be written as a sum of detuning due to change in free space optical path length,  $\Delta_{fs}^j$ ; and detuning due to a change in crystal optical path length,  $\Delta_{cr}^j$

$$\Delta^j = \Delta_{fs}^j + \Delta_{cr}^j(\delta T), \quad (10.9)$$

The next case considered here assumes that the harmonic cavity is actively controlled by a feedback loop, which actuates on the free space length of the cavity to suppress any cavity detuning ( $\Delta^b \rightarrow 0$ ). If the crystal is at the phase matched temperature, and there are no other forms of dispersion, the fundamental cavity will also be on resonance, and optimal nonlinear interaction will occur. If the temperature of the crystal is changed from phase matching, the optical path length in the crystal will change for both the harmonic and fundamental fields according to equation 10.8. The control system will then change the free space optical path length to compensate for the change in crystal optical path length by an amount  $\Delta_{fs}^b = -\Delta_{cr}^b(\delta T)$  in order to maintain cavity resonance. The resulting detuning of the fundamental cavity can be found by substituting

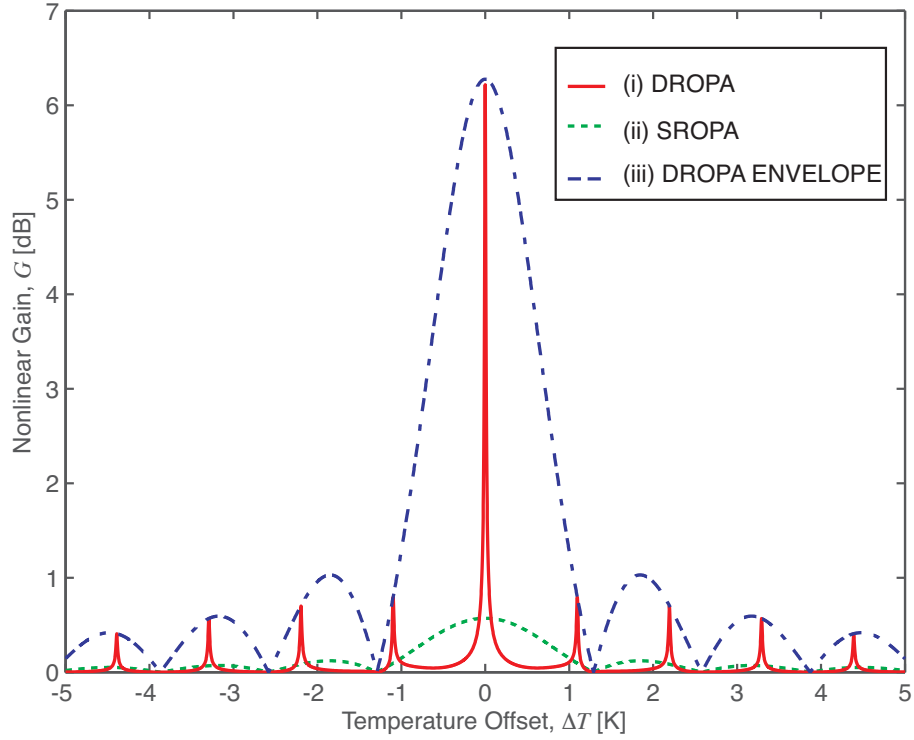


**Figure 10.2:** Examples of nonlinear gain (equation 10.14) vs temperature offset from phase matching. Curve (i) is a doubly resonant (DR) OPA with the harmonic cavity held on resonance ( $\Delta^b = 0$ ) and the fundamental detuning given by equation 10.11. Curve (ii) is a singly-resonant (SR) OPA with the fundamental cavity held on resonance ( $\Delta^a = 0$ ). The dashed curve (iii) gives the nonlinear gain envelope of the DROPA found when both fundamental and harmonic cavities are held on resonance ( $\Delta^b = \Delta^a = 0$ ). Parameters used are  $P_{in}^b = .1\text{W}$ ,  $\epsilon_0 = 60\text{ 1/s}$ , and  $\theta = 0$ .

this into the total detuning of the fundamental cavity

$$\Delta^a = \Delta_{fs}^a + \Delta_{cr}^a(\delta T), \quad (10.10)$$

$$= \Delta_{cr}^a(\delta T) - 2\Delta_{cr}^b(\delta T), \quad (10.11)$$

where we have used  $\Delta_{fs}^a = 2\Delta_{fs}^b$ . Thus the detuning for the fundamental cavity is proportional to the change in crystal optical path length at the fundamental and harmonic frequencies, which is caused by temperature tuning of the crystal. Equation 10.11 can be extended to include more than one longitudinal mode of the fundamental cavity; and an arbitrary differential phase shift between the fundamental and harmonic fields,  $\theta$ . The total detuning then becomes

$$\Delta_l^a = \Delta^a - 2\pi\nu_{fsr}[\theta/(2\pi) + l], \quad (10.12)$$

where  $l$  is the longitudinal cavity mode number. The intra-cavity amplitude of an  $l$ th mode is

$$a_l = \frac{\sqrt{2\kappa_{in}^a} A_{in} [(\kappa^a - i\Delta_l^a) + |\epsilon^* b^*| e^{i\phi_l}]}{(\kappa^a)^2 + (\Delta_l^a)^2 - |\epsilon b|^2}, \quad (10.13)$$

where the phase  $\phi_l$  is the combined angle  $\angle(\epsilon^* b^*)$ , which can be varied by choosing the pump/seed phase to control the sign of the parametric gain. Experimentally, a control loop can be used to set the angle  $\phi_l = \mp \angle(\kappa^a + i\Delta_l^a)$  which maximizes (–) or minimizes (+) the parametric gain.

**Table 10.1:** Doubly-resonant OPA Cavity/Mg:LiNbO<sub>3</sub> Parameters

Parameter	Symbol	Value	Units
Fundamental Wavelength	$\lambda_a$	1064	nm
Second-Harmonic Wavelength	$\lambda_b$	532	nm
Reflectivity of Input Coupler at $\lambda_a$	$R_a^{in}$	99.99	%
Reflectivity of Output Coupler at $\lambda_a$	$R_a^{out}$	90	%
Reflectivity of Input Coupler at $\lambda_b$	$R_b^{in}$	97	%
Absorption Rate at $\lambda_a$	-	0.1	%/cm
Absorption Rate at $\lambda_b$	-	2.0	%/cm
Crystal Length	$L_c$	0.0065	m
Cavity Free Space Length	$L$	0.65	m
Phase-Matched Refractive Index	$n$	2.233	-
Phase Mismatch Constant	$\xi$	749	1/m/K
Nonlinear Coupling Parameter	$\varepsilon$	60	1/s
Intracavity pump field amplitude	$b$	$2 \times 10^5$	$\sqrt{\text{photons}}$
Thermal Expansion Const. of Ordinary Axis	$\alpha_a$	$14 \times 10^{-6}$	1/K
Thermal Expansion Const. of Extraordinary Axis	$\alpha_b$	$4 \times 10^{-6}$	1/K
Photo-refractive Const. of Ordinary Axis	$dn_a/dT$	$3.3 \times 10^{-6}$	1/K
Photo-refractive Const. of Extraordinary Axis	$dn_b/dT$	$37.0 \times 10^{-6}$	1/K

The parametric gain is calculated from the ratio of the transmitted power with and without the pump field

$$\frac{P_{trans}}{P_{trans}|_{b=0}} = \frac{|a_l|^2}{|a_l|_{b=0}|^2}. \quad (10.14)$$

The parametric gain is plotted in figure 10.2 as a function of temperature offset from phase matching, with parameters similar to those in our experiment, given in table 10.1. The compromise between nonlinear gain and temperature stability requirements can be seen in the comparison between the doubly-resonant OPA with a high reflectivity input coupler at the harmonic frequency of 97%, curve (i), compared to the singly-resonant OPA, curve (ii) which has 0% reflectivity. The resonant enhancement of the nonlinearity gives the doubly-resonant OPA additional nonlinear gain over the singly-resonant OPA, however the FWHM of the nonlinear gain is significantly smaller than for the singly-resonant OPA. The doubly-resonant OPA envelope, curve (iii), shows the envelope of the possible nonlinear gains as the differential phase shift  $\theta$  is varied. Changing  $\theta$  moves the ‘comb’ of longitudinal cavity modes along the temperature axis, and the gain is scaled by  $\varepsilon$ . The doubly-resonant OPA envelope trace can also be realized experimentally using individually tunable cavities for the fundamental and harmonic fields, as done by Longchambon *et. al* [171].

### 10.3 Derivation of a phase matching locking error signal

Near the phase matching temperature, the cavity resonance conditions can be monitored using standard cavity readout techniques, and this readout can be used to produce a phase matching error signal. Here we derive the phase-matching error signal using the PDH technique for the harmonic cavity and transmission dither locking for the fundamental cavity. In the experimental demonstration presented in the following section, we derive the PDH error signal in reflection for the harmonic field, and use transmission dither locking for the fundamental field. This provides

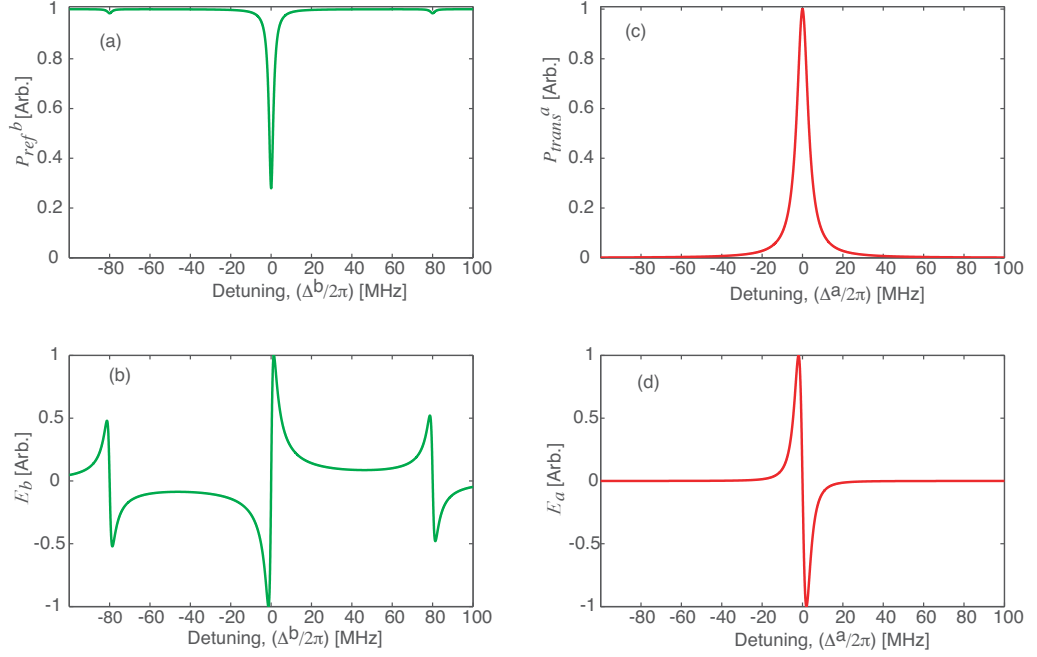


**Figure 10.3:** (a) The reflected power of the harmonic field as a function of cavity detuning; (b) the corresponding PDH error signal (equation 10.15) derived from the reflected light; (c) the transmitted power of the fundamental field as a function of detunings; and (d) the corresponding PDH error signal derived on transmission.

optimal shot noise limited performance for the harmonic field, which ‘sees’ a near impedance matched cavity. The fundamental field is injected through a highly reflective mirror, and is highly undercoupled. The PDH error signal for the harmonic cavity is [143]

$$\mathcal{E}_b = -2\sqrt{P_c^b P_s^b} \text{Im}(\mathcal{R}(\Delta^b) \mathcal{R}(\Delta^b + \omega_m)^* - \mathcal{R}(\Delta^b)^* \mathcal{R}(\Delta^b - \omega_m)), \quad (10.15)$$

where  $\mathcal{R}(\Delta)$  is the cavity reflectivity parameter given by equation 3.77<sup>2</sup>;  $\omega_m$  is the modulation frequency chosen to be much greater than the cavity linewidth and  $P_c^b$  and  $P_s^b$  are the powers in the carrier and modulation sideband fields. These are given by

$$P_c^j = J_0(\beta^j)^2 P_0^j, \quad (10.16)$$

$$P_s^j = J_1(\beta^j)^2 P_0^j, \quad (10.17)$$

where  $P_0^j$  is the input power in the  $j$ th field and  $J_0^j(\beta^j)$  and  $J_1^j(\beta^j)$  are Bessel functions of the first kind. By using the coefficient  $\mathcal{R}(\Delta)$ , pump depletion has (again) been neglected. The error signal for the fundamental field is given by

$$\mathcal{E}_a = -2\sqrt{P_c^a P_s^a} (\text{Re}(\mathcal{T}_G(\Delta^a) \mathcal{T}_G(\Delta^a + \omega_n)^* - \mathcal{T}_G(\Delta^a)^* \mathcal{T}_G(\Delta^a - \omega_n))), \quad (10.18)$$

where  $\omega_n$  is the modulation frequency, chosen to be much less than the cavity linewidth and  $\mathcal{T}_G(\Delta^a)$  is a modified version of the cavity transmission parameter  $\mathcal{T}(\Delta^a)$  (equation 3.77), which includes

<sup>2</sup>Note that the coefficient  $\mathcal{R}(\Delta)$  corresponds to  $\mathcal{F}(\omega)$  in reference [143]. These coefficients have different forms because of the difference in formalism used here. We note that near cavity resonance  $\mathcal{R}(\omega) = \mathcal{F}(\omega)$ .

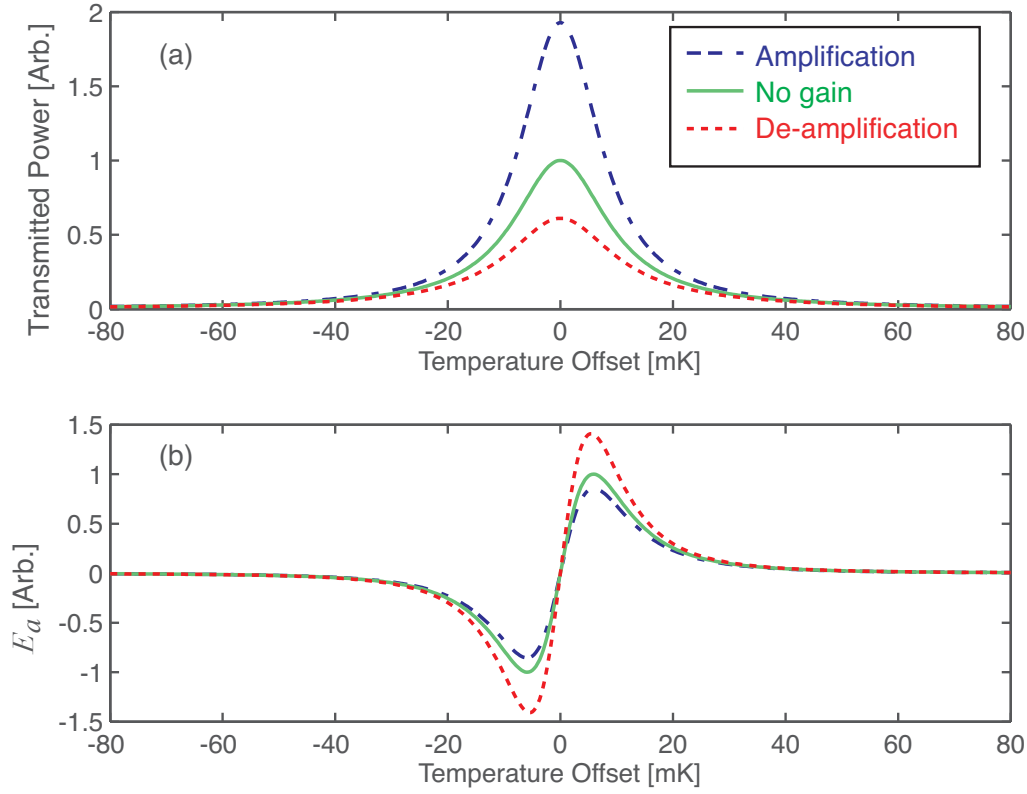


**Figure 10.4:** (a) The transmitted power of the fundamental field as a function of detuning; and (b) the corresponding phase-matching error signal derived on transmission. Here  $|\epsilon\bar{b}| = 0.28\kappa_a$ .

parametric gain

$$\mathcal{T}_G(\Delta^a) = \frac{2\sqrt{\kappa_{in}^a \kappa_{out}^a}[(\kappa^a - i\Delta^a) + |\epsilon^* b^*| e^{i\phi}]}{(\kappa^a)^2 + (\Delta^a)^2 - |\epsilon b|^2}. \quad (10.19)$$

The error signals of equations 10.15 and 10.18 are shown in figure 10.3 as a function of cavity detuning. As described in section 10.2, the harmonic error signal is used to control the cavity length, therefore the detuning at the harmonic frequency is driven to zero. In this case, if we assume no other forms of cavity dispersion, the detuning of the fundamental cavity is given by equation 10.11. The phase matching error signal can then be readout from the fundamental field

$$\mathcal{E}_{pml} = -2\sqrt{P_c^a P_s^a} \text{Re}(\mathcal{T}_G(\Delta^a) \mathcal{T}_G(\Delta^a + \omega_n)^* - \mathcal{T}_G(\Delta^a)^* \mathcal{T}_G(\Delta^a - \omega_n)). \quad (10.20)$$

Figure 10.4 shows the modeled transmitted power at the fundamental frequency and the phase-matching error signal as a function of crystal temperature. The form of the phase-matching error signal is exactly the same as the error signal in figure 10.3 (a), except the error signal is plotted as a function of temperature deviation from phase matching. The transmitted power and error signal have been plotted for three different cases; amplification, deamplification and with no parametric gain.

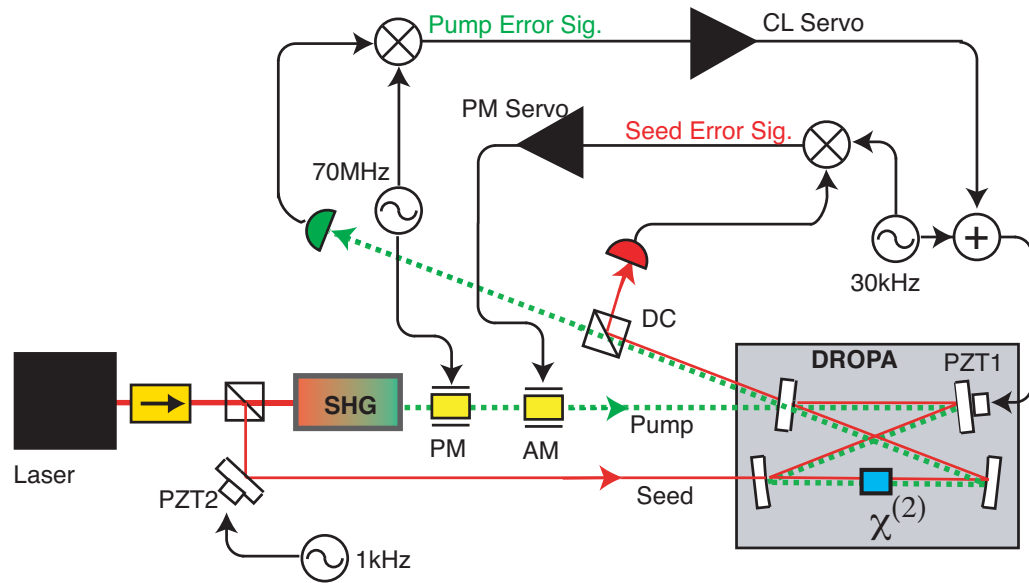


**Figure 10.5:** A schematic of the experimental layout. Most of the laser power is used to produce the harmonic beam for the OPA. The harmonic beam is passed through a broadband amplitude modulator (AM) and a resonant (70MHz) phase modulator (PM) before reaching the OPA. The cavity length error signal is derived from the reflected harmonic field, and is fed back to PZT1. The phase matching error signal is derived from the transmitted fundamental field, and is fed back to the amplitude modulator on the harmonic field. The temperature of the crystal oven is actively controlled to 63°C.

## 10.4 An experimental demonstration of phase matching locking

### 10.4.1 Experimental setup

A schematic of the experimental setup is shown in figure 10.5. This doubly resonant OPA and core optics were similar to those used in chapter 7. A 1.2W Nd:YAG laser operating at 1064nm was used to provide the fundamental (seed) field and to drive the SHG which provided the OPA pump beam at 532nm. The nonlinear medium was a 6.5mm long, type-I phase-matched MgO:LiNbO<sub>3</sub> crystal with 7% doping. The optical surfaces were flat and coated for anti-reflection at both wavelengths. The crystal was placed in a peltier driven oven held at  $\sim 63^\circ\text{C}$ , with approximately 5mK accuracy, using a Newport 3040 temperature controller. The doubly-resonant bow-tie cavity configuration consisted of three dichroic high reflectivity mirrors ( $R > 99.95@532\text{nm}$ ,  $R > 99.98@1064\text{nm}$ ) and the input/output coupler had transmissivity of 10% and 3% at 1064nm and 532nm, respectively. The intra-cavity loss at both wavelengths was dominated by the absorption in the crystal, which was 2%/cm at 532nm and 0.1%/cm at 1064nm. The incident harmonic (pump) power was 100mW, resulting in a circulating pump power of  $\sim 2.7\text{W}$ , corresponding to a parametric gain of just under 3dB. The harmonic cavity error signal was derived using the PDH technique from the reflected harmonic field with modulation frequency of 70MHz. This error signal was fed back to a piezo-electric transducer (PZT1) bonded to a cavity mirror. PZT1 was also modulated at 30kHz to produce phase modulation on the intra-cavity fields. The incident fundamental (seed) field was injected through a highly reflective mirror and had  $\sim 10\text{mW}$  of power. The transmission of the fundamental field was detected and demodulated (at 30kHz) to produce the phase matching error signal. The phase matching error signal was sent to an amplitude-modulator in the pump field's path to actuate on the crystal temperature via the photothermal effect. Photothermal actuation on the region of nonlinear interaction proved very effective, since most of the

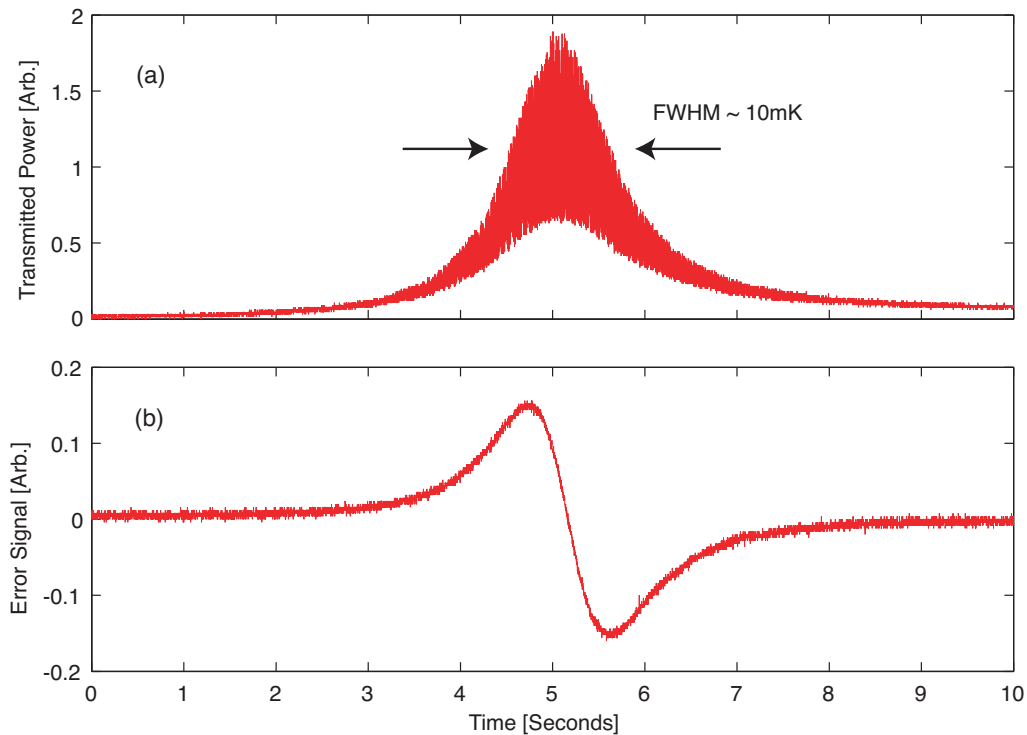


**Figure 10.6:** (a) The transmitted power from the OPA as the temperature of the crystal was varied by sweeping the oven temperature. The nonlinear gain was dithered at approximately 1kHz, which showed the nonlinear gain envelope (amplification and de-amplification). (b) The corresponding error signal of the phase matching condition. The dither signal of the nonlinear gain was filtered out of the error signal.

harmonic field was absorbed in the crystal.

## 10.4.2 Results

Figure 10.6 shows the transmission of the cavity at the fundamental frequency, plot (a), and the associated phase-matching error signal, plot (b), as the temperature of the crystal was swept across the phase matching temperature. This data was taken with the harmonic cavity locked on resonance. The relative phase of the harmonic and fundamental frequencies was swept rapidly by dithering PZT2 at 1kHz in order to sample amplification and de-amplification, to show the parametric gain envelope. The error signal here has been low pass filtered to remove any component associated with the nonlinear gain at 1kHz<sup>3</sup>.

With the harmonic field locked and the crystal's oven temperature set to the phase matched temperature, the parametric gain was found to wander. This nonlinear gain wander is evident from the transmitted power and phase-matching error signal shown in figure 10.7. Again, this measurement was taken whilst the phase of the nonlinear gain was dithered to display the nonlinear gain envelope. Up until 12.6 seconds into the measurement, the crystal was temperature controlled by the oven with temperature sensor on the crystal exterior. Even though a high precision temperature controller was used, the nonlinear gain and the error signal are seen to drift significantly over a fairly short time scale. This drift may be a result of air currents or photothermal fluctuations of the crystal temperature. At 12.6 seconds the phase matching temperature control loop was closed

<sup>3</sup>When using this technique for applications the phase difference of the fundamental and harmonic fields would be locked to either amplification or deamplification, rather than scanned rapidly, as is done here.

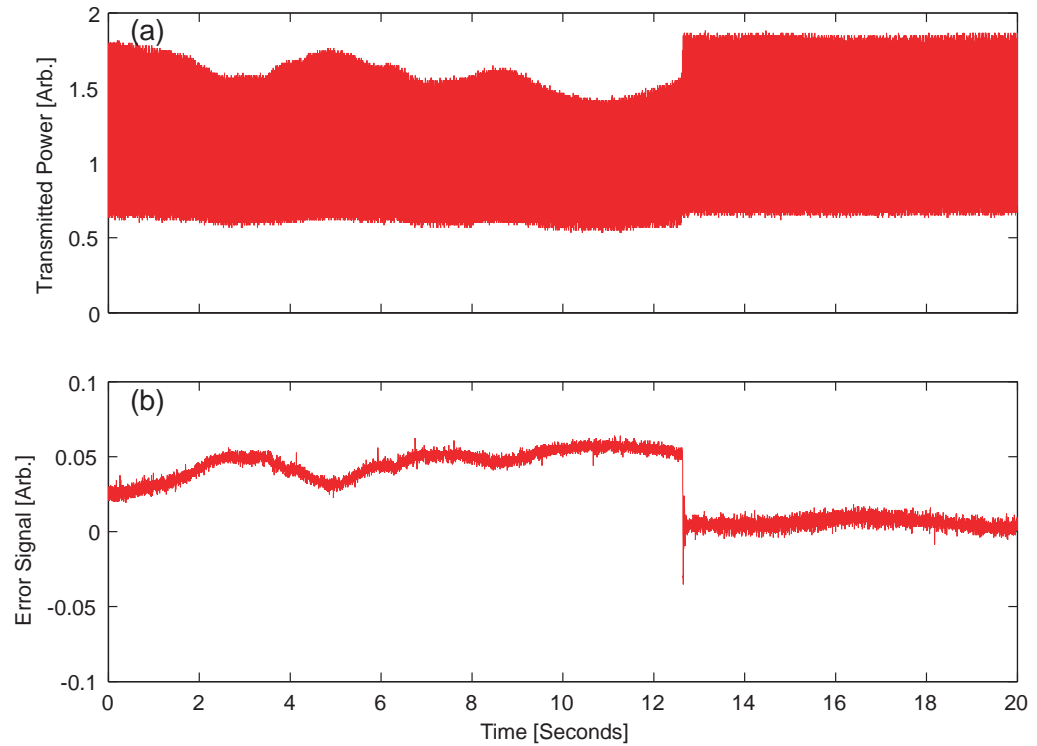


**Figure 10.7:** (a) The transmitted power of the OPA as a function of time. (b) The phase matching error signal. At 12.5 seconds the control loop is closed and the nonlinear gain is optimized.

and the parametric gain moved to its maximum value. The phase-matching control loop provided a stable lock, however it had limited dynamic range due to the limitations of the photothermal actuator.

A comparison of the temperature stability with and without phase matching control was made by comparing the phase-matching error signal with the control loop active and inactive. Without phase-matching control, the mean temperature offset was 3mK and the standard deviation was 0.7mK, whereas, with phase-matching control, the mean temperature offset was 0.5mK and the standard deviation was 0.3mK. These data were calculated over a 5 second interval with the error signal slope calibrated (to Kelvins/Volt) using the a measured value of the FWHM in temperature space.

Figure 10.8 shows the phase matching locking error signal spectra calibrated as a function of temperature fluctuation. Curve (i) shows the spectrum with the control loop open and curve (ii) shows the spectrum with the control loop closed. Closed loop operation shows significant low frequency gain below 10Hz and suppression of temperature jitter. Also, shown is the noise amplification frequency near 10Hz.

### 10.4.3 Discussion

The phase-matching locking demonstration showed a small but clear improvement in the nonlinear gain stability. The phase-matching control loop performance was limited by the phase delay inherent in photothermal actuation. The photothermal phase delay limited the control bandwidth to a unity gain frequency of 10 Hz, since the controller was not designed to compensate for this

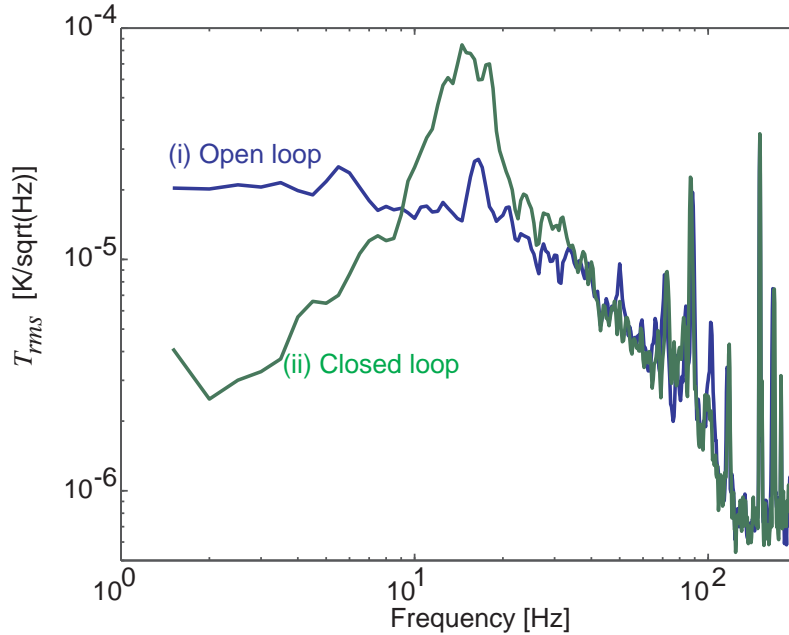


**Figure 10.8:** The calibrated spectra of the phase matching locking error signal (i) with the control loop open, and (ii) with the control loop closed.

delay. The measured photothermal response of the crystal is shown in figure 10.9. The measured trace (solid line) was fitted with a theoretical response from equation 24 given in reference [170] (dashed line), which has a corner frequency of 140Hz. This data was taken by measuring the transfer function from the amplitude modulator in the harmonic field to the fundamental error signal. This was done whilst the harmonic field was locked to the cavity resonance and the crystal temperature set so that the fundamental field was also on resonance, but detuned 8 Kelvin from the phase matching temperature to eliminate any  $\chi^{(2)}$  effects. We expect that a high bandwidth ( $\sim 100\text{kHz}$ ), high gain, control loop could be implemented if the photothermal response was considered and appropriate controller electronics designed. Also, an integrator would be useful to increase low frequency gain and drive residual phase mismatch (and temperature deviation) lower.

Using the photothermal feedback via the harmonic (pump) field is convenient and potentially very fast. An issue that may arise using this type of actuator is that the phase matching error signal changes the pump power, which is coupled to the amount of the nonlinear gain. This was a second order effect with phase mismatch error. To limit this effect, photothermal actuation could be used in parallel with a slow feedback to the crystal oven temperature so any low frequency temperature variation could be nulled and the average pump power could be constant.

Another noteworthy noise source is residual cavity locking error coupling into the phase-matching error signal. The experimental demonstration presented here relies on the cavity being locked with sufficiently small error so that the phase-matching error signal is dominated by phase matching error. In general, the residual cavity fluctuations are likely to be much smaller than the effect of thermal fluctuations. If cavity locking error was a limiting noise source, a degree of isolation could be achieved by differencing the cavity error signals (with appropriate gain) before feeding back to the phase matching condition as per the figure 10.1.

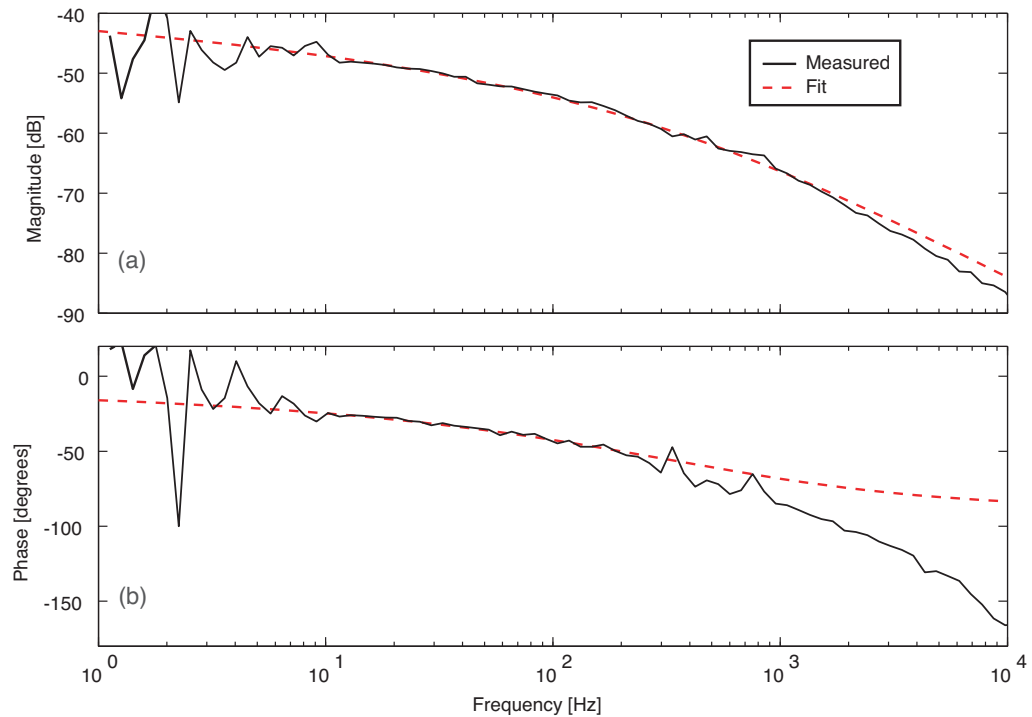


**Figure 10.9:** Measured (solid line) and theoretical (dashed line) photothermal response of the nonlinear crystal. (a) the amplitude response, and (b) the phase response.

## 10.5 Chapter summary

We have introduced a technique to interferometrically readout the phase matching condition in a doubly-resonant OPA. High precision readout of the phase matching condition is obtained by differencing cavity error signals of the fundamental and harmonic frequencies. An experimental demonstration of phase matching locking was performed, showing temperature control to a mean value of 0.5mK from the phase matching temperature, with a standard deviation of 0.3mK. With the phase matching locked, a substantial improvements in both nonlinear gain and the nonlinear gain stability were obtained. The temperature of the nonlinear interaction region was controlled by amplitude modulation of the harmonic field, thereby changing the photothermal absorption. This enabled a unity gain bandwidth of the phase matching control loop of approximately 10Hz. With a more sophisticated servo design taking the photothermal phase response into account, a unity gain bandwidth of  $\sim 100\text{kHz}$  is achievable using photothermal actuation. Phase matching locking may have applications in nonlinear experiments where short and long term conversion efficiency stability are important.



---

# Conclusions and further work

---

## 11.1 Summary of audio frequency squeezing research

- A theoretical investigation into the coupling of classical noise sources into squeezed states generated in optical parametric down-conversion process was undertaken. This investigation showed that:
  - Squeezed vacuum states produced from a sub-threshold optical parametric oscillator are, to first order, immune to classical noise sources such as; seed noise, pump noise, and cavity detuning noise. This property makes sub-threshold optical parametric oscillation ideal for generating squeezed states at low sideband frequencies, where classical noise sources are large.
  - Squeezed states produced from an optical parametric amplifier are degraded by classical noise sources. The coupling of the classical noise sources in an optical parametric amplifier is directly proportional to the intra-cavity power at the fundamental field frequency.
- An experimental investigation of squeezed states produced in optical parametric amplifiers and optical parametric oscillators was presented. This research highlighted the differences of the coupling of classical noise sources to squeezed states produced in the two processes. In optical parametric amplifiers, classical noise sources were shown to degrade the squeezed state in direct proportion to the seed power. In the measured frequency band of 1kHz to 10kHz, quantum noise reduction was measured only for seed powers of 20nW and below. Squeezed states produced in a sub-threshold optical parametric oscillator displayed immunity to the same classical noise that degraded squeezing from optical parametric amplifier, in agreement with theoretical predictions. Broadband quantum noise reduction, from 280Hz to 100kHz, was measured from the squeezed states produced in a sub-threshold optical parametric oscillator. Squeezing had not previously been reported in this frequency band.
- An experiment focused on producing stable audio-frequency squeezing was presented. In this experiment stable, high magnitude, audio-frequency squeezing was produced from a doubly-resonant optical parametric oscillator. The stability of the system was demonstrated by measuring the squeezed state for 30 minutes. Stable quantum noise suppression of up to 5.5dB (72%) was measured. Squeezing was measured at sideband frequencies down to 70Hz. Low frequency measurements of squeezing were found to be contaminated by excess noise in the detection system. Candidates for the excess noise were investigated, and it was speculated that scattered light was the source of the excess noise, as was found by Vahlbruch *et al.* [17] in a similar experiment.

- A brief theoretical investigation into squeezing enhancements of Advanced LIGO was presented. This investigation included the classical noise sources and optical losses of the interferometer. This calculation showed that for Advanced LIGO in wideband operation with 10dB of optimally rotated frequency dependent squeezing, the contribution of quantum noise to the total noise over the frequency window of 5Hz-1kHz is reduced from 48% to 24%.

## 11.2 Summary of locking techniques

- A theoretical and experimental investigation into the quantum noise locking technique was presented. The noise performance of quantum noise locking was measured out-of-loop using a standard dither locking technique. A comparison of quantum noise locking with dither locking showed that quantum noise locking was two orders of magnitude poorer in noise performance. The lock stability was found to be sufficient to lock for indefinite periods. A theoretical calculation of the noise performance of quantum noise locking was found to agree closely with the measured noise performance.
- A new technique called phase matching locking was developed to interferometrically read-out the phase matching condition of a second order nonlinear material. Phase matching locking was demonstrated experimentally in a doubly-resonant optical parametric amplifier and analysed theoretically. Phase matching locking was shown to improve the stability and accuracy of phase matching when compared with standard temperature control of the medium.

## 11.3 Further work

### 11.3.1 Shot noise limited measurement of squeezing across the audio band

One shortcoming of the squeezing measurements presented in this thesis was caused by excess noise in the homodyne detection system at low frequencies. To obtain a shot noise limited measurement of squeezing across the audio band and confirm the production of squeezing to very low frequencies two methods could be attempted:

- Build the homodyne detector in a cleaner environment to reduce dust settling on the optics and therefore scattering centers due to dust. A vacuum tank evacuated to moderate level vacuum might be ideal to reduce the dust in the air and would also remove acoustic noise.
- Perform heterodyne detection of the squeezed vacuum state. Consider a heterodyne detection scheme shown in figure 11.1. Here the local oscillator field contains only two RF sidebands, i.e. the power of the field at the carrier frequency is zero. This detection scheme would provide a level of immunity to scattered light because after demodulation the primary scattered light noise is located in the frequency band of  $\Omega_m$  whereas the squeezed signal has been converted to baseband. Note that, because most heterodyne detection schemes, such as this one, allow two quadratures to be measured simultaneously, there is excess quantum noise that couples into the measurement [172]. The measured squeezing magnitude is therefore less than that of a homodyne measurement.

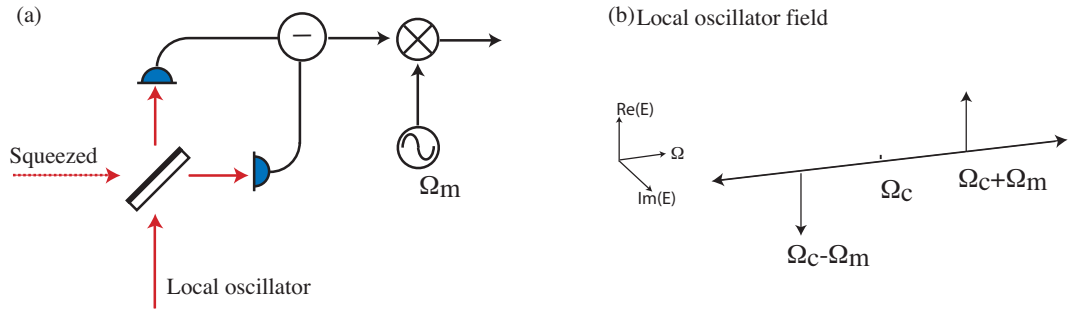


**Figure 11.1:** (a) A layout for a heterodyne detection system, and (b) a phasor diagram of the local oscillator field.

### 11.3.2 Considerations for a squeezer to use in an interferometric gravitational wave detector

Successful integration of a squeezed state generator (or squeezer) into long baseline detectors requires careful design and engineering. The research presented here, along with the concurrent experiments from the groups of Roman Schnabel at Hannover University and Nergis Mavalvala at MIT, provides a stepping stone towards the injection of squeezed states into long baseline interferometers. Important issues for the design of such a squeezer are considered in the following list.

**Coherent control of the squeezed vacuum state** Quantum noise locking was used in this thesis and the work of Goda *et al.* for phase control of the squeezing ellipse. Although the quantum noise locking works well and with sufficient phase stability for locking the homodyne detection phase, it may not be suitable for use in more complex interferometers. A coherent control technique of squeezed vacuum, such as the frequency shifted sideband used by Vahlbruch *et al.*, would provide a higher possible stability and versatility than quantum noise locking.

The frequency shifted sideband locked to the squeezed vacuum phase could be used to control both the squeezed state phase with respect to the interferometer field and the alignment of the squeezed state relative to the interferometer.

**Type of crystal** Mg:LiNbO<sub>3</sub> and PPKTP have been successfully used to generate large magnitudes of quantum noise reduction and similar magnitudes of squeezing. In the experiments performed here, PPKTP produced better results and was found to be easier to work with for the following reasons

- PPKTP has significantly higher nonlinear gain. The optical parametric oscillation threshold power was 14 times less than with Mg:LiNbO<sub>3</sub>.
- The FWHM temperature of the phase matching curve of PPKTP was four times broader than that of Mg:LiNbO<sub>3</sub>.
- The photothermal effect seen in PPKTP was significantly smaller than in Mg:LiNbO<sub>3</sub> making it much easier to operate at high pump powers.

From these reasons PPKTP was the crystal of choice. An outstanding question about both crystals is how they age when operated continuously over periods of months. For example,

gray tracking may become a problem for a PPKTP based system (though ‘gray tracking resistant’ PPKTP can now be purchased), or GRIIRA for a LiNbO<sub>3</sub> based system. Long term measurements will be needed to evaluate the performance of these two crystals.

**Cavity configuration** To generate large magnitude squeezed states, high escape efficiency is required. High escape efficiency is achieved by reducing intra-cavity loss and increasing output coupler transmissivity at the squeezing wavelength. The intrinsic linear loss of the crystal is difficult to modify, (crystal engineering is needed) but the intra-cavity losses due to scatter and absorption on interfaces can be reduced by reducing the number of interfaces. The minimum number of interfaces (two reflections) is found in monolithic standing wave resonators (see e.g. [14, 18]). Monolithic squeezers are not readily applicable to gravitational wave detectors since their resonance frequency cannot be tuned to follow the interferometer laser wavelength. Temperature tuning the length can’t be used because the temperature is set to phase-match the nonlinear process.

The hemilithic design (such as that in chapter 6) or bow-tie designs (such as that in chapter 7) are tunable configurations. In terms of intra-cavity loss the second best configuration is the hemilithic design since it has two reflections and two transmissions per round trip. The bow-tie cavity has four reflections and two transmissions. The caveat that puts the bow-tie configuration ahead of the hemilithic cavity is its relative immunity to backscattered light from the gravitational wave detector dark port.

For the experiments that have used standing wave resonators, an additional Faraday isolator was required to prevent back-scattered light seeding the OPO cavity [24, 26, 128]) whereas the bow-tie cavity didn’t require this.

So to consider the total loss a standing-wave hemilithic cavity must also include the extra loss devices of a single pass through a Faraday isolator. For the typical losses of Faraday isolators (a few percent), the bow-tie cavity without Faraday isolator would have less total loss than a hemilithic cavity with Faraday isolator.

**Singly resonant verses doubly resonant cavities** The advantages and disadvantages of singly and doubly resonant cavities were discussed in chapter 7. In terms of producing stable squeezing over long time periods singly- and doubly-resonant systems offer different possibilities. Doubly resonant systems require more stringent temperature control, but these requirements can be met using phase matching locking. Singly resonant systems require less temperature stability but cannot use phase matching locking.

We have neglected to discuss the integration of the squeezer into the control and diagnostics system as well as the significant task of delivering a frequency dependent phase shift to optimize the quantum noise reduction.

### **Design of a second generation audio frequency squeezer**

Taking into account the design considerations above, a design for a next generation audio frequency squeezer can be developed. Figure 11.2 shows an outline of such a design. The architecture of this design is essentially the same as the experiment presented in chapter 7 however with some minor changes and additional fields.

The design is a doubly resonant, bow-tie cavity. The nonlinear medium is a wedged PPKTP crystal. The wedged PPKTP crystal can be used to compensate for the round trip dispersion introduced by the mirror coatings by tuning the path length [173]. A frequency shifted sideband

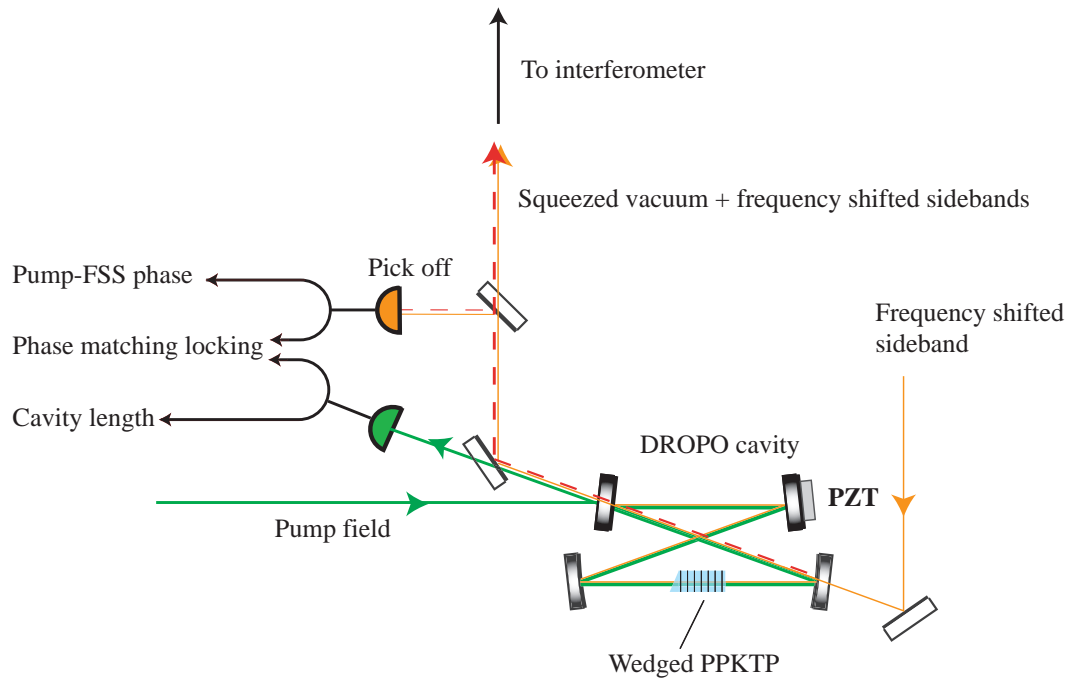


**Figure 11.2:** Schematic of a next generation squeezer.

field is injected into the cavity to be used to control the phase of the squeezed vacuum relative to the interferometer. This is achieved by locking the sideband field to the pump phase, a signal which can be detected from a pick off of the cavity. The cavity length error signal could be readout from the pump field.

The frequency shifted sideband field could also be used, along with the reflected pump field to generate a phase matching locking error signal. This could be fed back to the crystal temperature to maintain long term stability.



# Quantum Noise in a Michelson Interferometer

This appendix presents a calculation of quantum noise in a simple Michelson interferometer. This calculation follows the derivation presented in the Appendix B of Kimble *et al.* [38]. Here we perform the quantum noise limited sensitivity for a simple Michelson, whereas Kimble *et al.* includes Fabry-Perot cavities in the Michelson arms. A similar calculation is presented for a signal recycling Michelson without arm cavities [108] and with both signal recycling and arm cavities [117, 118].

The figure A.1 shows the fields in the Michelson interferometer. We are interested in calculating the output signal and noise of the interferometer as a function of the input fields;  $D + d$  from the laser port, and  $a$  from the dark port. The positive component of the electric field entering the laser port, in two photon formalism [109, 110], is given by (equation B1 of reference [38]);

$$E_{LP}^{(+)} = \sqrt{\frac{2\pi\hbar\omega_0}{\mathcal{A}c}} e^{-i\omega_0 t} \left[ D + \int_0^\infty (d_+ e^{-i\Omega t} + d_- e^{+i\Omega t}) \frac{d\Omega}{2\pi} \right] \quad (\text{A.1})$$

So the total electric field entering the laser port is given by;

$$E_{LP} = \sqrt{\frac{4\pi\hbar\omega_0}{\mathcal{A}c}} \left[ \cos \omega_0 t \left( \sqrt{2}D + \int_0^\infty (d_1 e^{-i\Omega t} + d_1^\dagger e^{+i\Omega t}) \frac{d\Omega}{2\pi} \right) + \sin \omega_0 t \int_0^\infty (d_2 e^{-i\Omega t} + d_2^\dagger e^{+i\Omega t}) \frac{d\Omega}{2\pi} \right] \quad (\text{A.2})$$

The convention used here is the field  $D$  is the classical amplitude of the laser field of frequency  $\omega_0$  with units of  $\sqrt{\text{photons/sec}}$ . The amplitude and phase quadrature fluctuations of the laser field at sideband frequencies  $\Omega$  are given by  $d_1, d_2$ . The power incident on the beamsplitter is given by

$$I_0 = \hbar\omega D^2. \quad (\text{A.3})$$

The total electric field entering the dark port is

$$E_{DP} = \sqrt{\frac{4\pi\hbar\omega_0}{\mathcal{A}c}} \left[ \cos \omega_0 t \int_0^\infty (a_1 e^{-i\Omega t} + a_1^\dagger e^{+i\Omega t}) \frac{d\Omega}{2\pi} + \sin \omega_0 t \int_0^\infty (a_2 e^{-i\Omega t} + a_2^\dagger e^{+i\Omega t}) \frac{d\Omega}{2\pi} \right] \quad (\text{A.4})$$

The beamsplitter relation give the following fields.

$$f_j^n = \frac{1}{\sqrt{2}}[d_j + a_j], \quad f_j^e = \frac{1}{\sqrt{2}}[d_j - a_j], \quad (\text{A.5})$$

$$b_j = \frac{1}{\sqrt{2}}[g_j^n - g_j^e], \quad e_j = \frac{1}{\sqrt{2}}[g_j^n + g_j^e]. \quad (\text{A.6})$$

where  $j = 1, 2$  for the amplitude and phase quadratures and the superscripts  $n$  and  $e$  differentiate the fields in the North and East arms.

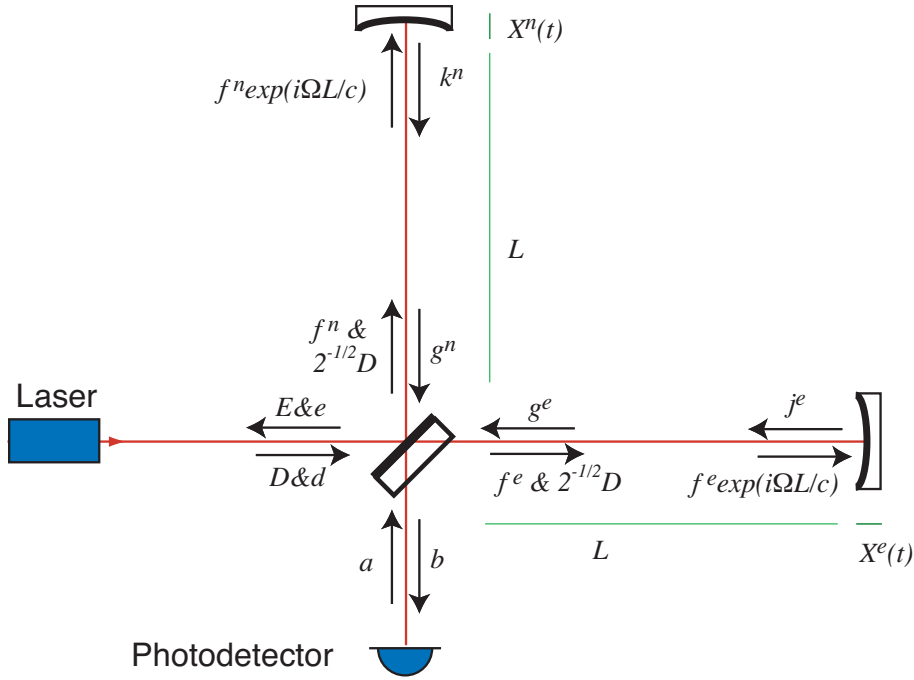


**Figure A.1:** The fields in the Michelson interferometer. Capitalised letters represent classical fields, the quadrature fields are represented by the lower case letters.

### Fields in the arms

As the fields propagate along the arms of length  $L$  they receive a phase shift. Consider the length  $L$  to contain an integral number of wavelengths for the carrier frequency. The quadrature sidebands receive a relative phase shift of  $\beta = \Omega L/c$ . The relations of the fields at the beamsplitter and the end test mass's is

$$k_j' = f_j e^{i\Omega L/c} \quad g_j = k_j e^{i\Omega L/c} \quad (\text{A.7})$$

### Source Term

If the end mirror position fluctuates by  $X(t)$  the field reflecting back towards the beamsplitter receives a phase shift  $\phi(t) = 2\omega_0 X(t)/c$ . This process imposes phase modulation sidebands on the field with amplitude proportional to the coherent amplitude of the carrier incident on the end

---

mirror,  $D/\sqrt{2}$ . The phase modulation on the coherent field  $D/\sqrt{2}$

$$E_{carrier} = \frac{D}{\sqrt{2}} \cos(\omega_0 t + \phi(t)) \quad (\text{A.8})$$

$$= \frac{D}{\sqrt{2}} [\cos \omega_0 t \cos \phi(t) + \sin \omega_0 t \sin \phi(t)] \quad (\text{A.9})$$

$$\approx \frac{D}{\sqrt{2}} [\cos \omega_0 t + \sin \omega_0 t \phi(t)] \quad (\text{A.10})$$

We consider the carrier amplitude to be unchanged. The small time varying fluctuations in the mirror position give rise to a source term in the phase quadrature;

$$\delta X_1^s = 0 \quad \delta X_2^s = \frac{2D\omega_0 X}{c} \quad (\text{A.11})$$

where  $X$  is the Fourier transform of  $X(t)$ . Thus field reflected off the end mirror is the field at the beamsplitter with a phase shift due to the travel time in the arm plus the source term.

$$k_j = k'_j + \delta X_j^s \quad (\text{A.12})$$

### Fluctuating mirror displacement

The position of suspended mirrors in gravitational wave detectors fluctuates at some level due to many sources. In this section only the fluctuations in the mirror displacement due to radiation pressure noise on the end test masses<sup>1</sup> and the apparent fluctuations due to the gravitational wave signal are considered.

The force due to radiation pressure for a 100% reflective mirror at normal incidence is given by

$$\delta F = \frac{2P_{inc}}{c} \quad (\text{A.13})$$

where  $P_{inc}$  is the laser power incident on the mirror. The power incident on the mirror is

$$P_{inc} = \bar{E}_{inc}^2 \frac{Ac}{4\pi} \quad (\text{A.14})$$

$$= \bar{P}_{inc} + \delta P_{inc} \quad (\text{A.15})$$

where

$$\bar{P}_{inc} = \hbar\omega_0 \frac{D^2}{2} \quad (\text{A.16})$$

$$\delta P_{inc} = \hbar\omega_0 D \int_0^\infty (f_1 e^{-i\Omega t} + f_1^\dagger e^{+i\Omega t}) \frac{d\Omega}{2\pi}. \quad (\text{A.17})$$

The gravitational wave disturbance is a stretching and contracting of the orthogonal arms. This length perturbation is evenly distributed over the entire arm length, and does not act as a force on the mirror. The equation of motion of the mirror of one of the end test masses due to the gravitational wave disturbance and the radiation pressure force (assuming it behaves like a free

---

<sup>1</sup>Radiation pressure on the beamsplitter is assumed to be negligible for simplicity. Radiation pressure effects on the beamsplitter in the GEO interferometer have been considered by Harms *et. al* [174].

mass) is [38]

$$\frac{d^2 X^{n,e}(t)}{dt^2} = \frac{\eta^{n,e}}{2} L \frac{d^2 h(t)}{dt^2} + \frac{2\delta P^{n,e}(t)}{mc} \quad (\text{A.18})$$

where  $\eta^{ne}$  is the Minkowski metric, which if has values of  $\eta^n = 1, \eta^e = -1$ . Taking the Fourier transform of the equation of motion;

$$(i\Omega)^2 X = (i\Omega)^2 \frac{\eta_{ne}}{2} Lh + \frac{2\delta P}{mc} \quad (\text{A.19})$$

$$(\text{A.20})$$

which gives for the north and east arms;

$$X^n = \frac{1}{2} Lh - \frac{\sqrt{2}\hbar\omega_0 D}{mc^2\Omega^2} (d_1 + a_1) e^{i\beta} \quad (\text{A.21})$$

$$X^e = -\frac{1}{2} Lh - \frac{\sqrt{2}\hbar\omega_0 D}{mc^2\Omega^2} (d_1 - a_1) e^{i\beta} \quad (\text{A.22})$$

The difference in sign of the first term in the north and east arms shows the quadrupole nature of gravitational wave moves orthogonal arms anti-symmetrically. The second terms, due to radiation pressure<sup>2</sup> is dependent on the amplitude quadrature fluctuations that enter from the laser port  $d_1$  and those from the dark port  $a_1$ . The field measured at the dark (anti-symmetric) port is proportional to the differential motion of the north and east arm length,

$$x = X^n - X^e \quad (\text{A.23})$$

$$= Lh - \frac{2\sqrt{2}\hbar\omega_0 I_0}{mc^2\Omega^2} a_1 e^{i\beta} \quad (\text{A.24})$$

Here the radiation pressure fluctuations from the laser port cancel and radiation pressure fluctuations from the vacuum port add. If the common mode displacement  $X^n + X^e$  were to be measured the opposite situation is true.

The field at the output of the interferometer we will be interested in the difference of the source fields,

$$\frac{\delta X^n - \delta X^e}{\sqrt{2}} = \frac{\sqrt{2}D\omega_0 x}{c} \quad (\text{A.25})$$

$$= \sqrt{2} \frac{I_0}{\hbar\omega_0} \frac{\omega_0 x}{c} \quad (\text{A.26})$$

The output quadratures are given by the beamsplitter relations (equation A.6)

$$b_1 = a_1 e^{2i\beta} \quad (\text{A.27})$$

$$b_2 = a_2 e^{2i\beta} + \frac{1}{\sqrt{2}} (\delta X^n - \delta X^e) e^{i\beta} \quad (\text{A.28})$$

---

<sup>2</sup>The factor of 2 difference in the radiation pressure term in this derivation and that of Kimble *et al.* is because we have only one test mass. With arm cavities the radiation pressure on the each of the ETM and ITM increases the radiation pressure by a factor of 2.

---

which goes to

$$b_1 = a_1 e^{2i\beta} \quad (\text{A.29})$$

$$b_2 = (a_2 - \mathcal{K}a_1) e^{2i\beta} + \sqrt{2\mathcal{K}} \frac{h}{h_{SQL}} e^{i\beta} \quad (\text{A.30})$$

where the coefficient

$$\mathcal{K} = \frac{4I_0\omega_0}{mc^2\Omega^2} \quad (\text{A.31})$$

is the radiation pressure coupling constant. The (single sided) standard quantum limit in strain sensitivity of a simple Michelson interferometer is

$$h_{SQL} = \sqrt{\frac{4\hbar}{m\Omega^2 L^2}}. \quad (\text{A.32})$$

which is  $\sqrt{2}$  larger than the SQL for an individual test mass because the difference of the Michelson interferometer test masses behaves like a free particle with reduced mass  $m \rightarrow m/2$  (see footnote 3 in Kimble *et al.*).



---

# Comparison of MgO:LiNbO<sub>3</sub> and PPKTP for OPO

---

The two nonlinear media were used in the doubly resonant OPO experiments presented in this thesis. They were:

**(i) Periodically poled potassium titanyl phosphate (KTiOPO<sub>4</sub>) (PPKTP)**

A quasi-phase matched crystal from Raicol Crystals [141]. This was a rectangular prism with dimensions: 10mm×2mm×1mm. The end faces were coated for AR at both wavelengths.

**(ii) 7% Magnesium doped lithium-niobate (Mg:LiNbO<sub>3</sub>)**

from Photon LaserOptik [175] which was type-I birefringence phase matched. This was a rectangular prism with dimensions: 6.5mm×2mm×2.5mm. The end faces were coated for AR at both wavelengths

This appendix summarizes some of the properties of the media and compares measurements of the squeezing from the doubly resonant OPO with the two media.

## B.1 Phase-matching curves

Phase matching of both mediums were tuned via the crystal temperature. The single pass second harmonic nonlinear conversion efficiencies PPKTP and LiNbO<sub>3</sub> were measured using a setup shown schematically in figure B.1. Figure B.2 shows the measured single pass SHG conversion

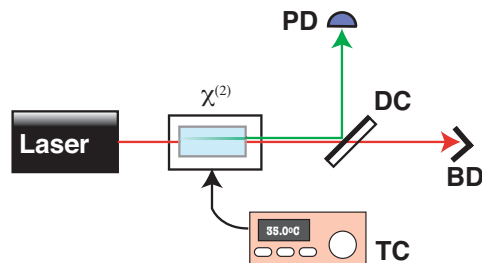


**Figure B.1:** Experimental Setup used to measure single pass SHG efficiency vs temperature.

efficiencies measured as a function of temperature for (i) PPKTP and (ii) LiNbO<sub>3</sub>. The measured conversion efficiencies are indicated by 'x's and the solid line is a fitted  $\text{sinc}^2$  curve. The phase matched temperature of PPKTP was 35.5°C with FWHM of 5.0°C. The PPKTP conversion efficiency deviates from a  $\text{sinc}^2$  shape near the first zero on the lower temperature side. The deviation may be due to random errors in the width of the polling domain [176]. The phase matched

temperature for LiNbO<sub>3</sub> was 63.9°C and the FWHM was 1.3°C. The larger FWHM of PPKTP was beneficial in the doubly resonant OPO cavity, which significantly reduces the phase matching FWHM compared to singly resonant or single pass systems.

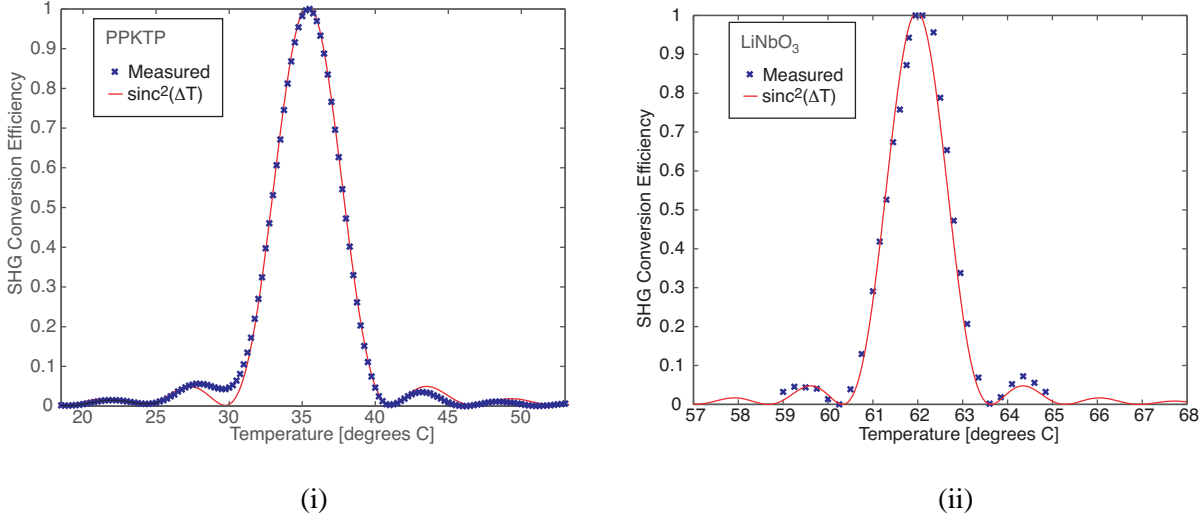


**Figure B.2:** Single pass second harmonic nonlinear conversion efficiencies as a function of temperature for: (i) PPKTP and (ii) LiNbO<sub>3</sub>. Note the different temperature scales on the horizontal axis.

## B.2 Measurement of the parametric gain

The measurements of the parametric gain of the doubly resonant OPO are plotted versus input pump power in figure B.3 for LiNbO<sub>3</sub> and PPKTP. The parametric gain was measured for LiNbO<sub>3</sub> for two input/output couplers and only for one with PPKTP. The specifications of the input/output couplers were

$$\begin{aligned} \text{Coupler (A)} \quad T_{out}^a &= 0.1/T_{out}^b = 0.03 \\ \text{Coupler (B)} \quad T_{out}^a &= 0.06/T_{out}^b = 0.06 \end{aligned}$$

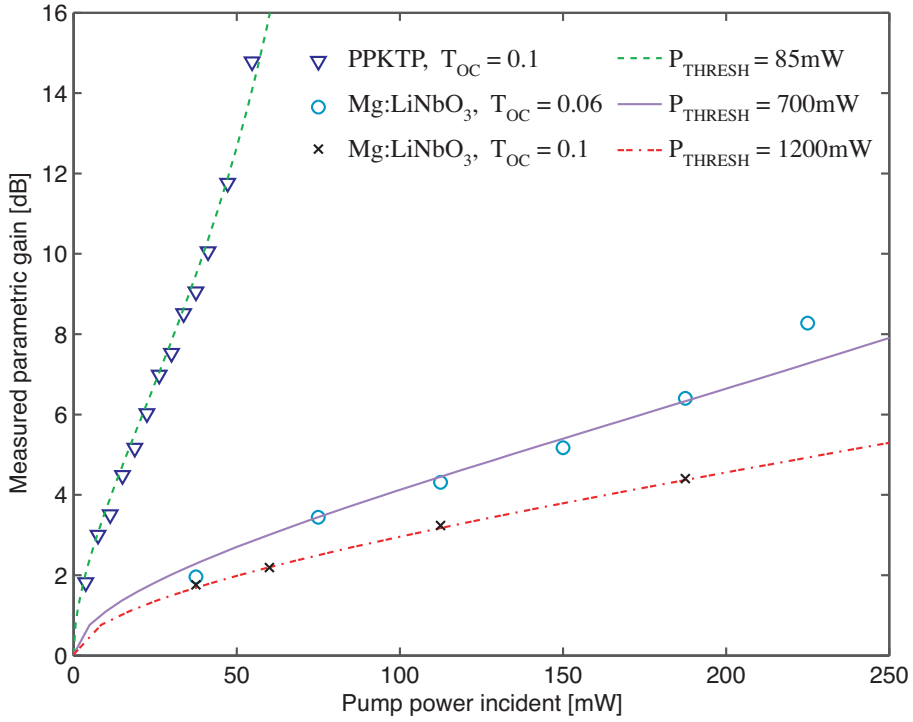
The data points can be compared with fitted curves given by Equation 3.116 used to determine the OPO threshold power. With the coupler (A) the threshold was  $P_{thresh} = 85\text{mW}$  for PPKTP and  $P_{thresh} = 1200\text{mW}$  for LiNbO<sub>3</sub>. The threshold power with coupler (B) was  $P_{thresh} = 700\text{mW}$  for LiNbO<sub>3</sub>. The much larger pump powers required for LiNbO<sub>3</sub> were accompanied by a strong photothermal effect which interacted with the length control loop making stable operation difficult. PPKTP had a significantly larger nonlinear gain and also a smaller photothermal effect which made it more desirable to work with.

## B.3 Squeezing from a doubly resonant OPO

The squeezed states generated from the doubly resonant OPO were detected by a balanced homodyne detection system. The measured squeezed states at sideband frequency of 100kHz plotted in Figure B.4 for (a) using Mg:LiNbO<sub>3</sub> with output coupler (A), in Figure B.4 (b) for the Mg:LiNbO<sub>3</sub> with output coupler (B) and in Figure B.4 (c) for PPKTP with output coupler (A). These plots are

**Table B.1:** doubly resonant OPO cavity parameters for (i) PPKTP and (ii) Mg:LiNbO<sub>3</sub>

Parameter	Value at 1064nm	Value at 532nm	Units
Optical Path Length	756	756	mm
FSR	397	397	MHz
$T_{out}(A)$	10	3	%
$T_{out}(B)$	6	6	%
Round Trip Loss	(i) 0.9(ii) 0.6	(i) & (ii) 2.2	%
Finesse (with $T_{out}(A)$ )	(i) 55 (ii) 56	(i) & (ii) 117	-
Finesse (with $T_{out}(B)$ )	(ii) 92	(ii) 77	-
FWHM (with $T_{out}(A)$ )	(i)3.6 (ii)3.5	(i) & (ii) 1.7	MHz
FWHM (with $T_{out}(B)$ )	(ii) 2.1	(ii) 2.7	MHz
$\eta_{esc}$ (with $T_{out}(A)$ )	(i) 92 (ii)94	-	%
$\eta_{esc}$ (with $T_{out}(B)$ )	(ii)90	-	%


**Figure B.3:** Measurements of parametric gain as function of pump power and fitted curves.

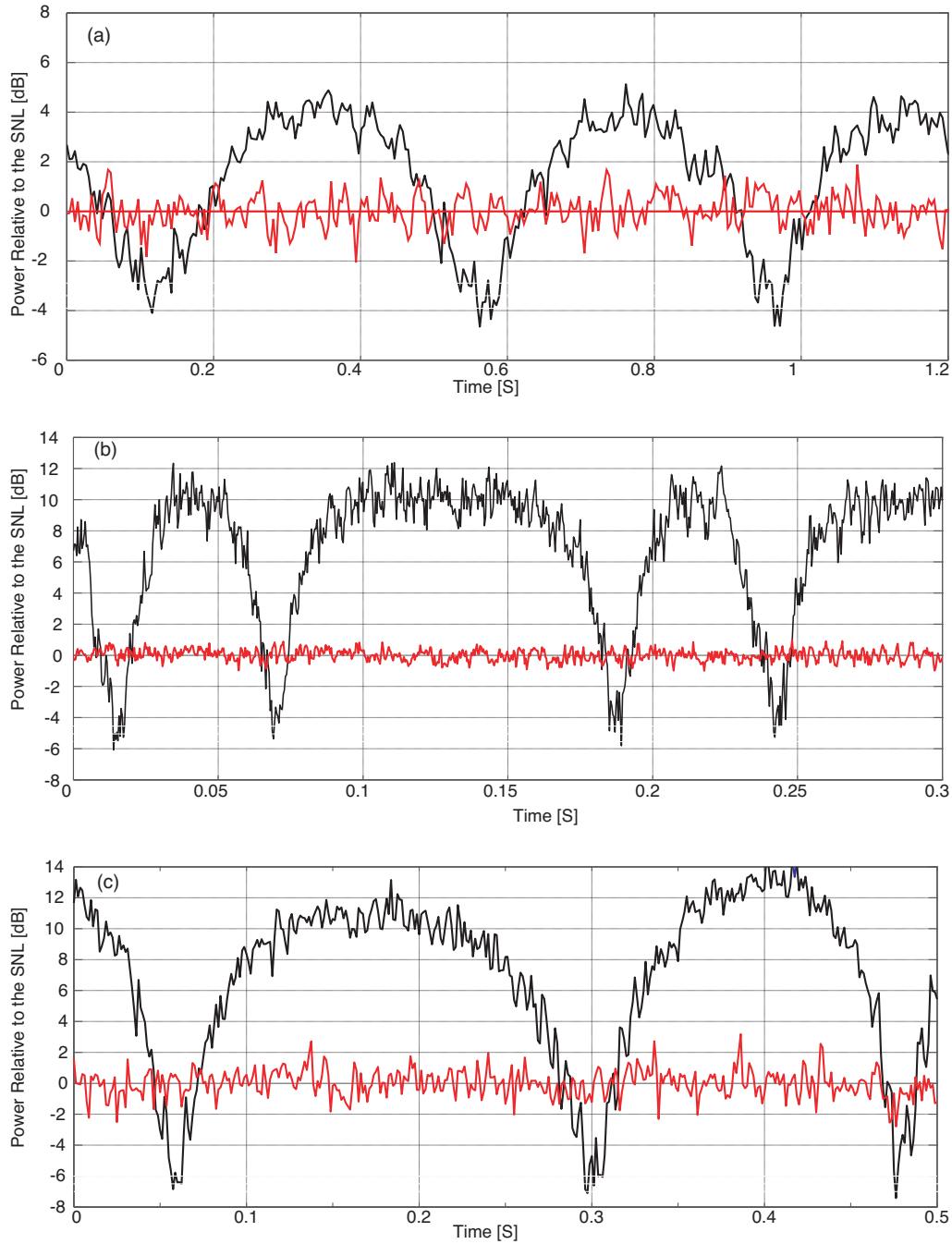


**Figure B.4:** Measured noise relative to the shot noise limit (SNL) obtained from (a)  $LiNbO_3$  with output coupler (A), (b)  $LiNbO_3$  with output coupler (B) and (c) PPKTP with output coupler (A). Figure (a) was measured at 50kHz and had  $RBW=3kHz$ ,  $VBW=30Hz$ . Figures (b) and (c) were measured at 100kHz with  $RBW=10kHz$ ,  $VBW=300Hz$ .

normalised to the shot noise limit. The electronic noise floor (greater than 11dB below the SNL in all traces) was subtracted from all of the traces. The level of squeezing for the three traces is

$$(a) \quad 3.5 \pm 0.5\text{dB}, \quad (b) \quad 5.0 \pm 0.5\text{dB}, \quad (c) \quad 6.5 \pm 0.5\text{dB}. \quad (\text{B.1})$$

There are two reasons for the difference in the squeezing amplitude measured in (a), (b) and (c).

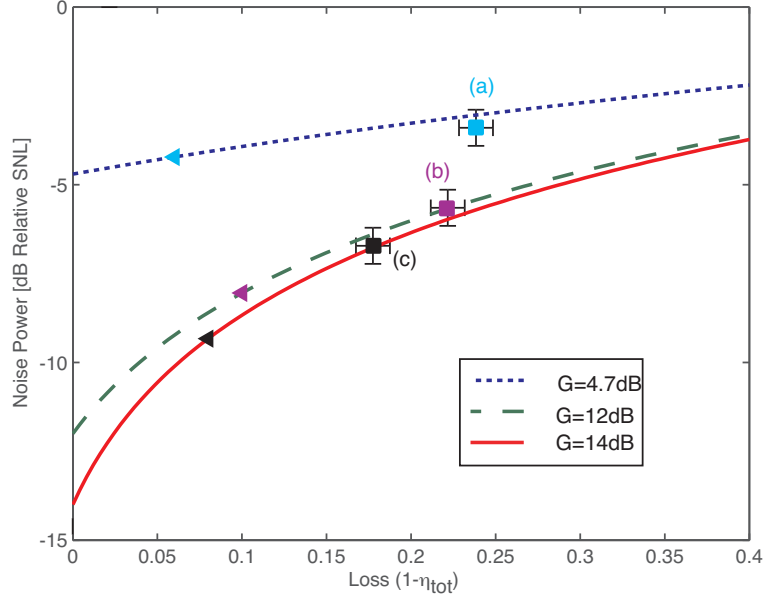


**Figure B.5:** Expected squeezing level as a function of total loss and measured data points (squares).

Firstly, the parametric gain was not the same for all three traces. In (a) the parametric gain was just 4.7dB, which was limited by photothermal instability at high input powers ( $>150\text{mW}$ ) required to get large enough parametric gain. In (b) and (c) the parametric gains were 12dB and 14dB, respectively. Secondly, the total detection efficiency was not the same for each measurement. The total detection efficiencies were

$$(a) \quad \eta_{tot} = 77 \pm 2\%, \quad (b) \quad \eta_{tot} = 78 \pm 2\%, \quad (c) \quad \eta_{tot} = 84 \pm 2\%. \quad (\text{B.2})$$

The total detection efficiency were different because the escape efficiency and the homodyne interference efficiency were different in all three experiments. Table B.2 summarizes the experimental efficiencies.

**Table B.2:** Experimental Efficiencies

	Experiment (a)	Experiment (b)	Experiment (c)
$\eta_{esc}$	$94 \pm 1\%$	$91 \pm 1\%$	$92 \pm 1\%$
$\eta_{opt}$	99%	99%	99%
$\eta_{hom}$	$88 \pm 1\%$	$94 \pm 1\%$	$97 \pm 1\%$
$\eta_{det}$	$93 \pm 2\%$	$93 \pm 2\%$	$93 \pm 2\%$
$\eta_{tot}$	$77 \pm 2\%$	$78 \pm 2\%$	$84 \pm 2\%$

Figure B.5 shows the expected squeezing amplitude as a function of optical loss ( $1-\eta_{tot}$ ) for the three different parametric gains in (a), (b) and (c). This plot shows the effect of loss on the amplitude of squeezing measured and what level of squeezing could be expected given an particular loss. The measured squeezing levels are indicated by ‘■’. The amount of squeezing which exits the OPO cavity can be inferred by taking into account the losses in propagation and detection. The inferred squeezing out of the OPO cavity can be found from

$$V_{inf} = \frac{V_{meas} - \eta_{opt}\eta_{hom}\eta_{det} + 1}{\eta_{opt}\eta_{hom}\eta_{det}}, \quad (\text{B.3})$$

where  $V_{meas}$  is the measured squeezing level. The inferred squeezing levels at the output of the OPO cavity are

$$\text{(a) } 4.2\text{dB}, \quad \text{(b) } 8.0\text{dB}, \quad \text{(c) } 9.3\text{dB}. \quad (\text{B.4})$$

These data points are indicated in Figure B.5 by a ‘▲’.

---

# Experimental components and techniques

---

In this appendix details core components of the doubly resonant OPO experiment. In section C.1 details of the laser, the second harmonic generator (SHG), and the modecleaner cavity are given. In section C.2 an overview of the dispersion compensation in the doubly resonant cavity is presented. In section C.3 details of the reaction mass for the cavity peizo-electric transducer (PZT) are presented.

## C.1 The laser, SHG, and modecleaner

### C.1.1 The laser

The laser was a CW, Nd:YAG, non-planar ring oscillator (NPRO) type [84] operating at 1064nm (1.2W Mephisto 1200 model from Innolight GmbH [27]). An overview of the lasers properties are given in Table C.1. The inherent stability of the free running Nd:YAG laser was sufficient to operate the experiments without requiring frequency or intensity stabilization.

**Table C.1:** Mephisto 1200 Properties. For additional details see [27]

Parameter	Value	Units
Wavelength	1064	nm
Output Power	1200	mW
Spectral Linewidth	$\sim 1$	kHz
Frequency Stability	$\sim 1$	MHz/min
Intensity Noise (10Hz to 2MHz)	$< 0.1$	% rms
Spatial Mode ( $M^2 < 1.1$ )	TEM <sub>00</sub>	—

The laser field was first passed through a Faraday Isolator (Gsänger FR 1060/5), some polarization and modematching optics, then through a resonant phase modulator (New Focus model 4003) driven at 12MHz and a broadband amplitude modulator (New Focus model 4102, with appropriate polarization optics). The 12MHz phase modulation sidebands were used to derive error signals for the SHG and modecleaner cavities'. The amplitude modulator was used in characterization of the homodyne detector, as described in Section 7.5. The majority ( $\sim 99\%$ ) of the laser power was directed to the SHG to generate the pump field (at 532nm) for the OPO. Less than 10 mW of the laser light was directed through the modecleaner to be used for the local oscillator field for the homodyne detector.

### C.1.2 The second harmonic generator

The SHG was a singly resonant (at 1064nm) device custom built by Innolight GmbH (Diabolo model [27]). The SHG cavity was constructed out of type-I phase-matched, 5% doped MgO:LiNbO<sub>3</sub> hemilithic crystal, and an external mirror, which was mounted on a peizo electric transducer (PZT) to allow the cavity length to be actuated. The curved surface of the crystal was coated for high reflectivity (HR) at both wavelengths (532nm and 1064nm) and the flat surface coated for anti-reflectivity (AR) at both wavelengths. The external mirror had R= 95% at 1064nm and was AR coated at 532nm. The crystal was mounted on a peltier element which was used to maintain the crystal temperature at the phase matching temperature. Selected parameters of the SHG can be found in Table C.2.

**Table C.2:** Diabolo Properties. For details see [27]

Parameter	Value	Units
Input Wavelength	1064	nm
Input Power	<1000	mW
Output Wavelength	532	nm
Output Power	< 650	mW
Input/Output Mirror Transmission	5	% @ 1064nm
Input/Output Mirror Transmission	>95	% @ 532nm
Nonlinear Medium	Mg:LiNbO <sub>3</sub>	–
Phase Matched Temperature	99.85	°C
Free Spectral Range	2	GHz
Spatial Mode Output ( $M^2 < 1.1$ )	TEM <sub>00</sub>	–

The SHG cavity was locked using dither locking on transmission. The cavity error signal was derived by demodulation of the photocurrent of the transmitted photodetector at 12MHz. From ~ 1W input power (at 1064nm) the SHG produced up to 650mW of frequency doubled light, greater than the amount required as a pump field for the OPO.

### C.1.3 The Modecleaner Cavity

The layout of the modecleaner cavity is shown in figure C.1. The three mirrors were attached to a invar spacer which had geometry and cavity g-parameter [90] similar to that of the LIGO pre-mode cleaner [177, 178]. Parameters of the modecleaner can be found in Table C.3. The modecleaner’s primary function was to filter the spatial and polarization mode of the laser field, to provide a high quality TEM<sub>00</sub> mode for the local oscillator field. This allowed the local oscillator field to be matched to the TEM<sub>00</sub> mode of the OPO with high fringe visibility. At the low frequencies of interest in this thesis the modecleaner offered little in terms of intensity and phase noise filtering.

The modecleaner cavity was locked laser frequency using the PDH technique. The cavity error signal was derived by demodulating the the reflected light at 12MHz. The cavity length was actuated using the end mirror (M3) which was mounted on a PZT.

Figure C.2 shows the magnitude response of cavity transmission for the low finesse (p-polarized) and high finesse (s-polarized) cavity modes. This measurement was taken by measuring the transfer function from the amplitude modulator located before the modecleaner to a photodetector at the transmitted port using a network analyzer (HP3598A). The fitted curves indicate FWHM values of 470kHz and 54kHz for low and high finesse modes. The low finesse mode was used in the experiments here.

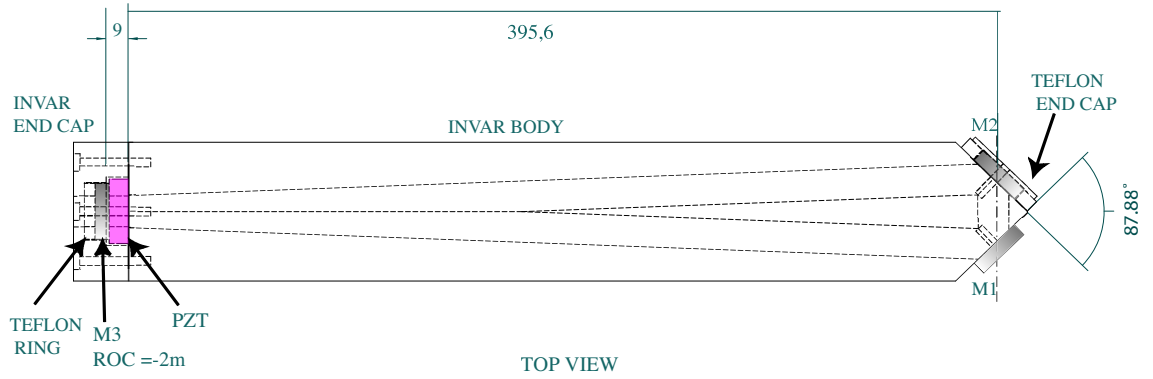


**Figure C.1:** Top view of the modecleaner cavity design. Lengths are in millimeters, angles in degrees. modecleanerdesign.

**Table C.3:** Modecleaner Cavity Parameters

Parameter	Value	Units
M1, M3 reflectivity (p-pol)	99.6	%
M2 reflectivity	99.997	%
Round trip length	840	mm
FSR	357	MHz
FWHM (measured p-pol)	470	kHz
FWHM (measured s-pol)	54	kHz
Finesse (measured p-pol)	760	—
Finesse (measured s-pol)	6614	—
M2 ROC	-2	m
Cavity g parameter	.58	
Waist Size	525	$\mu\text{m}$

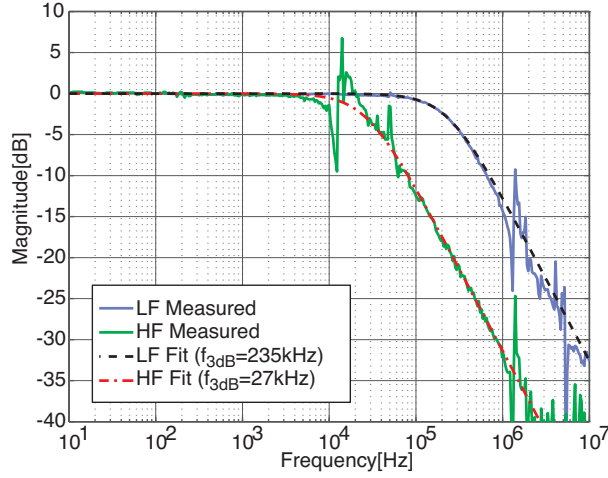


**Figure C.2:** The measured (solid lines) and fitted (dashed lines) frequency responses for the mode cleaner in low finesse (LF) and high finesse (HF) modes. The notch at 10.5kHz in the HF trace is thought to be a result of interaction of the amplitude modulation sidebands and the cavity length servo.

## C.2 Dispersion compensation in a doubly resonant cavity

Dispersion from the dichroic mirror coatings causes the fundamental and harmonic cavity resonances to be offset. This effect can be seen in figure C.3 (a), which shows the transmitted power as the cavity length was varied of a doubly resonant free space cavity, with driving fields at both 1064nm and 532nm. This was taken with no nonlinear medium in the cavity. The transmitted power was detected on a silicon photodetector, which is sensitive to both 1064nm and 532nm light. The broader transmission peak of the fundamental field can be distinguished from the narrower peak from the harmonic field <sup>1</sup>.

If the fundamental and harmonic fields do not co-resonate then the nonlinear gain is interferometrically suppressed. Often in  $\chi^{(2)}$  experiments, dispersion of the cavity mirrors is compensated by adding a phase mismatch of the nonlinear material to achieve co-resonance. This non-ideal operation can be avoided by compensating for the dispersion by adding a tunable dispersive element into the cavity. This can be done by using a wedged crystal [173] in a QPM system or a dispersive optic, as shown in a laser intracavity SHG [179].

We introduced a AR/AR coated BK-7 glass optic into the cavity and angled it so that the dispersion of the glass cancelled the dispersion of the mirror coatings (to the nearest integral number of wavelengths), see figure C.3 (b). This dispersion compensation optic was used for both the PPKTP and LiNbO<sub>3</sub> crystals. The dispersion from the doubly resonant OPO cavity optics was compensated using a angled BK-7 glass optic. The dispersion in the glass comes from two terms, firstly, the dispersion of the glass, and secondly, the extra path-length the field with higher refractive index travels <sup>2</sup>.

The differential path length of two fields can be determined using geometrical arguments.

<sup>1</sup>Although the FSR's for the two fields are the same (they share the same optical cavity), they appear different because the horizontal axis on this plot has different scales for the two frequencies (a change in the cavity length by 1 $\mu$ m corresponds to 1 FSR at 1064nm and 2 FSR's at 532nm)

<sup>2</sup>The AR coatings of the glass also add extra dispersion which needs to be compensated for.

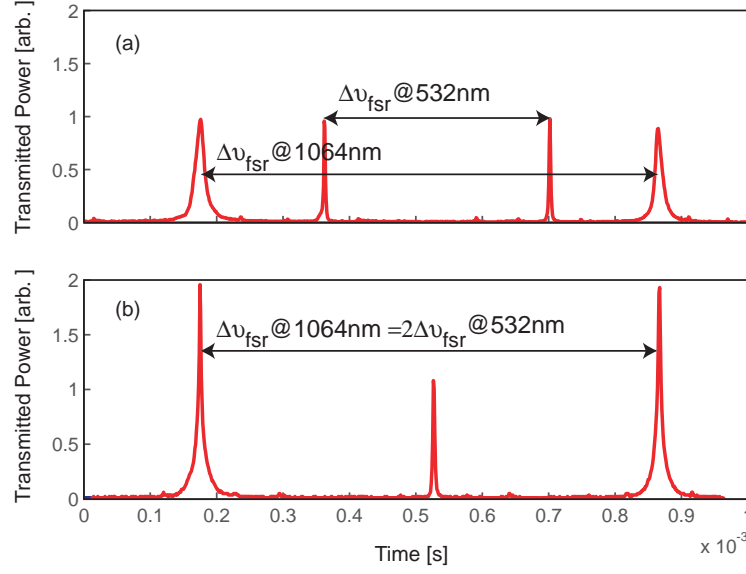


**Figure C.3:** Transmission of the doubly resonant bow-tie cavity as the cavity length was scanned. (a) was taken without the dispersion compensation plate in the cavity, and it can be seen that the resonances for the 1064nm and 532nm cavities do not coincide. In (b), the dispersion compensation plate was in the cavity and tuned such that the 1064nm and 532nm resonances overlap. The silicon photo-detector used for these measurements was sensitive to both the 1064nm and 532nm light. These measurements were taken without a nonlinear crystal in the cavity, so the dispersion seen was a result of the cavity mirror coatings.

Refer to figure C.4 (a), the angle of refraction for the field at frequency  $\omega_i$  is given by

$$\theta_2(\omega_i) = \sin^{-1}(n_1 \sin(\theta_1)/n_2(\omega_i)), \quad (\text{C.1})$$

the path length through the BK7 as a function of angle of incidence is simply

$$\Delta L(\omega_i) = L_T n_2(\omega_i) / \cos(\theta_2(\omega_i)). \quad (\text{C.2})$$

The difference in path length of the harmonic field and the fundamental field is given by

$$\Delta L_{b-a} = \Delta L(\omega_b) - \Delta L(\omega_a), \quad (\text{C.3})$$

The corresponding extra phase delay of the harmonic field (which has a higher refractive index for the parameters used in this experiment) as a function of angle of incidence is plotted in figure C.4 (b). It can be seen that an extra phase delay of the harmonic field relative to the fundamental field by more than  $2\pi$  with an angle of incidence between 0-10 degrees. Accordingly we had the BK7 optic AR coated for the range 0-10 degrees.

### C.3 High resonance frequency PZT Design

When the doubly resonant OPO was operated with the  $\text{LiNbO}_3$  crystal as the nonlinear medium, a strong photothermal effect [76] in the crystal caused a technical challenge. At high pump power, the photothermal effect interacted with the cavity length control loop and caused an instability. If a pump power was greater than  $\sim 130\text{mW}$ , approximately 1/5 of the power required to reach the oscillation threshold, the cavity would drop lock.

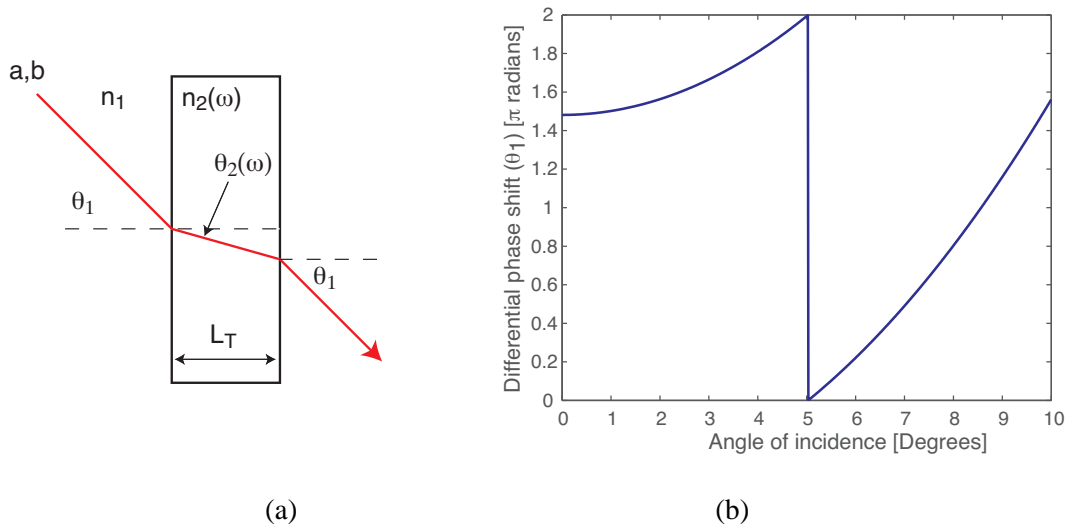


**Figure C.4:** (a) The dispersion compensation plate. (b) differential phase shift as a function of angle of incidence. Parameters used match the experimental values, the thickness  $d = 6.35\text{mm}$ ,  $n(\omega_a) = 1.50663$ ,  $n(\omega_b) = 1.51947$ .

To overcome the photothermal instability, the cavity locking bandwidth was enhanced. The unity gain bandwidth of the cavity length was originally  $\sim 7\text{kHz}$ , imposed by the piezo-mechanical resonance of the PZT, located at  $45\text{kHz}$ . A higher bandwidth PZT was designed and built<sup>3</sup>. The attempt was to push the first mechanical resonance beyond  $200\text{kHz}$ , thereby enabling a larger unity gain bandwidth for the cavity length loop, to squash the photothermal effect. A drawing of mount is shown in figure C.5. The key components are labeled in the diagram. They are; (1) molybdenum rod, which has ridges on the side to enhance the coupling of the molybdenum with the damping material; (2) the damping material was a mixture of epoxy glue and iron filings; (3) the stainless steel housing, which had a small hole in the centre used to attach the molybdenum rod; (4) the single layer PZT from piezomechanik GmbH (model Pst 150  $7\text{mm} \times 7\text{mm}$ ) which had a natural resonance at  $500\text{kHz}$ . A  $1\text{mm}$  thick,  $6.35\text{mm}$  diameter mirror was glued onto the PZT.

The outer diameter of the stainless steel case was set to be 1 inch, allowing mounting into standard optical mounts. A transfer function of applied voltage to displacement can be seen in the figure C.6. This measurement was taken by applying a swept sine voltage to the pzt mirror, which was used as one end mirror of a Michelson interferometer. Whilst the michelson was held at  $1/2$  fringe the photodetector output at the asymmetric port was recorded. The first mechanical resonance can be seen to be  $\sim 270\text{kHz}$ . The low pass filter shape was a due to the capacitance of the PZT ( $220\text{nF}$ ) combined with the source resistance ( $50\text{ Ohms}$ ). Also shown in the figure C.6 is a model of the response of a LPF with pole frequency of  $f_c = 14\text{kHz}$ . This capacitance was taken into account in the design of the servo controller. We recorded a unity gain frequency of  $50\text{kHz}$ .

<sup>3</sup>Stefan Göbler designed this PZT reaction mass based older sketches. The source of the original design is not known.

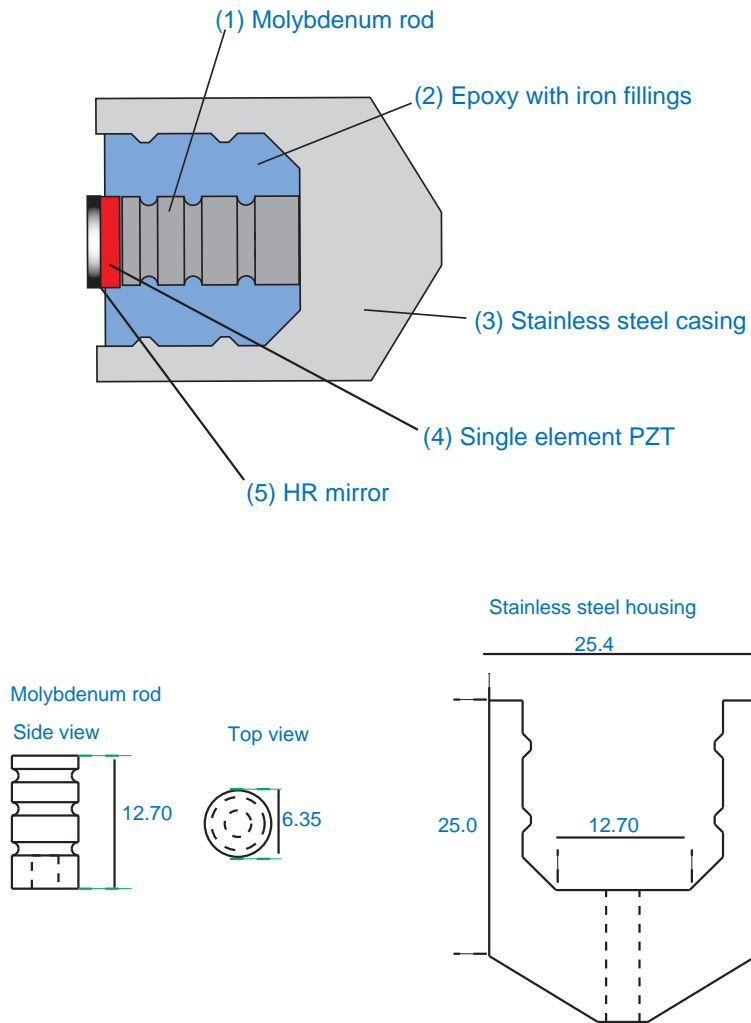


**Figure C.5:** Drawings of the high resonance frequency piezo mount.

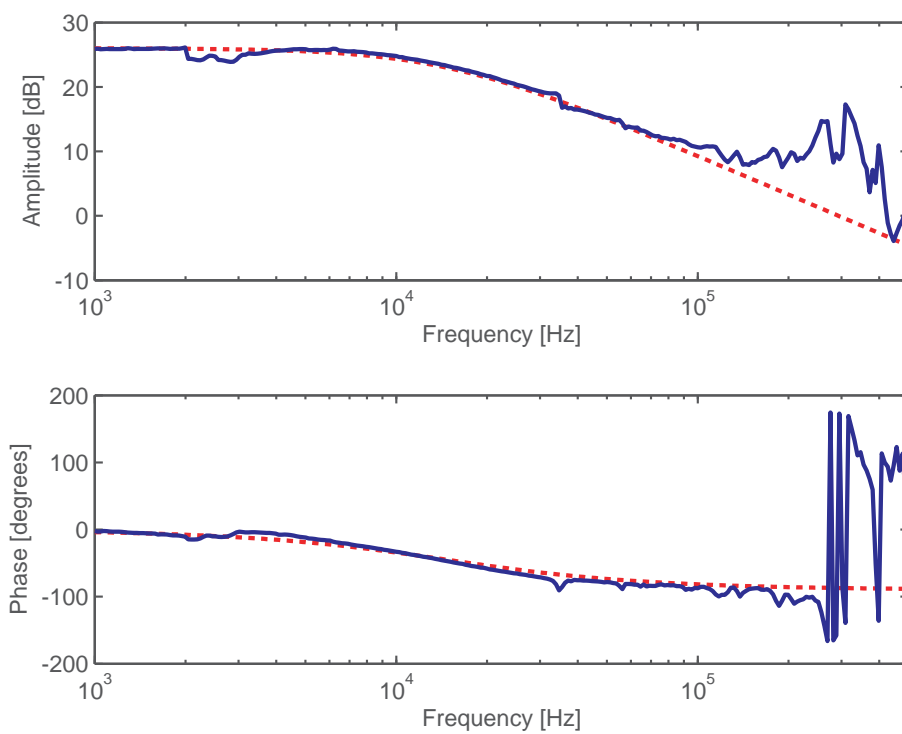


**Figure C.6:** Transfer function of the high resonance frequency PZT. The low pass filter shape was caused by the combination of the capacitance of the PZT and the resistance of the source.

---

# Homodyne detector noise budget

---

In chapter 7 a homodyne noise budget is presented. This appendix details measurements of the noise sources in the noise budget.

## D.1 Homodyne detector experiment

A schematic of the homodyne detector is shown in figure D.1. The field used as the local oscillator for the homodyne detector was passed through the phase modulator, the amplitude modulator, and the modecleaner cavity. The modecleaner cavity provided filtering of the spatial and polarization modes of the laser field and stripped the phase modulation sidebands. The local oscillator field then passed through modematching optics and was steered onto the homodyne detectors beamsplitter. A 150mm lens was placed immediately before the homodyne beamsplitter in both the local oscillator and signal paths to reduce the spot size of the fields on the photodiodes. Each output of the homodyne beamsplitter was steered onto one of a pair of matched photodetectors. The photodetectors used InGaAs photodiodes (model ETX 500T [180]) which had their protective windows removed to minimize potential scattering sources and loss. The photodetector circuits had high transimpedance (10kOhms) gain which allowed low local oscillator powers to be used<sup>1</sup>. Refer to the schematic in appendix E.

### D.1.1 Local oscillator intensity noise coupling

The contribution of the local oscillator intensity noise can be measured directly. Figure D.2 (a) shows the measured common mode rejection to intensity noise from 10Hz-100kHz. This was measured by taking the transfer function from the amplitude modulator to the homodyne output with gain optimized, then normalising this by the transfer function from the amplitude modulator to the a single photodetector. The level was approximately -80dB from 10Hz - 1kHz (possibly limited by the noise floor of the instrument) and deteriorated to -55dB at 100kHz. The deviation from -80dB above 1kHz may be due to a mismatch of the gains of the two photodetectors approaching the pole frequency of the photodetectors (~800kHz). The dashed line is a curve fitted to the experimental data.

Figure D.2 (b) curve (i) shows the measured local oscillator intensity noise normalized to the shot noise limit. The peak near 10kHz coincides with the modecleaner control loop amplification frequency, above the unity gain frequency. The peaks at and below 1kHz are thought to be intensity noise induced by beam jitter of the input beam or the modecleaner cavity mode. Figure D.2 (b) curve (ii) is the product of the common mode rejection and the intensity noise. This inference

---

<sup>1</sup>The effective trans-impedance gain including the gain of the buffer stage at the output of the circuit was 49kOhms.

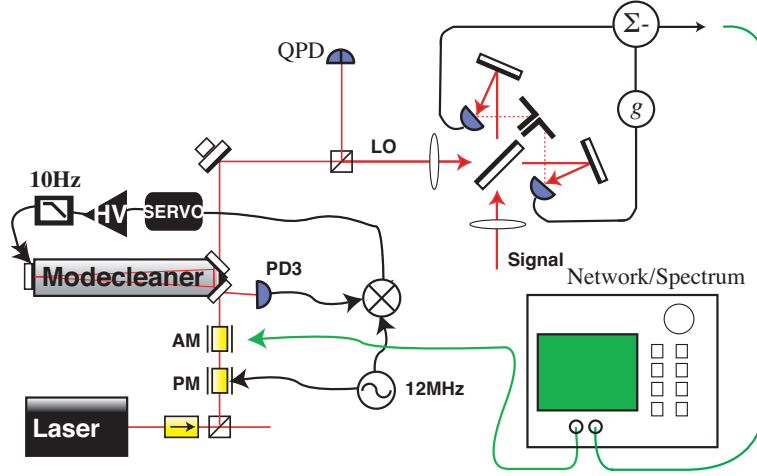


**Figure D.1:** Schematic of the experimental set up Homodyne detection system. The laser field is passed through a phase modulator (PM), a broadband amplitude modulator (AM) a modecleaner cavity and is incident on the fast steering mirror (FSM). The signal beam was a vacuum state. QPD - quad-photodetector

of the contribution of local oscillator intensity noise to the homodyne noise budget is less than; -30dB relative to the SNL, sufficiently small to suggest laser intensity noise is not the limiting noise source no active intensity noise stabilization of the laser was required.

### D.1.2 Beam jitter noise

Beam jitter noise of the local oscillator beam can couple as intensity noise in the homodyne photocurrent via spatial variations of photodiode efficiency.

In this section measurements of the local oscillator beam jitter are used to estimate the contribution of beam jitter to the homodyne noise budget. We do not measure the spatial variations of the efficiency of the photodiode, rather we infer the coupling of beam jitter to relative intensity noise (RIN).

The beam jitter spectrum for the local oscillator beam is shown in the figure D.3 (a) curve (i) for the vertical axis and curve (ii) for the horizontal axis. This measurement was taken on the quad-photodetector with a waist size of  $250\mu\text{m}$ . The beam jitter amplitude is approximately an order of magnitude smaller across the frequency band when the laboratory air-conditioning (AC) unit is switched off. The larger amplitude of the beam jitter with the air-conditioning on assists in the characterization of the beam jitter noise in the homodyne detection system.

The beam jitter coupling to RIN can be inferred by fitting the beam jitter displacement to the homodyne, ie

$$RIN_{BJ} = A\Delta x(f) \quad (\text{D.1})$$

where the beam jitter to RIN coupling constant,  $A$ , has units  $1/\text{m}$ , and the quadrature sum of the horizontal and vertical  $\Delta x(f) = \sqrt{\Delta x_H(f)^2 + \Delta x_V(f)^2}$  has units  $\text{m}/\text{Hz}^{1/2}$ . The relative intensity noise (RIN) of the shot noise in units  $1/\text{Hz}$  is given by

$$RIN_{SNL} = \frac{2e}{\rho P_{opt}} \quad (\text{D.2})$$

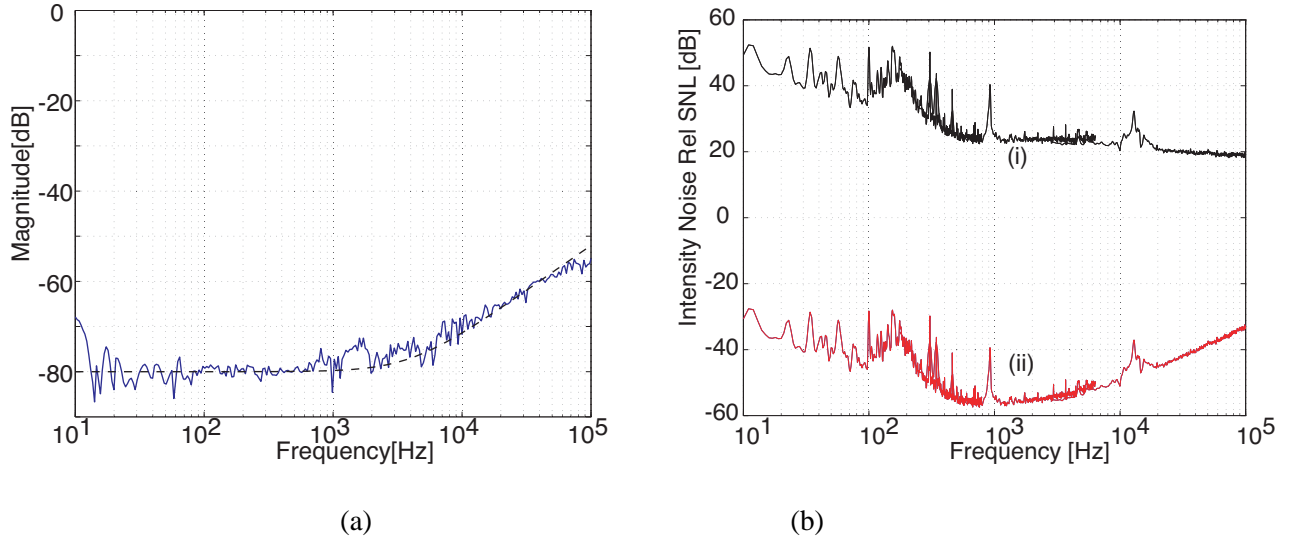


**Figure D.2:** (a) The common mode rejection of the homodyne detector as a function of frequency measured via a transfer function measurement (solid line) and fitted curve (dashed line). The variable electronic gain was set to optimize the common mode rejection at low frequencies. (b) Curve (i), the intensity noise spectrum of the laser relative to the shot noise limit (SNL) measured from 10Hz-100kHz. Curve (ii) the intensity noise contribution to the homodyne detector spectrum inferred using curve (a) and the measured common mode rejection.

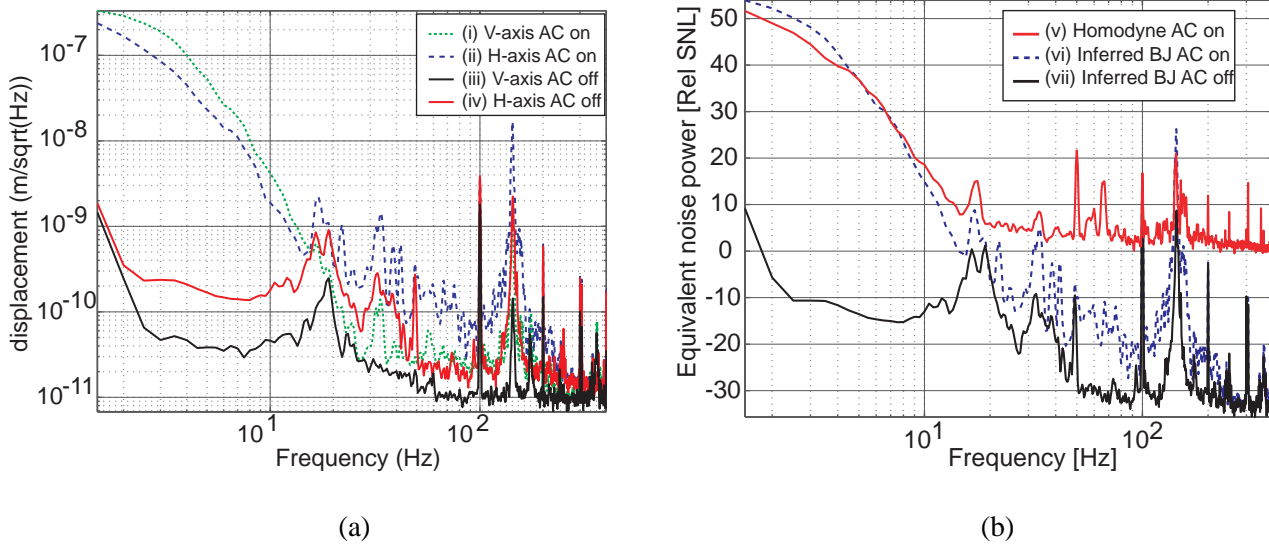
where  $e$  is the electron charge,  $\rho$  the photodetector responsivity in Amps/Watt, and  $P_{opt}$  the optical power detected.

Figure D.3 (b) shows the RIN of low frequency homodyne spectrum, curve (v), and the inferred beam jitter noise contribution, curve (vi) inferred from Eqn. D.1. Here  $A$  has been used as a free parameter to fit common features in the beam jitter to the homodyne spectrum thereby allowing an estimate of the beam jitter noise contribution to the homodyne spectrum. The beam jitter to RIN coupling has been inferred to have a value of  $A = 42$  1/m.

The similarities in the curves (v) and (vi) suggest that large amplitude beam jitter noise may contribute to the homodyne spectrum. Inconsistency in the features may arise from a number of effects. Firstly, the unrepeatable nature of the beam jitter measurements due to varying acoustic noise. Secondly, the coupling of beam jitter could change, as spatial variations in efficiency of the photodiode can change day to day due to dust on the photodiode surface. Thirdly, the beam jitter data and the homodyne data have some uncommon beam path length and optics, which means they have different acoustic excitations, and also different Gouy phases [181], meaning different combinations of near-field beam jitter and far-field beam jitter were measured. Using the inferred value of  $A$  and the measured vertical and horizontal beam jitter taken with the air-conditioning off the RIN caused by beam jitter was inferred. This is given by curve (vii).

### D.1.3 The use of a ‘low’ local oscillator power

The photodetector circuits were designed to operated with minimal local oscillator power ( $380\mu\text{W}$  or below). The limit to low local oscillator power was the electronic noise from the photodetector Op-Amp. Low local oscillator power was desirable because of the scaling of classical and quantum noise with local oscillator power. As local oscillator power,  $P$ , decreases the classical noise sources decrease directly proportional to  $P$  whereas shot noise decreases as  $\sqrt{P}$ . Thus lower local



**Figure D.3:** (a) Beam jitter measurements for the (a) vertical axis and (b) horizontal axis using the quad photodetector. (b) The RIN of the low frequency homodyne spectrum taken with AC on, curve (a) and, the estimated  $RIN_{BJ}$  noise contribution of beam jitter to the homodyne spectrum, curve (b). Curve (c) is the calculated  $RIN_{SNL}$  for  $P_{opt} = 380\mu\text{W}$  and  $\rho=0.7$  Amps/Watt.

oscillator power gives a higher ratio of quantum to classical noise. Not using a low local oscillator power is contrary to most interferometry measurements where quantum noise limited sensitivity that making the homodyne detector quantum noise limited by using low local oscillator power is different to achieving good displacement sensitivity in interferometry. An interferometers shot noise limited displacement sensitivity improves as the  $\sqrt{P}$ .

---

# Photodetector Circuit

---

# Photodetector Circuit

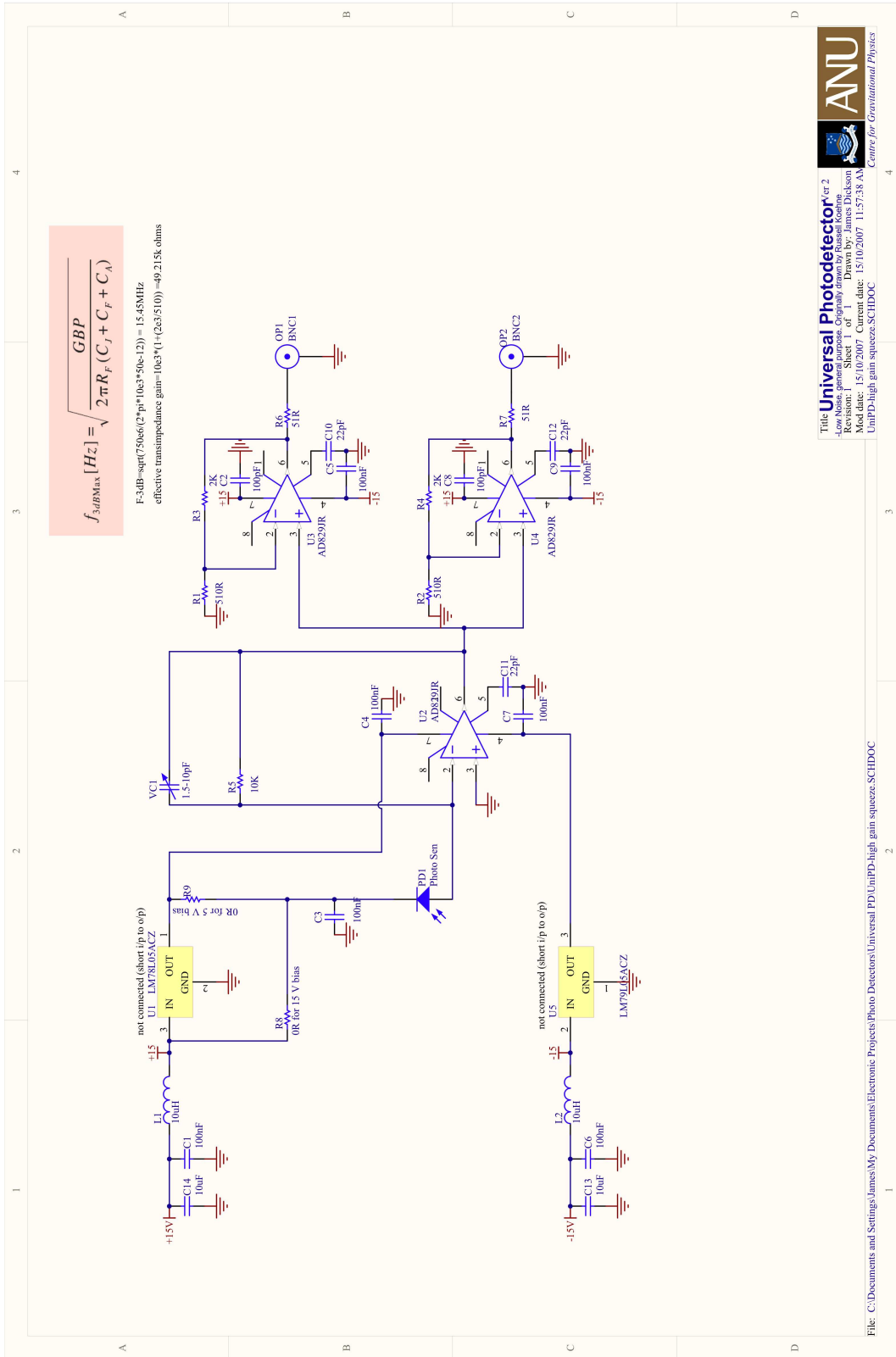


**Figure E.1:** Circuit layout of the photodetectors used in the homodyne detection system.

---

# The shot noise limit of phase-matching locking

---

The shot noise limit in phase-matching locking comes from the shot noise of the individual cavity error signals. The shot noise limit of the error signals is derived in this section following the calculations of Day *et al.* [182] and Black [143]. However, we do not make the assumptions of an impedance matched cavity, and include non-stationary shot noise [183]. The derivation starts with calculation of the error signal slope (in Watts/m). The shot noise of the signal is then calculated (in Watts/ $\sqrt{\text{Hz}}$ ). These are then combined to give the shot noise limited displacement sensitivity (in m/ $\sqrt{\text{Hz}}$ ). Finally, we combine the shot noise of the two error signals to realise the shot noise of phase-matching locking.

## The slope of the PDH error signal in reflection

Starting with the cavity reflectivity parameter for a empty cavity (equation ??)

$$\mathcal{R}(\Delta) = \frac{2\kappa_{in} - \kappa - i\Delta}{\kappa + i\Delta}, \quad (\text{F.1})$$

near resonance, we can write

$$\frac{\Delta}{\nu_{fsr}} = 2\pi N + \frac{\delta\Delta}{\nu_{fsr}}, \quad (\text{F.2})$$

so equation F.1 becomes

$$\mathcal{R}(\Delta) = \frac{2\kappa_{in} - \kappa - i\delta\Delta}{\kappa + i\delta\Delta}. \quad (\text{F.3})$$

For a cavity with high reflectivity mirrors (approximately  $R > 0.8$ ) we can write the finesse of the cavity in terms of the total fractional power loss per round trip<sup>1</sup>, given by the sum of the mirror transmissivities (equation 3.89),

$$\mathcal{F} \approx \frac{2\pi}{T_{in} + T_{out} + T_{loss}}. \quad (\text{F.4})$$

---

<sup>1</sup>Siegman calls this the "Delta Notation", see section 11.4 [90].

The total decay rate for the cavity can be rewritten in terms of the cavity FWHM,  $\delta\nu = \nu_{fsr}/\mathcal{F}$ ,

$$\kappa = \kappa_{in} + \kappa_{out} + \kappa_{loss}, \quad (\text{F.5})$$

$$= \frac{\nu_{fsr}}{2}(T_{in} + T_{out} + T_{loss}), \quad (\text{F.6})$$

$$\approx \frac{\pi\nu_{fsr}}{\mathcal{F}} = \pi\delta\nu. \quad (\text{F.7})$$

Similarly, the decay rate for the input mirror can be written

$$\kappa_{in} = \frac{T_{in}}{2}\delta\nu\mathcal{F}. \quad (\text{F.8})$$

If we consider the case close to resonance, ( $2\pi\delta\nu \gg \delta\Delta$ ), then we can write the cavity reflectivity coefficient as

$$\mathcal{R}(\delta\Delta) \approx (T_{in}\mathcal{F}/\pi - 1) - \frac{i\delta\Delta}{\pi\delta\nu}. \quad (\text{F.9})$$

For high modulation frequency (with respect to the cavity linewidth)  $\mathcal{R}(\Delta \pm \omega) = -1$  and the error signal (equation ??) can be rewritten using equation F.9 as

$$\mathcal{E}_R = 2\sqrt{P_c P_s}(\text{Im}(\mathcal{R}(\Delta) - \mathcal{R}(\Delta)^*)), \quad (\text{F.10})$$

$$= 2\sqrt{P_c P_s} \left( \frac{-2\delta\Delta}{\pi\delta\nu} \right), \quad (\text{F.11})$$

$$= \frac{4}{\pi}\sqrt{P_c P_s} \frac{\delta\Delta}{\delta\nu}. \quad (\text{F.12})$$

Rewriting in terms of fluctuating cavity length,  $dp$ , rather than laser frequency we find the error signal near resonance

$$\mathcal{E}_R = 8\sqrt{P_c P_s} \frac{p\mathcal{F}}{\lambda} \left( \frac{dp}{p} \right), \quad (\text{F.13})$$

which has the slope

$$\mathcal{D}_R = 8\sqrt{P_c P_s} \frac{\mathcal{F}}{\lambda} \left[ \frac{W}{m} \right]. \quad (\text{F.14})$$

### The slope of the dither locking error signal in transmission

The transmission coefficient of the cavity is

$$\mathcal{T}(\Delta) = \frac{2\sqrt{\kappa_{in}\kappa_{out}}(\kappa - i\Delta)}{\kappa^2 + \Delta^2}. \quad (\text{F.15})$$

In this calculation the parametric gain is neglected for simplicity. The carrier-sideband beat term in the transmission error signal (equation 10.18) is

$$\mathcal{T}(\Delta)\mathcal{T}^*(\Delta + \omega_n) - \mathcal{T}^*(\Delta)\mathcal{T}(\Delta - \omega_n) = \frac{-8\kappa_{in}\kappa_{out}\Delta\omega_n[(\kappa + i\omega_n)^2 + \Delta^2]}{(\kappa^2 + \Delta^2)(\kappa^2 + (\Delta - \omega_n)^2)(\kappa^2 + (\Delta + \omega_n)^2)}. \quad (\text{F.16})$$

Consider the case near resonance (making the substitution from equation F.2), with modulation frequency much smaller than the cavity linewidth, the error signal on transmission is

$$\mathcal{E}_T = \frac{16}{\pi^2} \sqrt{P_c P_s} T_{in} T_{out} \mathcal{F}^3 \frac{f_n}{\delta \nu} \frac{P}{\lambda} \left( \frac{dp}{p} \right), \quad (\text{F.17})$$

where the detuning terms of second order have been neglected ( $\delta\Delta^2 \ll \kappa^2$ ,  $(\delta\Delta \pm \omega_n)^2 \ll \kappa^2$ ). The slope of the error signal is

$$\mathcal{D}_T = \frac{16}{\pi^2 \lambda} \sqrt{P_c P_s} T_{in} T_{out} \mathcal{F}^3 \frac{f_n}{\delta \nu} \quad \left[ \frac{\text{W}}{\text{m}} \right]. \quad (\text{F.18})$$

### The shot noise of the PDH error signal in reflection

The shot noise on the error signals is now calculated. First the reflected power is calculated

$$P_{ref} = P_c |\mathcal{R}(0)|^2 + 2P_s + 2\sqrt{P_c P_s} \text{Im}[\mathcal{R}(0) - \mathcal{R}(0)^*] \sin \omega_m t - 2P_s \cos 2\omega_m t. \quad (\text{F.19})$$

In the shot noise limited case, the variance of the power  $V(P) = \langle h\nu P \rangle$ , thus

$$V(P_{ref}) = h\nu \langle P_c |\mathcal{R}(0)|^2 + 2P_s + 2\sqrt{P_c P_s} \text{Im}[\mathcal{R}(0) - \mathcal{R}(0)^*] \sin \omega_m t - 2P_s \cos 2\omega_m t \rangle. \quad (\text{F.20})$$

The variance at the output of the mixer is then given by the product of equation F.20 with  $\sin^2 \omega_m t$ , that is

$$\begin{aligned} M_R &= h\nu \langle (P_c |\mathcal{R}(0)|^2 + 2P_s + 2\sqrt{P_c P_s} \text{Im}[\mathcal{R}(0) - \mathcal{R}(0)^*] \sin \omega_m t - 2P_s \cos 2\omega_m t) \sin^2 \omega_m t \rangle, \\ &= h\nu (P_c |\mathcal{R}(0)|^2 + 2P_s) \left\langle \frac{1}{2} (1 - \cos 2\omega_m t) \right\rangle + 2h\nu \sqrt{P_c P_s} \text{Im}[\mathcal{R}(0) - \mathcal{R}(0)^*] \langle \sin^3 \omega_m t \rangle - \\ &\quad 2h\nu P_s \left\langle \frac{1}{4} (1 - \cos 2\omega_m t)(1 + \cos 2\omega_m t) - \left( \frac{3}{8} - \frac{1}{2} \cos 2\omega_m t + \cos 4\omega_m t \right) \right\rangle, \\ &= h\nu \left( \frac{1}{2} P_c |\mathcal{R}(0)|^2 + \frac{3}{2} P_s \right), \end{aligned} \quad (\text{F.21})$$

over the bandwidth of 1Hz. Substituting in the modulation depths, the standard deviation is then,

$$\sqrt{M_R} = \sqrt{\frac{h\nu P_0}{2}} \sqrt{J_0^2 |\mathcal{R}(0)|^2 + 3J_1^2} \quad \left[ \frac{\text{W}}{\sqrt{\text{Hz}}} \right]. \quad (\text{F.22})$$

### F.0.4 The shot noise in of the dither locking error signal in transmission

The shot noise of the error signal in transmission is calculated in the same manner as that in reflection. Instead of  $\sin(\omega_n t)$  demodulation,  $\cos(\omega_n t)$  is used since the error signal is in the orthogonal quadrature. The reflectivity coefficients are replaced with the corresponding transmission coefficients, and we note that  $|\mathcal{T}(\omega_n)|^2 = |\mathcal{T}(-\omega_n)|^2$ . The variance at the output of the mixer is found to be

$$M_T = h\nu \left( \frac{1}{2} P_c |\mathcal{T}(0)|^2 + \frac{3}{2} P_s |\mathcal{T}(\omega_n)|^2 \right), \quad (\text{F.23})$$

Substituting in the modulation depths, the standard deviation is then

$$\sqrt{M_T} = \sqrt{\frac{h\nu P_0}{2}} \sqrt{J_0^2 |\mathcal{T}(0)|^2 + 3J_1^2 |\mathcal{T}(\omega_n)|^2} \left[ \frac{\text{W}}{\sqrt{\text{Hz}}} \right]. \quad (\text{F.24})$$

### F.0.5 Shot noise limited displacement sensitivity of PDH

The shot noise limited displacement sensitivity in reflection is given by

$$\begin{aligned} S_{snl} &= \frac{\sqrt{M_R}}{\mathcal{E}_R}, \\ &= \frac{1}{8} \sqrt{\frac{hc\lambda}{2P_0 \mathcal{F}^2} \frac{J_0^2 |\mathcal{R}(0)|^2 + 3J_1^2}{J_0^2 J_1^2}} \left[ \frac{\text{m}}{\sqrt{\text{Hz}}} \right]. \end{aligned} \quad (\text{F.25})$$

Optimal sensitivity is reached when the cavity is impedance matched ( $\mathcal{R}(0)=0$ )

$$S_{snl} = \frac{1}{8} \sqrt{\frac{3}{2}} \sqrt{\frac{hc\lambda}{J_0 P_0 \mathcal{F}^2}} \left[ \frac{\text{m}}{\sqrt{\text{Hz}}} \right], \quad (\text{F.26})$$

This is the (single sided) sensitivity<sup>2</sup>. The shot noise limited displacement sensitivity in transmission is given by

$$\begin{aligned} S_{snl} &= \frac{\sqrt{M_T}}{\mathcal{E}_T}, \\ &= \frac{\pi^2}{16 \mathcal{F}^3 T_{in} T_{out}} \frac{\delta\nu}{f_n} \sqrt{\frac{hc\lambda}{2P_0}} \sqrt{\frac{J_0^2 |\mathcal{T}(0)|^2 + 3J_1^2 |\mathcal{T}(\omega_n)|^2}{J_0^2 J_1^2}} \left[ \frac{\text{m}}{\sqrt{\text{Hz}}} \right]. \end{aligned} \quad (\text{F.27})$$

### F.0.6 Shot noise in phase matching locking

Phase matching locking uses two error signals to readout the cavity length and the phase matching condition. The shot noise of both error signals needs to be considered to calculate the total shot noise. The shot noise sources are considered to be uncorrelated sources of noise

$$S_{snl,Tot} = \sqrt{S_{snl,a}^2 + S_{snl,b}^2}. \quad (\text{F.28})$$

In most OPA cases, it will be the shot noise of the fundamental field (seed) error signal that dominates, because the harmonic field (pump) is generally more than two orders of magnitude higher in optical power. For the parameters listed in table 8.1, the shot noise limit, in terms of differential cavity length is;

$$S_{snl,Tot} = 1.01 \times 10^{-17} (\text{m}/\sqrt{\text{Hz}}). \quad (\text{F.29})$$

This error signal can be converted from units of differential cavity length ( $\text{m}/\sqrt{\text{Hz}}$ ) to temperature mismatch ( $\text{K}/\sqrt{\text{Hz}}$ ) via a conversion factor derived from equation 10.8

$$C = \left[ nL_c \left( \frac{1}{n} \left( \frac{dn_b}{dT} - \frac{dn_a}{dT} \right) + (\alpha_b - \alpha_a) \right) \right]^{-1} (\text{K}/\text{m}). \quad (\text{F.30})$$

<sup>2</sup>This result is  $\sqrt{3/2}$  greater than that in reference [143] because we include non-stationary shot noise.

---

For the parameters used here,  $C = 2.19 \times 10^{-7}$ . So the shot noise limit to reading out the temperature fluctuations is

$$S_{snl,Tot} = 4.63 \times 10^{-11} (\text{K}/\sqrt{\text{Hz}}), \quad (\text{F.31})$$

Much smaller than the noise floor measured here.



---

# Bibliography

---

- [1] <http://ilog.ligo-wa.caltech.edu:7285/advligo/Bench>.
- [2] <http://lisa.jpl.nasa.gov/gallery.html>.
- [3] <http://www.srl.caltech.edu/shane/sensitivity/>.
- [4] Amnon Yariv, *Quantum Electronics*, John Wiley & Sons., Singapore, 3rd edition, 1989.
- [5] M. L. Bortz, *Quasi-Phasematched Optical Frequency Conversion in Lithium Niobate Waveguides*, PhD thesis, Stanford University, Stanford, California, 1994.
- [6] R. E. Slusher, L. W. Hollberg, B. Yurke, J. C. Mertz, and J. F. Valley, *Observation of Squeezed States Generated by Four-Wave Mixing in an Optical Cavity*, Phys. Rev. Lett. **55**, 2409 (1985).
- [7] L.-A. Wu, H. J. Kimble, J. L. Hall, and H. Wu, *Generation of squeezed states by parametric down conversion*, Phys. Rev. Lett. **57**, 2520 (1986).
- [8] P. Grangier, R. E. Slusher, B. Yurke, and A. LaPorta, *Squeezed-light enhanced polarization interferometer*, Phys. Rev. Lett. **59**, 2153 (1987).
- [9] M. Xiao, L. A. Wu, and H. J. Kimble, *Precision measurement beyond the shot-noise limit*, Phys. Rev. Lett. **59**, 278 (1987).
- [10] E. S. Polzik, J. Carri, and H. J. Kimble, *Atomic spectroscopy with squeezed light for sensitivity beyond the vacuum-state limit*, Appl. Phys. B **55**, 279 (1992).
- [11] G. Breitenbach, T. Müller, S. F. Pereira, J.-Ph. Poizat, S. Schiller, and J. Mlynek, *Squeezed vacuum from a monolithic optical parametric oscillator*, J. Opt. Am. Soc. B **12**, 2304 (1995).
- [12] K. Schneider, R. Bruckmeier, H. Hansen, S. Schiller, and J. Mlynek, *Bright squeezed-light generation by a continuous-wave semimonolithic parametric amplifier*, Opt. Lett. **21**, 1396 (1996).
- [13] K. Schneider, M. Lang, J. Mlynek, and S. Schiller, *Generation of strongly squeezed continuous-wave light at 1064 nm*, Opt. Ex. **2**, 59 (1997).
- [14] P.K. Lam, T.C. Ralph, B.C. Buchler, D.E. McClelland, H-A. Bachor, and J. Gao, *Optimization and transfer of vacuum squeezing from an optical parametric oscillator*, J. Opt. B **1**, 469 (1999).
- [15] B. C. Buchler, *Electro-optic Control of Quantum Measurements*, PhD thesis, Physics Department, The Australian National University, Canberra, Australia, 2001.
- [16] S. Suzuki, H. Yonezawa, F. Kannari, M. Sasaki, and A. Furusawa, *7 dB quadrature squeezing at 860 nm with periodically poled KTiOPO<sub>4</sub>*, Appl. Phys. Lett. **89**, 061116 (2006).

## Bibliography

---

- [17] H. Vahlbruch, S. Chelkowski, K. Danzmann, and R. Schnabel, *Quantum engineering of squeezed states for quantum communication and metrology*, *New J. Phys.* **9**, 371 (2007).
- [18] H. Vahlbruch, M. Mehmet, N. Lastzka, B. Hage, S. Chelkowski, A. Franzen, S. Goßler, K. Danzmann, and R. Schnabel, *Observation of squeezed light with 10dB quantum noise reduction*, *quant-ph arXiv:0706.1431v1* (2007).
- [19] K. Goda, *Development of Techniques for Quantum-Enhanced Laser-Interferometric Gravitational-Wave Detectors*, PhD thesis, Massachusetts Institute of Technology, Cambridge, 2007.
- [20] Yuishi Takeno, Mitsuyoshi Yukawa, Hidehiro Yonezawa, and Akira Furusawa, *Observation of -9 dB quadrature squeezing with improvement of phase stability in homodyne measurement*, *Opt. Express* **15**, 4321 (2007).
- [21] W. P. Bowen, R. Schnabel, N. Treps, H.-A. Bachor, and P. K. Lam, *Recovery of continuous wave squeezing at low frequencies*, *J. Opt. B* **4**, 421 (2002).
- [22] R. Schnabel, H. Vahlbruch, A. Franzen, S. Chelkowski, N. Grosse, H.-A. Bachor, W.P. Bowen, P.K. Lam, and K. Danzmann, *Squeezed light at sideband frequencies below 100 kHz from a single OPA*, *Opt. Com.* **240**, 185 (2004).
- [23] J. Laurat, T. Coudreau, G. Keller, N. Treps, and C. Fabre, *Compact source of Einstein-Podolsky-Rosen entanglement and squeezing at very low noise frequencies*, *Phys. Rev. A* **70**, 042315 (2004).
- [24] K. McKenzie, N. Grosse, W. P. Bowen, S. E. Whitcomb, M. B. Gray, D. E. McClelland, and P. K. Lam, *Squeezing in the Audio Gravitational-Wave Detection Band*, *Phys. Rev. Lett.* **93**, 161105 (2004).
- [25] Kirk McKenzie, Malcolm B Gray, Stefan Goßler, Ping Koy Lam, and David E McClelland, *Squeezed state generation for interferometric gravitational-wave detection*, *Classical and Quantum Gravity* **23**, S245 (2006).
- [26] H. Vahlbruch, S. Chelkowski, B. Hage, A. Franzen, K. Danzmann, and R. Schnabel, *Coherent Control of Vacuum Squeezing in the Gravitational-Wave Detection Band*, *Phys. Rev. Lett.* **97**, 011101 (2006).
- [27] <http://www.innolight.de/>.
- [28] S. Whitcomb, *Ground-based gravitational wave detection: now and future*, Proceedings of Amaldi 7 LIGO document LIGO-P070146-00-Z (2007).
- [29] <http://www.ligo.caltech.edu/advLIGO/>.
- [30] E. Gustafson, D. Shoemaker, K. Strain, and R. Weiss, *LSC White Paper on Detector Research and Development*, LIGO T990080-00-D (1999).
- [31] C. M. Caves, *Quantum-mechanical radiation-pressure fluctuations in an interferometer*, *Phys. Rev. Lett.* **45**, 75 (1980).
- [32] V. B. Braginsky, M. L. Gorodetsky, F. Ya. Khalili, A. B. Matsko, K. S. Thorne, and S. P. Vyatchanin, *Noise in gravitational-wave detectors and other classical-force measurements is not influenced by test-mass quantization*, *Phys. Rev. D* **67**, 082001 (2003).

- [33] V. B. Braginsky and F. Y. Khalili, *Quantum Measurement*, ed. K. S. Thorne, Cambridge University Press, Cambridge, 1st edition, 1992.
- [34] C. M. Caves, *Quantum-mechanical noise in an interferometer*, Phys. Rev. D **23**, 1693 (1981).
- [35] W. G. Unruh, p. 647. in *Quantum Optics, Experimental Gravitation and Measurement Theory*, Edited by P. Meystre and M. O. Scully, Plenum, New York University Press, 1983.
- [36] M. T. Jaekel and S. Reynaud, *Quantum Limits in Interferometric Measurements*, Europhysics Letters (EPL) **13**, 301 (1990).
- [37] V. Chickarmane, S. V. Dhurandhar, T. C. Ralph, M. B. Gray, H-A. Bachor, and D. E. McClelland, *Squeezed light in a frontal-phase-modulated signal-recycled interferometer*, Phys. Rev. A **57**, 3898 (1998).
- [38] H. J. Kimble, Y. Levin, A. B. Matsko, K. S. Thorne, and S. P. Vyatchanin, *Conversion of conventional gravitational-wave interferometers into quantum nondemolition interferometers by modifying their input and/or output optics*, Phys. Rev. D **65**, 31 (2002).
- [39] J. Harms, Y. Chen, S. Chelkowski, A. Franzen and H. Vahlbruch, K. Danzmann, and R. Schnabel, *Squeezed-input, optical-spring, signal-recycled gravitational-wave detectors*, Phys. Rev. D **68**, 042001 (2003).
- [40] A. Buonanno and Y. Chen, *Improving the sensitivity to gravitational-wave sources by modifying the input-output optics of advanced interferometers*, Phys. Rev. D **69**, 102004 (2004).
- [41] C. A. J. Putman, B. G. De Grooth, N. F. Van Hulst, and J. Greve, *A detailed analysis of the optical beam deflection technique for use in atomic force microscopy*, J. of App. Phys. **72**, 6 (1992).
- [42] E. S. Polzik, J. C. Carri, and H. J. Kimble, *Spectroscopy with squeezed light*, Phys. Rev. Lett. **68**, 3020 (1992).
- [43] S. A. Haine, M. K. Olsen, and J. J. Hope, *Generating Controllable Atom-Light Entanglement with a Raman Atom Laser System*, Phys. Rev. Lett. **96**, 133601 (2006).
- [44] A. Einstein, *Die grundlage der allgemeinen relativitätstheorie*, Ann. Phys. Lpz **49**, 769 (1916).
- [45] A. Einstein, *Näherungsweise integration der feldgleich der gravitation*, Preuss. Akad. Wiss. Berlin , 688 (1916).
- [46] R. A. Hulse and J. H. Taylor, *Discovery of a pulsar in a binary system*, Astrophys. J. (Letters) **195**, L51 (1975).
- [47] J. H. Taylor and J. M. Weisberg, *A new test of general relativity: gravitational radiation and the binary pulsar PSR 1913+16*, Astrophys. J. **253**, 908 (1982).
- [48] J. H. Taylor and J. M. Weisberg, *Further experimental tests of relativistic gravity using the binary pulsar PSR 1913+16*, Astrophys. J. **345**, 434 (1989).
- [49] S. A. Hughes, S. Marka, P. L. Bender, and C. J. Hogan, *New physics and astronomy with the new gravitational-wave observatories*, arXiv:astro-ph/0110349v2 (2001).

- [50] P. R. Saulson, *Fundamentals of interferometric gravitational wave detectors*, World Scientific, Singapore, 1st edition, 1994.
- [51] J. Weber, *Detection and Generation of Gravitational Waves*, Phys. Rev. **117**, 306 (1960).
- [52] P. Astone, D. Babusci, L. Baggio, M. Bassan, M. Bignotto, M. Bonaldi, M. Camarda, P. Carelli, G. Cavallari, M. Cerdonio, A. Chincarini, E. Coccia, L. Conti, S. D'Antonio, M. De Rosa, M. di Paolo Emilio, M. Drago, F. Dubath, V. Fafone, P. Falferi, S. Foffa, P. Fortini, S. Frasca, G. Gemme, G. Giordano, G. Giusfredi, W. O. Hamilton, J. Hanson, M. Inguscio, W. W. Johnson, N. Liguori, S. Longo, M. Maggiore, F. Marin, A. Marini, M. P. McHugh, R. Mezzena, P. Miller, Y. Minenkov, A. Mion, G. Modestino, A. Moleti, D. Nettles, A. Ortolan, G. V. Pallottino, R. Parodi, G. Piano Mortari, S. Poggi, G. A. Prodi, L. Quintieri, V. Re, A. Rocchi, F. Ronga, F. Salemi, G. Soranzo, R. Sturani, L. Taffarello, R. Terenzi, G. Torrioli, R. Vaccarone, G. Vandoni, G. Vedovato, A. Vinante, M. Visco, S. Vitale, J. Weaver, J. P. Zendri, and P. Zhang IGEC-2 Collaboration, *Results of the IGEC-2 search for gravitational wave bursts during 2005*, Phys. Rev. D **76**, 102001 (2007).
- [53] M. E. Gertsenshtein and V. I. Pustovoit, Soviet Physics - JETP **16**, 433 (1963).
- [54] G. E. Moss, L. R. Miller, and R. L. Forward, *Photon-noise-limited laser transducer for gravitational antenna*, Appl. Opt. **10**, 2495 (1971).
- [55] M. Cerdonio, L. Conti, J. A. Lobo, A. Ortolan, L. Taffarello, and J. P. Zendri, *Wideband Dual Sphere Detector of Gravitational Waves*, Phys. Rev. Lett. **87**, 031101 (2001).
- [56] <http://wwwcascina.virgo.infn.it/advirgo/>.
- [57] B. Abbott *et al* (The LIGO Scientific Collaboration), *Detector description and performance for the first coincidence observations between LIGO and GEO*, Nuclear Instruments and Methods **517**, 154 (2004).
- [58] The LIGO Scientific Collaboration: B. Abbott *et al.*, LIGO: The Laser Interferometer Gravitational-Wave Observatory, quant-ph arXiv:0711.3041v1 (2007).
- [59] <http://www.ligo.caltech.edu/>.
- [60] F. Acernese, P. Amico, M. Alshourbagy, F. Antonucci, S. Aoudia, P. Astone, S. Avino, D. Babusci, G. Ballardín, F. Barone, L. Barsotti, M. Barsuglia, F. Beauville, S. Bigotta, S. Birindelli, M. A. Bizouard, C. Boccara, F. Bondu, L. Bosi, C. Bradaschia, S. Braccini, A. Brillet, V. Brisson, D. Buskulic, E. Calloni, E. Campagna, F. Carbognani, F. Cavalier, R. Cavalieri, G. Cella, E. Cesarini, E. Chassande-Mottin, N. Christensen, C. Corda, A. Corsi, F. Cottone, A.-C. Clapson, F. Cleva, J.-P. Coulon, E. Cuoco, A. Dari, V. Dattilo, M. Davier, M. del Prete, R. De Rosa, L. Di Fiore, A. Di Virgilio, B. Dujardin, A. Eleuteri, I. Ferrante, F. Fidecaro, I. Fiori, R. Flaminio, J.-D. Fournier, S. Frasca, F. Frasconi, L. Gammaitoni, F. Garufi, E. Genin, A. Genai, A. Giazotto, G. Giordano, L. Giordano, R. Gouaty, D. Grosjean, G. Guidi, S. Hebri, H. Heitmann, P. Hello, S. Karkar, S. Kreckelbergh, P. La Penna, M. Laval, N. Leroy, N. Letendre, B. Lopez, M. Lorenzini, V. Loriette, G. Losurdo, J.-M. Mackowski, E. Majorana, C. N. Man, M. Mantovani, F. Marchesoni, F. Marion, J. Marque, F. Martelli, A. Masserot, M. Mazzoni, L. Milano, F. Menzinger, C. Moins, J. Moreau, N. Morgado, B. Mours, F. Nocera, C. Palomba, F. Paoletti, S. Pardi, A. Pasqualetti, R. Passaquieti, D. Passuello, F. Piergiovanni, L. Pinard, R. Poggiani, M. Punturo, P. Puppó, K. Qipiani, P. Rapagnani, V. Reita, A. Remillieux, F. Ricci, I. Ricciardi, P. Ruggi, G. Russo, S. Solimeno, A. Spallicci, M. Tarallo, M. Tonelli, A. Toncelli,

- E Tournefier, F Travasso, C Tremola, G Vajente, D Verkindt, F Vetrano, A Viceré, J-Y Vinet, H Vocca, and M Yvert, *Status of Virgo detector*, *Classical and Quantum Gravity* **24**, S381 (2007).
- [61] <http://www.virgo.infn.it/>.
- [62] H Lück, M Hewitson, P Ajith, B Allen, P Aufmuth, C Aulbert, S Babak, R Balasubramanian, B W Barr, S Berukoff, A Bunkowski, G Cagnoli, C A Cantley, M M Casey, S Chelkowski, Y Chen, D Churches, T Cokelaer, C N Colacino, D R M Crooks, C Cutler, K Danzmann, R J Dupuis, E Elliffe, C Fallnich, A Franzen, A Freise, I Gholami, S Goßler, A Grant, H Grote, S Grunewald, J Harms, B Hage, G Heinzl, I S Heng, A Hepstonstall, M Heurs, S Hild, J Hough, Y Itoh, G Jones, R Jones, S H Huttner, K Kötter, B Krishnan, P Kwee, M Luna, B Machenschalk, M Malec, R A Mercer, T Meier, C Messenger, S Mohanty, K Mossavi, S Mukherjee, P Murray, G P Newton, M A Papa, M Perreux-Lloyd, M Pitkin, M V Plissi, R Prix, V Quetschke, V Re, T Regimbau, H Rehbein, S Reid, L Ribichini, D I Robertson, N A Robertson, C Robinson, J D Romano, S Rowan, A Rüdiger, B S Sathyaprakash, R Schilling, R Schnabel, B F Schutz, F Seifert, A M Sintes, J R Smith, P H Sneddon, K A Strain, I Taylor, R Taylor, A Thüring, C Ungarelli, H Vahlbruch, A Vecchio, J Veitch, H Ward, U Weiland, H Welling, L Wen, P Williams, B Willke, W Winkler, G Woan, and R Zhu, *Status of the GEO600 detector*, *Classical and Quantum Gravity* **23**, S71 (2006).
- [63] <http://geo600.aei.mpg.de/>.
- [64] M. Ando, K. Arai, R. Takahashi, G. Heinze, S. Kawamura, D. Tatsumi, N. Kanda, H. Tagoshi, A. Araya, H. Asada, Y. Aso, M. A. Barton, M-K. Fujimoto, M. Fukushima, T. Futamase, K. Hayama, G. Horikoshi, H. Ishizuka, N. Kamikubota, K. Kawabe, N. Kawashima, Y. Kobayashi, Y. Kojima, K. Kondo, Y. Kozai, K. Kuroda, and N. Matsuda, *Stable Operation of a 300-m Laser Interferometer with Sufficient Sensitivity to Detect Gravitational-Wave Events within Our Galaxy*, *Phys. Rev. Lett.* **86**, 3950 (2001).
- [65] <http://tamago.mtk.nao.ac.jp/>.
- [66] B Willke, P Ajith, B Allen, P Aufmuth, C Aulbert, S Babak, R Balasubramanian, B W Barr, S Berukoff, A Bunkowski, G Cagnoli, C A Cantley, M M Casey, S Chelkowski, Y Chen, D Churches, T Cokelaer, C N Colacino, D R M Crooks, C Cutler, K Danzmann, R J Dupuis, E Elliffe, C Fallnich, A Franzen, A Freise, I Gholami, S Goßler, A Grant, H Grote, S Grunewald, J Harms, B Hage, G Heinzl, I S Heng, A Hepstonstall, M Heurs, M Hewitson, S Hild, J Hough, Y Itoh, G Jones, R Jones, S H Huttner, K Kötter, B Krishnan, P Kwee, H Lück, M Luna, B Machenschalk, M Malec, R A Mercer, T Meier, C Messenger, S Mohanty, K Mossavi, S Mukherjee, P Murray, G P Newton, M A Papa, M Perreux-Lloyd, M Pitkin, M V Plissi, R Prix, V Quetschke, V Re, T Regimbau, H Rehbein, S Reid, L Ribichini, D I Robertson, N A Robertson, C Robinson, J D Romano, S Rowan, A Rüdiger, B S Sathyaprakash, R Schilling, R Schnabel, B F Schutz, F Seifert, A M Sintes, J R Smith, P H Sneddon, K A Strain, I Taylor, R Taylor, A Thüring, C Ungarelli, H Vahlbruch, A Vecchio, J Veitch, H Ward, U Weiland, H Welling, L Wen, P Williams, W Winkler, G Woan, and R Zhu, *The GEO-HF project*, *Classical and Quantum Gravity* **23**, S207 (2006).
- [67] T Uchiyama, K Kuroda, M Ohashi, S Miyoki, H Ishitsuka, K Yamamoto, H Hayakawa, K Kasahara, M-K Fujimoto, S Kawamura, R Takahashi, T Yamazaki, K Arai, D Tatsumi, A Ueda, M Fukushima, S Sato, Y Tsunesada, Zong-Hong Zhu, T Shintomi, A Yamamoto,

- T Suzuki, Y Saito, T Haruyama, N Sato, Y Higashi, T Tomaru, K Tsubono, M Ando, K Numata, Y Aso, K-I Ueda, H Yoneda, K Nakagawa, M Musha, N Mio, S Moriwaki, K Somiya, A Araya, A Takamori, N Kanda, S Telada, H Tagoshi, T Nakamura, M Sasaki, T Tanaka, K-I Ohara, H Takahashi, S Nagano, O Miyakawa, and M E Tobar, *Present status of large-scale cryogenic gravitational wave telescope*, *Classical and Quantum Gravity* **21**, S1161 (2004).
- [68] D. E. McClelland, S. M. Scott, M. B. Gray, D. A. Shaddock, B. J. Slagmolen, A. Searle, D. G. Blair, L. Ju, J. Winterflood, F. Benabid, M. Baker, J. Munch, P. J. Veitch, M. W. Hamilton, M. Ostermeyer, D. Mudge, D. Ottaway, and C. Hollitt, *Second-generation laser interferometry for gravitational wave detection: ACIGA progress*, *Class. Quant. Grav.* **18**, 4121 (2001).
- [69] P. R. Saulson, *Terrestrial gravitational noise on a gravitational wave antenna*, *Phys. Rev. D* **30**, 732 (1984).
- [70] S. A. Hughes and K. S. Thorne, *Seismic gravity-gradient noise in interferometric gravitational-wave detectors*, *Phys. Rev. D* **58**, 122002 (1998).
- [71] J-Y Vinet, V Brisson, and S Braccini, *Scattered light noise in gravitational wave interferometric detectors: Coherent effects*, *Phys. Rev. D* **54**, 1276 (1996).
- [72] R Abbott, R Adhikari, G Allen, S Cowley, E Daw, D DeBra, J Giaime, G Hammond, M Hammond, C Hardham, J How, W Hua, W Johnson, B Lantz, K Mason, R Mittleman, J Nichol, S Richman, J Rollins, D Shoemaker, G Stapfer, and R Stebbins, *Seismic isolation for Advanced LIGO*, *Classical and Quantum Gravity* **19**, 1591 (2002).
- [73] H. B. Callen and T. A. Welton, *Irreversibility and generalised noise*, *Phys. Rev.* **83**, 34 (1951).
- [74] P. R. Saulson, *Thermal noise in mechanical experiments*, *Phys. Rev. D* **42**, 2437 (1990).
- [75] G. M. Harry, A. M. Gretarsson, P. R. Saulson, S. E. Kittelberger, S. D. Penn, W. J. Startin, S. Rowan, M. M. Fejer, D. R. M. Crooks, G. Cagnoli, J. Hough, and N. Nakagawa, *Thermal noise in interferometric gravitational wave detectors due to dielectric optical coatings*, *Class. and Quant. Grav.* **19**, 897 (2002).
- [76] V. B. Braginsky, M. L. Gorodetsky, and S. P. Vyatchanin, *Thermodynamical fluctuations and photo-thermal shot noise in gravitational wave antennae*, *Phys. Lett. A* **264**, 1 (1999).
- [77] V. B. Braginsky, M. L. Gorodetsky, and S. P. Vyatchanin, *Thermo-refractive noise in gravitational wave antennae*, *Phys. Lett. A* **271**, 303 (2000).
- [78] <http://lisa.nasa.gov/> and [http://sci.esa.int/science\\_e/www/area/index.cfm?fareaid=27](http://sci.esa.int/science_e/www/area/index.cfm?fareaid=27).
- [79] <http://www.universe.nasa.gov/program/bbo.html>.
- [80] D. F. Walls and G. J. Milburn, *Quantum Optics*, Springer-Verlag, Berlin, 1st edition, 1994.
- [81] W. Heisenberg, *The Physical Principles of the Quantum Theory*, Dover, New York, 1st edition, 1930.
- [82] D. J. Griffiths, *Introduction to Quantum Mechanics*, Prentice Hall, New Jersey, 1st edition, 1994.

- [83] J. M. Shapiro, G. Saplakoglu, S.-T. Ho, P. Kumar, B. E. A. Saleh, and M. C. Teich, *Theory of light detection in the presence of feedback*, J. Opt. Soc. Am. B **4**, 1604 (1987).
- [84] T. Day, A. C. Nilsson, M. M. Fejer, A. D. Farinas, E. K. Gustafson, C. D. Nabors, and R. L. Byer, *30 Hz-linewidth, diode-laser-pumped, Nd:GGG nonplanar ring oscillators by active frequency stabilisation*, Electron. Lett. **25**, 810 (1989).
- [85] A. Rüdiger, R. Schilling, L. Schnupp, W. Winkler, H. Billing, and K. Maischberger, *A mode selector to suppress fluctuations in laser beam geometry*, Optica Acta **28**, 641 (1981).
- [86] S. U. Seel R.L. Savage Jr, P.J. King, *A Highly-Stabilized 10-Watt Nd: YAG Laser for the Laser Interferometer Gravitational-Wave Observatory*, LIGO Document-P980002-00-D (1998).
- [87] B. Yurke, *Use of cavities in squeezed state generation*, Phys. Rev. A **20**, 408 (1984).
- [88] H. P. Yuen and V. W. S. Chen, *Noise in homodyne and heterodyne detection*, Opt. Lett. **8**, 177 (1983).
- [89] A. G. White, *Classical and quantum dynamics of optical frequency conversion*, PhD thesis, Physics Department, The Australian National University, Canberra, Australia, 1995.
- [90] A. E. Siegman, *Lasers*, University Science Books, Mill Valley, California, 1986.
- [91] B. E. A. Saleh and M. C. Teich, *Fundamentals of Photonics*, John Wiley & Sons, Inc., New York, 1st edition, 1991.
- [92] P. D. Maker, R. W. Terhune, M. Nisenoff, and C. M. Savage, *Effects of dispersion and focusing on the production of optical harmonics*, Phys. Rev. Lett. **8**, 21 (1962).
- [93] J. A. Giordmaine, *Mixing of light beams in crystals*, Phys. Rev. Lett. **8**, 19 (1962).
- [94] J. A. Armstrong, N. Bloembergen, J. Ducuing, and P. S. Pershan, *Interactions between light waves in a nonlinear dielectric*, Phys. Rev. **127**, 1918 (1962).
- [95] P. A. Franken and J. F. Ward, *Optical harmonics and nonlinear phenomena*, Rev. Mod. Phys. **35**, 23 (1963).
- [96] R. C. Eckardt, C. D. Nabors, W. J. Kozlovsky, and R. L. Byer, *Optical parametric oscillator frequency tuning and control*, J. Opt. Soc. Am. B **8**, 646 (1991).
- [97] D.S. Hum and M.M. Fejer, *Quasi-phase-matching*, C. R. Physique **8**, 180 (2007).
- [98] M. J. Collett and C. W. Gardiner, *Squeezing of intracavity and travelling-wave light fields produced in parametric amplification*, Phys. Rev. A **30**, 1386 (1984).
- [99] P. K. Lam, *Applications of quantum electro-optic control and squeezed light*, PhD thesis, Physics Department, The Australian National University, Canberra, Australia, 1998.
- [100] K. Wodkiewicz and M.S. Zubairy, *Effect of laser fluctuations on squeezed states in a degenerate parametric amplifier*, Phys. Rev. A **27**, 2003 (1983).
- [101] G. Scharf and D. F. Walls, *Effect of pump quantisation of squeezing in parametric amplifiers*, Opt. Comm. **50**, 245 (1984).

## Bibliography

---

- [102] C. M. Caves and D. D. Crouch, *Quantum wideband traveling-wave analysis of a degenerate parametric amplifier*, J. Opt. Soc. Am. B **4**, 1535 (1987).
- [103] D.D. Crouch and S.L. Braunstein, *Limitations to squeezing in a parametric amplifier due to pump quantum fluctuations*, Phys. Rev. A **38**, 4696 (1988).
- [104] J. Gea-Banacloche and M.S. Zubairy, *Influence of pump-phase fluctuations on the squeezing in a degenerate parametric oscillator*, Phys. Rev. A **42**, 1742 (1990).
- [105] S. Prasad, *Quantum noise and squeezing in an optical parametric oscillator with arbitrary output-mirror coupling. III. Effect of pump amplitude and phase fluctuations*, Phys. Rev. A **49**, 1406 (1994).
- [106] K.-X. Sun, M. M. Fejer, E. K. Gustafson, and R. L. Byer, *Sagnac interferometer for gravitational-wave detection*, Phys. Rev. Lett. **76**, 3053 (1996).
- [107] Y. Chen, *Sagnac interferometer as a speed-meter-type, quantum-nondemolition gravitational-wave detector*, Phys. Rev. D **67**, 122004 (2003).
- [108] J. Harms, *Quantum Noise in the Laser-Interferometer Gravitational-Wave Detector GEO600*, Master's thesis, Universitat Hannover, Hannover, Germany, 2002, available at <http://www.geo600.uni-hannover.de/personal/harms.html>.
- [109] C. M. Caves and B. L. Schumaker, *New formalism for two-photon quantum optics. I. Quadrature phases and squeezed states*, Phys. Rev. A **31**, 3068 (1985).
- [110] B. L. Schumaker and C. M. Caves, *New formalism for two-photon quantum optics. II. Mathematical foundation and compact notation*, Phys. Rev. A **31**, 3093 (1985).
- [111] V. B. Braginsky, M. L. Gorodetsky, F. Ya. Khalili, and K. S. Thorne, *Dual-resonator speed meter for a free test mass*, Phys. Rev. D **61**, 044002 (2000).
- [112] P. Purdue, *Analysis of a quantum nondemolition speed-meter interferometer*, Phys. Rev. D **66**, 022001 (2002).
- [113] P. Purdue and Y. Chen, *Practical speed meter designs for quantum nondemolition gravitational-wave interferometers*, Phys. Rev. D **66**, 122004 (2002).
- [114] S. P. Vyatchanin and A. B. Matsko, *Quantum limit on force measurements*, Sov. Phys. JETP **77**, 218 (1993).
- [115] K. McKenzie, D. A. Shaddock, D. E. McClelland, B. C. Buchler, and P. K. Lam, *Experimental Demonstration of a Squeezing-Enhanced Power-Recycled Michelson Interferometer for Gravitational Wave Detection*, Phys. Rev. Lett. **88**, 231102 (2002).
- [116] K. McKenzie, *Experimental Demonstration of a Gravitational Wave Detector Configuration Below the Shot Noise Limit*, Master's thesis, Physics Department, The Australian National University, Canberra, Australia, 2002.
- [117] A. Buonanno and Y. Chen, *Quantum noise in second generation, signal-recycled laser interferometric gravitational-wave detectors*, Phys. Rev. D **64**, 042006 (2001).
- [118] A. Buonanno and Y. Chen, *Signal recycled laser interferometer gravitational wave detectors as optical springs*, Phys. Rev. D **65**, 042001 (2002).

- [119] P. Nutzman, V. Kalogera, S. L. Finn, C. Hendrickson, and K. Belczynski, *Gravitational Waves from Extragalactic Inspiral Binaries: Selection Effects and Expected Detection Rates*, The Astrophysical Journal **612**, 364 (2004).
- [120] K. Bergman and H. A. Haus, *Squeezing in fibers with optical pulses*, Opt. Lett. **16**, 663 (1991).
- [121] K. Goda, K. McKenzie, E.E. Mikhailov, P.K. Lam, D.E. McClelland, and N. Mavalvala, *Photothermal fluctuations as a fundamental limit to low-frequency squeezing in a degenerate optical parametric oscillator*, Phys. Rev. A **72**, 043819 (2005).
- [122] A. G. White, M. S. Taubman, T. C. Ralph, P. K. Lam, D. E. McClelland, and H.-A. Bachor, *Experimental test of modular noise propagation theory for quantum optics*, Phys. Rev. A **54**, 3400 (1996).
- [123] Y. Lai, H. A. Haus, and Y. Yamamoto, *Squeezed vacuum from amplitude squeezed states*, Opt. Lett. **16**, 1517 (1991).
- [124] T. C. Ralph and A. G. White, *Retrieving squeezing from classically noisy light in second-harmonic generation*, J. Opt. Soc. Am. B **12**, 833 (1995).
- [125] G. Hétet, O. Glöckl, K. A. Pilypas, C. C. Harb, B. C. Buchler, H-A Bachor, and P. K. Lam, *Squeezed light for bandwidth-limited atom optics experiments at the rubidium D1 line*, J. Phys. B **40**, 221 (2007).
- [126] K. Goda, E. E. Mikhailov, O. Miyakawa, S. Saraf, S. Vass, A. Weinstein, and N. Mavalvala, *Generation of a stable low-frequency squeezed vacuum field with periodically-poled KTiOPO<sub>4</sub> at 1064nm*, arXiv:quant-ph/0703001v1 (2007).
- [127] C. F. McCormick, A. M. Marino, V. Boyer, and P. D. Lett, *Relative-intensity squeezing at audio frequencies using four-wave mixing in an atomic vapor*, arXiv:quant-ph/0703111v1 (2007).
- [128] K. Goda, O. Miyakawa, E. E. Mikhailov, S. Saraf, R. Adhikari, K. McKenzie, R. Ward, S. Vass, A. Weinstein, and N. Mavalvala, *Quantum Enhancement in a Prototype Gravitational Wave Detector*, LSC Technical Review (2007).
- [129] [http://www.ligo.caltech.edu/~ajw/40m\\_upgrade.html](http://www.ligo.caltech.edu/~ajw/40m_upgrade.html).
- [130] H. Mabuchi, E. S. Polzik, and H. J. Kimble, *Blue-light induced infrared absorption in KNbO<sub>3</sub>*, J. Opt. Soc. Am. B **11**, 2023 (1994).
- [131] Y. Furukawa, K. Kitamura, A. Alexandrovski, R. K. Route, M. M. Fejer, and G. Foulon, *Green-induced infrared absorption in MgO doped LiNbO<sub>3</sub>*, Appl. Phys. Lett. **78**, 1970 (2001).
- [132] J. C. Jacco, D. R. Rockafellow, and E. A. Teppo, *Bulk-darkening threshold of flux-grown KTiOPO<sub>4</sub>*, Opt. Lett. **16**, 1307 (1991).
- [133] R. Blachman, P. F. Bordui, and M. M. Fejer, *Laser-induced photochromic damage in potassium titanyl phosphate*, Appl. Phys. Lett. **64**, 1318 (1994).
- [134] N. B. Grosse, W. P. Bowen, K. McKenzie, and P. K. Lam, *Harmonic Entanglement with Second-Order Nonlinearity*, Phys. Rev. Lett. **96**, 063601 (2006).

## Bibliography

---

- [135] W. P. Bowen, *Experiments towards a Quantum Information Network with Squeezed Light and Entanglement*, PhD thesis, Physics Department, The Australian National University, Canberra, Australia, 2003.
- [136] D. A. Shaddock, M. B. Gray, and D. E. Mclelland, *Frequency locking a laser to an optical cavity by use of spatial mode interference*, *Opt. Lett.* **24**, 1499 (1999).
- [137] Simon Chelkowski, Henning Vahlbruch, Karsten Danzmann, and Roman Schnabel, *Coherent control of broadband vacuum squeezing*, *Physical Review A (Atomic, Molecular, and Optical Physics)* **75**, 043814 (2007).
- [138] G. D. Boyd and D. A. Kleinman, *Parametric Interaction of Focussed Gaussian Light Beams*, *J. Appl. Phys.* **39**, 3597 (1968).
- [139] <http://www.isowave.com>.
- [140] H. Vahlbruch, S. Chelkowski, B. Hage, A. Franzen, K. Danzmann, and R. Schnabel, *Squeezed-field injection for gravitational wave interferometers*, *Classical and Quantum Gravity* **23**, S251 (2006).
- [141] <http://www.raicol.com/>.
- [142] R. W. P. Drever, J. L. Hall, F. V. Kowalski, J. Hough, G. M. Ford, A. J. Munley, and H. Ward, *Laser phase and frequency stabilization using an optical resonator*, *Appl. Phys. B* **31**, 97 (1983).
- [143] E. D. Black, *An introduction to Pound-Drever-Hall laser frequency stabilization*, *Am. J. Phys.* **69**, 79 (2001).
- [144] B. Lantz, D. Shoemaker, and J. Kerman, *Spatial Uniformity of Silicon Photodiodes*, LIGO document T952007, <http://www.ligo.caltech.edu/docs/T/T952014-00.pdf> (1999).
- [145] P. Csatorday, A. Marin, and M. Zucker, *Photodiodes for Initial and Advanced LIGO*, LIGO document G980022-00-D. <http://www.ligo.caltech.edu/docs/G980022-00-D> (1998).
- [146] J-Y. Vinet, V. Brisson, S. Braccini, I. Ferrante, L. Pinard, F. Bondu, and E. Tournié, *Scattered light noise in gravitational wave interferometric detectors: A statistical approach*, *Phys. Rev. D* **56**, 6085 (1997).
- [147] H. Vahlbruch, 2006, Private communication.
- [148] A.M. Joshi, G.H. Olsen, V.S. Ban, E. Mykiety, M.J. Lange Sr, and D.T. Mohr, *Reduction of 1/f noise in multiplexed linear In<sub>0.53</sub>Ga<sub>0.47</sub>As detector arrays via epitaxial doping*, *Electron Devices* **40**, 303 (1993).
- [149] F. Seifert, P. Kwee, M. Heurs, B. Willke, and K. Danzmann, *Laser power stabilization for second-generation gravitational wave detectors*, *Opt. Lett.* **31**, 2000 (2006).
- [150] L. He, Y. Lin, A. D. van Rheenen, A. van der Ziel, A. Young, and J. P. van der Ziel, *Low-frequency noise in small InGaAs/InP p-i-n diodes under different bias and illumination conditions*, *J. of Appl. Phys.* **68**, 5200 (1990).
- [151] *Large-area InGaAs photodiodes*, 2000.

- [152] S. Chua, Noise Sources in Experimental Squeezed Light Generation, Master's thesis, Physics Department, The Australian National University, Canberra, Australia, 2007, Available at <http://www.anu.edu.au/Physics/honours/past.html>.
- [153] <http://www.mathworks.com/>.
- [154] *Hewlett-Packard Technical Note, Application Note 150: Spectrum Analyser Basics*, 1992.
- [155] K. Krishnamoorthy, *Handbook of Statistical Distributions and their Applications*, Wiley-Interscience, 3rd edition, 2000.
- [156] E. D'Ambrosio, *Nonspherical mirrors to reduce thermoelastic noise in advanced gravitational wave interferometers*, Phys. Rev. D **67**, 102004 (2003).
- [157] Reference Design and Astrophysical Targets, <http://www.ligo.caltech.edu/advLIGO/>.
- [158] B Willke, K Danzmann, C Fallnich, M Frede, M Heurs, P King, D Kracht, P Kwee, R Savage, F Seifert, and R Wilhelm, *Stabilized High Power Laser for Advanced Gravitational Wave Detectors*, Journal of Physics: Conference Series **32**, 270 (2006).
- [159] W. Winkler, K. Danzmann, A. Rudiger, and R. Schilling, *Heating by optical absorption and the performance of interferometric gravitational-wave detectors*, Phys. Rev. A **44**, 7022 (1991).
- [160] V. B. Braginsky, S.E. Strigin, and S. P. Vyatchanin, *Parametric oscillatory instability in FabryPerot interferometer*, Phys. Lett. A **287**, 331 (2001).
- [161] C. Zhao, L. Ju, J. Degallaix, S. Gras, and D. G. Blair, *Parametric Instabilities and Their Control in Advanced Interferometer Gravitational-Wave Detectors*, Phys. Rev. Lett. **94**, 121102 (2005).
- [162] P. Fritschel, R. Adhikari, and R. Weiss, *Enhancements to the LIGO detectors*, LIGO Technical Document T050252-00-I, <http://www.ligo.caltech.edu/docs/T/T050252-00.pdf> (2005).
- [163] R. Adhikari, P. Fritschel, and S. Waldman, *Enhanced LIGO*, LIGO Technical Document T060156-01-I, <http://www.ligo.caltech.edu/docs/T/T060156-01.pdf> (2006).
- [164] Z. Y. Ou, S. F. Pereira, and H. J. Kimble, *Realization of the Einstein-Podolsky-Rosen paradox for continuous variables in nondegenerate parametric amplification*, Appl. Phys. B **55**, 265 (1992).
- [165] W. P. Bowen, R. Schnabel, P. K. Lam, and T. C. Ralph, *An experimental investigation of criteria for continuous variable entanglement*, Phys. Rev. Lett. **90**, 043601 (2003).
- [166] K. Goda, 2004, Private communication.
- [167] C. Schori, J. L. Sørensen, and E. S. Polzik, *Narrow-band frequency tunable light source of continuous quadrature entanglement*, Phys. Rev. A **66**, 033802 (2002).
- [168] L. W. Couch, *Digital and Analog Communications*, Prentice Hall, New Jersey, 6th edition, 2001.
- [169] Y. T. Liu and K. S. Thorne, *Thermoelastic noise and homogeneous thermal noise in finite sized gravitational-wave test masses*, Phys. Rev. D **62**, 122002 (2000).

## Bibliography

---

- [170] M. Cerdonio, L. Conti, A. Heidmann, and M. Pinard, *Thermoelastic effects at low temperatures and quantum limits in displacement measurements*, Phys. Rev. D **63**, 082003 (2001).
- [171] Laurent Longchambon, Nicolas Treps, Thomas Coudreau, Julien Laurat, and Claude Fabre, *Experimental evidence of spontaneous symmetry breaking in intracavity type II second-harmonic generation with triple resonance*, Opt. Lett. **30**, 284 (2005).
- [172] A. Buonanno, Y. Chen, and N. Mavalvala, *Quantum noise in laser-interferometer gravitational-wave detectors with a heterodyne readout scheme*, Phys. Rev. D **67**, 122005 (2003).
- [173] G. Imeshev, M. Proctor, and M. M. Fejer, *Phase correction in double-pass quasi-phase-matched second-harmonic generation with a wedged crystal*, Opt. Lett. **23**, 165 (1998).
- [174] J. Harms, R. Schnabel, and K. Danzmann, *Finite mass beam splitter in high power interferometers*, Phys. Rev. D. **70**, 102001 (2004).
- [175] <http://www.photon-laseroptik.de/>.
- [176] M.M. Fejer, G.A. Magel, D.H. Jundt, and R.L. Byer, *Quasi-phase-matched second harmonic generation: tuning and tolerances*, J. Quant. Elect. **28**, 2631 (1992).
- [177] N. Uehara, *Ring mode cleaner for the initial LIGO 10 Watt laser*, Internal report, Ginzton Laboratory, Stanford University (1997).
- [178] B. Willke, N. Uehara, E. K. Gustafson, R. L. Byer, P. J. King, S. U. Seel, and Jr. R. L. Savage, *Spatial and temporal filtering of a 10-W Nd:YAG laser with a Fabry–Perot ring-cavity premode cleaner*, Opt. Lett. **23**, 1704 (1998).
- [179] S. Pearl, H. Lotem, Y. Shimony, and S. Rosenwaks, *Optimization of laser intracavity second-harmonic generation by a linear dispersion element*, J. Opt. Soc. Am. B **16**, 1705 (1999).
- [180] <http://www.jdsu.com/>.
- [181] LG Gouy, *Sur une propriete nouvelle des ondes lumineuses*, CR Acad. Sci. Paris **110**, 1251 (1890).
- [182] T. Day, E. K. Gustafson, and R. L. Byer, *Sub-Hertz relative frequency stabilization of two diode laser pumped Nd:YAG lasers locked to a Fabry-Perot interferometer*, IEEE J. Q. Elect. **28**, 1106 (1992).
- [183] M. B. Gray, A. J. Stevenson, H.-A. Bachor, and D. E. McClelland, *Harmonic demodulation of nonstationary shot noise*, Opt. Lett. **18**, 759 (1993).